
Pulsed Electrodeposited Nanocrystalline Co-Cu alloys: Synthesis and Characterisation of Thermal and Mechanical Properties

Dissertation

Zur Erlangung des Grades
des Doktors der Ingenieurwissenschaften (Dr.-Ing.)
der Naturwissenschaftlich-Technischen Fakultät
der Universität des Saarlandes

Von
M. Sc. Killang Pratama

Saarbrücken

2021

Tag des Kolloquiums : 28. Juli 2021

Dekan : Prof. Dr. Jörn Erik Walter

Berichterstatter : Prof. Dr. Christian Motz
Prof. Dr. -Ing. Frank Mücklich

Vorsitz : Prof. Dr. -Ing. Stefan Diebels

Akad. Mitglied : Dr. -Ing. Frank Aubertin

**Printed and/or published with the support of
German Academic Exchange Service (DAAD)**

Acknowledgments

Remembering my time at the Chair of Materials Science and Methods in Saarland University, it was so memorable and amazing experiences for working in this place. I would like to express my gratefully acknowledge and appreciation to my supervisors, colleagues, friends, and family for giving supports and contributions for the accomplishment of my PhD work and dissertation.

First, I would like to show my gratitude to Prof. Dr. Christian Motz for giving me an opportunity and supervision of my PhD study. During my first time at the Institute, I had a lack of knowledges and experiences for working in advanced material science. Prof. Motz exceptionally helped me a lot with his valuable discussion, guidance, and support during my time working with some experiments and publications. His expertise in the wide range of materials science also inspired me for more exploration in this subject.

I would like to express my gratitude for the financial support from German Academic Exchange (DAAD) under Graduate School Scholarship Program (GSSP) (funding-ID: 57320205). I am grateful to financial support for SEM and APT devices from German Research Foundation (DFG INST 256/298-1 FUGG and DFG INST 256/340-1FUGG) and the Federal State Government of Saarland.

I am grateful to acknowledge Prof. Dr. Frank Mücklich for being a part of supporting supervisor and giving some suggestions in publication. I am grateful also for his permission to work with some devices (XRD, FIB, and APT) in the Institute of Functional Materials of Saarland University.

I would like also to express my sincere gratitude to Dr. Michael Marx for his support and supervision to working with the scanning electron microscope (SEM). I would like also to thank him to design sample holders for the bulk mechanical test. I would like to thank Dr. Florian Schäfer for performing the fatigue test experiment. I really appreciate also for the valuable discussion and suggestion from him regarding of fatigue experiments.

I would like to thank Dr. Mohammad Zamanzadeh and Jorge Rafael Velayarce for introducing a campus life during my initial period working at Saarland University and giving some support and suggestion for living better in Saarbrücken. I would like to express my appreciations and thanks to Francesco Kunz and Laura Lindner for the supporting help at the experimental works such as pulsed deposition, microhardness test, and micro-bending test. I

would like also to thank the all colleagues at the Chair of Materials Science and Methods: Dominic Rathman, Xiaolei Chen, Patrick Grünewald, Jutta Luksch, Marc Laub, and Jonas Rauber for the cooperation and collaboration in our working place.

I am very grateful to Peter Limbach and Stephan Schmitz for helping to design and prepare the specimens and specimen holders. Thanks also for Peter Limbach for helping me to improve my German language by having conversation for almost every day we met. Much appreciations and thanks to Andreas Kirsch and Rita Maron for their availability, support and help for performing a lot of experimental work for almost anytime I needed. I would like also to thank Isabelle Wagner and Alice Goldschmidt for their helps and supports in administrative works.

I would like to express my great appreciation for Dr. Flavio Soldera and DocMASE team members for providing a lot of support and information for my PhD program. Many thanks go for Dr. Jenifer Barrirero from Institute of Functional Materials of Saarland University for performing atom probe tomography (APT) sample preparation, APT measurement, and analysis. I am also grateful to Jörg Schmauch from Department of Experimental Physics for conducting transmission electron microscope (TEM) sample preparation and measurement. I would like to thank Sebastian Slawik from Institute of Functional Materials of Saarland University for performing XRD measurement.

I would like to thank my parents and my parents-in-law for their support, encouragement, and love for passing any difficulties in my life. I am very grateful for my lovely wife Fitria and son Arlan for their happiness, supports and loves given anytime and anywhere so I have much power, strength, confidence, and enthusiasms for finishing all challenges in my work.

Abstract

Single component nanocrystalline materials exhibits outstanding mechanical and physical properties, but they are unstable against thermal and mechanical loading. Addition of alloying elements are subjected to improve the thermal and mechanical stability. In the present work, supersaturated solid solution nanocrystalline Co-Cu (Co-rich) alloys were developed through the pulsed electrodeposition (PED) technique and the thermal and mechanical stability were investigated. Microstructural evolution during thermal and mechanical loading was also investigated for exploration the possible microstructural evolution mechanisms in this nanocrystalline alloy. This work shows the huge potential of supersaturated solid solution nanocrystalline Co-Cu alloys, where the thermal and mechanical stability of microstructure can be optimized by controlled de-mixing processes.

Zusammenfassung

Einkomponentige nanokristalline Werkstoffe weisen hervorragende mechanische und physikalische Eigenschaften auf, sind aber instabil gegenüber thermischer und mechanischer Belastung. Durch die Zugabe von Legierungselementen wird eine Verbesserung der thermischen und mechanischen Stabilität erwartet. In der vorliegenden Arbeit wurden übersättigte Co-reiche nanokristalline Co-Cu-Legierungen in fester Lösung durch die gepulste Elektroabscheidung (PED) entwickelt und die thermische und mechanische Stabilität untersucht. Die strukturelle Entwicklung während der thermischen und mechanischen Belastung wurde ebenfalls untersucht, um die möglichen strukturellen Entwicklungsmechanismen in dieser nanokristallinen Legierung zu erforschen. Diese Arbeit konnte das große Potenzial von übersättigten nanokristallinen Co-Cu Mischkristallen aufzeigen, bei welchen durch kontrollierte Entmischungprozesse die thermische und mechanische Stabilität gesteigert werden konnte.

List of Contents

Acknowledgments	i
Abstract	iii
Zusammenfassung	iv
List of Contents	v
List of Figure	vii
List of Table	xiv
Chapter 1 - Introduction	1
Chapter 2 - Literature Review and State of the Art	4
2.1 The processing of bulk nanocrystalline materials	4
2.2 Pulsed electrodeposition of nanocrystalline materials	8
2.2.1. Theory of pulsed electrodeposition of nanocrystalline materials	8
2.2.2 Electrodeposition of nanocrystalline Co, Cu, and Co-Cu	15
2.3. Thermal stability of nanocrystalline materials	25
2.4. Mechanical properties of nanocrystalline Co-Cu systems	34
2.4.1. Strength and ductility	34
2.4.2. Cyclic loading behavior	44
Chapter 3 – Materials and Experimental Methods	47
3.1. Pulsed electrodeposition of nanocrystalline Co-Cu	47
3.2. Characterization of nanocrystalline Co-Cu	50
3.3. Static and cyclic micro-bending test	51
3.4. Static and cyclic tensile tests of bulk samples	54
Chapter 4 - Selection of the Pulse-deposition Parameters	56
Chapter 5 - Thermal Stability and Microstructural Evolution	61
5.1. As deposited state	61
5.2. Thermal stability	63
5.3. Microstructural evolution: On the spinodal decomposition at 300°C	66

5.4. Microstructural evolution: Phase decomposition at 450°C and 600°C.....	72
5.5. Effect of Cu concentration on the thermal stability.....	75
5.6. Grain growth mechanisms in nanocrystalline Co-Cu.....	78
5.7. Magnetic properties	80
5.8. Discussion of the results in Chapter 5	83
Chapter 6 – Micro-mechanical Properties	87
6.1. Static micro-bending behaviour	87
6.2. Cyclic micro-bending behaviour	91
6.3. Discussion of the results in Chapter 6	98
Chapter 7 – Strength and ductility of bulk nanocrystalline Co-Cu	101
7.1. Effect of pulsed deposition parameters	101
7.1.1. Effect of Cu concentration	106
7.1.2. Grain size effect	109
7.1.3. Effect of processing flaws	112
7.2. Effect of annealing temperatures	118
7.3. Discussion of the results in Chapter 7	124
Chapter 8 – Fatigue properties of bulk nanocrystalline Co-Cu	128
8.1. Fatigue test methods	128
8.2. Constant amplitude fatigue test	130
8.3. Load increase fatigue test	136
8.4. Microstructure change during fatigue test.....	138
8.5. Discussion of the results in Chapter 8	140
Chapter 9 – Conclusion and Suggestions.....	141
9.1. Conclusion.....	141
9.2. Suggestions.....	143
References.....	144
Appended Papers	157

List of Figure

Figure 2.1 Schematic pictures of different severe plastic deformation (SPD) techniques: (a) high-pressure torsion (HPT) (from [59]), (b) equal channel angular extrusion (ECAE) (from [59]), and (c) accumulative roll-bonding (ARB) (from [60]).	4
Figure 2.2 Schematic pictures of (a) mechanical alloying process (from [48]) and (b-d) consolidation stage through different techniques: (b) Hot isostatic pressing (HIP) (from [76]), (c) fast-assisted sintering technology (FAST) [from [72]], and (d) equal channel angular extrusion (from [48]).	6
Figure 2.3 Schematic diagram of low-field and high-field approximations to the Butler-Volmer for a single electrode process (adapted from [81]).	9
Figure 2.4 Schematic pictures of (a) dependence of the free energy of nucleation (ΔG) on n -atomic nucleus at the different thermodynamic supersaturation ($\Delta\mu_1 < \Delta\mu_2 < \Delta\mu_3$) and (b) the critical n -atomic nucleus (n^*) as a function of the thermodynamic supersaturation ($\Delta\mu$) (adapted from [82] and [83]).	9
Figure 2.5 (a) Four different regimes in the current-overpotential relationship showing different mechanism upon the electrochemical deposition (from [87]). (b) Schematic diagrams of the concentration profile of metal ions as a function of distance from the electrode surface upon the non-steady electrochemical deposition. The concentration of metal ions in bulk solution (C_{OXb}) drops significantly at the electrode surface (C_{OX}) caused by formation of the Nernst diffusion layer (from [87]).	11
Figure 2.6 (a) Schematic diagram of the current density profile (i) as a function of the time period (t) upon the pulsed electrochemical deposition (PED). (b) Schematic diagrams of the linear (black solid line) and the actual (black dashed line) concentration profiles of metal ions as a function of distance from the electrode surface at the end of a single pulse of PED in comparison with the continuous DC electrodeposition (blue solid line and blue dashed line) (adapted from [88, 89]).	12
Figure 2.7 (a) Schematic diagrams of the pulsating diffusion layer profiles during the very initial single pulse of the PED-process (adapted from [89]) for the same pulse current density (i_p) at different pulse-on times ($t' < T < \tau$). (b) Schematic diagrams of the modified Nernst diffusion layer profiles (i.e. comprise the pulsating diffusion layer and the stationary diffusion layer) at the end of a single pulse of the PED at the same pulse current density (i_p) at different pulse-on times ($t' < T < \tau < t^*$) (adapted from [89, 95]).	14
Figure 2.8 Effect of saccharin concentration in bath electrodeposition on (a) grain size, (b) sulphur (square) and carbon (circle) contents in the PED-processed nanocrystalline Ni deposits (from [115]).	21
Figure 2.9 (a) Schematic picture of two-dimensional atomic structure of nanocrystalline materials, whereas black and white circles correspond to the atoms within grains and grain boundaries, respectively (from [1]). (b) Measured volume fraction of grain boundary, triple junction, and inter-crystal regions as a function of grain size by assuming 1 nm width of grain boundaries (modified from [116]). (c) Some values of time exponent ($1/n$) for isothermal grain growth of various nanocrystalline materials as a function of normalized annealing temperature (T/T_M), whereas T_M is a melting or liquidus temperature of materials (from [2]).	24
Figure 2.10 (a) Schematic picture of molecular dynamic simulation showing drag effect of pinning particles at a grain boundary (from [133]). (b) Atom probe tomography elemental maps of Ni (blue) and sulphur (red) observing solute sulphur segregation at a grain boundary of an annealed nanocrystalline Ni (from [25]). (c-d) Microstructural images show abnormal grain growth in (c) nanocrystalline Ni after annealing at 210°C for 150 minutes (from [25]) and (d) nanocrystalline Co after annealing at 300°C for 2 minutes (from [23]).	28
Figure 2.11 Long-term thermal stability of (a) Cu-rich (26 at% Co) and (b) Co-rich (75 wt% Co) nanocrystalline Co-Cu processed through high pressure torsion (HPT) at various annealing temperatures for up to 100 h. Figures (a) and (b) were taken from references [27] and [13], respectively.	33

Figure 2.12 (a) Schematic picture of dislocation pile-up at the grain boundary describing the Hall-Petch phenomena (from [151]). (b) Schematic illustration of a dislocation movement across the grain boundary showing the changes direction of slip planes (from [150]) (c) Schematic representation of dislocation pile-up generated from the centre of a grain (Frank-Read source) in microcrystalline and nanocrystalline regimes at the same applied stress level showing a grain size effect (from [3]).	35
Figure 2.13 (a) Schematic pictures of dependence of strength on grain sizes showing the different regimes of deformation mechanisms (from [154]). (b) Schematic illustration of dislocation pile-up at the grain boundary showing the distance between two dislocations (l) (from [155]). (c) Compilation of data of hardness and yield stress (tensile and compression) of the nanocrystalline copper as a function of grain size collected from some literatures by Tschopp [48].	36
Figure 2.14 Schematic pictures of grain boundary sliding mechanism: (a) initial condition where the upper part of grains (grey colour) will move to the right part relative to the lower part of grains (white) and (b) final condition of which grain boundary sliding has occurred (from [3]).	38
Figure 2.15 Schematic pictures of grain rotation during plastic deformation: (a) initial condition grains having different orientation of slip systems, (b) rotated grains having the same orientation of slip systems, and (c) grain coalescence in which an elongated grain is formed (from [3, 168]).	38
Figure 2.16 (a) Stress vs- strain curves of bulk nanocrystalline Cu (grain size: 12 nm) and bulk polycrystalline Co (grain size: 4.2 μm) (from [39]). (b) Stress vs- strain curves of bulk nanocrystalline Cu (grain size: 26 nm), bulk coarse-grained Cu (grain size: 80 μm), and in situ consolidated micro-sample of nanocrystalline Cu (grain size: 23 nm) (from [173]). Compilation of data of (c) tensile elongation to failure versus grain size (picture and complete data are available in [172]) and (d) normalised yield stress vs. %elongation (picture and complete data are available in [171]) of various nanocrystalline materials.	40
Figure 2.17 (a) Effect of the fraction porosity on the Young's modulus of nanocrystalline Cu and Pd (from [153]). (b) Effect of the consolidation density on the compressive yield strength of nanocrystalline Cu and Pd (picture provided in [3] with data available in [174]).	40
Figure 2.18 (a) S-N curves of fatigue response and (b) fatigue crack length as a function of the number of loading cycles for nickel at various grain size whereas the average grain sizes of nanocrystalline (nc), ultrafine crystalline (ufc) and microcrystalline (mc) were 30 nm, 300 nm, and 10 μm , respectively. (from [186]).	45
Figure 3.1 Photographs of electrodeposition cell and equipment used for the electrodeposition of nanocrystalline Co-Cu deposits with Cu-cathode and the platinised titanium anode.	48
Figure 3.2 Pictures of the nanocrystalline Co-Cu deposits at two different size of Cu-cathodes: (a) Dep-I: surface diameter of 12 mm and (b) Dep-II: surface dimension of 21x21 mm ² .	49
Figure 3.3 (a) Schematic picture of the beam position at the cross-section of a nanocrystalline film. (b) A secondary electron (SE) image of a micro beam for cyclic bending tests. (c-d) Schematic pictures of micro beam geometries were used for (c) static and (d) cyclic micro bending tests. The dimensions of micro beams can be found in Chapter 6 . Schematic pictures of (e) a nanoindenter and (f) a double blade griper were used for static and cyclic micro bending tests, respectively.	52
Figure 3.4 (a) Schematic picture of two tensile specimens in the as-deposited and annealed samples. (b) Schematic picture of the detailed dimension of tensile specimens (from [194]). The typical of (c) a secondary electron (SE) image of a cross-section of deposited films and (d) energy dispersive spectroscopy (EDS) line profiles of Co and Cu concentration in weight percent (wt.%) along the cross-section, showing removed parts and thickness of tensile specimen.	53
Figure 3.5 (a) Design of the tensile specimen holder (from [194]). (b) Set up of the tensile specimen and the tensile specimen holder at the static tensile testing machine in which the supporting holder is removed before the static tensile test (from [194]).	54
Figure 3.6 Photographs of the experimental setup of test and specimen devices were used for the fatigue tests of bulk nanocrystalline Co-Cu viewed from (a) the front and (b) the side.	55

Figure 4.1 Cross-sectional images of Dep-I samples with a surface diameter of 12 mm deposited at various duty cycles of (a) 10%, (b) 20% (from [194]), (c) 30% (from [194]), and (d) 40% (from [194]). Pulse current density and on-time were fixed at 1000 A/m ² and 2 ms, respectively. The films were deposited for different times of deposition which are (a) 30 h, (a) 13 h, (b) 8.5 h, and (c) 6.5 h to get ~300 μm of thickness. The crystal growth borders are marked with red arrows	56
Figure 4.2 Energy dispersive spectroscopy (EDS) maps and EDS lines profiles of cross-sectional Dep-I samples (surface diameter of 12 mm) at various pulse current densities: (a-b) 500 A/m ² , (c-d) 1000 A/m ² (from [188, 189]), and (e-f) 1500 A/m ² at a duty cycle of 10% and a pulse-on time of 2 ms.	57
Figure 4.3 Back-scattered electron (BSE) images of Dep-I samples deposited at pulse current densities of (a) 500 A/m ² (from [188]) and (b) 1000 A/m ² (from [189]) at a pulse duty cycle of 10% and a pulse-on time of 2 ms. Figure (a) was taken at a position marked with a white rectangular in Figure 4.2a	58
Figure 4.4 Combined SE and EDS-line profiles images of cross-sectional Dep-II samples (surface area of 21×21 mm ²) at various pulse-on times: (a) 2 ms, (b) 0.5 ms, and (c) 0.3 ms. The PED-process were performed at a fixed pulse current density and duty cycle of 1000 A/m ² and 17.5%, respectively.	59
Figure 5.1 (a) Bright-field (BF) (from [188]) and (b) dark-field (DF) transmission electron microscope (TEM) images of the as-deposited sample (Dep-I). (c) Grain size distribution of the as-deposited sample measured from BF-TEM image (from [188]). (d-e) Phase and orientation observations of the as-deposited sample through (d) selected area diffraction (SAD) in TEM (from [188]) and (e) x-ray diffraction (XRD) (from [188]).	62
Figure 5.2 APT measurement of Co (blue) and Cu (orange) in the as-deposited sample: (a) Elemental map of a selected slice (5 nm thick) through a reconstruction of region of interest (ROI) (from [188]). (b) One-dimensional concentration profiles constructed from the white dashed line in the respective elemental map (from left to right) (from [188]).	63
Figure 5.3 Back-scattered electron (BSE) images of microstructure of the (a) as deposited (from [189]) and (b-j) annealed (from [188]) samples in cross-sectional direction. All pictures were taken at the same magnification. Some interesting microstructural features are marked with red arrows in Figure (e-j) . (UFG: Ultrafine grained; NC: Nanocrystalline). Some interesting microstructural features (dark particles) are marked with red arrows.	66
Figure 5.4 (a) BF-TEM image of a sample annealed at 300°C for 64 h (from [188]). (b) Grain size distribution corresponds to Figure (a) (from [188]). (c-d) Phase and orientation observations of an annealed sample through (c) SAD-TEM and (d) XRD measurements (from [188]).	67
Figure 5.5 APT investigation of Co (blue) and Cu (orange) elements of a sample annealed at 300°C for 64 h: Elemental map of selected slices (5 nm thick) (a and b) of two different reconstructions from a similar sample and one-dimensional concentration profiles constructed along the a white dashed lines in the respective elemental maps (from left to right) (from [188]).	68
Figure 5.6 (a) A typical combined APT elemental map and iso-concentration surfaces at 85 at.% Co and 60 at.% Cu showing the regions used to calculate the approximated volume fraction of Co- and Cu-rich regions in a sample annealed at 300°C for 64 h. (b) Approximated volume fraction of Co- and Cu-rich regions (i.e. >85 at.% Co and >60 at.% Cu) measured from four different reconstructions.	69
Figure 5.7 Back-scattered electron (BSE) images of the microstructure of samples subjected to two steps of annealing (TSA). (a) TSA-I: Annealed at 300°C for 64 h → Rapid cooling to room temperature → Annealing at 600°C for 1 h. (b) TSA-II: Annealing at 300°C for 64 h → Rapid cooling to room temperature → Annealing at 600°C for 5 h.	71
Figure 5.8 X-ray diffraction (XRD) patterns of samples annealed at (a-b) 450°C and (c-d) 600°C for different time periods of 5 h and 24 h (from [188]).	73
Figure 5.9 (a) A back-scattered electron (BSE) image of the microstructure of a sample annealed at 600°C for 24 h. (b-c) EDS-map of (b) Co and (c) Cu elements from area marked within yellow dashed box on Figure (a)	74

Figure 5.10 Pulse profiles and parameters of electrodeposition used to produce nanocrystalline Co-Cu with different Cu concentration: (a) 38 at.% Cu (S2) and (b) 43 at.% Cu (S3). BSE images of microstructure of (c) S2 (38 at.% Cu) and (d) S3 (43 at.% Cu) samples.	75
Figure 5.11 (a) Microhardness of as deposited and annealed samples (S1, S2, and S3) containing different Cu concentration. The numbers within individual bars (in vertical direction) show the relative increase (positive) and decrease (negative) of microhardness compared with the as-deposited state (in percent). (b-c) BSE images of microstructure of (b) S2 (38 at.% Cu) and (c) S3 (43 at.% Cu) samples annealed at 300°C for 5 h.....	77
Figure 5.12 Determination of grain growth exponent (n) by using equation [2.17] ($D = K' \cdot t^{1/n}$) for nanocrystalline Co-Cu annealed at (a) 450°C and (b) 600°C. The grain sizes data were taken from Table 5.1	78
Figure 5.13 Determination of grain growth exponent (n) by using equation [2.16] ($Dn - D_0n = Kt$). The grain sizes data were taken from Table 5.1 . The n -value were varied to get the highest coefficient of determination for linear regression (R^2) as shown in (a) 450°C with $n = 70$ and (b) 600°C with $n = 9$. The coefficient of determination (R^2) at different grain growth exponent (n) for samples annealed at (c) 450°C and (d) 600°C.....	79
Figure 5.14 Combined AFM-MFM images of surface morphology and magnetic domain pattern of nc and ufg Co-Cu: (a) as deposited and annealed at (b) 450°C, (c) 600°C, and (d) 800°C for 5 h. (e) One-dimensional profiles of normalized MFM phase signal corresponding to the white dashed lines marked in (a-d) from left to right.	82
Figure 5.15 (a) X-ray diffraction (XRD) pattern and (b) energy dispersive spectroscopy (EDS) map of a sample annealed at 800°C for 5 h.....	82
Figure 5.16 Microhardness profiles of PED-processed nanocrystalline Co-Cu (28 at.% Cu) upon isothermal annealing treatments compared with (a) HPT-processed nanocrystalline Co-Cu (25 at.% Cu) with high (H) and low (L) purity [13] and (b) HPT-processed nanocrystalline Co-Cu (24 at.% Cu) [29]. Pictures from [188].	84
Figure 6.1 (a) Engineering surface stress vs.- strain curve of micro beam-I (black solid line) tested through the static bending test at surface strain rate of $1.24 \times 10^{-2} \text{ s}^{-1}$. Red dashed line is 0.2% offset for determination of yield stress (from [188]). (b) Detailed picture of the elastic to plastic transition shows a smooth transition regime (black solid circle). Red and blue solid lines represent elastic regime projection and 0.2% offset, respectively. The actual yield strength lays at some point marked within the green dashed box (from [188]).	87
Figure 6.2 (a-b) Secondary electron (SE) images show (a) top and (b) side surfaces of micro beam-I after bending deformation (from [188]). (c-d) Back-scattered electron (BSE) images of microstructure were observed at two different positions marked with a black dashed box in Fig (a) namely (c) zone-A and (d) zone-B (from [188]).	89
Figure 6.3 Secondary electron (SE) images of surface morphology show initial condition of (a) side and (b) top surfaces of micro beam-I.	90
Figure 6.4 (a,c) Surface-stress amplitude as a function of load cycles at different plastic surface-strains amplitudes of (a) $\epsilon_{s,amp} = 1.0 \times 10^{-4}$ (beam-II) and (c) $\epsilon_{s,amp} = 1.8 \times 10^{-4}$ (beam-II) (from [188]). (b,d) Cyclic hysteresis loops of (b) micro beam-II ($\epsilon_{s,amp} = 1.0 \times 10^{-4}$) and (d) micro beam-III ($\epsilon_{s,amp} = 1.0 \times 10^{-4}$) at selected load cycles.	92
Figure 6.5 Back-scattered electron (BSE) images of microstructure observed from the same position at a side surface of micro beam-III: (a) initial condition and (b) after 5000 load cycles (from [188]). Magnifications are similar for these two pictures.	93
Figure 6.6 (a) Surface-stress amplitude as a function of load cycles of micro beam-IV at two different stages of plastic surface-strains amplitude of $\epsilon_{s,amp} = 4.0 \times 10^{-4}$ (stage-I) and $\epsilon_{s,amp} = 6.5 \times 10^{-4}$ (stage-II)	

(from [189]). (b,c) Cyclic hysteresis loops of micro beam-IV at selected cycles at different plastic surface-strain amplitudes of (b) $\epsilon_{s,amp} = 4.0 \times 10^{-4}$ (stage-I) and (c) $\epsilon_{s,amp} = 6.5 \times 10^{-4}$ (stage-II) (from [189]).	94
Figure 6.7 (a,b) Secondary electron (SE) images of micro beam-IV that show a crack formation after 4000 load cycles observed at (a) top and (b) side surfaces of the micro beam (from [189]). (c,d) Back-scattered electron (BSE) images of the microstructure at the area adjacent to the crack observed at (b) top surface (marked with red dashed rectangular in (a)) and (c) side surface (marked with white dashed rectangular in (b)) (from [189]).	95
Figure 6.8 (a) Surface-stress amplitude as a function of load cycles at four different stages of plastic surface-strain amplitudes of micro beam-V (from [188]). (b) Cyclic hysteresis loops of micro beam-V at plastic surface-strain amplitude of stage-IV ($\epsilon_{s,amp} = 7.0 \times 10^{-3}$) at selected load cycles (from [188]).	96
Figure 6.9 (a) Secondary electron image of micro beam-V that show cracks formation after four stages of cyclic bending from side-view (from [188]). (b,c) Back-scattered electron (BSE) images of microstructure at (b) the area marked with a red dashed rectangular shape in Fig (a) and the area adjacent to (c) crack-I and (d) crack-II marked with the white dashed rectangular shapes in Fig (b) (from [189]).	97
Figure 6.10 Schematic pictures illustrating dissociation of dislocations at the boundary (point B), whereas some parts of dislocations move to a neighbouring grain (grain-II) and another parts of dislocations move along the boundary. Dislocations movement along the boundary may result in dislocation shear (marked with red solid arrow).	100
Figure 7.1 Engineering stress vs. strain curves of tensile tests of different nanocrystalline Co-Cu samples (TS1-TS8) at a strain rate of $1.0 \times 10^{-3} \text{ s}^{-1}$. (a) Effect of duty cycle and (b) effect of current density (i) and pulse-on time ($t-on$) (from [194]).	102
Figure 7.2 (a-c) Secondary electron images of surface morphology of (a) TS-5, (b) TS-6, and (c) TS-7 after tensile deformation. (d) Secondary electron images of fracture surface of TS-7.	104
Figure 7.3 (a-d) Secondary electron images of surface morphology of (a) TS-2, (b) TS-3 (from [194]), (c) TS-4 (from [194]), and (d) TS-8 (from [194]) after tensile deformation. (e-f) Secondary electron images of fracture surface of TS-8 at areas marked with red rectangular shapes: (e) area A and (f) area B.	105
Figure 7.4 Effect of the Cu concentration on the tensile fracture strain of PED-processed nanocrystalline Co-Cu.	107
Figure 7.5 (a-e) Back-scattered electron (BSE) images of initial microstructure of (a) TS-1 (from [194]), (b) TS-2, (c) TS-3 (from [194]), (d) TS-4, and (e) TS-8 (from [194]) at the same magnification. (f) XRD patterns of selected tensile samples in which continuous black lines correspond for the fitted XRD data (from [194]). The red and green vertical dashed lines represent the position of fcc structure of Cu and Co, respectively.	108
Figure 7.6 (a) Bright-field (BF) and (b) dark-field (DF) images obtained by transmission electron microscope (TEM) of tensile sample-8 (TS-8) and (c) selected area diffraction (SAD) pattern. (d) Grain size distribution of TS-8 measured from BF-TEM image.	110
Figure 7.7 (a) Secondary electron image of initial surface morphology of sample TS-1 in planar-view showing crystal growth borders and micro-pores marked with white and black arrows, respectively (from [194]). (b) Combined SEM-EDS images of TS-1 observing chemical inhomogeneity along the crystal growth borders (from [194]). (c) Schematic illustration of growth mechanism in electrodeposition of fcc-structured materials. Black arrows correspond to the growth direction (from [217]).	112
Figure 7.8 Secondary electron images of typical fracture surface of tensile sample-1 (TS-1) showing ductile (D1 and D2) and brittle (B) fracture regions with a clear visibility of crystal growth borders (from [194]).	114
Figure 7.9 Secondary electron images of fracture surface of tensile samples deposited at a pulse current density of 1000 A/m^2 , a pulse-on time of 0.5 ms, and various duty cycles: (a) 20% (TS-1), (b) 17.5% (TS-2), (c) 15% (TS-5), (d) 12.5% (TS-6), and (e) 10% (TS-7). Brittle fracture zones at the crystal growth borders are marked with the red freeform shapes.	116

Figure 7.10 (a) Schematic graph of fractional area of brittle fracture at crystal growth borders as a function of duty cycle from 10% to 20% at a pulsed current density and a pulsed-on time of 1000 A/m ² and 0.5 ms, respectively. Effect of decreasing pulsed current density to 800 A/m ² (TS-3) and shortening pulsed-on time to 0.3 ms (TS-4) on the fractional area of brittle fracture at crystal growth borders is also shown in the graph. (b) Schematic graph of fracture strain as a function of fractional area of brittle fracture at crystal growth borders.	117
Figure 7.11 BSE images of the microstructure of (a) as deposited sample (TS-9) and (b-d) samples annealed at different temperatures for 24 h: (b) 200°C (TS-10), (c) 300°C (TS-11), and (d) 450°C (TS-12) (from [194]).	119
Figure 7.12 XRD patterns of TS-9 and TS-10, whereas continuous black lines correspond to the fitted XRD data (grey lines). The red and green vertical dashed lines represent the position of fcc the structure of Cu and Co, respectively (from [194]).	119
Figure 7.13 Engineering stress vs. strain curves of tensile tests at a strain rate of $1.0 \times 10^{-3} \text{ s}^{-1}$ of as deposited (TS-9) and annealed (TS-10, TS-11, and TS-12) samples (from [194]).	120
Figure 7.14 (a,c) SE images of surface morphology of (a) TS-9 and (c) TS-10 after tensile deformation (from [194]). (b,d) SE images of fracture surface of (a) TS-9 and (b) TS-10 (from [194]).	121
Figure 7.15 Secondary electron images of fracture surface of samples annealed at (a) 300°C (TS-9) and (b) 450°C (TS-10) for 24 h (from [194]).	123
Figure 7.16 Compilation of data of the yield strength and the fracture strain of various nanocrystalline and nanotwin Cu, Co, and Co-Cu: (a) yield strength vs. fracture strain; (b) fracture strain vs. grain size. Data were collected from literatures (see the reference number in the legend notes of the respective data).	125
Figure 8.1 Schematic picture of stress profile used in the stress-controlled fatigue test. Fatigue tests parameters for constant amplitude test (CAT) and load increase test (LIT) are shown in Table 8.1 and Table 8.2 , respectively.	128
Figure 8.2 Schematic picture of the resonant fatigue testing machine showing some important components such as the load frame, the actuator, the fatigue sample, and the sample holder.	129
Figure 8.3 (a) Secondary electron image of surface morphology of CAT-I sample after 64,237 load cycles showing a crack formation. (b) Δ Frequency profile as a function of load cycles from fatigue test of CAT-I sample. (c) Back-scattered electron image of microstructure at the area marked with red rectangular shape in (a)	131
Figure 8.4 (a) Secondary electron (SE) image of surface morphology of CAT-II sample after 831,193 load cycles showing materials rupture with necking. (b) Δ Frequency profile as a function of load cycles from stress-controlled fatigue test of CAT-II sample. (c) SE electron image of fracture surface of CAT-II sample showing different characteristic of fracture surface: (i) brittle fracture surface (crack initiation region), (ii) slow fatigue fracture surface, and (iii) ductile fracture surface.	132
Figure 8.5 Stress level, Δ frequency, and strain range profiles as a function of load cycles from stress-controlled fatigue tests of (a-c) CAT-III and (d-f) CAT-IV samples. Strain measurement was recorded from cross-head displacement.	133
Figure 8.6 (a) Stress levels, (b) Δ frequency, and (c) strain range as a function of load cycles from stress-controlled fatigue test of CAT-V sample. Strain measurements were recorded from cross-head displacement and video extensometer.	134
Figure 8.7 (a) Stress level, (b) Δ frequency, and (c) strain range profiles as a function of load cycles from stress-controlled fatigue test of LIT-I sample. Strain measurements were recorded from cross-head displacement.	135
Figure 8.8 (a) Stress level, (b) Δ frequency, and (c) strain range profiles as a function of load cycles from stress-controlled fatigue test of LIT-II sample. Strain measurements were recorded from cross-head displacement and video extensometer.	137

Figure 8.9 (a) Secondary electron (SE) image of surface morphology of CAT-III sample shows plastic strain at the area nearby the crack tip. (b) Secondary electron (SE) image shows the actual position for APT lift-out nearby the crack tip indicated by a red rectangular shape. 137

Figure 8.10 Combined APT elemental maps and iso-concentration surface profiles at 40 at.% Cu and 70 at.% Co from (a) reconstruction-I and (b) reconstruction-II. (c) Combined APT elemental maps and iso-concentration surface profiles at 50 at.% Cu from reconstruction-I. (a-c) The one-dimensional concentration profiles were constructed from blue vertical tubes on the respective elemental maps (black arrows: measurement direction). Length scale is in nm. 139

List of Table

Table 2.1 The example of electrolyte composition used in direct- and pulsed-current electrodeposition of nanocrystalline Cu, Co, and Co-Cu from various literatures. Detailed information about the deposition parameters (current density, pulsed duration, and other) are summarised in **Table 2.2**.18

Table 2.2 Examples of deposition parameters (direct and pulse current density, pulse-on and –off time) used in electrodeposition of nanocrystalline Cu, Co, and Co-Cu from various literatures. The quantities of i_{dc} , i_{pulsed} , t_{on} , and t_{off} are direct current density, pulse current density, pulse-on time, and pulse-off time.22

Table 2.3 The thermal stability of nanocrystalline pure Co and pure Co processed through various techniques from some previous works. (IGC = Inert gas condensation; FCAT = Filtered cathodic arc technique; MS = Magnetron sputtering; PED = Pulsed electrodeposition; SPD = Severe plastic deformation; HPT = High pressure torsion).30

Table 2.4 The thermal stability of Co-rich and Cu-rich nanocrystalline Co-Cu processed through high pressure torsion (HPT) and electrodeposition (ED) techniques from some literatures. (SPD = Severe plastic deformation).....32

Table 2.5 Tensile yield stress (σ_y), ultimate tensile stress (σ_u), and elongation to fracture (ϵ_f) of nanocrystalline (nc) and nano-twin (nt) Co, Cu, and Co-Cu processed through various techniques. (GS: Grain size; TT: Twin Thickness; ECAE: Equal channel angular Extrusion; IsC: In-situ consolidation; IGC: Inert gas condensation; ED: Electrodeposition; PED: Pulsed electrodeposition; HPT: High pressure torsion)42

Table 3.1 Chemical composition of electrolyte used for the pulsed electrodeposition (PED) of nanocrystalline Co-Cu. The roles of individual ingredient are also provided in the table.47

Table 5.1 Microhardness and grains size of samples annealed at the various temperatures (300-600 °C) for different time periods (1-24 h). Grain size determinations were performed through the BSE image of individual samples as provided in **Figure 5.3**. For comparison, microhardness and grain size of the as-deposited sample are 22.7 ± 8.2 nm and 4.45 ± 0.07 GPa, respectively.64

Table 5.2 Distances of atomic diffusion of Co and Cu at 300°C for 64 h calculated through the classical theory of diffusion. The diffusion coefficients were selected from some literatures and they were extrapolated to 300°C through the Arrhenius relation ($D = A \exp [-E_A/RT]$). (mc: microcrystalline; nc: nanocrystalline).....70

Table 6.1 The actual micro beam dimensions, where L, W, T, L_B are the length, width, thickness, and bending length. Cyclic micro bending tests were performed at various plastic strain amplitude (ϵ_s ,a) for different number of cycles (N).91

Table 7.1 Pulsed electrodeposition (PED) parameters which were used to produce tensile samples of nanocrystalline Co-Cu with different chemical composition. Deposition time is calculated by assuming a current efficiency of 85% and a deposit thickness of ~ 750 μm . Chemical composition of Co and Cu elements were measured through energy dispersive spectroscopy (EDS) (from [194]).101

Table 7.2 Tensile sample thicknesses and mechanical properties parameters of nanocrystalline Co-Cu synthesized at different deposition parameters. Two samples were mechanically tested except for samples TS-1, TS-5, TS-6, and TS-7 (from [194]).103

Table 7.3 Grain size analysis of different nanocrystalline Co-Cu deposits approximated through Scherer and Williamson-Hall approaches as well as the mean grain size from both of these methods (from [194]).109

Table 7.4 Mechanical properties of as deposited (TS-9) and annealed (TS-10, TS-11, TS-12) samples calculated from engineering stress vs. strain curves in **Figure 7.13**. Two samples were mechanically tested for each temperature except for samples TS-10 and TS-11 (from [194]).120

Table 8.1 Stress parameters that were used in constant amplitude/load fatigue test (CAT). Stress ratio was kept constant at 0.1. Description of the fatigue test parameters are shown in **Figure 8.1** (NA = Not available)..... 129

Table 8.2 Stress parameters that were used in load increase fatigue test (LIT). Stress ratio is kept constant at 0.1. Description of the fatigue test parameters are shown in **Figure 8.1**..... 130

Chapter 1 - Introduction

Single-component nanocrystalline metals (i.e. polycrystalline with typical grain size of less than 100 nm) exhibit magnificent mechanical and physical properties compared to conventional coarse-grained counterpart [1, 2, 3, 4, 5]. However, these types of materials are prone to grain growth because of high internal interfacial energy (i.e. grain boundaries and triple junctions) which may degrade their magnificent properties [6, 7, 8, 9]. Nanocrystalline materials are also mechanically unstable [10, 11, 12] because of processing flaws and unstable plasticity. Improvements on the thermal and mechanical stability are crucial for high-performance structural applications.

Improving thermal and mechanical stability of nanocrystalline materials is possible through various techniques, for instance, addition of alloying elements (e.g. Co-Cu, Co-Ni and Co-Cu-Ag alloys) [13, 14, 15, 16, 17] and secondary nanoparticles (e.g. oxides and carbon) [13, 18, 19] and application of modified microstructures (e.g. bimodal and nano-twinned structures) [20, 21, 22]. Incorporation of contaminants (e.g. sulphur and phosphor) at grain boundaries has also an impact on the stabilisation of the nano-sized grains [23, 24], but segregation of contaminants may lead to the embrittlement of grain boundaries in high temperature applications [25], thus this option should be not considered. Addition of secondary nanoparticles is difficult because of particles agglomeration and inhomogeneous particles distribution which lead on degradation of materials properties, while formation of nano-twinned and bimodal structures is not applicable for most metals and alloys. Therefore, application of multi-component and/or -phase nanocrystalline metals is a favoured way to improve thermal and mechanical stability.

One of the most promising materials is a supersaturated solid solution nanocrystalline alloy, e.g. immiscible Co-Cu system, whereas an improved thermal and mechanical stability can be achieved by tailoring microstructure and phase through adjusting parameters of synthesis process and conducting specific thermal treatment [13, 26, 27, 16, 28, 29, 30, 31, 32, 33]. Considering physical properties, these materials are receiving great interest as a candidate for advanced electronic application caused by their giant magnetoresistance (GMR) effect of the modulated nanostructures of Co and Cu [34, 35, 36, 37, 38]. Regarding potential applications, nanocrystalline Co-Cu alloys must have an excellent stability against thermal and mechanical loading. However, comprehensive information of the thermal and mechanical stability of nanocrystalline Co-Cu is only available for selected chemical composition which processed

through selected approaches (i.e. severe plastic deformation), thus, investigation on the different nanocrystalline Co-Cu systems and its potential development are needed.

Most nanocrystalline Co-Cu alloys are produced through the severe plastic deformation process (SPD), mainly the high-pressure torsion (HPT) technique, caused by an ability to produce very fine grain materials with a wide range dimension, including bulk nanocrystalline materials. The production of bulk samples of nanocrystalline materials is important to understand the macroscopic mechanical and physical properties. According to previous works [13, 27, 29], the HPT-processed nanocrystalline Co-Cu shows a significant improvement on the thermal stability compared with nanocrystalline pure Co [7, 23] and pure Cu [8, 9]. Interesting spinodal and phase decomposition of solid solution Co-Cu could be also obtained at different annealing temperatures [13, 27]. The decomposition of solid solution Co-Cu is an interesting feature for improving mechanical and physical properties of nanocrystalline Co-Cu caused by a different characteristic of Co- and Cu-rich regions/phases formed during tailoring of nanostructure. However, the grain coarsening during decomposition of Co-Cu at high temperatures must be taken into consideration. Regarding mechanical properties, nanocrystalline pure Co exhibits a magnificent strength with low ductility [39, 40, 41], while the current type of nanocrystalline pure Cu shows a decent ductility [42, 43, 44, 21, 45]. A solid solution strengthening of the Co-Cu systems could contribute also on the additional strength enhancement. A combination of Co and Cu components in the nanocrystalline Co-Cu system is expected to generate excellent mechanical strength and ductility compared with nanocrystalline pure Co and Cu. However, significant improvement in ductility was still not observed in the HPT-processed bulk nanocrystalline Co-Cu [16] in which an elongation to fracture of below 10% was still observed. In addition, the SPD-processes have a limitation to produce nanocrystalline materials with grain sizes of below 50 nanometers, whereas a typical grain size of nearly 100 nm was frequently observed [13, 27]. Development of nanocrystalline Co-Cu through different processing routes is needed to produce nanocrystalline Co-Cu with different characteristics and properties.

Among common alternative processing routes to produce bulk nanocrystalline metals/alloys are mechanical alloying (MA) and electrodeposition (ED). However, mechanical alloying is a complex processing route which has major issues on the powder processing (e.g. expensive cost and contamination of milled powder) and consolidation (e.g. grain coarsening and porosity) even through the novel consolidation processing [46]. The processing on the bulk nanocrystalline Co-Cu through the MA and consolidation has not been reported. Another technique, i.e. conventional direct current (DC) electrodeposition at high current density, leads

on the formation of unstable deposits with inhomogeneous microstructure and chemical distribution caused by the limiting current density. In the last 25 years, pulsed electrodeposition (PED) has been developed to solve the problems on the processing of bulk nanocrystalline metals/alloys and showed some promising results. PED is a simple route of production with established technology and wide-range controllable parameters (e.g. pulse current density, duty cycle, pulse on time, and composition of electrolyte) in which bulk nanocrystalline materials with significantly different characteristic and properties can be obtained [4]. Therefore, the PED method was selected as an alternative processing route of bulk nanocrystalline Co-Cu.

In the present work, synthesis of the bulk nanocrystalline Co-Cu through the PED process are employed and optimized. Microstructure characterisation and development are also investigated. This research is aimed to produce different type of nanocrystalline materials, specifically Co-Cu systems, which leads on the comprehensive understand of reciprocal relationship between nanostructures, thermal stability and mechanical properties, thus different nano-structured materials for wide-range applications can be produced. According to the research objectives, three different parts are established in this thesis. In the first part, synthesis of the PED-processed nanocrystalline Co-Cu and characterisation of the microstructure and the thermal stability are investigated to study the possible structural development regarding potential applications. The micro-mechanical stability of the PED-processed nanocrystalline Co-Cu and possible structural changes under mechanical loading are also studied through the static and cyclic micro-bending test in the first part. In the second part, strategies to improve tensile strength and ductility of the bulk PED-processed nanocrystalline Co-Cu are studied by adjusting deposition parameters and conducting subsequent annealing treatment. In the second part, the effect of the parameter of deposition on the processing flaws (e.g. porosity, internal stresses, and chemical inhomogeneity) and the impact on the mechanical properties are investigated. In the last part, microstructural behaviour of bulk PED-processed nanocrystalline Co-Cu under cyclic loading is investigated.

Chapter 2 - Literature Review and State of the Art

2.1 The processing of bulk nanocrystalline materials

For over 30 years, processing of nanocrystalline materials with different properties has been developed through various processing techniques. The processing of nanocrystalline materials can be classified based on the initial state of materials divided into two different approaches: (i) bottom-up and (ii) top-down [47, 48]. In the bottom-up approaches, nanocrystalline materials are gradually assembled from small groups of atoms, ions, or molecules through a step-by-step deposition and/or consolidation [47]. The nanocrystalline films from few nanometer up to hundreds micrometer of thicknesses can be produced through the bottom-up approach. Some processing routes can be classified into this category, for instance, electrodeposition [4, 49, 50], inert gas condensation and consolidation [51, 52, 11], and lithography [53, 54]. The top-down approach starts with a bulk material with a coarse microstructure ($>1 \mu\text{m}$) and then the bulk materials are subjected to structural decomposition or refinement stages down to the nanometers scale of microstructure [48]. The top-down approaches are used to produce nanostructured powders and structural nanocrystalline material in the order of millimeters of thicknesses. The severe plastic deformation (SPD) [55, 56, 57] and mechanical alloying (MA) [46, 48, 58] methods are popular top-down approaches used to produce nanocrystalline materials.

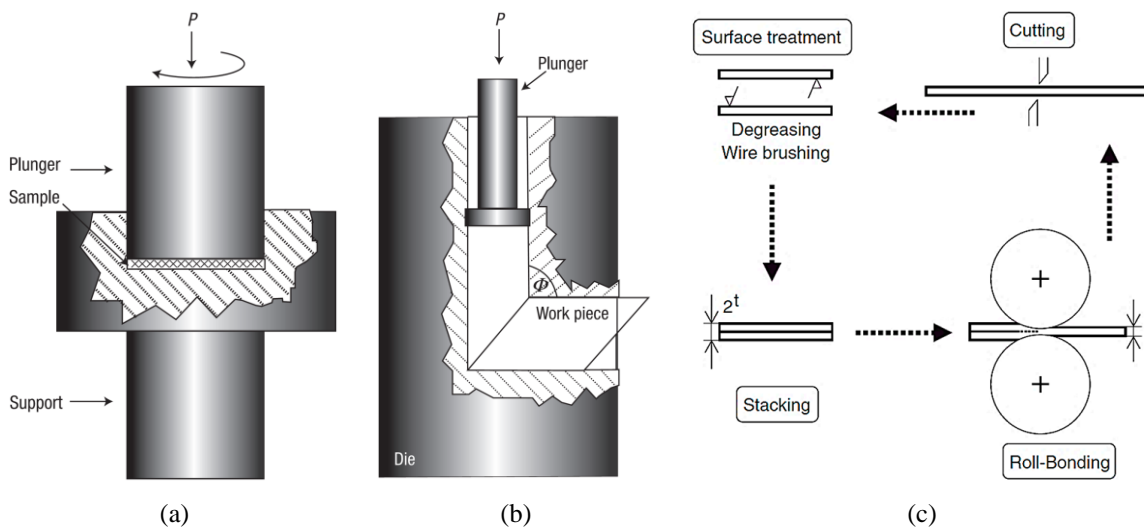


Figure 2.1 Schematic pictures of different severe plastic deformation (SPD) techniques: (a) high-pressure torsion (HPT) (from [59]), (b) equal channel angular extrusion (ECAE) (from [59]), and (c) accumulative roll-bonding (ARB) (from [60]).

Currently, the key challenge in the processing of nanocrystalline materials is production of bulk samples with thicknesses of hundreds of micrometer up to some millimeters to access the macroscopic mechanical and physical properties. However, there are only particular techniques for producing bulk nanocrystalline materials. For example, the SPD-processes are among popular approaches used to produce bulk nanocrystalline materials. For raw materials, conventional SPD-processes normally use the bulk materials with a coarse grained microstructure, but current development shows that pre-compacted powders can be used also in the SPD-processes. In the SPD-processes, a very large plastic strain is applied to the bulk materials or pre-compacted powders to produce nanocrystalline materials through various techniques [55, 56], for instance, high-pressure torsion (HPT) [55, 59, 61], equal channel angular extrusion (ECAE) [62, 63], and accumulative roll-bonding (ARB) [64, 60]. Schematic pictures of the various SPD-processes are summarised in **Figure 2.1**.

One advantage of the SPD-processes is the ability to produce a wide-range of dimensions of nanocrystalline samples. Different materials can be alloyed through the SPD-processes including the incorporation of nanoparticles (e.g. carbide, oxide, CNT) in the nanocrystalline metals and alloys [13, 19, 57]. However, the SPD-processes have limitations to produce nanocrystalline materials with microstructural sizes of few to tens of nanometers. The materials with ultrafine grain sizes (0.1–1.0 μm) were commonly produced through the SPD processes [48]. In addition, microstructure and chemical inhomogeneity was also frequently observed in the SPD-processed nanocrystalline materials caused by inhomogeneous strain distribution and particle/chemical distribution, which has a direct impact on the bulk mechanical properties [65, 66, 67]. Caused by some limitations of the SPD-processes, alternative processing routes are developed to produce a bulk nanocrystalline materials with a smaller size and more homogeneous microstructure.

The synthesis of nanocrystalline materials with smaller grain size is possible through mechanical alloying (MA) and consolidation. One advantage of the MA and consolidation process is the ability to produce a wide range type of materials, including nanostructured composites. In the mechanical alloying stage, the nanostructured powders with sizes of few to tens of nanometers are synthesised from coarser powders of metals, alloys, oxides, or carbides in the high-energy ball mill [46, 48]. A schematic picture of the mechanical alloying stage is shown in **Figure 2.2a**. Afterwards, these nanostructured powders are subjected to the consolidation stage through conventional sintering technology at high temperatures (i.e. beyond 50% of melting temperature) to achieve full densification with no porosity [46]. However, the high temperature sintering process induces normally grain coarsening of the nanocrystalline

materials and undesirable phase transformations, thus alternative consolidation techniques are needed. Currently, novel consolidation techniques of nanostructured powders have been developed at significantly lower temperatures involving external pressure or shear, for instance, hot isostatic pressing (HIP) [68, 69, 70], field-assisted sintering technology (FAST) [71, 72, 73], and equal channel angular extrusion (ECAE) [48, 74, 75]. **Figure 2.2(b-d)** depict schematic illustrations of the consolidation stage through different techniques. Bulk nanocrystalline materials with a grain size of 50-70 nm can be produced through the MA and novel consolidation processes, but no further grain refinement was reported. According to literature [46], the major problems in the processing of nanocrystalline materials through the MA and consolidation processes are expensive production cost, complex and difficult consolidation stage (minor grain coarsening and porosity), and the contamination of milled powders. Therefore, further development is needed to overcome the difficulties.

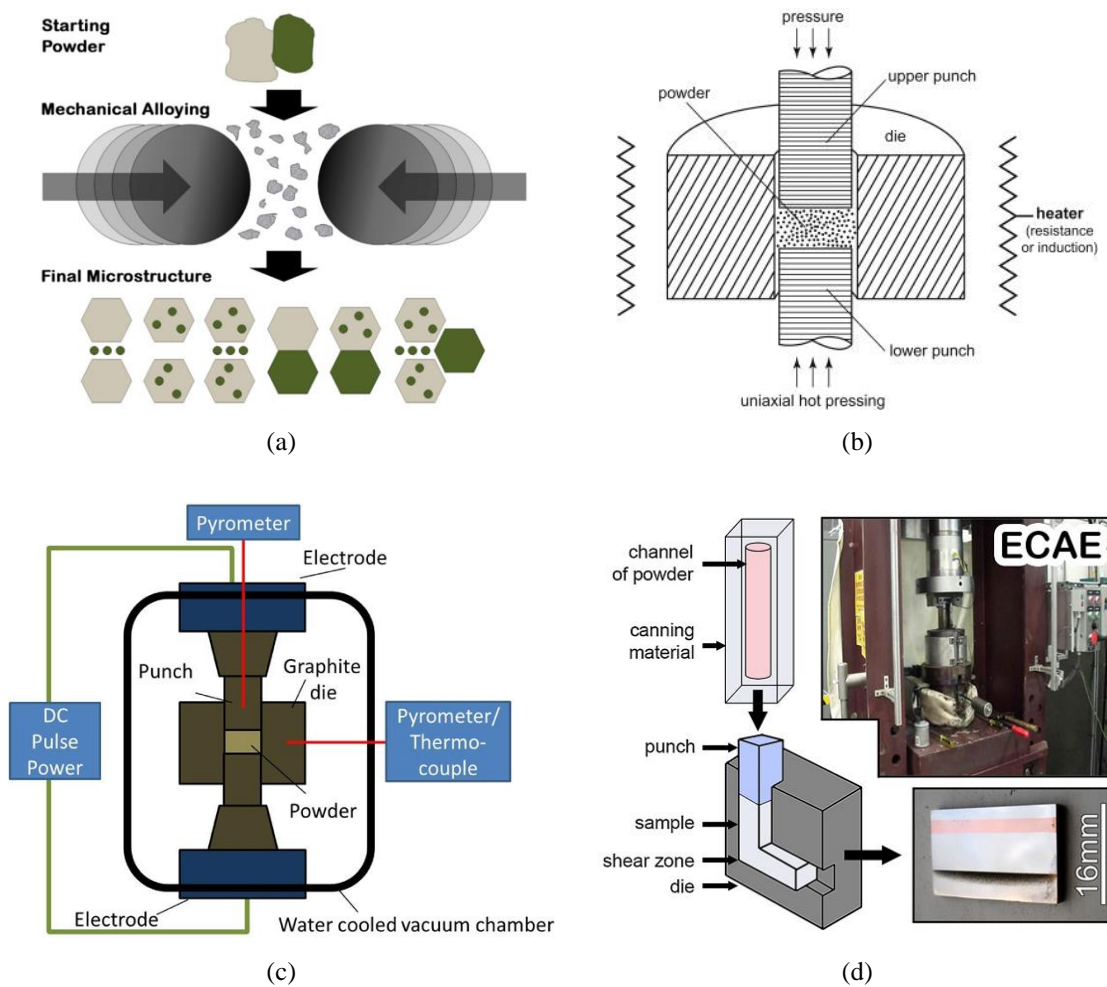


Figure 2.2 Schematic pictures of (a) mechanical alloying process (from [48]) and (b-d) consolidation stage through different techniques: (b) Hot isostatic pressing (HIP) (from [76]), (c) fast-assisted sintering technology (FAST) [from [72]], and (d) equal channel angular extrusion (from [48]).

The production of bulk nanocrystalline materials is also possible through the pulsed electrodeposition (PED) technique. The PED-process is a simple route of production with a low capital cost of investment [4]. The technology transfer of PED-process from the laboratory to the industrial scales are relatively easy [4]. Previous works have shown that the production of the bulk nanocrystalline pure metals with thicknesses of hundreds micrometer to few millimeters is possible through the PED-process [40, 25, 22, 42, 44, 39]. The production of bulk nanocrystalline alloys including the Co-Cu system with thicknesses of hundreds of micrometers is also possible in particular circumstances [29, 77, 78, 79, 80]. In the PED-process, the synthesis of the nanocrystalline materials with grain size of few to tens of nanometers (5-50 nm) is possible, which is difficult to achieve through SPD- and MA-processes. This would be a crucial opportunity to understand the mechanical and physical properties of bulk nanocrystalline materials with a different size range of microstructure compared to SPD- and MA-processed nanocrystalline materials. In addition, the PED-process does not need any compaction and consolidation process, which are crucial issues in the SPD-(from powder) and the MA-processes. However, the PED-process has limitations to produce a wide range of materials, whereas only selected metals and alloys can be electrochemically deposited. Furthermore, incorporation of some impurities (e.g. sulphur, carbon, hydrogen) during the PED-process may have a crucial impact on mechanical and physical properties of nanocrystalline materials.

The synthesis of bulk nanocrystalline materials through the SPD, the MA and consolidation, and the PED processes has distinct advantages and challenges. Synthesis of the bulk nanocrystalline Co-Cu through the MA and consolidation has not been reported yet. The nanocrystalline Co-Cu with a grain size of ~90 nm can be obtained through the SPD-processes from pre-compacted powders of Co and Cu [13, 16, 27]. The thermal stability, structural transformation, and mechanical properties of the bulk HPT-processed nanocrystalline Co-Cu have been also investigated [38, 16, 27]. The synthesis of the PED-processed bulk nanocrystalline Co-Cu with thicknesses of hundreds of micrometers has been also performed [77, 29]. However, further developments relating to inhomogeneous microstructure and dimensional scale-up are needed. The information about the thermal stability, mechanical and physical properties of PED-processed nanocrystalline Co-Cu is also limited. Therefore, further investigation and development is needed. In addition, the nanocrystalline materials processed through SPD and PED may exhibit different characteristic of microstructures (e.g. grain size), lattice defects (e.g. dislocations and twins) and processing flaws (e.g. porosity and contaminants), which have a significant impact on the properties of these materials. In the

present work, further investigation and development on the synthesis and characterisation of the PED-processed nanocrystalline Co-Cu are conducted to get a more comprehensive understanding of these types of materials.

2.2 Pulsed electrodeposition of nanocrystalline materials

2.2.1. Theory of pulsed electrodeposition of nanocrystalline materials

In the electrodeposition of metals and alloys, deposition parameters (e.g. working potential and current) have a significant influence on the properties of the electrodeposited materials, including the initial grain size. In this part, the fundamental theory of the electrodeposition of nanocrystalline materials is described. The electrochemical deposition reaction of a pure metal (M) at the cathode in the solution containing of metal ions (M^{n+}) is commonly written as [2.1]. The equilibrium potential (E_{eq}) between metal (M) and metal ions (M^{n+}) at the cathode can be calculated through the Nernst equation [2.2] which depends on the actual molar concentration ($C_{M^{n+}}$) and the activity coefficient ($\gamma_{M^{n+}}$) of metal ions. The quantities of E^0 , R , T , n , and F are the standard reduction potential, the ideal gas constant, the absolute temperature, the number of involved electrons, and the Faraday's constant, respectively.



$$E_{eq} = E^0 + 2.303 \frac{RT}{nF} \ln(C_{M^{n+}} \cdot \gamma_{M^{n+}}) \quad [2.2]$$

The equilibrium potential is a half-cell potential in the absence of an applied current (I). Upon the deposition of metal at cathode, the applied current (I) flows through the cathode and the potential move to more negative values (working potential E). The difference between the working potential (E) and the equilibrium potential (E_{eq}) is called as overpotential (η). The current density ($i = I/A$, where A is a surface area of cathode) is a function of the overpotential (η) as expressed by the Butler-Volmer equation [2.3], whereas i_0 , α , n , F , R , and T are the exchange current density, the transfer coefficient, the number of involved electrons, the Faraday's constant, the gas constant, and the absolute temperature, respectively.

$$i = i_0 \cdot \left[\exp\left(\frac{\alpha_{anode} nF}{RT} \eta\right) - \exp\left(-\frac{\alpha_{cathode} nF}{RT} \eta\right) \right] \quad [2.3]$$

The deposition of metals (cathodic process) is usually conducted at large negative values of overpotential ($\eta \geq 100$ mV). The adaptation of this condition to the cathodic process of Butler-Volmer equation [2.3] gives the Tafel equation [2.4]. Schematic diagrams of the Butler-

Volmer [2.3] and the Tafel [2.4] equations are shown in **Figure 2.3**.

$$\eta = E - E_{eq} = \frac{2.303RT}{\alpha_{cathode}zF} \log i_0 - \frac{2.303RT}{\alpha_{cathode}zF} \log |i| \quad [2.4]$$

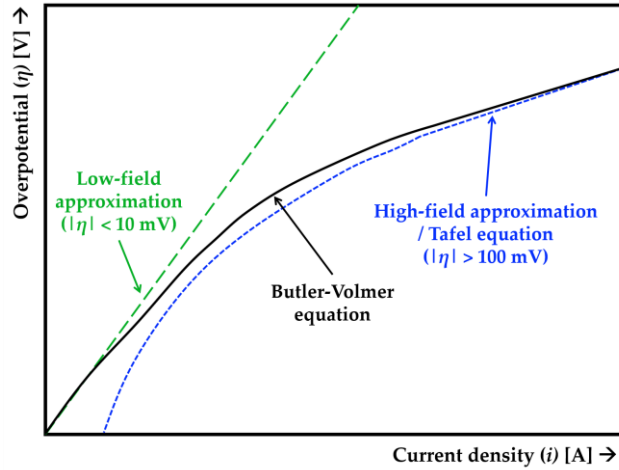


Figure 2.3 Schematic diagram of low-field and high-field approximations to the Butler-Volmer for a single electrode process (adapted from [81]).

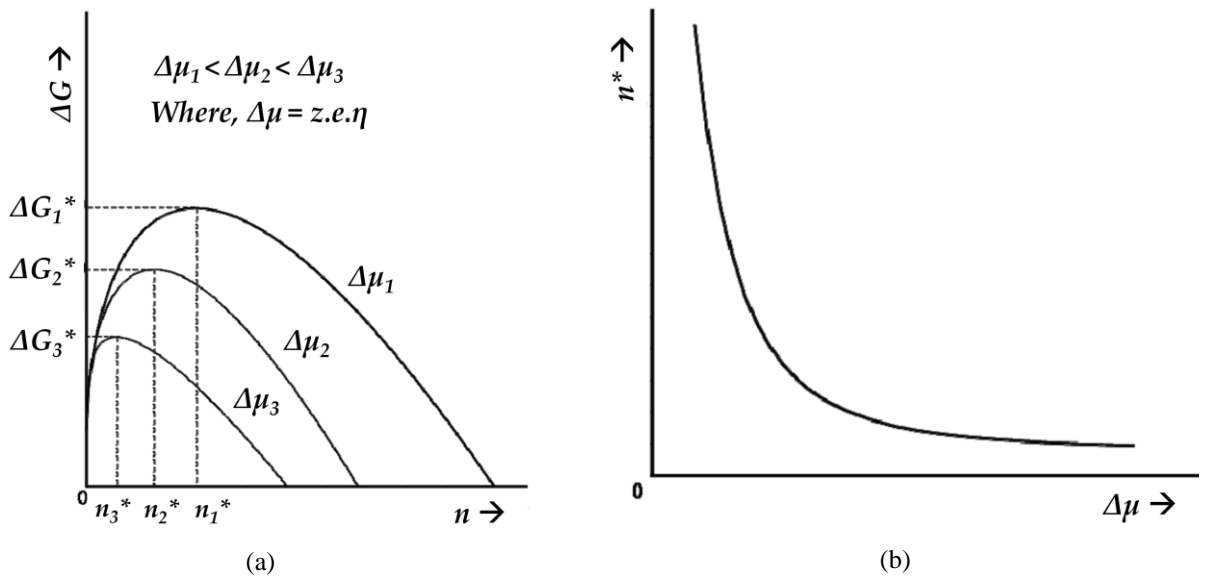


Figure 2.4 Schematic pictures of (a) dependence of the free energy of nucleation (ΔG) on n -atomic nucleus at the different thermodynamic supersaturation ($\Delta\mu_1 < \Delta\mu_2 < \Delta\mu_3$) and (b) the critical n -atomic nucleus (n^*) as a function of the thermodynamic supersaturation ($\Delta\mu$) (adapted from [82] and [83]).

The Butler-Volmer [2.3] and Tafel equations [2.4] are important to understand the overpotential-current density relation which has a direct impact on the grain size of deposited materials. According to the classical theory of electrochemical nucleation [84, 85], the

electrodeposition of materials starts with step-by-step deposition of atoms to form an atomic nucleus or cluster developing into a crystal and grain at the cathode. Upon the nucleation stage, the thermodynamic supersaturation ($\Delta\mu$), which is a function of overpotential η ($\Delta\mu = z.e.\eta$), has a direct impact on the free energy of nucleation ($\Delta G(n)$) for n -atomic nucleus as expressed in [2.5] [83, 82]. The quantity $\phi(n)$ is the energy excess of the n -atomic nucleus at the nucleus/cathode and nucleus/electrolyte interfaces. The schematic diagrams of the free energy of nucleation as a function of n -atomic nucleus at the different thermodynamic supersaturations ($\Delta\mu$) are shown in **Figure 2.4a**.

$$\Delta G(n) = -n \cdot \Delta\mu + \phi(n) \quad [2.5]$$

The critical free energy of nucleation (ΔG^*) is required to form the critical n -atomic nucleus (n^*), afterwards, a stable nucleus is formed at the electrode surface. Working mathematical operation to [2.5] (detail of derivation in [82] and [83]), the critical n -atomic nucleus (n^*) [2.6] and the critical free energy of nucleation (ΔG^*) [2.7] can be determined. The quantities v_M and a^* are the molar volume of nucleus substance and the material constant relating to the Gibbs-Curie-Wulff theorem, respectively.

$$n^* = \frac{a^* v_M^2}{\Delta\mu^3} \quad [2.6]$$

$$\Delta G^* = \frac{1}{2} \frac{a^* v_M^2}{\Delta\mu^2} = \frac{1}{2} n^* \Delta\mu \quad [2.7]$$

According to [2.6] and [2.7], early nucleation at the low critical free energy of nucleation (ΔG^*) with a small critical number of atomic nucleus (n^*) can be obtained by increasing the overpotential η ($\Delta\mu = z.e.\eta$). Here the size of the critical n -atomic nucleus is established as r^* . According to classical Gibbs-Kelvin relation (details of derivation in [86]), the critical crystal nucleation size (r^*) is a function of overpotential (η) [2.8]. The quantities σ , M , ρ , z , F are the interfacial tension of the nucleus/electrolyte interface, the molecular weight, the density, the number of involved electrons, and the Faraday's constant, respectively.

$$r^* = \frac{2 \cdot \sigma \cdot M}{\rho \cdot z \cdot F \cdot \eta} \quad [2.8]$$

According to [2.8], reduction of the critical crystal nucleation size (r^*) can be achieved by increasing the overpotential (η) or current density (i). Therefore, synthesise of the nano-structured materials (i.e. very small r^*) through the electrochemical deposition is possible at extremely high overpotentials or current densities.

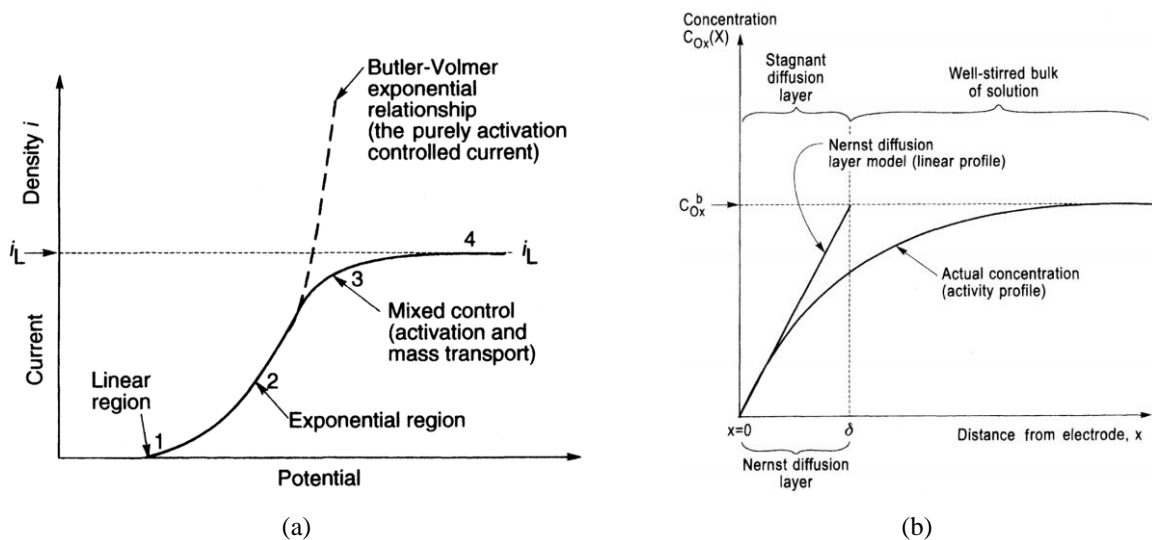


Figure 2.5 (a) Four different regimes in the current-overpotential relationship showing different mechanism upon the electrochemical deposition (from [87]). (b) Schematic diagrams of the concentration profile of metal ions as a function of distance from the electrode surface upon the non-steady electrochemical deposition. The concentration of metal ions in bulk solution (C_{Ox}^b) drops significantly at the electrode surface (C_{Ox}) caused by formation of the Nernst diffusion layer (from [87]).

However, conventional direct current (DC) electrodeposition at extremely high overpotentials has a limitation relating to the limiting current density (i_L) as shown in the **Figure 2.5a**. The limiting current density is a direct impact from the extreme concentration gradient of metal ions in the bulk solution and at the electrode surface caused by formation of the Nernst diffusion layer as shown in **Figure 2.5b**. The limiting current density is commonly observed during the long-time DC electrodeposition when the concentration of metal ions at the electrode surface significantly drops to zero ($C_{Ox} \sim 0$), thus, the rate of the deposition is controlled by the mass transport of metal ions from the outermost part of the Nernst diffusion layer to the electrode surface. The DC electrodeposition is commonly worked below the limiting current density, whereas the potential or the current density of the critical nucleation size of nanocrystalline formation may be not achieved. In case of the deposition potential was achieved, the long-time DC electrodeposition of bulk nanocrystalline materials is difficult caused by the concentration drops of metal ions in bulk solution (C_{Ox}^b) which speeds up the establishment of the limiting current density. Modification of the Nernst diffusion layer characteristic (i.e. thickness, diffusivity, concentration gradient) plays a key role for depositing the bulk nanocrystalline materials.

In the 1970s to 1980s, the theoretical and practical aspects of the pulsed electrodeposition (PED) were introduced as the alternative technique mainly by the research groups of Ibl [88, 89, 90] and Popov [91, 92, 93, 94]. One of the most crucial aspects in the PED is the modification of the Nernst diffusion layer [89], which enhances the concentration of metal ions

at the electrode surface. In the PED, the current density (i_p) is periodically switched on (t_{on}) and off (t_{off}) till the desirable thickness of deposit is obtained (see **Figure 2.6a**). The negative value of the pulse current density ($i_p < 0$) shows the cathodic process. The ratio between the pulse-on time (t_{on}) and the pulse-off time (t_{off}) is called as duty cycle (γ) [2.9]. The average current density (i_{avg}) is a function of the duty cycle (γ) and the pulse current density (i_p) [2.10].

$$\gamma = \frac{t_{on}}{t_{on} + t_{off}} \quad [2.9]$$

$$i_{avg} = i_p \cdot \gamma \quad [2.10]$$

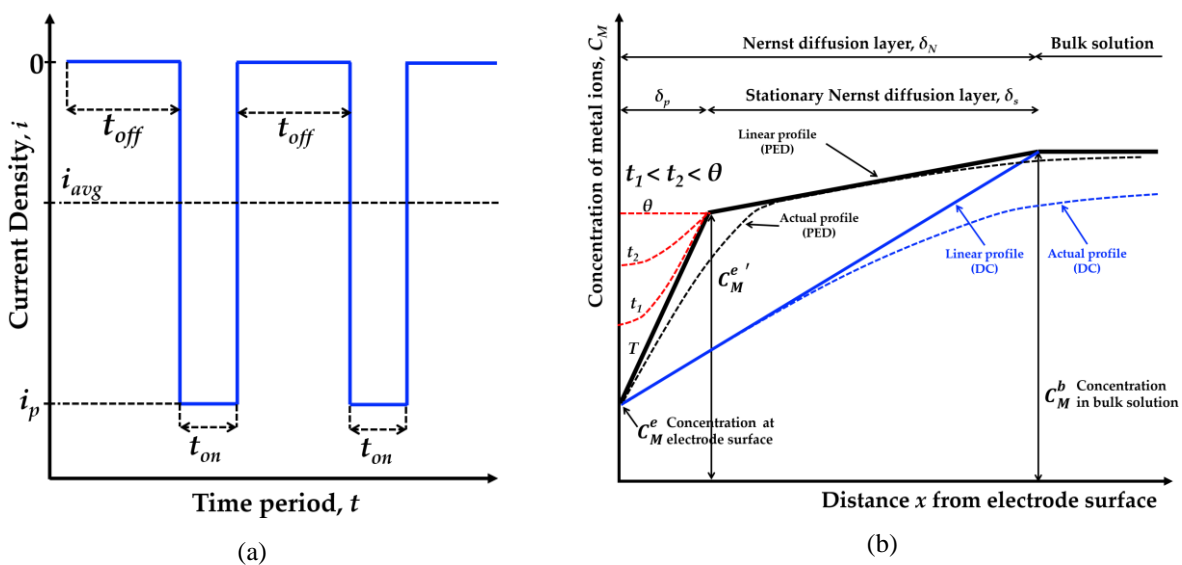


Figure 2.6 (a) Schematic diagram of the current density profile (i) as a function of the time period (t) upon the pulsed electrochemical deposition (PED). (b) Schematic diagrams of the linear (black solid line) and the actual (black dashed line) concentration profiles of metal ions as a function of distance from the electrode surface at the end of a single pulse of PED in comparison with the continuous DC electrodeposition (blue solid line and blue dashed line) (adapted from [88, 89]).

Figure 2.6b depicts schematic pictures of the linear (black solid line) and the actual (black dashed line) concentration profiles of metal ions in the modified Nernst diffusion layer at the end of a single pulse, which comprises the stationary diffusion layer (δ_s) and the pulsating diffusion layer (δ_p). When the pulse current is on (t_{on}), the concentration of metal ions at the cathode decreases which is followed by the formation of the pulsating diffusion layer with a thickness of δ_p . When the pulse current is off (t_{off}), metal ions are supplied from the bulk solution towards the cathode which leads to the relaxation of the diffusion layer. In the PED-process, the pulse-off time is commonly longer than the pulse-on time for extensive relaxation of the diffusion film. The concentration profiles of metal ions at the end of different pulse-off times

($T < t_1 < t_2 < \theta$, where $T = 0$) are shown by red dashed lines in **Figure 2.6b** showing a significant effect of the prolonged pulse-off time. It must be noted here that the pulsating diffusion layer is not completely disappeared during the off time. When the pulse current is off, the concentration of metal ions at the cathode recovers for supplying metal ions (i.e. through the diffusion mechanism) from the bulk solution towards the cathode. This transport mechanism leads to the formation of the stationary Nernst diffusion layer (δ_s) from the bulk solution to the outermost part of the pulsating diffusion layer (δ_p). The concentration gradient in the stationary diffusion layer does not change when the pulse current is on and off. **Figure 2.6b** shows that the concentration of metal ions in the diffusion layer of the PED-process is significantly higher compared to DC electrodeposition (blue solid and dashed lines). As a result, electrodeposition of nanocrystalline materials at the extremely high current density ($i_p > i_{L,DC-deposition}$) is possible.

The PED of nanocrystalline materials is commonly employed at very high deposition rates (high i_p), which means that the concentration of metal ions at the cathode surface may decrease rapidly to zero ($C_M^e \sim 0$). The limiting current density ($i_{L,PED}$) will be reached at this condition. The time required for the zero concentration of metal ions at the cathode surface in the single pulse is so-called transition time (τ). The pulse-on time (t_{on}) must be significantly shorter than the transition time to prevent the occurrence of the limiting current density ($i_{L,PED}$). The derivations of the transition time (τ), the thickness of the pulsating diffusion layer (δ_p), and the concentration of metal ions at the electrode surface (C_M^e) at the end of a single pulse has been explained by Ibl [89]. The current efficiency is assumed 100% with no capacitance effect in the diffusion layer, and the metal ions are homogeneously distributed just before the first pulse current. According to derivation, the transition time (τ) is dependent on the pulse current density (i_p) and the concentration of metal ions in the bulk solution (C_M^b) as shown in [2.11]. The quantity D is the diffusion coefficient of the metal ions. The thickness of the pulsating diffusion layer (δ_p) depends only on the pulse-on time (t_{on}) as shown in [2.12]. The concentration of metal ions at the electrode surface at the end of a single pulse (C_M^e) is a function of the pulse current density (i_p) and pulse-on time (t_{on}) as shown in [2.13].

$$\tau = \frac{\pi \times (nF)^2 \times (C_M^b)^2 \times D}{4 \times (i_p)^2} \quad [2.11]$$

$$\delta_p = 2 \sqrt{\frac{D \times t_{on}}{\pi}} \quad [2.12]$$

$$C_M^e = C_M^b - \left(\frac{2 \times i_p \times t_{on}}{z \times F \times \delta_p} \right) \quad [2.13]$$

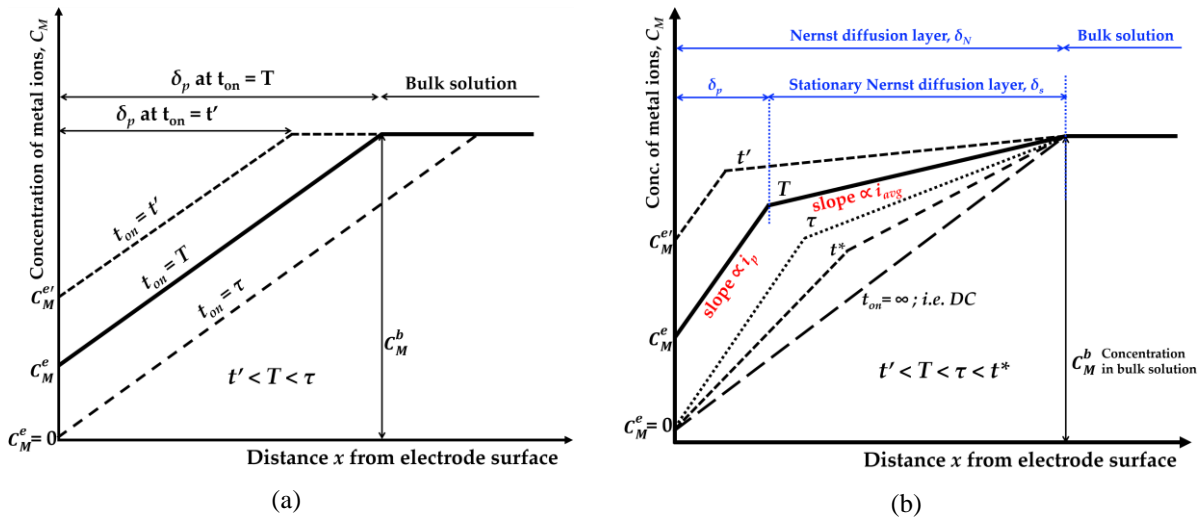


Figure 2.7 (a) Schematic diagrams of the pulsating diffusion layer profiles during the very initial single pulse of the PED-process (adapted from [89]) for the same pulse current density (i_p) at different pulse-on times ($t' < T < \tau$). (b) Schematic diagrams of the modified Nernst diffusion layer profiles (i.e. comprise the pulsating diffusion layer and the stationary diffusion layer) at the end of a single pulse of the PED at the same pulse current density (i_p) at different pulse-on times ($t' < T < \tau < t^*$) (adapted from [89, 95]).

Figure 2.7a shows the schematic diagrams of the concentration profiles of metal ions as a function of distance from the electrode surface at different pulse-on times ($t' < T < \tau$) relating to the equations [2.11]-[2.13]. The pulse-on time (t_{on}) has a crucial role in the PED of nanocrystalline materials at very high pulse current density. For $t_{on} < \tau$, higher concentrations of metal ions at the cathode surface with thinner pulsating diffusion layers can be observed at shorter pulse-on times. It must be also considered that the pulse-on time has a direct impact on the characteristic of stationary diffusion layer. **Figure 2.7b** depicts more realistic condition of the concentration profiles of metal ions at different pulse-on time ($t' < T < \tau < t^*$) at the end of a single pulse showing different profiles of the pulsating and the stationary diffusion layers. The concentration gradients in the stationary and the pulsating diffusing layers are proportional to the average (i_{avg}) and the pulse (i_p) current densities, respectively [89]. For $t_{on} < \tau$, the gradient concentrations in the stationary diffusion layer decreases prior to a shorter pulse-on time and smaller average current density, but the gradient concentrations in the pulsating diffusion layer remain the same. For $t_{on} > \tau$, the gradient concentration in the pulsating diffusion layer and pulse current density, which may show the formation of nanocrystalline materials with coarser grain size. In addition, nanocrystalline materials with compact and non-dendritic structure may not be achieved when $t_{on} > \tau$ [96]. In the PED-process of nanocrystalline materials, short duration of pulse current with small pulsating diffusion layer ($\delta_N/\delta_p > 3$) is preferred to gain an extremely high pulse current density [88, 89]. However, the nucleation and growth of a stable nano-sized structure requires a minimum pulse-on time (t_{min}). Thus, the pulse-on time is usually employed

between the minimum and transition times ($t_{min} < t_{on} < \tau$) for producing compact deposits of nanocrystalline materials.

The successful PED-process at extremely high pulse current density (i_p) does not depend only on the pulse-on time (t_{on}), but the pulse-off time has also a crucial impact. The influence of the pulse-off time (t_{off}) is mainly on the recovery of metal ion concentration at the cathode surface and relaxation of the diffusion layer (see **Figure 2.6**). The displacement reaction [33, 97, 98, 99], desorption of additives and impurities (e.g. sulphur, hydrogen, and carbon) [88, 99, 100, 101], and reduction of processing flaws (e.g. porosity and internal stresses) [88, 91, 102, 103, 104] are other possible mechanisms when the pulse current is off. In the previous works [49, 50, 77, 96, 105], the successful PED-process of bulk nanocrystalline Cu, Co, and Co-Cu were performed at the typical pulse-on time of less than 10 ms and a long off period (i.e. duty cycles of less than 50%). A more detailed discussions on the effect of deposition parameters on the properties of nanocrystalline Cu, Co, and Co-Cu is reviewed in the next section.

2.2.2 Electrodeposition of nanocrystalline Co, Cu, and Co-Cu

Electrolyte composition

In the electrodeposition of nanocrystalline Cu, Co, and Co-Cu, the electrolyte may comprise some ingredients, which are salts containing Co or Cu (e.g. CuSO_4 and CoSO_4), conducting salts (e.g. NaCl and Na_2SO_4), pH adjuster (e.g. sulfuric acid) and/or buffer solution (e.g. boric acid), complex former (e.g. citrate and tartrate), and additive (e.g. saccharine and sodium dodecyl sulphate). Each component has a significant impact on the properties of deposits, so controlling concentration and types of the individual components will be crucial. Previous works have been successfully produced nanocrystalline Co, Cu, and Co-Cu through direct- and pulsed current electrodeposition in various bath compositions. The electrolyte compositions used in these works are summarized in **Table 2.1**.

The salts containing Co or Cu are the most important part of the electrolyte. Co or Cu salts could be in various forms such as sulphates, chlorides, acetates, and others. These salts have different characteristics in the electrolyte such as different solubility, dissociation degree, and conductivity. Combining different Co or Cu salts in the single bath of electrodeposition is commonly used to achieve particular characteristics of the electrolyte. Concentration of salts must be controlled to ensure a sufficient supply of Co or Cu ions during deposition. Additional Co or Cu ions can be supplied through titration techniques or dissolution of Co or Cu anodes. Electrodeposition of multi-component metals is more complicated, whereas individual components may have different electrochemical behaviour and degree of nobility such as

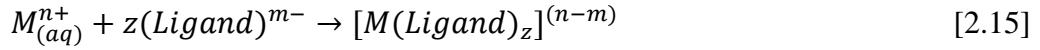
standard reduction potential, Tafel slope, and exchange current density. The concentration of individual salts (i.e. with controlling other parameters) must be controlled carefully to obtain deposit with desired chemical compositions and microstructures.

The conducting salts are crucial to enhance the conductivity of the electrolyte. The electrolyte conductivity is related to ionic transport and mobility and must ensure to be high enough for high current efficiency and high deposition rate. In the PED-process, the pulsed-on time in a single pulse is usually very short (could be in μs or ms), thus the solution must be highly conductive to ensure the vast transport of metal ions towards the cathode surface. Some alkali salts such as sodium sulphate and sodium chloride are usually added to enhance conductivity.

The solution acidity is usually kept at a certain level to get certain characteristics of the deposits. Upon the electrodeposition at high current density, side reactions such as hydrogen and oxygen evolutions can be observed at the electrode surfaces indicated by bubbles formation. These side reactions may consume or generate hydrogen ions, which results in the alteration of solution acidity. The change of solution acidity may influence the homogeneity of the microstructure of the deposits. A buffer solution (e.g. boric acid) is usually added to the initial electrolyte, while some strong acid (e.g. sulphuric acid) or base (e.g. sodium hydroxide) solution is usually added during deposition if solution acidity changes (i.e. solution pH usually measured for a certain period during deposition).

Complex former improves certain characteristic of metal ions in the aqueous solution. In the absence of complex former, metal ions (i.e. in this case Co and Cu ions) are usually hydrated by some water molecules in the electrolyte as expressed in [2.14]. These water molecules could be a barrier in the electrodeposition process caused by different ionic characteristics of hydrated ions compared to free metal ions. The size of hydrated metal ions is significantly bigger compared to free metal ions, which has a direct impact on the decrease of ionic mobility [106]. Reduction of ionic mobility can also be caused by interaction of hydrogen atoms in hydrated metal ions with surrounding hydrogen atoms of the water molecules (i.e. hydrogen bonding) [105]. In addition, the deposition reaction of metals from hydrated metal ions may need additional energy (i.e. energy for dissociation), which decreases the actual rate of nucleation and deposition. Desired characteristics of the deposition process (i.e. small nuclei formation for nanocrystalline) may not be achieved under this condition. Other molecules should be added to substitute these water molecules to change the ionic characteristics, for instance, through the formation of complex metal ions (see complexed ion formation in [2.15]). The formation of complex metal ions simply enhances ionic mobility compared with hydrated metal ions and

improves overall deposition process. Some organic and alkali-organic compounds are usually added to form complex metal ions, for instance, citrate, tartrate, acetate, and others. The concentration of complexing agents should be stoichiometrically proportional with the concentration of free metal ions to ensure complete complexed ion formation.



The last electrolyte ingredient are additives, which are usually added to achieve particular characteristics of the deposits, for instance, grain refiner/modifier, stress reliever, leveller, surface smoother, and others. Additives are commonly organic compounds such as saccharin, sodium dodecyl sulphate (SDS), diNa-EDTA, thiourea, and others. Sometimes, complexing agent and additive could be the same compound, but its concentration is different. The concentration of additives is usually very small compared with the concentration of complexing agent (i.e. usually less than 1% of the metal salt concentration). The concentration of additives must be considered carefully, whereas high concentration of additives may have side effects on deposits, for instance, formation of micro-pores, high internal stresses, undesired chemical compositions, increase of grain size, and co-deposition of impurities (e.g. sulphur and carbon).

Various electrolyte compositions have been used in electrodeposition of nanocrystalline Co, Cu, and Co-Cu as shown in **Table 2.1**. Some works performed the production of bulk nanocrystalline Cu, Co and Co-Cu with thicknesses of tens to hundreds of micrometers through direct- and pulsed-currents [8, 29, 31, 32, 42, 44, 77, 107, 108]. Here, we discuss particularly the deposition of nanocrystalline Co-Cu alloys. The Co and Cu salts which are commonly used are in sulphate form. The initial concentrations of Co- and Cu-sulphate can be adjusted by considering expected chemical composition and thicknesses of the deposits. Of course, pulse parameters (e.g. pulse current density and pulse-on and -off time) have also a significant contribution on chemical composition and thicknesses of the deposits (this point will be reviewed in the next sub-section). For a deposition of Co-rich nanocrystalline Co-Cu layers with thicknesses of >10 μm [29, 31, 32, 77], the concentration of Co-salt is usually higher than 0.4 M, whereas Cu-salt concentration could be by 10-fold magnitude lower.

Some works in electrodeposition of thick layers (>100 μm) of nanocrystalline Co, Cu, and Co-Cu [29, 42, 44, 77, 107, 108] showed that the addition of conducting salt was important to ensure high electrolyte conductivity. An improved conductivity enhances transport mechanism of Co and Cu ions and produces good properties of deposits. A common conducting salt is

sodium sulphate with concentrations of up to 1.0 M. This concentration can be adjusted depending on the desired condition of electrolyte and deposits. Boric acid is a common buffer solution in electrodeposition of nanocrystalline Co and Co-Cu to maintain the solution acidity with typical concentrations of 0.1 M to 0.5 M as shown in previous works [29, 77, 108]. Sulphuric acid can be used also to adjust the initial pH of solution.

Table 2.1 The example of electrolyte composition used in direct- and pulsed-current electrodeposition of nanocrystalline Cu, Co, and Co-Cu from various literatures. Detailed information about the deposition parameters (current density, pulsed duration, and other) are summarised in **Table 2.2**.

Ref	Component	Conc.	Important remark	
[105]	Cu salt	CuSO ₄ .H ₂ O	128 g/L	PED of nanocrystalline Cu in the bath containing different organic compound. The addition complex former significantly reduced the grain size from 50 nm (without complex former) to 29 nm (citric acid) and 20 nm (DiNa-EDTA). Increasing concentration of citric acid (up to 100 g/L) led to further grain refinement. Malonic and tartaric acid led to the formation of coarse grained of with strong polycrystalline texture.
	Conducting salt	(NH ₄) ₂ .SO ₄	50 g/L	
	Complex former	Citric acid	21 g/L	
		DiNa-EDTA	42 g/L	
	Additive	Malonic acid	12 g/L	
	Tartaric acid	17 g/L		
[8]	Cu salt	CuSO ₄	NA	Electrodeposition of nanocrystalline Cu with grain sizes of 23-30 nm [8, 42]. PED-process of ultrafine grain sized of Cu (300-1000 nm) with nano-scale twin spacing (15 nm) [44, 107].
[42]	Conducting salt	NaCl	< 0.1 % v/v	
[44]				
[107]	Additive	Gelatine	<0.02 % v/v	
[109]	Cu salt	Cu(CH ₃ COOH) ₂ .H ₂ O	100 g/L	DC electrodeposition of nc Cu. No significant change of grain size from all electrolyte (10-18 nm). Deposits with a preferred (220) orientation obtained in the absence of additive and with additive (3). In the presence of additives (1) and (2), deposits showed a preferred (111) orientation. Saccharin is a brightener not a grain refiner. Compact deposits were obtained from bath containing additives (1) and (3).
	Complex former	Methane sulphonic acid	90 ml/L	
	Buffer	Na(CH ₃ COOH)	20 g/L	
	Additive	(1) Thiamine hydrochloride	0.25g/L	
		(2) Saccharin	0.25 g/L	
		(3) C ₁₀ H ₉ NO ₄ S	0.25 g/L	
[110]	Cu salt	CuSO ₄	200 g/L	DC electrodeposition in the absence and presence of additives. All deposits showed a preferred (220) orientation. Additives are effective grain refiner (i.e. without and with additives are ~80 nm and <30 nm, respectively). Additives led to the formation of more dense deposits.
	pH adjuster	H ₂ SO ₄	54 g/L	
	Additive	(1) Benzotriazole	0.5 g/L	
		(2) Sodium lauryl sulphate	0.1 g/L	
[111]	Cu salt	CuSO ₄ .5H ₂ O	0.05 M	DC electrodeposition of nc Cu. Lactic acid led to deposits smooth, compact and bright nc Cu films. Cathodic efficiency is high (>80%). Particle size ranged 25-30 nm and could be coarser with increasing temperature.
	Complex former	Lactic acid	0.30 M	
	Conducting salt	Na ₂ SO ₄	0.10 M	
[112]	Co salt	CoSO ₄ .7H ₂ O	0.200 M	DC electrodeposition of ~40 nm thick of nanocrystalline Co deposits at pH of 4.5. Nanocrystalline Co has hcp-structure with average grain sizes of 71-81 nm.
	Complex former	Sodium citrate	0.600 M	
[113]	pH adjuster	H ₂ SO ₄	0.100 M	
	Additive	DiNa-EDTA	0.025 M	

Ref	Component	Conc.	Important remark	
[108]	Co salt	CoSO ₄ .7H ₂ O	112 g/L	Electrodeposition of nanocrystalline Co (thick: 100-150 μm) with different mode of current: direct, pulsed, and pulsed-reverse currents. All deposits consisted of hcp-structure with different preferred orientation. Grain size: DC (~51 nm) > Pulsed (~36 nm) > Pulsed-reverse (~11 nm). No information about effect of electrolyte composition on the characteristic of deposits.
	Complex former	Sodium citrate	59 g/L	
	Conducting salt	Na ₂ SO ₄	100 g/L	
	Buffer	H ₃ BO ₃	19 g/L	
	Additive	Saccharin sodium C ₁₈ H ₂₉ NaO ₃ S	2 g/L 0.1 g/L	
[7] [23] [39] [40] [50] [114]	Co salt Buffer Conducting salt Additive	CoSO ₄ H ₃ BO ₃ NaCl Saccharin	Not mentioned	PED of thick deposits (50-250 μm) nc Co. Saccharin is stress reliever and grain refiner. Grain sizes is 12-20 nm. Saccharin concentration was varied to get different content sulphur in deposits [23]. PED-process of ~50 μm thick nanocrystalline Co at various pulsed current density and pulsed duration with smallest grain size of ~25 nm [114].
[29] [77]	Co and Cu salts	CoSO ₄ .7H ₂ O CuSO ₄ (varied)	0.40 M 0.04 M	[29] DC deposition of nc Co-Cu (76 at% Co) in citrate-bath at a current density of 300 A/m ² . [77] PED of nc Co-Cu (40-80 wt% Co) in bath containing citrate or tartrate. Deposition at high current density (up to 1500 A/m ²) from tartrate bath showed compact deposits of nanocrystalline Co-Cu, whereas no porosity observed in contrast to citrate bath. Cu content and grain size increased with increasing Cu concentration in the electrolyte. Saccharin reduced deposition of Co, increased deposition of Cu. SDS led to deposition of Co. .
	Conducting salt	Na ₂ SO ₄	1.00 M	
	Buffer	H ₃ BO ₃	0.30 M	
	Complex former	KNa-tartrate.4H ₂ O Na ₃ -citrate-4H ₂ O	0.20 M 0.20 M	
	Additive	Saccharin Sodium dodecyl sulphate	2.00 g/L 0.10 g/L	
[31] [32] [37]	Co and Cu salts pH adjuster Additive	CoSO ₄ .7H ₂ O CuSO ₄ .5H ₂ O H ₂ SO ₄ Saccharin (only in ref [37])	1.000 M 0.025 M NA 0.015 g/L	DC deposition of 10 μm thick nc Co-Cu (93 wt% Co) with nanoscale lamellar structure. The pH of solution was adjusted to 5 by H ₂ SO ₄ . Saccharin acted as grain refiner, whereas nano grains could be obtained at significantly lower current density in contrast to deposition with no additive.
[33]	Co and Cu salts	CoSO ₄ .7H ₂ O CuSO ₄ .5H ₂ O	0.60 M 0.15 M	Pulsed plating of ~500 nm thick nanocrystalline Co-Cu (0.6-73 wt% Co) at fixed pulsed current density (400 A/m ²) and varied pulsed-on and -off time with high current efficiency (>70%). The typical grain sizes are 5-55 nm with 80% of grains below 20 nm. Saccharin promoted the phase separation of Co-Cu, whereas fcc (Co and Cu) and hcp (Co) were detected.
	Complex former	Trisodium-citrate-2H ₂ O	0.30 M	
	Buffer	H ₃ BO ₃	0.48 M	
	Additive	Sodium dodecyl sulphate Saccharin	0.20 g/L 0.10 g/L	
	Co and Cu salts	CoSO ₄ CuSO ₄	0.300 M 0.005 M	
Buffer	H ₃ BO ₃	0.400 M		
[97] Complex former	Sodium acetate	0.100 M		
pH adjuster	H ₂ SO ₄	NA		
Additive	Saccharin Sodium dodecyl sulphate	2.0 g/L 0.2 g/L		

Ref	Component	Conc.	Important remark	
[98]	Co and Cu salts	CoSO ₄ .7H ₂ O	0.700 M	Pulsed plating of thin layer (up to 1.3 μm thick) Co-Cu alloy (<50 at% Cu) at fixed pulsed current density and duty cycle at various off-times. Columnar structure as well as multilayer of Co-Cu with two phases of Co-rich and Cu-rich regions were observed indicating displacement reaction of Co by Cu. The FC99 additive used to reduce the surface tension and pit formation caused by evolution of hydrogen gas bubbles.
		CuSO ₄ .5H ₂ O	0.025 M	
	Complex former	Trisodium-citrate-2H ₂ O	0.180 M	
	Additive	Premixed FC99 fluorinated surfactant (3M®)	1/50 parts	

There are various types of complex formers used in electrodeposition of nanocrystalline Co, Cu, and Co-Cu. A citrate-based solution was commonly used as complex former in electrodeposition of very fine grained Co and Co-Cu [29, 77, 108]. Electrodeposition of nanocrystalline Cu in a bath containing citrate was only performed by Hempelmann et al. [105]. Interestingly, investigations by Müller [77] showed that 400-500 μm thick deposits of nanocrystalline Co-Cu could be obtained from a bath containing tartrate as complex former with a homogeneous chemical composition and microstructure and no porosity was observed even at a high current density (1500 A/m²). This condition could not be obtained from a bath containing citrate. This observation is important for improving the deposition of bulk nanocrystalline Co-Cu with a good homogeneity of microstructure and chemical composition and low processing defects (e.g. porosity).

Saccharin has been used regularly as an additive in electrodeposition of nanocrystalline Co, Cu, and Co-Cu. Saccharin acts mainly as grain refiner. This additive is effective to produce nano-structured grains even at significantly lower current density in comparison with a deposition with no additive as shown in [37]. Deposition at lower current density is crucial to decrease the possible hydrogen generation, which may reduce current efficiency and hydrogen embrittlement. Saccharin may also act as crystal growth inhibitor, whereas the formation of undesired structures (e.g. dendritic structure) can be suppressed. In the pulsed deposition of nanocrystalline metals, saccharin has also a contribution on the chemical composition by inhibiting Co displacement reaction by Cu ions when the pulsed current is off. **Figure 2.8a** shows that the concentration of saccharin has a direct impact on grain refinement in the PED-process of nanocrystalline Ni [115]. It shows that 2-5 g/L saccharine is an optimum range to deposit nanocrystalline materials with grain sizes of below 30 nm. Higher concentration of saccharin is not effective for further grain refinement. Deposition in a bath containing saccharin led to co-deposition of sulphur and carbon impurities as shown in **Figure 2.8b** [115]. Sulphur and carbon impurities may have a good impact on the improvement of thermal stability of

nanocrystalline materials through the segregation to grain boundaries [14, 23], but it has also undesired effects on the mechanical properties, e.g. grain boundary embrittlement [25]. Other additive such as sodium dodecyl sulphate (SDS) can also be included in the bath electrolyte with smaller concentration (i.e. usually lower than 0.2 g/L) to support grain refinement and improve quality and compactness of deposits. SDS were also reported to promote dissolution of Co, which enhances Cu content in deposit.

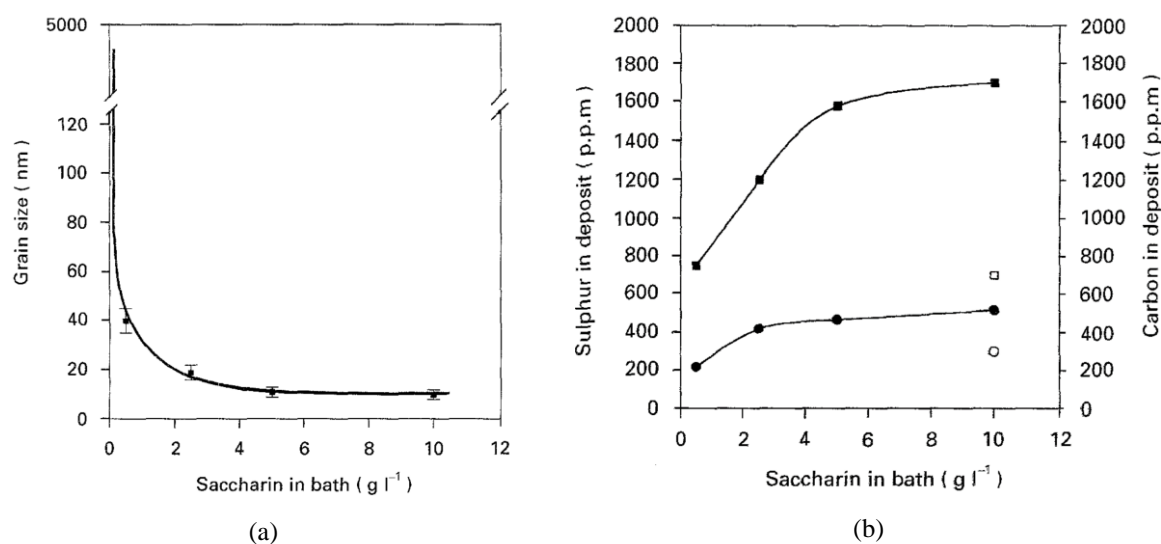


Figure 2.8 Effect of saccharin concentration in bath electrodeposition on (a) grain size, (b) sulphur (square) and carbon (circle) contents in the PED-processed nanocrystalline Ni deposits (from [115]).

Electrodeposition parameters: current density and pulse duration

In DC electrodeposition, there is only one parameter (i.e. current density) that can be controlled. On the other hand, there are three crucial parameters in the PED-process which are pulse current density, pulse-on and -off time. Controlling these parameters is important to obtain different characteristics and microstructures of the deposit. Especially the peak current density is a crucial parameter in electrodeposition of nanocrystalline materials. A high current density is needed to deposit small nuclei resulting in nanostructured grains. Therefore, the minimum value of deposition current densities that is resulting in nanocrystalline Co, Cu, and Co-Cu are reviewed from previous works. In the PED-process, pulse duration has a significant impact on the properties of deposit, for instance, on chemical composition, grain size, crystallographic orientation, and others. A summary of deposition parameters used in the previous works of electrodepositing nanocrystalline Co, Cu, and Co-Cu is shown in **Table 2.2**.

According to previous works shown in **Table 2.2**, the minimum current density (i.e. direct- and pulse-current) for depositing nanocrystalline Cu was 200 A/m² [109, 110] and it must be

higher for deposition of nanocrystalline Co and Co-Cu due to the more negative standard reduction potential of Co. The works showed that production of bulk nanocrystalline Co, Cu and Co-Cu with thicknesses of hundreds of micrometers was difficult to achieve through direct-current electrodeposition [31, 32, 37, 42, 112, 113]. Thick layers of nanocrystalline deposits up to 500 μm could be synthesised through the PED-process. It is believed that further process optimisation in PED may produce thicker layer of nanocrystalline metals and alloys. According to previous works, PED of nanocrystalline Co, Cu and Co-Cu was commonly performed at pulse current densities of hundreds to thousands A/m^2 , which cannot be done under conventional DC electrodeposition caused by the limiting current density. Deposition at higher current densities can produce smaller size of grain. The working duty cycle should be between 10-50%, but working duty cycle of higher than 30% might lead to a higher number of pore formation [77]. The pulse current density could be as high as hundreds of thousands A/m^2 by reducing duty cycle to less than 5% for producing a high-density of nano twins [50, 105, 107], but this range of deposition parameter is not studied in this thesis.

Table 2.2 Examples of deposition parameters (direct and pulse current density, pulse-on and –off time) used in electrodeposition of nanocrystalline Cu, Co, and Co-Cu from various literatures. The quantities of i_{dc} , i_{pulsed} , t_{on} , and t_{off} are direct current density, pulse current density, pulse-on time, and pulse-off time.

Ref	Deposition parameters	Thickness (μm)	Grain Size (nm)	Important Remarks
[105]	PED of nc Cu $i_{pulsed} = 12500 \text{ A}/\text{m}^2$ $t_{on} = 1 \text{ ms}$ $t_{off} = 100 \text{ ms}$	NA	No-add: 50 nm EDTA: 20 nm Citric: 29 nm	Pulsed parameters were varied. The biggest grain size (83 nm) was obtained at $i_{pulsed} = 780 \text{ A}/\text{m}^2$, $t_{on} = 1 \text{ ms}$, and $t_{off} = 6 \text{ ms}$ ($\theta = 14.3\%$). Deposition at 20-60 $^{\circ}\text{C}$ produced nc structure with grain sizes of 5-91 nm. Higher temperature deposits coarse grain.
[44] [107]	PED of nc Cu $i_{pulsed} = 4.10^5\text{-}1.10^6 \text{ A}/\text{m}^2$ $t_{on} = 0\text{-}50 \text{ ms}$ $t_{off} = 1000\text{-}3000 \text{ ms}$	30 μm	300-1000 nm Avg: 400 nm	Ultrafine grain sized of Cu (300-1000 nm) with nano-scale twin spacing (15 nm). Specific information about pulsed parameters are not available.
[109]	DC deposition of nc Cu $i_{dc} = 200 \text{ A}/\text{m}^2$	NA	10-18 nm	The biggest grain size (18 nm) deposited in bath containing no organic additive.
[110]	DC deposition of nc Cu $i_{dc} = 200 \text{ A}/\text{m}^2$	NA	20-80 nm	The biggest grain size (80 nm) deposited in bath containing no organic additive.
[112] [113]	DC deposition of nc Co $i_{dc} = 400\text{-}500 \text{ A}/\text{m}^2$	$\sim 40 \mu\text{m}$	71-81 nm	Nc Co deposits exhibited a hcp-structure. Surface roughness increased with increasing current density.
[108]	DC deposition of nc Co $i_{dc} = 400 \text{ A}/\text{m}^2$ PED of nc Co $i_{pulsed} = 2000 \text{ A}/\text{m}^2$ $t_{on} = 0.2 \text{ ms}$; $t_{off} = 0.8 \text{ ms}$	$\sim 100 \mu\text{m}$	DC dep: $\sim 50 \text{ nm}$ PED: $\sim 35 \text{ nm}$	DC and PED processes at the same deposition rate (400 A/m^2) resulted nc Co with hcp structures. Pulsed current promoted a (002)-hcp peak. Nodular (size 5-30 μm) and hay-stick (size 2-5 μm length) surface structures were observed from deposits with direct- and pulsed-current, respectively.

Ref	Deposition parameters	Thickness (μm)	Grain Size (nm)	Important Remarks
[7] [23] [39] [40] [50]	PED of nc Co $i_{\text{pulsed}} = 1.10^4\text{-}3.10^5 \text{ A/m}^2$ $t_{\text{on}} = 1\text{-}5 \text{ ms}$ $t_{\text{off}} = 30\text{-}50 \text{ ms}$	45-200 μm	12-20 nm	In ref [7, 23, 39, 40], details of deposition parameters were not mentioned. Ref [50] described range of deposition parameters and suggested duration of pulsed-on and -off time at 2.5 and 45 ms, respectively. Deposition at higher current density caused a burned deposit. Nc Co deposits exhibited mixed of hcp and fcc structures.
[114]	PED of nc Co $i_{\text{pulsed}} = 500\text{-}4000 \text{ A/m}^2$ $t_{\text{on}} = 0.2 \text{ ms}$ $t_{\text{off}} = 0.8 \text{ ms}$	NA	18-220 nm	Minimum current density to deposits nc Co (<100 nm) was 1500 A/m ² . Nc Co deposits exhibited a hcp-structure.
[29]	DC deposition of nc Co-Cu $i_{\text{dc}} = 300 \text{ A/m}^2$	NA	50-150 nm	Deposition of nc Co-Cu (76 at% Co) with fcc-structure. Exact value of grain size was not mentioned, but SEM and TEM measurement showed that grain sizes are 50-150 nm.
[77]	PED of nc Co-Cu $i_{\text{pulsed}} = 500\text{-}1500 \text{ A/m}^2$ $t_{\text{on}} = 1 \text{ ms}$ $t_{\text{off}} = 2.33 \text{ ms}$	300-500 μm	At 500 A/m ² : 50-250 nm At 1000-1500 A/m ² : 20-100 nm	Deposition in two different complex formers (citrate and tartrate). Co content increased (40-80 wt% Co) with increasing current density (500-1500 A/m ²). More compact deposits with less porosity from citrate-bath deposits (compared with citrate-bath). Nc Co-Cu contained of fcc-structure.
[33]	PED of nc Co-Cu $i_{\text{pulsed}} = 400 \text{ A/m}^2$ $t_{\text{on}} + t_{\text{off}} = 10 \text{ ms}$ $t_{\text{on}} = 1\text{-}5 \text{ ms}$ $t_{\text{off}} = 5\text{-}9 \text{ ms}$	$\sim 0.5 \mu\text{m}$	At $t_{\text{on}} = 1 \text{ ms}$ GS: 5-55 nm Avg: 17.1 nm	Pulsed duration: $t_{\text{on}} + t_{\text{off}} = 10 \text{ ms}$. Nc Co-Cu with fcc-structure were deposited. Hcp-Co observed with saccharin addition. Co content increased (19.4-51.5 wt% Co) with increasing on-time (1-5 ms). At $t_{\text{on}} \geq 5 \text{ ms}$, rough and burnt deposits was produced.
[31] [32] [37]	DC deposition of nc Co-Cu $i_{\text{dc}} = 400 \text{ A/m}^2$	10 μm	GS: 110 nm	Deposition of nanocrystalline Co-Cu (93 wt% Co) deposit with nano-scale lamellar structure. Average grain size was 110 nm with 3 nm lamellar spacing.
[97]	PED of nc Co-Cu $i_{\text{pulsed}} = 400 \text{ A/m}^2$ Duty cycle = 20% $t_{\text{on}} = 0.001\text{-}100 \text{ s}$ $t_{\text{off}} = 0.004\text{-}400 \text{ s}$	1.5 μm	At $t_{\text{on}} = 500 \text{ ms}$ GS: 10-15 nm	Cu content decreased and Co content increased with increasing on-time at the same duty cycle of 20%. Cu content is higher than 30at% at $t_{\text{on}} < 1 \text{ s}$ and it is 20-25 at% Cu at $t_{\text{on}} > 1 \text{ s}$. Short pulsed ($t_{\text{on}} = 50\text{-}500 \text{ ms}$) produced a columnar structure with Co-rich phase with surrounding Cu-rich matrix. Long pulsed ($t_{\text{on}} = 50 \text{ s}$) produced a multilayer Co-Cu with thickness layers of Co and Cu are 120 nm and 60 nm, respectively.

In the PED of nanocrystalline pure Co or Cu, deposition parameters have a powerful impact on the microstructure of the deposit. It is even more complicated in the PED-process of nanocrystalline Co-Cu. Previous works [33, 77, 97] showed that the pulse duration (i.e. on- and off-time) had significant effects on the chemical composition and microstructure of nanocrystalline Co-Cu. A work by Müller [77] observed an inhomogeneous microstructure of Co-Cu deposits (i.e. nano-sized grains at the next to the substrate and ultrafine-grains at the next to the solution) at a pulsed current density of 500 A/m². Hence, the pulse current density should be higher to ensure the formation of deposits with homogeneous nanostructure.

According to Müller [77], production of homogeneous nanocrystalline Co-Cu deposits was possible at the pulse current densities of 1000-1500 A/m². However, one must be careful since deposition at these high current densities may lead on hydrogen generation, which reduces current efficiency, induces pores, and incorporation of hydrogen atoms. Regarding pulse duration, a higher Cu content could be obtained by increasing off-time and decreasing on-time and duty cycle. It has been shown that the displacement reaction of deposited Co by Cu ions occurs when the current is off [33, 97], which is caused by the significantly different standard reduction potential of Co and Cu. Prolonged pulse-on and -off times up to thousands of milliseconds produced Co-Cu multilayer instead of nanocrystalline structure. Thus, the pulse-on time must be also limited for producing nanocrystalline Co-Cu.

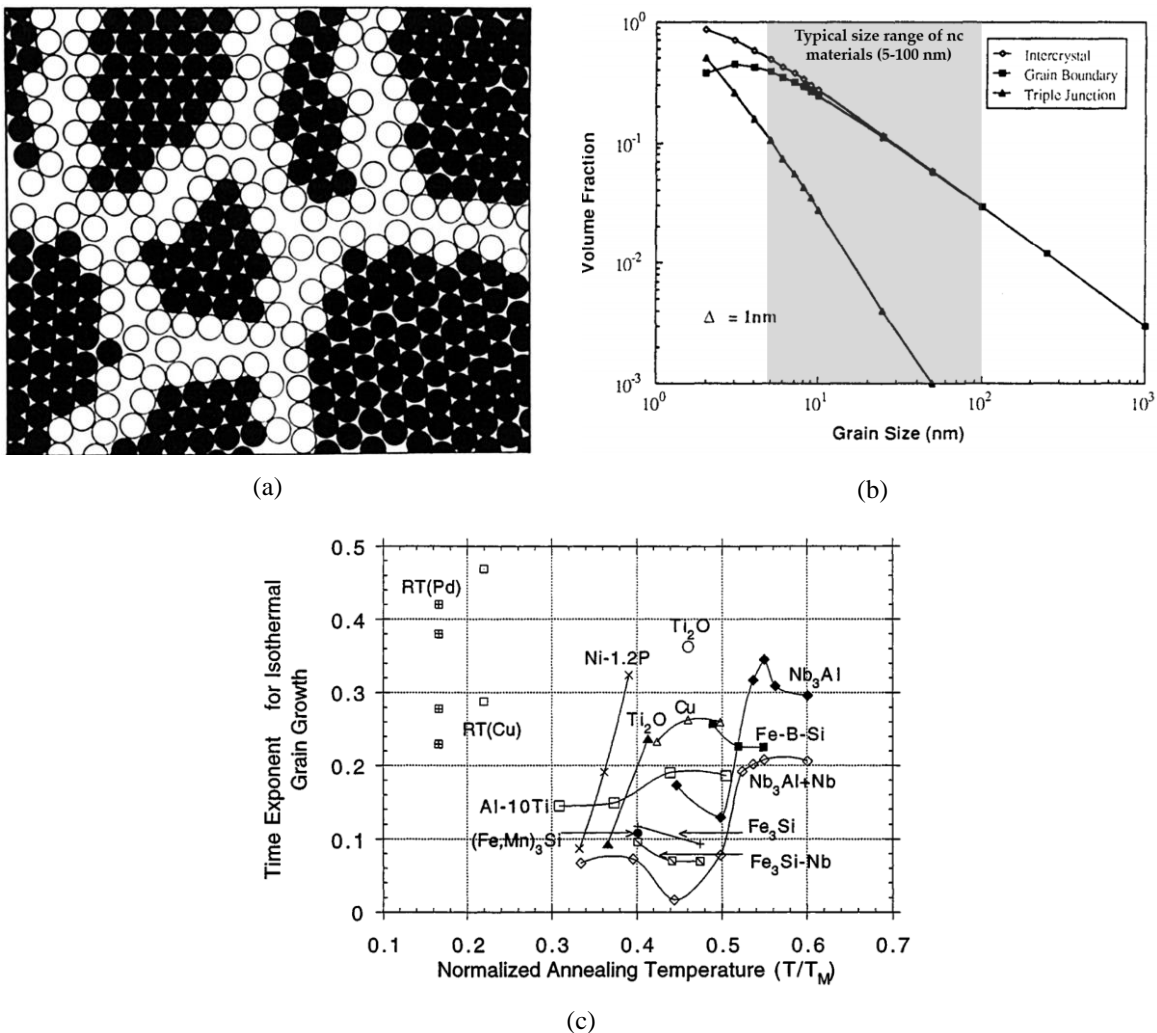


Figure 2.9 (a) Schematic picture of two-dimensional atomic structure of nanocrystalline materials, whereas black and white circles correspond to the atoms within grains and grain boundaries, respectively (from [1]). (b) Measured volume fraction of grain boundary, triple junction, and inter-crystal regions as a function of grain size by assuming 1 nm width of grain boundaries (modified from [116]). (c) Some values of time exponent ($1/n$) for isothermal grain growth of various nanocrystalline materials as a function of normalized annealing temperature (T/T_M), whereas T_M is a melting or liquidus temperature of materials (from [2]).

According to the previous works, it is believed that a homogeneous structure of nanocrystalline Co-Cu can be produced at specific pulse current density starting from 1000 A/m². The duty cycle should be kept lower than 30% with pulse-on times of less than 10 ms to deposit enough Cu content to enhance specific properties and to produce compact and low-porosity deposits. Electrolyte composition has a significant contribution on the properties of nanocrystalline Co-Cu deposits. Electrolyte composition as shown by Su [108] and Müller [77] are likely to be the ideal composition. Concentration of individual ingredient can be adjusted further to improve electrolyte and deposit characteristics.

2.3. Thermal stability of nanocrystalline materials

Grain growth in nanocrystalline materials

Nanocrystalline materials with typical grain sizes of 5-100 nm have an extensive area of grain boundaries as shown in **Figure 2.9a** [1, 2, 117]. **Figure 2.9b** shows more specific information about the volume fraction (1-17 vol.%) of grain boundaries in nanocrystalline materials compared to coarse grained counterparts. Grain boundaries are regions with misfit of atoms compared to the perfect crystal resulting in a high interfacial excess energy. Having a high energetic state in grain boundaries, nanocrystalline materials have a strong tendency to grain growth for reducing the total excess energy and achieving a more stable condition [118]. High interfacial excess energy can be found also in inter-crystal and triple junction regions, which have a quiet large volume fraction in nanocrystalline materials (see **Figure 2.9b**), contributing on microstructure instability under thermal and mechanical loading.

The isothermal grain growth kinetics in nanocrystalline materials can be studied by using the classical grain growth kinetic for conventional polycrystalline materials as established by Burke and Turnbull [119]. This approach assumes that grain boundary migration is driven by atomic transfer across the surface curvature of boundaries [120]. According to this approach, the mean grain size of polycrystalline materials (D) after a certain period of time (t) can be estimated by a simple relationship as shown by the following equation:

$$D^n - D_0^n = Kt , \quad [2.16]$$

where D_0 , K , and n are the initial grain size, the rate constant, and the grain growth exponent. In case of $D \gg D_0$, equation [2.16] can be simplified as follows:

$$D = K' \cdot t^{1/n} , \quad [2.17]$$

where K' and $1/n$ are another rate constant and the time exponent, respectively. The grain growth exponent (n) is a one of the crucial parameter for describing the grain growth kinetic and mechanism. The ideal value of $n = 2$ (parabolic relationship) is usually found in high purity elements of coarse-grained materials at a high value of normalized annealing temperatures, whereas the curvature-driven grain boundary migration is a dominant mechanism [2, 118]. Extreme deviations of n from the ideal value was observed in various nanocrystalline pure metals as shown in some literatures [8, 121, 122, 123, 124, 125]. Some values of time exponent ($1/n$) for isothermal grain growth of various nanocrystalline metals and alloys as a function of normalized annealing temperature (T/T_m) are shown in **Figure 2.9c**.

Extreme deviations of grain growth exponent (n) from the ideal value is an indication of other grain growth mechanism instead of a dominant curvature-driven mechanism in nanocrystalline pure metals. The large area of grain boundaries and triple junctions in nanocrystalline materials has a crucial contribution. According to Peng et al. [118], grain growth in nanocrystalline pure metals may be attributed to various mechanisms, which may delay grain growth process. These are: (i) free-volume and non-equilibrium vacancy drags [126, 127], (ii) limited mobility of triple junctions [128, 129], (iii) micro-strain induces nonlinear-response-type growth [130], and (iv) slow grain boundary roughening induces grain growth stagnation [131]. In these conditions, the grain boundary energy and mobility decrease, which could be thermodynamic and kinetic resistances for grain growth.

The activation energy for grain growth (Q) is another crucial parameter for describing the grain growth kinetic and mechanism in nanocrystalline materials. This parameter can be determined by using isothermal and non-isothermal (Kissinger) kinetic analysis. For isothermal kinetic analysis, the activation energy for grain growth can be determined by measuring the constant value (K) at the various annealing temperatures (T) as shown by equation [2.18].

$$K = K_0 \cdot \exp\left(\frac{-Q}{RT}\right) \quad [2.18]$$

where K_0 and R are the pre-exponential constant and the ideal gas constant, respectively. For Kissinger's analysis, the peak temperatures (T_p) from DSC measurement at the various heating rates (B) were plotted through the Arrhenius relationship using the following equation:

$$\ln\left(\frac{B}{T_p^2}\right) = \frac{-E}{RT_p} + \text{constant}, \quad [2.19]$$

where E and R are the activation energy for grain growth and the ideal gas constant, respectively. For nanocrystalline pure Co or Cu, the activation energies for grain growth have

been investigated and they can be found in some literatures as described in **Table 2.3**.

Stabilization of nanostructured grains

Basically, stable nanocrystalline microstructure can be achieved by reducing the driving force for grain growth. The driving force for grain growth (ΔP) is proportional to the grain boundaries energy (γ_{GB}) and inversely proportional to the grain size diameter (D) as shown in [2.20]. Derivation of this equation is available elsewhere [118].

$$\Delta P \propto \gamma_{GB}/D \quad [2.20]$$

According to [2.20], the grain size diameter (D) is given from materials itself, thus, the adjustable parameter is the grain boundaries energy (γ_{GB}). Reduction of the grain boundaries energy is crucial for grain growth inhibition. Some dragging mechanisms are proposed for reducing grain boundaries energy including (i) triple-junctions drag, (ii) vacancy drag, (iii) free-volume/pores drag, (iv) solute drag, and (v) second phase particles drag. Dragging mechanisms of (i)-(iii) are provided internally by nanocrystalline materials, which has a significant impact to non-ideal grain growth mechanism as described in the previous sub-section. Stabilization of nano-structured grains through triple junction drag has been utilized, for instance, by producing nanocrystalline materials with a larger area of grain boundary and triple junction (i.e. grain size reduction) [23]. However, the thermal stability of nanocrystalline materials remains low at this circumstance, and further improvement on the thermal stability with other techniques is needed (e.g. second phase particles drag and solute drag effect).

Second phase particles drag is one popular approach for reducing the driving force for grain growth. This approach implements Zener pinning effect [132], whereas second phase particles (e.g. precipitate, oxide, CNT) are incorporated in nanocrystalline materials. Interactions between these particles and grain boundaries results in Zener drag force, which acts as a barrier for grain boundary movement as shown in **Figure 2.10a**. The Zener force (ΔP_z) from spherical particles at a grain boundary can be described by the following equation:

$$\Delta P_z = 3F_v\gamma/2r, \quad [2.21]$$

where F_v , γ , and r are the volume fraction of particles, the particles-matrix surface energy, and the mean radius of particles, respectively. Pinning of grain boundary and grain growth inhibition are expected under specific condition: the Zener force (ΔP_z) is larger than the driving force for grain growth (ΔP).

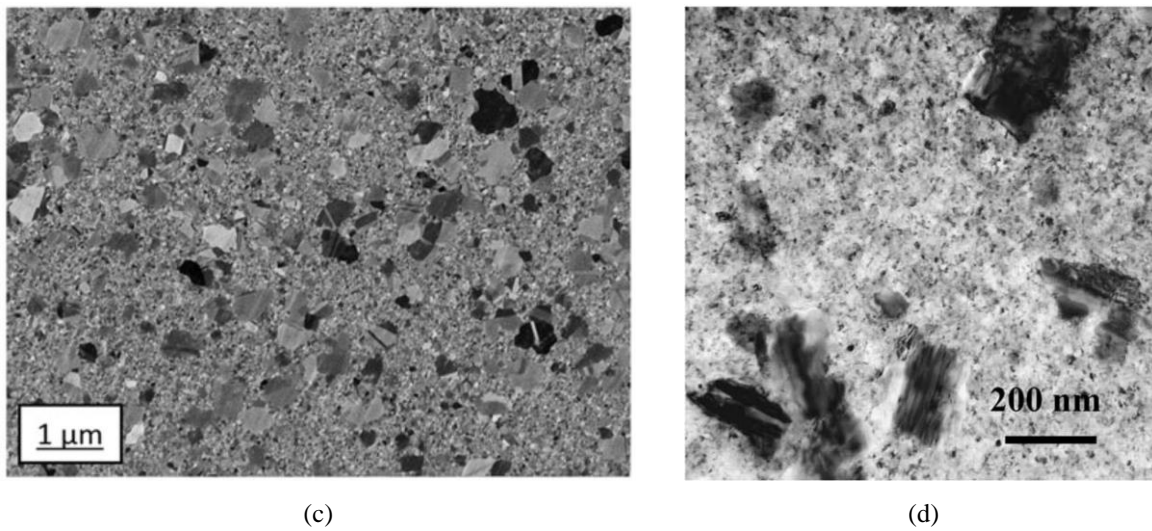
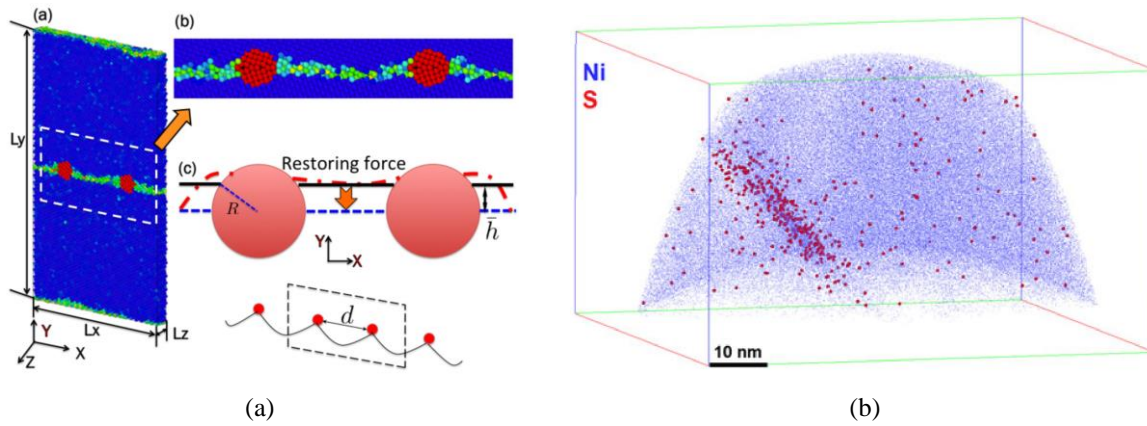


Figure 2.10 (a) Schematic picture of molecular dynamic simulation showing drag effect of pinning particles at a grain boundary (from [133]). (b) Atom probe tomography elemental maps of Ni (blue) and sulphur (red) observing solute sulphur segregation at a grain boundary of an annealed nanocrystalline Ni (from [25]). (c-d) Microstructural images show abnormal grain growth in (c) nanocrystalline Ni after annealing at 210°C for 150 minutes (from [25]) and (d) nanocrystalline Co after annealing at 300°C for 2 minutes (from [23]).

Applications of second phase particles for stabilizing nanostructured grains have been performed by researchers. Koch et al. suggested that this approach was effective for stabilizing nanostructures even at a high annealing temperatures, which corresponds to their results showing stabilization in nanocrystalline Fe with Zr intermetallic precipitates [134]. Significant improvement on the thermal stability of nanocrystalline Ni was also observed with the addition of metallic-oxide [57] or CNT [135] particles. In nanocrystalline Co, addition of carbon was effective to increase starting grain growth temperature from below 300°C for pure nanocrystalline Co to 400°C with doped carbon [13]. Distribution of particles is a major challenge in this approach, whereas the agglomeration and inhomogeneous distribution of particles were frequently reported [25, 67], which may have a direct impact to grain boundary embrittlement.

Solute drag effect is another important approach for stabilizing grain boundaries and improving thermal stability. The solute drag effect in nanocrystalline materials is established from solutes atoms acting as grain boundary segregation, which may reduce the grain boundaries energy. Theoretical determination of the grain boundary energy in the presence of solute atoms segregation at grain boundaries has been described comprehensively by some researchers [118, 136, 137, 138]. It shows that minimisation of the total grain boundary energy by solute atoms segregation is possible leading to stable grain boundary.

Experimental approaches have been performed for improving the thermal stability of nanocrystalline materials with the solute drag effect. In nanocrystalline materials, the roles of alloying elements and processing contaminants have been widely investigated in which grain boundary segregation were observed. Significant improvement on the thermal stability was observed at various solid solution nanocrystalline alloys, for instance, Ni-Co [14], Co-Cu [13, 27, 29], Ni-Cu [139], and Co-Cu-Ag [15] systems. In addition, phase transformation of metastable solid solution upon annealing at the specific temperatures may lead to formation of grain boundaries precipitates and phase/chemical decomposition, which could be a barrier for further grain growth.

The role of processing contaminants or impurities such as sulphur [6, 23, 25, 115], phosphor [24, 140, 141, 142], and carbon [13, 23] in nanocrystalline materials received great interest for grain boundary stabilization. These impurity elements are observed commonly in electrodeposited nanocrystalline metals. Electrolyte components such as saccharin, phosphate, thiourea, and other organic molecules could be the sources of impurity elements, which are adsorbed at the cathode during electrodeposition. The addition of organic molecules cannot be avoided for deposition of thick film nanocrystalline metals and alloys, which may act as grain refiner, growth inhibition, etc. Ideally, impurity elements should be distributed homogeneously in nanocrystalline materials (including grain boundaries), which provides grain boundary stabilization. Improvement on the thermal stability of nanocrystalline metals in the presence of impurity elements has been reported for nanocrystalline Ni [6] and Co [23, 24, 142].

In case of impurity elements are not distributed at grain boundaries, grain boundary segregation is also possible upon annealing at a high annealing temperature. Atomic mobility of impurity elements increases with increasing temperature, whereas elemental diffusion of impurity elements to grain boundary is possible leading to grain boundary segregation and grain growth inhibition. Grain boundary segregation by sulphur and phosphor elements after annealing has been reported elsewhere. For instance, Rathman et al. [25] observed sulphur

segregation at the grain boundary of an annealed nanocrystalline Ni as shown in **Figure 2.10b**. In addition, significant increase in phosphor concentration at grain boundary was also observed in annealed nanocrystalline Co by Choi et al. [24] and da Silva et al. [142], which may act as grain boundary segregation and phosphor-rich precipitates. In addition, abnormal grain growth in nanocrystalline Ni [25] and Co [23] was observed also due to inhomogeneous distribution of sulphur segregation, which leads to the formation bimodal microstructure as shown in **Figure 2.10c,d**. However, grain boundary segregation may also lead to grain boundary embrittlement if the local concentration of impurities is high enough.

Table 2.3 The thermal stability of nanocrystalline pure Co and pure Co processed through various techniques from some previous works. (IGC = Inert gas condensation; FCAT = Filtered cathodic arc technique; MS = Magnetron sputtering; PED = Pulsed electrodeposition; SPD = Severe plastic deformation; HPT = High pressure torsion).

Material	Processing Technique	Grain size (nm)	Information about thermal stability
Cu [9]	IGC	22-36	Abnormal grain growth at ambient room temperature for 18 days up to 50 nm grain size due to some factors: (i) non-uniform grain size distribution, (ii) impurity segregation, (iii) porosity induce hindering grain boundary migration.
Cu [124]	FCAT	25-30	Grain coarsening up to ~40 nm grain size was observed at 150°C. The grain growth exponent (N) was 3.0. The activation energy for grain growth from Arrhenius plot was 21-30 kJ/mol. The pinning force for grain growth was contributed by second phase particle and porosity drags.
Cu [143]	MS	Gs: ~700 Tt: ~40	Isothermal annealing technique for 3 h. Grain coarsening in nano-twinned Cu (grain size (Gs): ~700 nm and twin thickness (Tt): ~40 nm). Grain size was stable up to 300°C but it increased to ~700 nm at 400°C.
Cu [8]	PED	5-80 Mean: ~20	Grain growth start at 75°C. Grain growth was followed by micro-strain release. The activation energy for grain growth determined by Kissinger and isothermal kinetic analysis were 90 ± 16 kJ/mol and 83 ± 13 kJ/mol, respectively. Grain growth mechanism was controlled by grain boundary diffusion. The grain growth exponent (N) was 3.4 to 4.0.
Co [7]	PED	5-55 Mean: ~20	MDSC (non-isothermal) technique at 5°C/min showed that grain growth of hcp-structure nc Co could start at 346°C. Grain size increased to ~120 nm at 550°C (heating rate: 40°C/min) and followed by transformation fcc structures. The activation energy for grain growth was 152-163 kJ/mol.
Co [23]	PED	Mean: 8-20	MDSC (non-isothermal) technique at 0.67°C/s of 10 samples nc Co with different grain size (8-20 nm) and sulphur content (240-980 ppm). Grain growth could start at 337-410°C. The activation energy for grain growth increased from 157 to 221 kJ/mol with decreasing grain size from 20 to 8 nm. The activation energy for grain growth also increased significantly from 125 to 280 kJ/mol with increasing sulphur content from 240 to 980 ppm. Grain size increased to 0.1-1 μm during isothermal annealing at 300°C for 120 s and followed by abnormal grain growth and sulphur segregation at grain boundaries.
Co [13]	SPD-HPT	< 100	Isothermal annealing of nc Co with hcp-structure at 300°C for 1 h showed a significant decrease of hardness of about 40% showing grain coarsening. Non uniform microstructure (ufg and needle-shaped grain) was observed at 300°C but it was not observed at higher temperature (only needle-shaped grains).
Co [27]	SPD-HPT	Mean: 62 ± 31	DSC technique at different heating rate (10-120 °C/min) showed grain growth could start at 456-519°C. Hardness significantly decreased for about 20% upon isothermal annealing at 400°C for 1 h showing significant grain coarsening. The activation energy for grain growth is ~177 kJ/mol.

Thermal stability of nanocrystalline Co, Cu, and Co-Cu

Poor thermal stability in nanocrystalline materials were mainly observed in single phase materials. These materials have a relatively homogeneous microstructure whereas no other microstructural features (e.g. precipitates, solute atoms, grain boundary segregations, and others) can act as a barrier for grain growth. **Table 2.3** describes the thermal stability of nanocrystalline pure Co and pure Cu processed with various techniques with different microstructures (e.g. grain sizes, twins, impurities, and others). It shows that grain coarsening in nanocrystalline pure Cu could start even at ambient room temperature after several days, showing the very unstable grain structure [9]. Abnormal grain growth was also observed by the detection of coarse grained regions surrounded by nanocrystalline structures caused by a non-uniform distribution of grain sizes, impurities, and pores [9]. Grain coarsening of nanocrystalline pure Cu with a grain size of ~20 nm could start at 75°C [8], and it could be even faster for only 30 minutes at higher temperatures (130-150°C) [124].

Nanocrystalline pure Co showed a better thermal stability compared to nanocrystalline Cu. Previous works [7, 13, 23, 27] showed that grain coarsening in nanocrystalline pure Co could start at 300°C. Sulphur concentration had a crucial contribution for improving the thermal stability in nanocrystalline Co in which grain boundary segregation was expected [23]. However, this dragging mechanism may have detrimental effects on the mechanical properties. Improvement on the thermal stability was also detected with decreasing grain size of nanocrystalline Co showing the triple junctions and vacancies dragging mechanisms.

A modification of the microstructure in nanocrystalline pure Co and Cu is crucial to improve the thermal stability. This includes dragging mechanisms from different sources such as solute atoms, second-phase particles (Zener), triple-junctions, vacancies, and pores. Triple-junction and vacancy drags were implemented in high-density nano twinned Cu, which showed a significant improvement of the thermal stability compared to nanocrystalline Cu [143]. Very fine grained Cu with a grain size of ~700 nm and twin spacing of ~40 nm remained stable up to 300°C [143]. In nanocrystalline Co, the addition of a small amount of solute carbon up to ~400 ppm in HPT-processed nanocrystalline Co significantly improved the thermal stability in which grain coarsening was not detected up to 300°C [13]. Investigations on the thermal stability of nanocrystalline pure Cu and Co showed that small concentrations of impurities resulted in an improved thermal stability, but it may have undesired side effects such as grain boundary embrittlement and abnormal grain growth. Moreover, this approach is not significantly effective for stabilization of nanostructured grains at higher temperatures, in which significant grain coarsening were observed. It is believed that solute atoms have a significant

impact on the stabilisation of nanostructured grains using other mechanisms, for instances, formation of metastable solid solution and precipitates.

A supersaturated solid solution nanocrystalline Co-Cu with different Co and Cu concentrations were developed by Bachmaier and colleagues [13, 27, 29] for improving the thermal stability of nanocrystalline Co or Cu as summarized in **Table 2.4**. The HPT-processed nanocrystalline Co-Cu with different compositions (Cu rich: 26 at.% Co; Co-rich: 75 wt.% Co) showed a significant improvement on the thermal stability compared to nanocrystalline pure Cu and pure Co in which minor grain coarsening was observed at 400°C [13, 27]. Differential scanning calorimetry (DSC) measurements detected peak temperatures of the decomposition process of Cu-rich and Co-rich materials with ~440°C and ~545°C, respectively [29]. The thermal stability was improved with increasing of Co content. An improved thermal stability can be observed also in the electrodeposited (ED) nanocrystalline Co-Cu (i.e. in comparison with pure Cu and Co), but grain growth started at lower temperatures compared to HPT-processed materials in which massive decrease in hardness (i.e. indication of grain coarsening) was observed at 400°C. The HPT- and ED-processed nanocrystalline Co-Cu exhibited a supersaturated solid solution phase with face-centred-cubic (fcc) structure and confirmed that solute atoms improved the thermal stability of nanocrystalline materials. However, APT and TEM-EELS investigation for HPT-processed nanocrystalline Cu-26 at.% Co [27] showed that the evidence of Co or Cu segregation was difficult to observe, whereas Co and Cu elements were randomly distributed. The sizes of Co or Cu segregation might be very small, which could not be detected from the measurement. Grain boundary segregation of Co and Cu started to detect at 400°C after 100 hrs annealing, which could be a reason for stable nanostructured grain at 400°C (i.e. only minor grain coarsening observed).

Table 2.4 The thermal stability of Co-rich and Cu-rich nanocrystalline Co-Cu processed through high pressure torsion (HPT) and electrodeposition (ED) techniques from some literatures. (SPD = Severe plastic deformation)

Composition of Co-Cu	Processing Technique	Grain size (nm)	Information about thermal stability
Co-rich (75 wt% Co) [13, 29]	SPD-HPT	<100	Grain coarsening could be started at >400°C. Effect of impurities was uncertain. High and low purity of Co-Cu showed a slight differences of activation energy for grain growth.
Cu-rich (26 at% Co) [27, 29]	SPD-HPT	Mean: 91±39	Minor grain coarsening at 400°C with hardening effect at 300-400°C were observed. Impurities might improve thermal stability showed by higher activation energy.
Co-rich (76 at% Co) [29]	ED	<100	Grain coarsening could be started at 300-400°C. Hardening effect at 300°C. Hardness significantly dropped up to ~30% at 400°C showing significant grain coarsening.

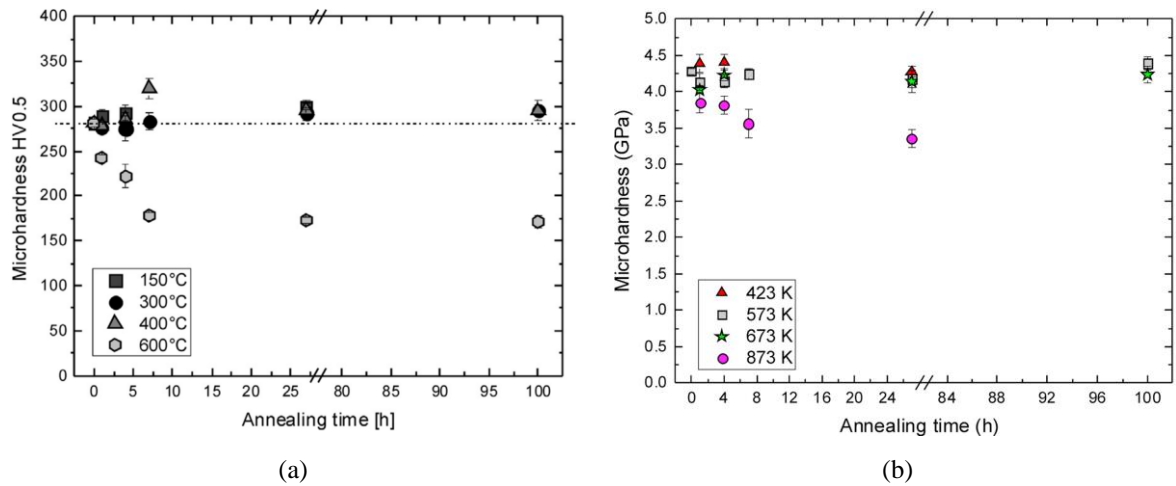


Figure 2.11 Long-term thermal stability of (a) Cu-rich (26 at% Co) and (b) Co-rich (75 wt% Co) nanocrystalline Co-Cu processed through high pressure torsion (HPT) at various annealing temperatures for up to 100 h. Figures (a) and (b) were taken from references [27] and [13], respectively.

It has been investigated that nanocrystalline Co-Cu alloys showed an improved thermal stability. Convincing microstructural evolutions during annealing at particular temperatures were also observed. **Figure 2.11a,b** show a long-term thermal stability of the HPT-processed nanocrystalline Co-Cu observed a hardening and a softening effects at different annealing temperatures. A hardening effect was detected in the Co-rich and Cu-rich nanocrystalline Co-Cu alloys at annealing temperatures of 300°C and 400°C, respectively [13, 27]. Atom probe tomography (APT) measurements of Cu-rich nanocrystalline Co-Cu confirmed spinodal decomposition of solid solution Co-Cu at 400°C, in which nanometers sized Co- and Cu-rich regions were observed [27]. It was believed that formation of Co- and Cu-rich regions had a crucial contribution on the hardening effect at these annealing temperatures. Further investigations are needed to observe the structural evolution at the lower temperatures (300°C) which would be studied in this thesis. Previous works [13, 27] observed a significant grain coarsening of the Co-rich and Cu-rich nanocrystalline Co-Cu alloys up to an ultrafine grained size (100-600 nm) at 600°C for annealing times of less than 10 h (see **Figure 2.11a,b**). Interestingly, a stable grain size could be achieved after 10 h annealing showed from unchanged microhardness. X-ray diffraction (XRD) and selected area diffraction (SAD) measurements of nanocrystalline Co-Cu confirm a distinct phase separation of Co and Cu, whereas the fcc-Cu, fcc-Co, and hcp-Co phases were detected [13, 27]. Complete phase separation and multi-component phases might have a contribution on the grain growth inhibition at 600°C.

The thermal stability and structural evolution of the SPD/HPT-processed nanocrystalline Co-Cu has been studied comprehensively. Structural evolutions in the electrodeposited

nanocrystalline Co-Cu at different temperatures are also convincing for a more comprehensive investigation. Electrodeposited nanocrystalline materials exhibit also other mechanism for stabilization of nanostructured grains such as segregation of impurities (solute drag effect), which is not observed in SPD/HPT-processed materials. Thus, an improved thermal stability is expected from electrodeposited materials. In addition, electrodeposited nanocrystalline materials may have a different characteristic of defect structures (e.g. number of dislocations, nano-twin formations, and others) [144, 145, 146, 147] which have a direct impact on the mechanical properties. In this thesis, the pulsed electrodeposition (PED) process is used instead of DC electrodeposition to obtain the desired nanocrystalline deposits which could not be achieved through conventional electrodeposition technique.

2.4. Mechanical properties of nanocrystalline Co-Cu systems

2.4.1. Strength and ductility

Hall-Petch effect in nanocrystalline materials

The concept of strengthening mechanism with grain size reduction is predicted from the Hall-Petch effect. Theoretical approach of the Hall-Petch effect can be explained with the dislocation pile-up model [148, 149] as depicted in **Figure 2.12a**. In this model, dislocations are generated at the centre of a grain (Frank-Read source) and they move along the slip plane within the grain approaching the boundary. For plastic deformation, dislocations have to pass across the grain boundary and move to the neighbouring grains, thus the yield point of material can be reached. However, there are two barriers for a continuous dislocation movement across the grain boundary, these are: (i) a large misfit atoms within the grain boundary [150], and (ii) a different crystallographic orientation of the neighbouring grains [150, 151]. As the movement of dislocations is blocked at the grain boundary, the occurrence of plastic deformation will be hindered. In this circumstance, dislocations need to change their direction of movement at the neighbouring grains as shown in **Figure 2.12b**. However, this process will need a higher applied stress [150]. As the applied stress increases, dislocations create a pile-up at the grain boundary with a length of L_p (see **Figure 2.12a**) [151]. The continuous pile-up process will produce the stress concentration at the grain boundary, which is needed to move the dislocations across the boundary. Sometimes, the stress concentration at the grain boundary may activate new dislocation sources in the adjacent grains. Plastic deformation occurs when the number of dislocations in a pile-up is high enough to achieve the critical value of the stress concentration at the grain boundary.

As a grain size decrease, very fine grained polycrystalline materials (grain size $< 1 \mu\text{m}$) have a larger total area of grain boundary compared to coarse grained polycrystalline materials (grain size $> 1 \mu\text{m}$) counterparts. Since the total grain boundary area for blocking dislocations movement increases in very fine grained materials, a higher applied stress is required for generating the same number of dislocations in the pile-ups for yielding. Thus, very fine grained polycrystalline materials are expected to exhibit a higher yield strength compared the coarse grained polycrystalline materials counterparts. According to the Hall-Petch relationship [152], the yield strength (σ_y) of polycrystalline materials is inversely proportional to the square root of the grain size (d) as shown in the following equation:

$$\sigma_y = \sigma_0 + kd^{-\frac{1}{2}}, \quad [2.22]$$

where σ_0 is the friction stress or the yield strength of single crystals [152, 151] and k is the Hall-Petch constant. In comparison to coarse grained polycrystalline materials, significant increase of strength can be achieved in nanocrystalline materials by decreasing grain size down to below 100 nm. For instance, nanocrystalline pure Cu and Co exhibit a significantly higher yield strength compared to their coarse grained counterparts [40, 153].

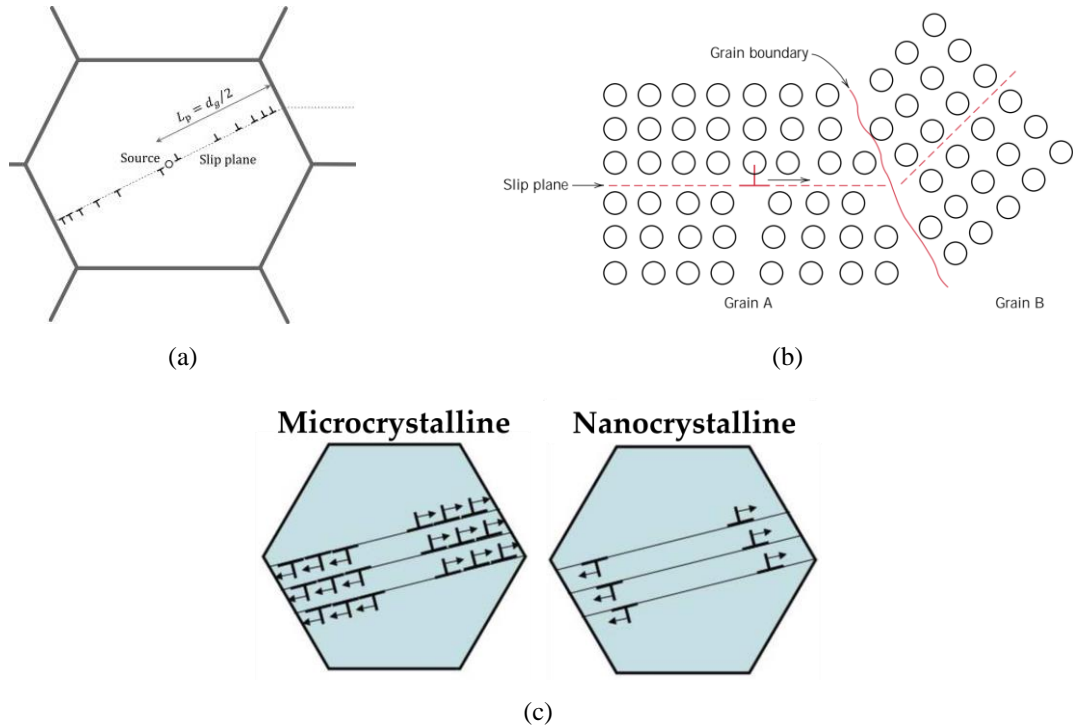


Figure 2.12 (a) Schematic picture of dislocation pile-up at the grain boundary describing the Hall-Petch phenomena (from [151]). (b) Schematic illustration of a dislocation movement across the grain boundary showing the changes direction of slip planes (from [150]) (c) Schematic representation of dislocation pile-up generated from the centre of a grain (Frank-Read source) in microcrystalline and nanocrystalline regimes at the same applied stress level showing a grain size effect (from [3]).

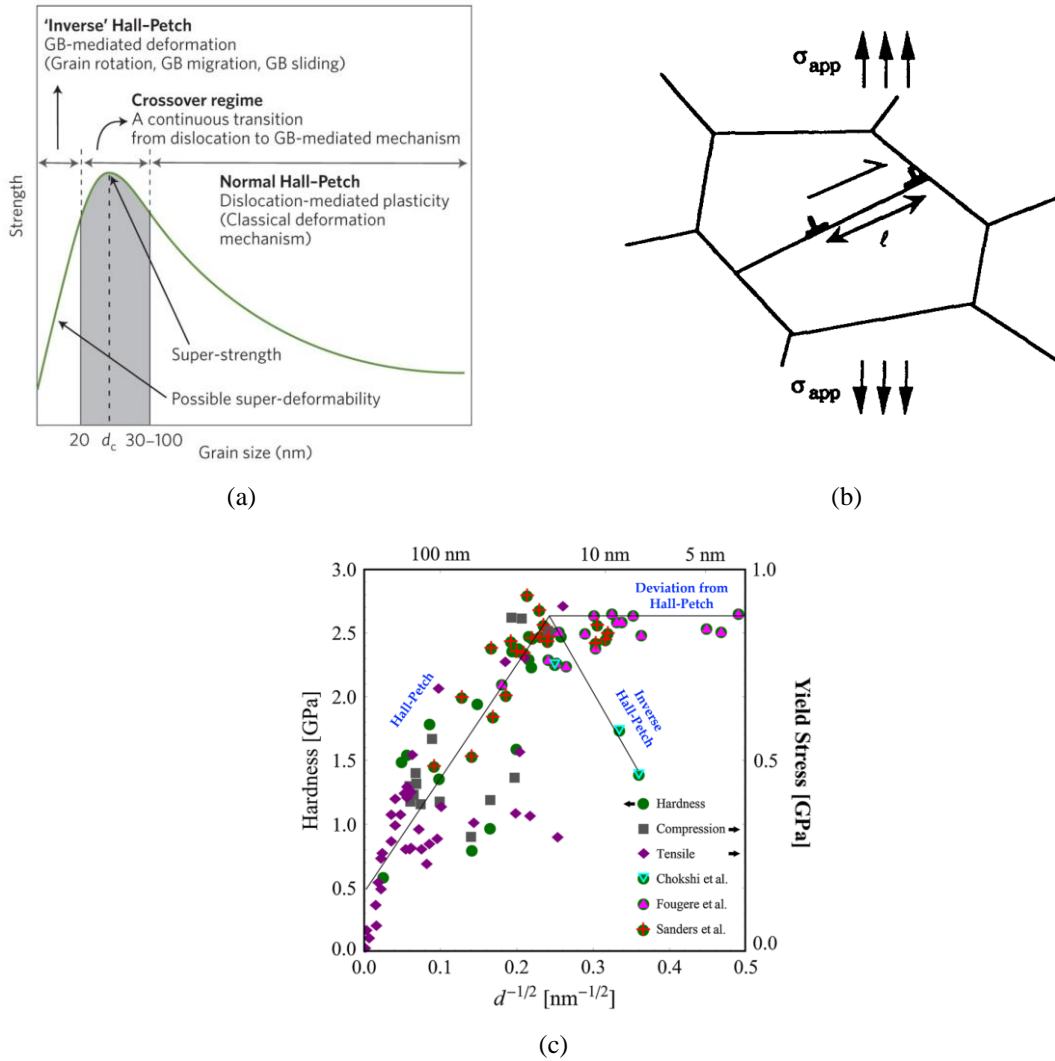


Figure 2.13 (a) Schematic pictures of dependence of strength on grain sizes showing the different regimes of deformation mechanisms (from [154]). (b) Schematic illustration of dislocation pile-up at the grain boundary showing the distance between two dislocations (l) (from [155]). (c) Compilation of data of hardness and yield stress (tensile and compression) of the nanocrystalline copper as a function of grain size collected from some literatures by Tschopp [48].

In the nanocrystalline materials, the Hall-Petch behaviour is different due to very small grain sizes. **Figure 2.12b** shows different mechanisms of dislocations in the pile-ups in microcrystalline and nanocrystalline regime at the same stress level as proposed by Pande et al. [156]. The number of dislocations in the pile-ups is reduced significantly with decreasing grain sizes down to the nanometer scale. Nieh and Wadsworth [155] proposed that the strength of materials does not increase indefinitely with decreasing grain size as shown by the Hall-Petch relationship, but there is an upper limit of strength at the critical grain size (d_c) as shown in **Figure 2.13a**. As the grain size decreases below d_c , the strength of materials will be constant or even declining. The d_c value can be estimated from the critical distance between two dislocations. **Figure 2.13b** shows a schematic picture of two edge dislocations in a pile-up

showing a distance between dislocations of l . These two edge dislocations exhibit a repulsive force upon the pile-up process, but the force is neutralized by the externally applied stress (σ_{app}). Thus, these two edge dislocations move to their equilibrium positions. The distance between two edge dislocations at their equilibrium positions is introduced as the critical equilibrium distance of dislocations (l_c). The l_c value is dependant of the shear modulus (G), the burger vector (b), the Poisson's ratio (ν), and the hardness (H) of materials as shown in equation [2.23]. Derivation of this equation is available elsewhere [155].

$$l_c = 3Gb/\pi(1 - \nu)H \quad [2.23]$$

As the grain sizes (d) decrease to below l_c , grains cannot afford for more than one dislocation inside. Thus, dislocation pile-ups cannot occur and the Hall-Petch relationship is no longer applicable [155]. Previous investigations in nanocrystalline Cu [155, 157] and Pd [155, 157] estimated the l_c value with 19.3 nm and 11.2 nm, and the Hall-Petch effect was not observed at the grain sizes of below 20 nm in both of materials. In this regime, deviation from the Hall-Petch behaviour will occur and the strength of materials will be constant or even decreases with decreasing grain size as shown in **Figure 2.13c**. Choskshi et al. [157] reported the inverse Hall-Petch relationship with decreasing grain size in nanocrystalline Cu and Pd with grain sizes of below 16 nm, but these phenomena is still debatable among researchers.

Grain-boundary mediated deformation

In very fine grained materials where $d < l_c$, weakening effects are frequently observed which may correspond to the breakdown of the Hall-Petch effect (no dislocation pile-up) [158, 159]. In case of dislocation pile-up does not work, deformation in the nanocrystalline materials is controlled by grain-boundary mediated deformation, for instance, grain boundary sliding and grain rotation as observed by some researchers [160, 161, 162, 163].

Figure 2.14a,b shows the schematic pictures of grain-boundary sliding model proposed by Ball and Hutchison [164]. In this model, the grain boundary sliding of a group of grains (the upper part of grains in **Figure 2.14 a,b**) produces shear strains at the resisted or unmoved grains (the bottom part of grains in **Figure 2.14 a,b**). In nanocrystalline materials, there are many grain boundaries in which individual atomic jumps and even movement of small group of atoms due to a shear strain are possible. The atomic shear movement can induce further grain boundary sliding and build-up of shear stress in the neighbouring nanostructured grains. This phenomenon is called as the thermally activated atomic shear sliding which was proposed by Conrad et al. [165].

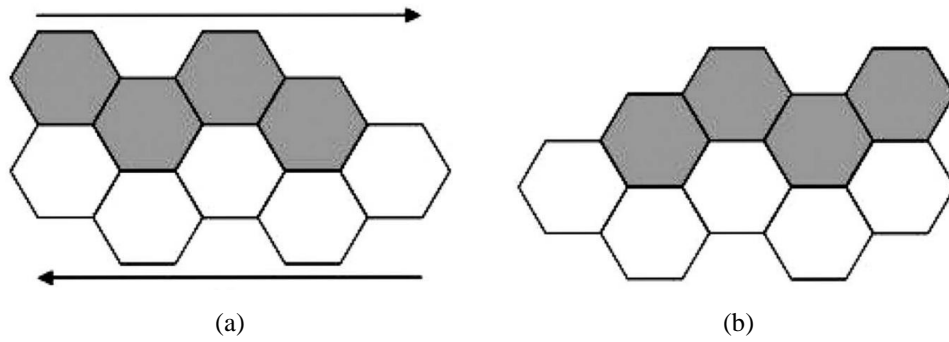


Figure 2.14 Schematic pictures of grain boundary sliding mechanism: (a) initial condition where the upper part of grains (grey colour) will move to the right part relative to the lower part of grains (white) and (b) final condition of which grain boundary sliding has occurred (from [3]).

In the absence of dislocation mediated deformation, grain boundary sliding may result in the inverse Hall-Petch effect (i.e. softening) as explained by Hahn et al. [166]. In this grain size regime ($d < l_c$), the hardness (H_v) of nanocrystalline materials as a function of grain size (d) can be predicted through equation [2.24]. The quantity of H_{v0} is the hardness of single crystals, while m_1 and m_2 are the constant parameters related to the grain boundary thickness [166].

$$H_v = H_{v0} - \frac{m_1}{d} (d - m_2)^{1/2} \quad [2.24]$$

The phenomena of superplasticity in polycrystalline materials have been observed by Ball et al. [164] and Raj et al. [167], whereas the dominant grain-boundary sliding mechanism is responsible for this effect. In nanocrystalline materials, grain boundary sliding mechanism may lead to achieve the super-deformability regime by reducing grain sizes down to below 20 nm as shown in **Figure 2.13a**. This could be a new approach to improve ductility of nanocrystalline materials. For reducing the weakening effect in the absence of Hall-Petch effect, nanocrystalline materials with a wide range of grain sizes distribution (5-100 nm) are preferred, whereas simultaneous dislocation and grain-boundary mediated deformations are expected.

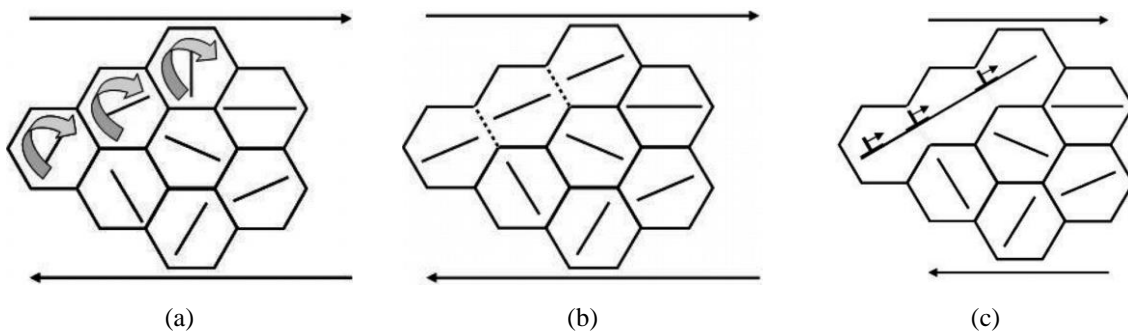


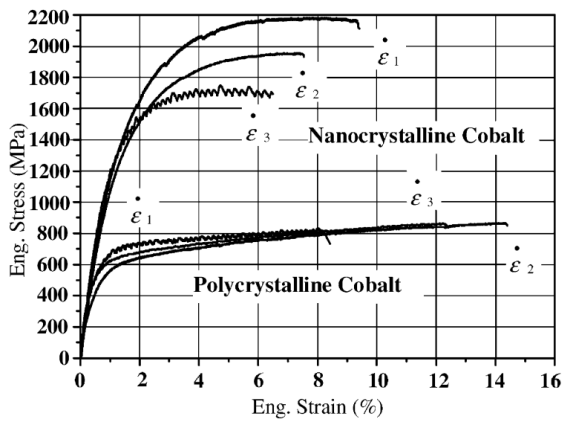
Figure 2.15 Schematic pictures of grain rotation during plastic deformation: (a) initial condition grains having different orientation of slip systems, (b) rotated grains having the same orientation of slip systems, and (c) grain coalescence in which an elongated grain is formed (from [3, 168]).

The atomic shear movement upon grain boundary sliding may cause also grain rotation and grain coalescence. This phenomenon was observed in ultrafine grained titanium [169] and nanocrystalline copper [170] by Ma et al. **Figure 2.15a-c** depict schematic illustrations of grain rotation during plastic deformation showing a coalescence effect once the grain orientations are exactly similar with the neighbouring grains as described by Meyers [3, 168]. The phenomena of grain coalescence lead to the formation of elongated grain having an extended path for dislocation movement. This may drive to weakening and strain localization, which may reduce strength and ductility of nanocrystalline materials.

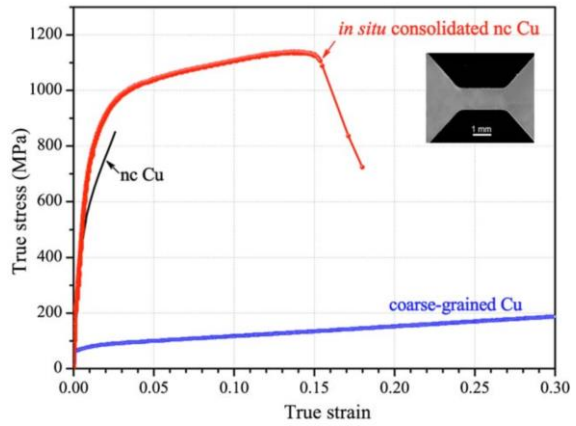
Strength and ductility of nanocrystalline Co, Cu, and Co-Cu

The theoretical background of the increased strength in nanocrystalline materials has been explained. However, nanocrystalline materials usually exhibit low ductility compared to their coarse grained counterpart as shown in the case of nanocrystalline Co and Cu (see **Figure 2.16a,b**). In addition, **Figure 2.16c,d** show that the ductility of various nanocrystalline materials decreased with decreasing grain size and increasing yield strength, showed the paradox of strength and ductility. Koch [171, 172] described three factors influencing on ductility in nanocrystalline materials which are: (i) processing flaws (e.g. pores formation, particles agglomeration and contamination, and microstructure-chemical inhomogeneity), (ii) unstable plasticity (e.g. low strain hardening, early necking, and strain localization), and (iii) crack nucleation or propagation instability.

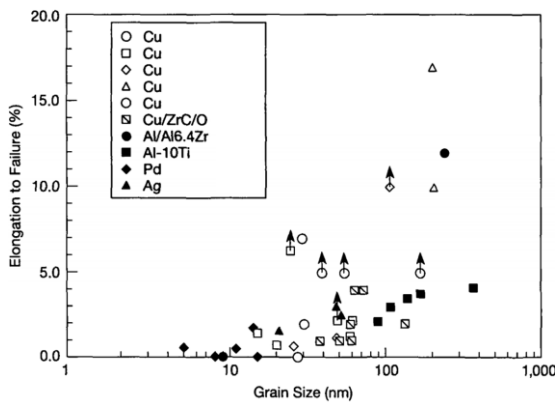
Processing flaws (e.g. pores formation and particle agglomeration and contamination) are usually found in nanocrystalline materials processed through the bottom-up approaches. Pore formation can be caused by many factors such as incomplete atomic and grain bonding, gas involvement and inclusion, and others. Particle agglomeration and contamination are frequently found also in nanocrystalline materials processed from nano-sized powders. Pore formation and particle agglomeration have detrimental effects on the mechanical properties of nanocrystalline materials. The presence of pores and particles agglomeration could be the initial sites of crack formation. The stress concentration at these existing flaws may surpass the critical toughness value which causes early failure [3]. Caused by early failure, the theoretical strength of nanocrystalline materials (e.g. high yield strength and high Young's modulus) cannot be achieved. For instance, nanocrystalline Cu and Pd processed through inert gas condensation exhibited lower Young's modulus and yield strength as the fraction of porosity increased (see **Figure 2.17a,b**). Processing of bulk nanocrystalline materials with small amount or even free from processing flaws will be a key role leading on the improvement of strength and ductility.



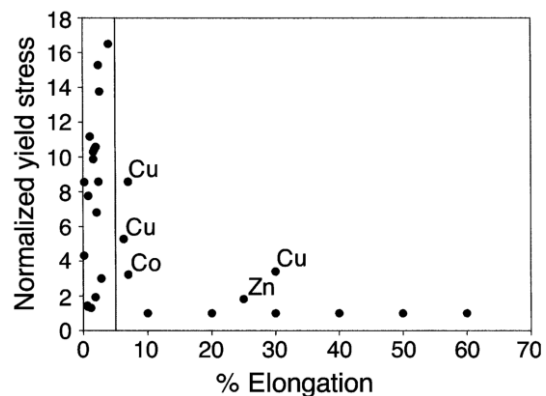
(a)



(b)

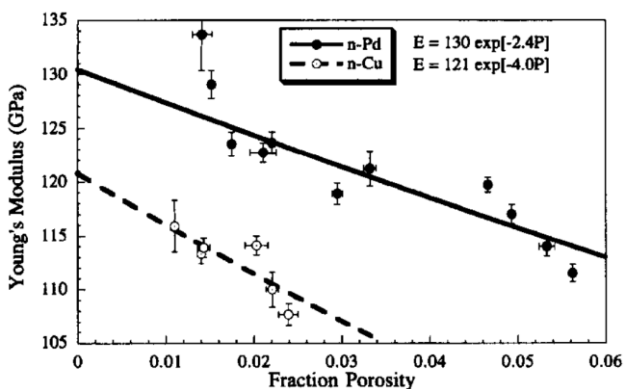


(c)

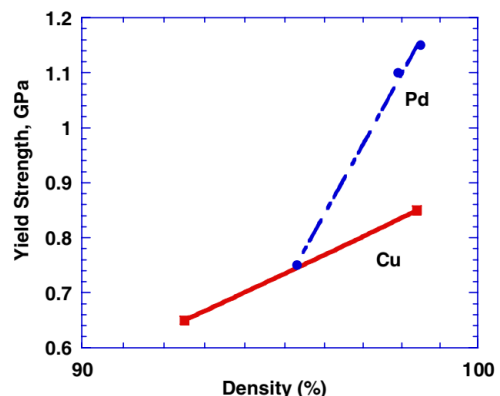


(d)

Figure 2.16 (a) Stress vs- strain curves of bulk nanocrystalline Cu (grain size: 12 nm) and bulk polycrystalline Co (grain size: 4.2 μm) (from [39]). (b) Stress vs- strain curves of bulk nanocrystalline Cu (grain size: 26 nm), bulk coarse-grained Cu (grain size: 80 μm), and in situ consolidated micro-sample of nanocrystalline Cu (grain size: 23 nm) (from [173]). Compilation of data of (c) tensile elongation to failure versus grain size (picture and complete data are available in [172]) and (d) normalised yield stress vs. %elongation (picture and complete data are available in [171]) of various nanocrystalline materials.



(a)



(b)

Figure 2.17 (a) Effect of the fraction porosity on the Young's modulus of nanocrystalline Cu and Pd (from [153]). (b) Effect of the consolidation density on the compressive yield strength of nanocrystalline Cu and Pd (picture provided in [3] with data available in [174]).

However, processing of flaw-free bulk nanocrystalline materials is difficult. Therefore, molecular dynamic simulations are usually conducted for investigation of the theoretical strength and ductility of nanocrystalline materials. Alternatively, the subsize or micron-sized samples of nanocrystalline materials with a low number of processing flaws can be used to get a better understanding on their theoretical strength and ductility. For instance, Youssef et al. [173] produced a subsize sample of nanocrystalline Cu (grain size: 23 nm) processed through the in situ consolidation technique with no porosity and other processing flaws within the sample. This subsize sample showed significantly improved strength and ductility compared with conventional nanocrystalline Cu as shown in **Figure 2.16a**. In the absence of processing flaws, this subsize sample of nanocrystalline Cu provided a high strain hardening and plastic deformation. Deformation in this nanocrystalline Cu was controlled by dislocation movement.

Table 2.5 shows the various data of strength and ductility of nanocrystalline Cu and Co, whereas the microstructures and processing flaws have the significant impacts. In the nanocrystalline Cu, processing flaws (e.g. pores and micro-cracks) have a crucial impact on ductility. Sanders et al. [153] found that the size of pores and grains were comparable as the grain size was below 50 nm, thus, a low ductility of below 2% was obtained. As a grain size increased beyond 50 nm, ductility was improved. A low ductility in nanocrystalline Cu due to processing flaws were reported also by Legros et al. [175]. A work by Cheng et al. [176] showed that decreasing the number of processing flaws significantly improved strength and ductility. In addition, a wide distribution of grain sizes of 20-100 nm was found from nanocrystalline Cu sample, which may have a contribution on the possible simultaneous dislocation-based and grain-boundary mediated deformation mechanisms [176]. The plastic deformation with a perfect shear banding or necking was observed during mechanical tensile loading [176]. The highest ductility in nanocrystalline Cu was reported by Lu et al. [42] with elongation to fracture up to 30%. Elimination of pores and contaminations through the electrodeposition process instead of compaction of ultrafine powders led to the enhancement of ductility. Grain boundary sliding mechanism, low angle grain boundaries, and low micro-strain had also significant contributions on the improved ductility [42]. However, this work showed the lowest strength compared to other works, whereas the reason for the decrease of strength is still unclear. However, it is believed that grain boundary sliding and low-angle grain boundaries have a contribution to weakening effect [42]. Investigations by Shen et al. [21] and Lu et al. [44] reported that the presence of nano-twins could improve also strength and ductility in nanocrystalline Cu. However, production of thick samples of nano-twins Cu had some crucial challenges.

Table 2.5 Tensile yield stress (σ_y), ultimate tensile stress (σ_u), and elongation to fracture (ϵ_f) of nanocrystalline (nc) and nano-twin (nt) Co, Cu, and Co-Cu processed through various techniques. (GS: Grain size; TT: Twin Thickness; ECAE: Equal channel angular Extrusion; IsC: In-situ consolidation; IGC: Inert gas condensation; ED: Electrodeposition; PED: Pulsed electrodeposition; HPT: High pressure torsion)

Material	Gauge (mm)	Mean GS (nm)	Mechanical Properties	Additional information
ED nc-Cu [42]	Length: 15 Width: 5 Thick: 1.55	GS: 27	σ_y : 119 ± 5 MPa σ_u : 202 ± 8 MPa ϵ_f : 30 %	Strain rate was $1 \times 10^{-4} \text{ s}^{-1}$. Failure at the ultimate tensile stress. Ductile fracture surface. Strain hardening exponent is large ($n = 0.22$). Grain boundary sliding deformation was observed.
PED nt-Cu [21, 44]	Length: 4 Width: 2 Thick: 16-25 μm	GS: 400 TT: 15	σ_y : 900 MPa σ_u : 1068 MPa ϵ_f : 13.5 %	Strain rate was $6 \times 10^{-3} \text{ s}^{-1}$. Twin structure provided significant dislocation accumulation during plastic deformation. Slight strain hardening was observed.
IGC nc-Cu [175]	Length: ~2.0 Width: 0.2 Thick: 0.2	GS: 26	σ_y : 535 MPa σ_u : 880 MPa ϵ_f : 2.1 %	Strain rate was not mentioned. Brittle fracture surface was obtained. Porosity and micro-crack led on the early failure.
IsC nc-Cu [173]	Length: ~2.0 Width: ~1.5 Thick: NA	GS: 23	σ_y : 791 ± 12 MPa σ_u : 1120 ± 29 MPa ϵ_f : 15.5 %	Strain rate was not mentioned. Sample was claimed to be free from processing flaws. Sample dimension was approximation from an image.
IGC nc-Cu [153]	Length: 3 Width: 2 Thick: 0.4-1.0	GS(1): 23 GS(2): 49	$\sigma_y(1)$: 365 ± 5 MPa $\sigma_u(1)$: 425 ± 5 MPa $\epsilon_f(1)$: 1.8 % $\sigma_y(2)$: 345 ± 5 MPa $\sigma_u(2)$: 460 ± 5 MPa $\epsilon_f(2)$: 1.6 %	Strain rate was not mentioned. Failure at the ultimate stress. Samples densities were less than 99.2% observing pores formation. Failure was dominantly caused by processing flaws.
IsC nc-Cu [176]	Length: 3 Width: 1-2 Thick: 0.15-0.3	GS(1): 54 GS(2): 62	$\sigma_y(1)$: ~688 MPa $\sigma_u(1)$: ~730 MPa $\epsilon_f(1)$: ~6 % $\sigma_y(2)$: ~600 MPa $\sigma_u(2)$: ~660 MPa $\epsilon_f(2)$: ~12 %	Strain rate was $1 \times 10^{-4} \text{ s}^{-1}$. Fracture was started through shear localisation. Fracture surface showed dimple formation showed ductile fracture, but pores formation was observed.
PED nc-Co [39, 40]	Length: 5 Width: 2.5 Thick: 0.2	GS: 12	σ_y : 1002 ± 58 MPa σ_u : 1902 ± 72 MPa ϵ_f : 6 ± 1 %	Strain rate was $5 \times 10^{-4} \text{ s}^{-1}$. Hcp-structure of nc Co. Fracture surface showed some dimples of ductile fracture. Fracture oriented at 37° - 53° towards load direction with slight plastic deformation from the shear stress.
PED nc-Co [41]	Length: 5 Width: 2 Thick: 0.12	GS: ~20	σ_y : 967 MPa σ_u : 1720 MPa ϵ_f : 9.4 %	Strain rate was $1 \times 10^{-4} \text{ s}^{-1}$. Hcp-structure of nc Co. Samples contained nano void sized comparable with grains and impurities. Dimples with size of 0.1-0.3 μm were observed from fractures surface. Fracture oriented at 50° - 60° towards load direction.
ED nt Co-Cu (7 wt% Cu) [31]	Length: 7 Width: 2 Thick: 10 μm	GS: 110 TT: 3	σ_y : 1420 MPa σ_u : 1857 MPa ϵ_f : 3.3 %	Strain rate was $1 \times 10^{-2} \text{ s}^{-1}$. High-density twins acted as a barrier for dislocation nucleation, accumulation, and movement caused low activation volume.
HPT nc Co-Cu (26 at% Co) [16]	Length: 2.5 Diameter: 0.5	GS: 100	σ_y : ~800 MPa σ_u : ~970 MPa ϵ_f : ~7.5 %	Strain rate was $1 \times 10^{-3} \text{ s}^{-1}$. Strength decreased and elongation increased with decreasing strain rate. Fracture surface showed micro-ductile fracture with observation of dimples (100-500 nm) and inclusions.

Compared to nanocrystalline Cu, investigations on tensile mechanical properties of nanocrystalline Co got less attention, whereas only three works were reported (see **Table 2.5**). Studies by Wang et al. [41] and Karimpoor et al. [39, 40] showed comparable results in which high strength and low ductility (less than 10%) in nanocrystalline Co were observed. Interestingly, some indications of ductile fracture were found, for instance, dimple features and fracture orientation (40° - 60°) to load direction. Deformation in nanocrystalline Co is dominated by a shear stress localisation. Formation of voids and co-deposition of impurities were believed to have a strong contribution on low ductility.

Regarding the limitation on ductility in nanocrystalline Co and Cu, improvements are necessary. According to Koch [171] and Ma [177], ductility of nanocrystalline materials can be improved through several ways which are: (i) reduction of processing flaws, (ii) utilisation of multi-component phases or structures, (iii) wide distribution of grain sizes, and (iii) addition of secondary particles (e.g. oxide, carbide, CNT). Among these promising strategies, the first and second option are the most commonly used in nanocrystalline materials. Processing flaws in nanocrystalline materials can be minimised by controlling the processing parameters, for instance, electrolyte composition, pulse current density, and pulse duration in the PED-process of nanocrystalline materials. Alloying nanocrystalline Co with Cu may enhance ductility, whereas the formation of fcc-structure of supersaturated solid solution nanocrystalline Co-Cu were observed instead of a hcp-structure [13, 27]. However, a work by Nakamoto et al. [31] revealed that twin structure did not show an improved ductility compared with nanocrystalline Co. Thin sample of nano-twin Co-Cu used in this work ($10\ \mu\text{m}$) was a main issue. Similar to nano-twin Cu [21, 44], synthesis of a bulk sample of these types of materials is difficult. A work by Bachmaier et al. [16] did not show a significant improvement of ductility compared with nanocrystalline Co [39, 40, 41]. However, it must be distinguished that Bachmaier et al. [16] worked at a higher strain rate of $1 \times 10^{-3}\ \text{s}^{-1}$. It showed that the elongation to fracture increased to $\sim 12\%$ with decreasing strain rate to $2 \times 10^{-4}\ \text{s}^{-1}$. This result revealed that improvement of ductility in nanocrystalline Co is possible by alloying with Cu.

An improved ductility in the HPT-processed nanocrystalline Co-Cu (Cu-rich) is promising. Investigations on nanocrystalline Co-Cu with different composition (i.e. Co-rich) and processed through different techniques (e.g. pulsed electrodeposition) are needed. Of course, the effect of chemical composition on the mechanical properties of materials is obvious, thus, discussion is now focussed on different processing techniques. In the previous section, a comparison between the SPD- and PED-process has been explained. The first concern is the grain size, whereas the grain size of PED-processed nanocrystalline materials could be below 50 nm or even 20 nm,

which is difficult to obtain from the SPD-process. It has been explained that the deformation mechanism in materials with small grain sizes of below 50 nm may be different due to effect from the critical grain size. The next concern is the processing flaws. The SPD-processed materials from nano-powders exhibit various processing flaws such as pores, internal and localized stresses, contamination, and particle agglomeration. In contrast, different types of processing flaws such as co-deposition of impurities (e.g. sulphur, carbon, hydrogen) is possibly present in the PED-processed materials. The pore formation remains a problem in the PED-processed materials, however, Lu et al. [42] showed that the number of pores can be reduced significantly. The last concern is different characteristics, types, and numbers of lattice defects (e.g. dislocations, vacancies, and twins) in the PED- and SPD-processed materials. In the SPD-process, dislocation formation is dominantly influenced by the large applied plastic strain during material processing [144]. Dislocation formation in the PED-process can be affected by two possible mechanisms: (i) stress generation and relaxation when the pulse current is on and off, respectively [102, 103, 178], and (ii) growth inhibition from organic additives [104, 145, 146]. Caused by different mechanisms, the number of dislocations in the SPD- and PED-process may be different. A direct comparison of dislocation behaviour in the two different materials processed through the DC electrodeposition and SPD-process was performed by Gubicza et al. [147] in nanocrystalline Ni-Mo with grain sizes of 30-40 nm. It was shown that the electrodeposited Ni-Mo had a higher dislocation density compared with the SPD-processed materials. In addition, significant twin fault probability was detected in the electrodeposited materials which was not found in the SPD-process. A significant increase of dislocation density and twin fault probability are expected from the pulsed-current instead of direct-current processes as shown by Lu et al. [44, 179, 180], which may give more opportunities to improve strength and ductility. Caused by different microstructures, processing flaws, and lattice defects in the PED- and SPD-processed nanocrystalline materials, investigations on mechanical properties of the PED-processed nanocrystalline materials is convincing to explore a more comprehensive understanding of these types of materials.

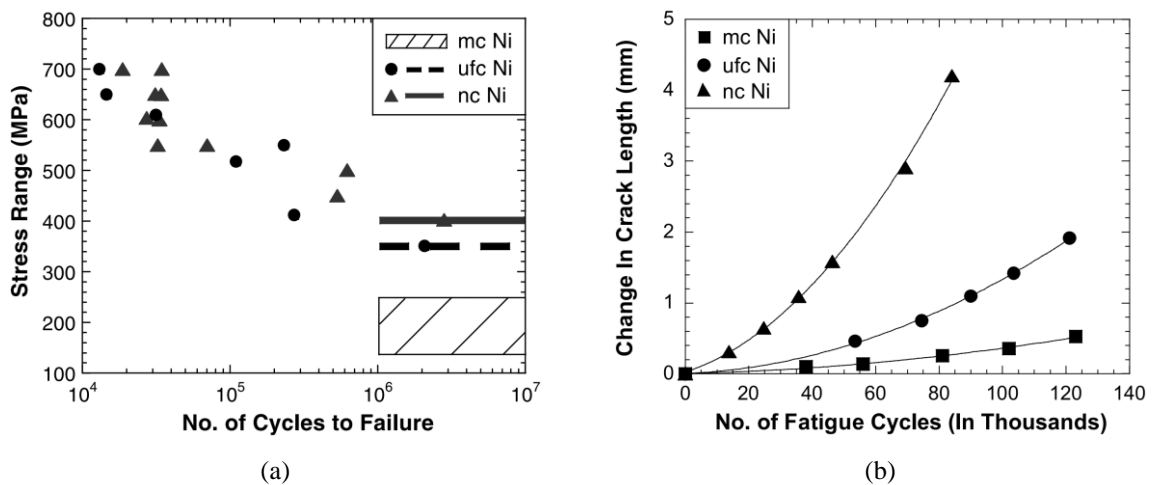
2.4.2. Cyclic loading behavior

Nanocrystalline materials exhibit an unstable microstructure due to a high volume fraction of grain boundaries and triple junctions. For instance, low temperature annealing of nanocrystalline Co-Cu alloys showed spinodal and phase decompositions and grain coarsening [13, 27]. Structural instability of nanocrystalline materials is also expected under cyclic loading or fatigue tests. However, investigations on the fatigue behaviour of nanocrystalline materials got little attention due to unavailable bulk samples for conventional fatigue testing, thus, fatigue

tests were performed at SPD-processed materials with ultrafine grained structures [181].

Fatigue behaviour of nanocrystalline materials still could be performed through alternative techniques. Early investigation was performed by Whitney et al. [182] for sub-sized samples of nanocrystalline copper processed through inert gas condensation and consolidation with grain sizes of 18-29 nm. The length and width of the gauge section of the test specimens were 3.0 mm and 2.0 mm, respectively, while the thicknesses could be varied from 0.15 to 0.23 mm. Fatigue test were performed at the maximum stresses of 50%-83% of the yield strength (100-165 MPa), while the minimum stress was fixed at 10 MPa. The investigations showed that slight elongation and elastic cyclic deformation were obtained, but the measured elastic modulus was significantly smaller compared with conventional coarse grained copper. Interestingly, softening effect due to grain coarsening up to 25-28 nm was observed after several hundreds of thousands of cycles.

The softening and grain coarsening effect were also observed in ultrafine grained Cu through the cyclic micro-bending technique by Kapp et al. [183]. Kapp et al. proposed that grain coarsening in ufg Cu was affected through accumulation of plastic strain, which activates a driving force for migration of high-angle grain boundaries. Different elastic strain energies in smaller and larger grains have a contribution also on the disappearing of small grains due to growth of larger grains. Grain coarsening induced by accumulated plastic deformation during crack propagation in nanocrystalline platinum films was also revealed by Muhlstein et al. [184]. A hardening effect was obtained from multiple-step indentation of electrodeposited nanocrystalline Co with a mean grain size of 20 nm by Cavaliere [185]. However, the mechanism of this hardening effect in nanocrystalline Co was not discussed in detail.



Comprehensive investigations on the fatigue behaviour of nanocrystalline materials was performed by Hanlon et al. [186, 187]. Fatigue tests were conducted for electrodeposited nanocrystalline Ni with a mean grain size of 30 nm. Specimens were of dog-bone type with a total length of 25 mm and thickness of 0.1 mm. **Figure 2.18a** shows that nanocrystalline (nc) Ni exhibits an improved fatigue resistance to stress-controlled fatigue compared with ultrafine crystalline (ufc) and microcrystalline (mc) Ni. However, fatigue crack growth in nc Ni seems significantly faster than in ufc Ni and mc Ni as depicted in **Figure 2.18b**. Hanlon et al. suggested that nanocrystalline materials offer an improved resistance to high-cyclic fatigue, but the resistance dropped significantly as soon as initial crack formation occurred. Results from Hanlon et al. confirm that reduction of processing flaws (e.g. porosity, micro-crack, and others) is crucial to improve mechanical stability and performance of nanocrystalline materials.

Chapter 3 – Materials and Experimental Methods

3.1. Pulsed electrodeposition of nanocrystalline Co-Cu

Pulsed electrodeposition of nanocrystalline Co-Cu were performed in an electrolyte containing cobalt- and copper-sulphate, tartrate complex former, and additives. The electrolyte composition used in the present work is adapted from previous works by Su et al. [108] and Müller [77] with some modification made to obtain thick, compact, and homogeneous deposits of supersaturated solid solution nanocrystalline Co-Cu. The chemical composition of electrolyte for deposition is provided in **Table 3.1**. The electrolyte composition was not varied in the present work. Pulsed electrodeposition were carried out in a double-wall electrodeposition cell connected to a water-heater thermostat to maintain the electrolyte's temperature at 40°C. The electrodeposition cell was connected with the power source and the programmable pulse generator to control the pulse parameter of deposition (i.e. current-controlled process). The electrodeposition cell was also equipped with an electrolyte's circulation system and a mechanical- or magnetic-stirrer. Pictures of the electrodeposition cell and the main equipments are shown in **Figure 3.1**.

Table 3.1 Chemical composition of electrolyte used for the pulsed electrodeposition (PED) of nanocrystalline Co-Cu. The roles of individual ingredient are also provided in the table.

No	Chemical formula of ingredient	Concentration		Role of each ingredient
		gram/Liter	mol/Liter	
1.	Cobalt sulphate heptahydrate (CoSO ₄ .7H ₂ O)	112.00	0.40	Salt containing cobalt ions as a source of deposited cobalt.
2.	Copper sulphate (CuSO ₄)	6.38	0.04	Salt containing copper ions as a source of deposited copper.
3.	Sodium sulphate (Na ₂ SO ₄)	142.04	1.00	Conducting salt to enhance electrolyte's conductivity.
4.	Boric acid (H ₃ BO ₃)	18.55	0.30	Buffer solution.
5.	Potassium sodium tartrate (C ₄ H ₄ KNaO ₆ .4 H ₂ O)	56.44	0.20	Complex ion forming to enhance Co and Cu ionic activities.
6.	Saccharin (C ₇ H ₅ NO ₃ S)	2.00	0.011	Additive: grain refinement and inhibition.
7.	Sodium dodecyl sulphate (C ₁₂ H ₂₅ NaO ₄ S)	0.20	0.0007	Additive: levelling and inhibition.

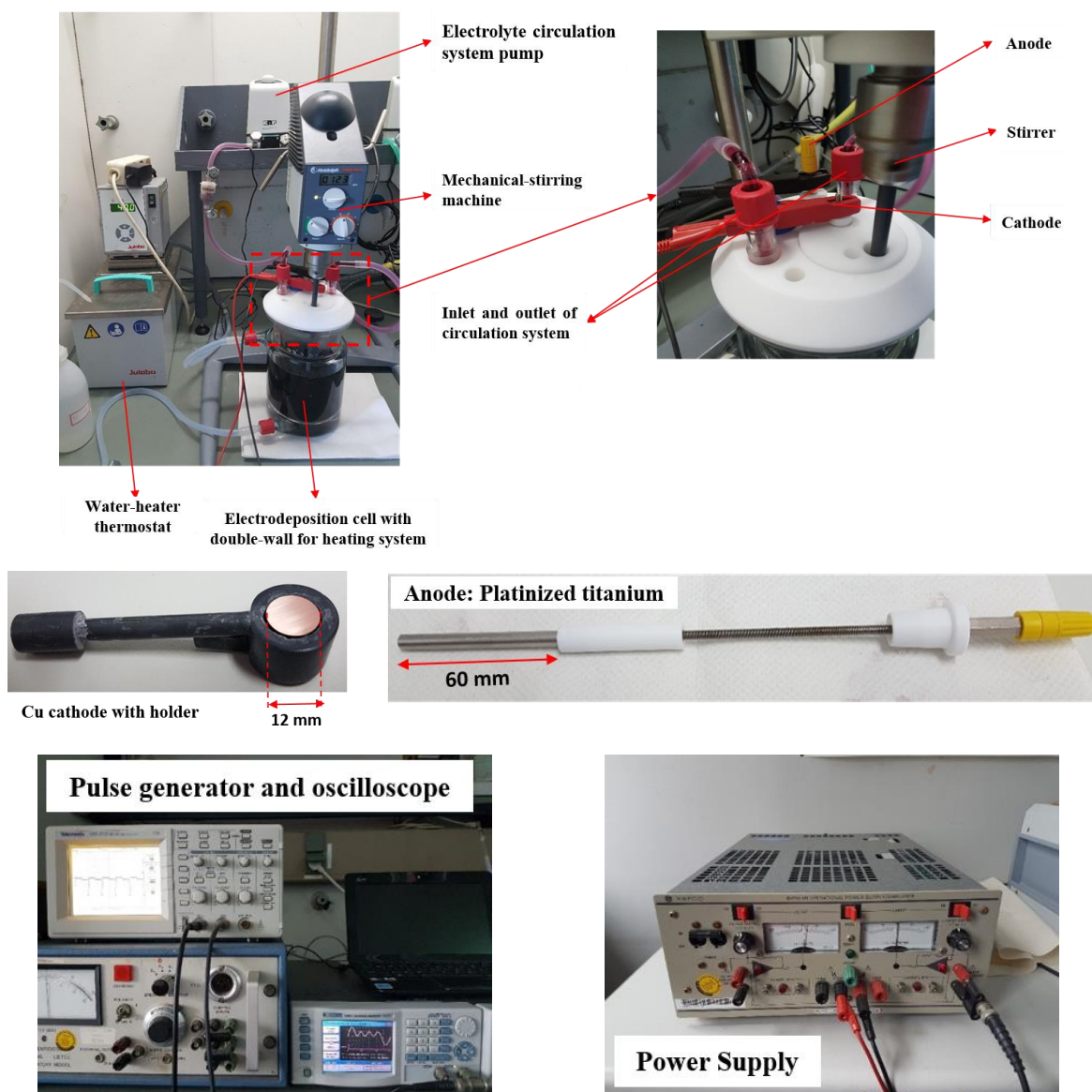


Figure 3.1 Photographs of electrodeposition cell and equipment used for the electrodeposition of nanocrystalline Co-Cu deposits with Cu-cathode and the platinised titanium anode.

Pulse electrodeposition of nanocrystalline Co-Cu were conducted at two different sizes of the Cu-cathode for different purposes. The first Cu-cathode has a surface diameter of 12 mm with a thickness of ~5 mm and deposits produced at this size of cathode are called as Dep-I. The platinised-titanium rod was used as an anode (length: 60 mm; surface diameter: ~5 mm) for deposition of the Dep-I samples. The second type of Cu-cathode has a surface dimension of 21x21 mm² with a thickness of ~2 mm and the deposited product is called as Dep-II. A double plate titanium-mesh was used as an anode (length: 120 mm; width: 60 mm) for deposition of Dep-II samples. A cellulose membrane was applied to cover the titanium-mesh anode surface to prevent excess side reaction. The mechanical and magnetic stirring systems were used for deposition of Dep-I and Dep-II samples, respectively. Dep-I samples were subjected for

characterisation of microstructure, investigation on the thermal stability and the micro-mechanical properties of nanocrystalline Co-Cu. Dep-II samples were subjected for investigation of tensile strength, ductility and tension-tension fatigue properties of bulk samples of nanocrystalline Co-Cu. Pictures of Dep-I and Dep-II samples are shown in **Figure 3.2**.

In the present work, caused by the wide-range of synthesis parameters, initial investigations must be performed to find the optimum range of deposition parameters. The criteria are based on quality and properties of the nanocrystalline Co-Cu deposits which are: (i) specific minimum thickness of hundreds micrometer (i.e. 700-800 μm of thicknesses are needed for tensile test specimens), (ii) homogeneous chemical composition and microstructure, and (iii) compact and porosity-free deposits. Investigations on the pulse duty cycle and current density were carried out with Dep-I samples, while determination of the pulse-on time was conducted with Dep-II samples. Initial investigations were performed at the various pulse current densities (500-1500 A/m^2), duty cycles (10%-40%), and the pulse-on times (0.3-2.0 ms). Results of these preliminary investigations are provided in **Chapter 4**. According to the initial investigation results, PED-processes of Dep-I were carried out at a pulse current density, a duty cycle, and a pulse-on time of 1000 A/m^2 , 10%, and 2 ms, respectively, which was presented also in the published results [188, 189]. Electrolyte composition and pulse-deposition parameters were not varied here due to acceptable quality and characteristics of the deposits. The PED-process of the Dep-II was performed at the various pulse current densities, duty cycles, and pulse-on times of 800-1000 A/m^2 , 10%-20%, and 0.3-0.5 ms. Pulse-deposition parameters were varied to produce different characteristic of deposits (e.g. chemical compositions, microstructure, and processing flaws), which has a direct impact on the mechanical properties of bulk samples of nanocrystalline Co-Cu.

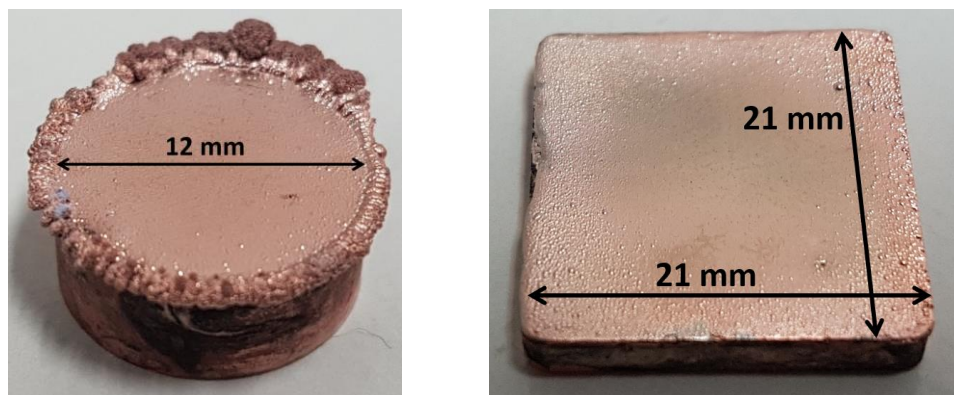


Figure 3.2 Pictures of the nanocrystalline Co-Cu deposits at two different size of Cu-cathodes: (a) Dep-I: surface diameter of 12 mm and (b) Dep-II: surface dimension of 21x21 mm^2 .

3.2. Characterization of nanocrystalline Co-Cu

Investigations on structural properties (e.g. morphology, grain size, and phase distribution), chemical composition, and microhardness of nanocrystalline Co-Cu were performed through various methods. Characterizations were conducted at the cross-section and/or the planar-section surfaces, depending on the required information and measurement techniques. Investigations on thermal stability and microstructure evolution of nanocrystalline Co-Cu were conducted for Dep-I samples by isothermal annealing treatments in vacuum (pressure of 10^{-6} mbar) at different temperatures (300°C - 800°C) for various time periods (1-64 h) and followed by rapid cooling to ambient room temperature.

All as-deposited and annealed specimens were employed for surface preparation through subsequent grinding and polishing steps till mirror-like finished and almost scratch-free surfaces were obtained. The subsequent grinding steps were conducted by using SiC papers grids of 240, 320, 600, 1200, and 2500 for 1-2 minutes of individual grid at a speed of 150 rpm and followed by ultrasonic cleaning in ethanol solution for 5-10 minutes. Afterwards, subsequent steps of polishing were performed by using polishing cloths with diamond suspension sizes of 6 μm , 3 μm , and 1 μm , respectively. Each individual step of polishing was conducted for 5 minutes at a speed of 150 rpm and followed by ultrasonic cleaning in ethanol solution for 5 minutes. For the last step, OPU polishing was conducted for 2-3 minutes and followed by ultrasonic cleaning in ethanol solution for 10 minutes.

Microstructure observation was performed in a Zeiss Sigma-VP scanning electron microscope (SEM) equipped with secondary electron (SE) and backscattered electron (BSE) detectors at acceleration voltages of 10-20 kV. Chemical composition analysis was carried out also in a SEM with an energy dispersive spectroscopy (EDS) detector and the AZtec software from Oxford Instruments Inc. at an acceleration voltage of 17 kV. Enhanced microstructural analysis and selective area diffraction (SAD) pattern of selected samples were gained in a JEOL JEM 2011 transmission electron microscope (TEM) at an acceleration voltage of 200 kV. Samples for the TEM measurement were prepared by cutting the polished specimens to a 3 mm-diameter disk. Further preparation was conducted by creating an electron transparent film in planar direction at the centre of the disc by GATAN PIPS ion milling. The microstructural images obtained from SEM and TEM observations were used for grain size determination through the line interception method measuring lengths of individual grains with the ImageJ Version 1 software [190].

Microhardness measurements (HV 0.2) were conducted at a test force of 1.962 N with a DuraScan hardness testing device from Struers equipped with an ecos Workflow software from

EMCO-TEST Prüfmaschine GmbH. Twenty indentations at a distance of 30 μm and 200 μm from the Cu-substrate were made at the cross-sections. The presented data will be the mean value of microhardness at each distance and its standard deviation is used as error. X-ray diffraction (XRD) measurements were performed for phase analysis with Cu K-alpha radiation (λ : 1.5405980 \AA) at a step size of 0.013 $^\circ$ 2 θ /s. Fityk software [191] was used for refining and fitting the XRD-peak data. Surface topography and magnetic domain pattern of selected samples were observed through simultaneous atomic force microscope (AFM) and magnetic force measurement (MFM) in a Bruker AFM device. Raw images from the AFM-MFM measurements were processed with the Gwyddion software Version 2.50 [192] to enhance images quality and to extract one-dimensional magnetic domain pattern profiles.

Atom probe tomography (APT) measurements were performed to get high-resolution mappings of the Co and Cu elements distribution at the nano scale, which could be less than 1 nm. APT specimens were prepared by using a Helios NanoLab 600TM dual-beam focused ion beam/scanning electron microscopy workstation (FIB/SEM) from FEI Company by the lift-out technique explained elsewhere [193]. APT specimens were extracted from the selected positions within the nanocrystalline Co-Cu sample. One-dimensional concentration profiles were constructed from the regions of interest (ROI) within the APT specimens. Complete information about this APT measurement for nanocrystalline Co-Cu is available in a published paper [188].

3.3. Static and cyclic micro-bending test

In the present work, micro-mechanical tests were performed through static and cyclic micro bending tests to get better understanding on the strength and ductility of nanocrystalline Co-Cu. The presence of processing flaws is expected to be lower in micro-size specimens compared with the bulk samples as described in **Chapter 2**. Free standing micro bending beams were prepared by using a Helios NanoLab 600TM dual-beam FIB/SEM workstation from FEI Company at cross-section of the deposit. Micro beams were at a distance of \sim 200 μm from the substrate as shown schematically in **Figure 3.3a**. An example of an actual picture of a micro bending beam is shown in **Figure 3.3b**. Two different micro beam geometries were prepared, whereas the first type of micro beam (see **Figure 3.3c**) was subjected for an in-situ static bending test, while the second type of micro beam (see **Figure 3.3d**) was subjected for in-situ cyclic bending tests at different plastic surface strain amplitudes. Detailed information of the micro beam dimensions are given in **Chapter 6**.

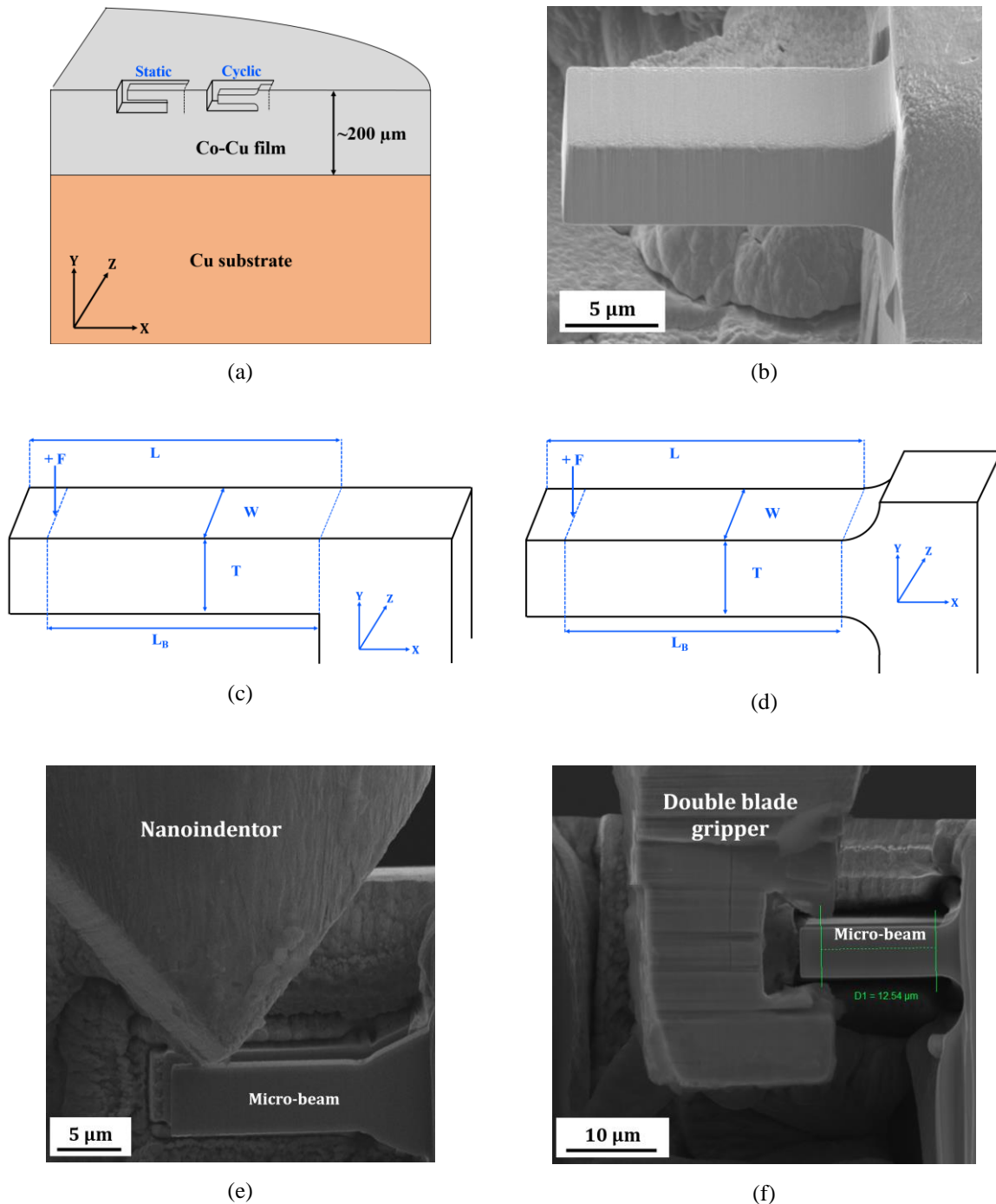


Figure 3.3 (a) Schematic picture of the beam position at the cross-section of a nanocrystalline film. (b) A secondary electron (SE) image of a micro beam for cyclic bending tests. (c-d) Schematic pictures of micro beam geometries were used for (c) static and (d) cyclic micro bending tests. The dimensions of micro beams can be found in **Chapter 6**. Schematic pictures of (e) a nanoindenter and (f) a double blade gripper were used for static and cyclic micro bending tests, respectively.

In situ static and cyclic micro-bending tests were conducted in a TESCAN-Vega SEM provided with the nanoindentation system and the InspectorX Version 2 UNAT software from Advanced Surface Mechanics (ASMEC). In situ static and cyclic micro bending tests were conducted by using a nanoindenter (see **Figure 3.3e**) and a double blade gripper (see **Figure**

3.3f), respectively, for transmitting mechanical loading onto the micro bending beams. The software recorded the force and displacement data, which were processed further and converted to surface stress (σ_s) and surface strain (ϵ_s) by using elastic bending beam theory as shown in **Equation [3.1]** and **Equation [3.2]**. The quantities of F and D are the recorded force and displacement, respectively. The length, width, and thickness of the micro bending beam are symbolised by L_B , W, and T, respectively. Information about these static and cyclic micro bending tests are also available in a published paper [188].

$$\sigma_s = \frac{6L_B F}{WT^2} \quad [3.1]$$

$$\epsilon_s = \frac{DT}{2L_B^2} \quad [3.2]$$

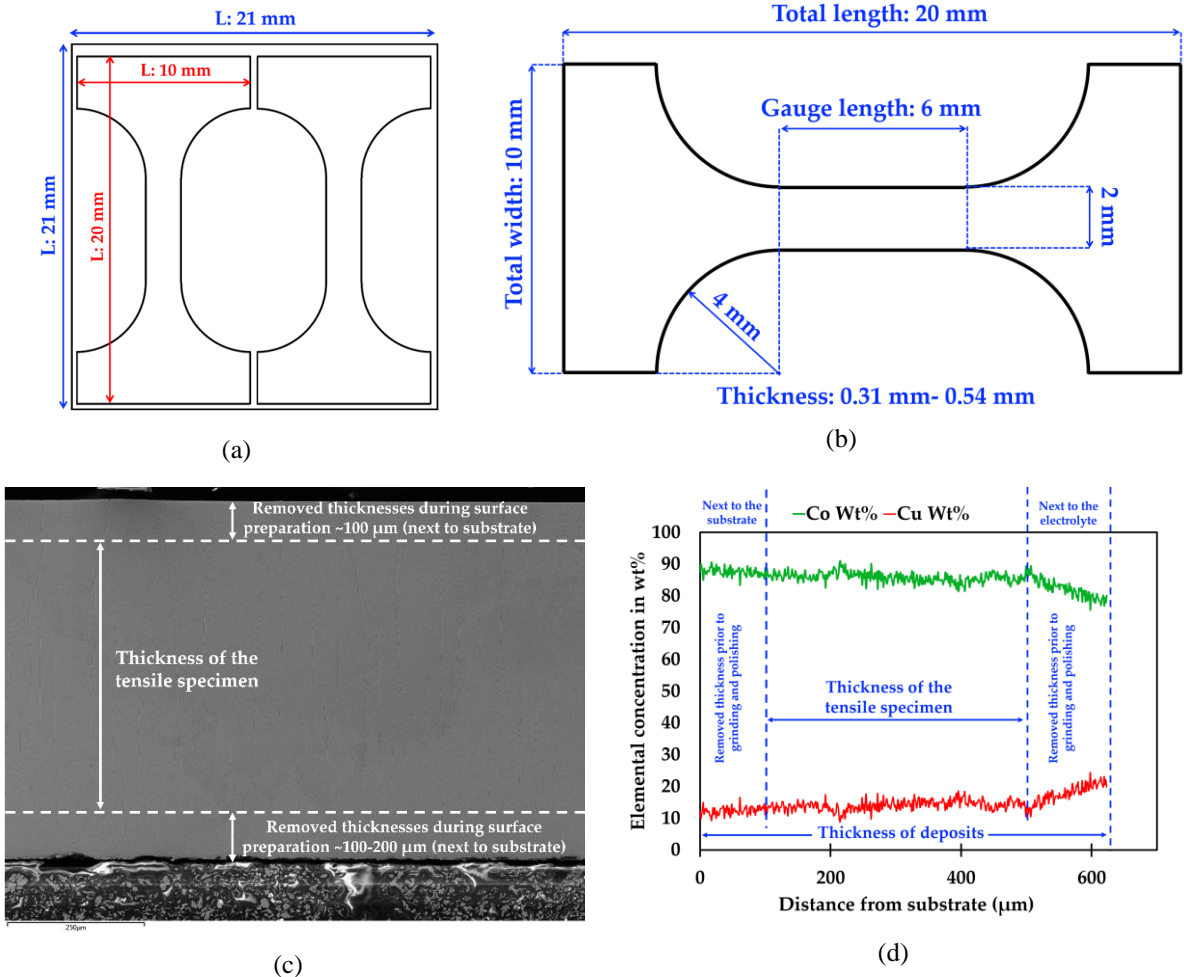


Figure 3.4 (a) Schematic picture of two tensile specimens in the as-deposited and annealed samples. (b) Schematic picture of the detailed dimension of tensile specimens (from [194]). The typical of (c) a secondary electron (SE) image of a cross-section of deposited films and (d) energy dispersive spectroscopy (EDS) line profiles of Co and Cu concentration in weight percent (wt.%) along the cross-section, showing removed parts and thickness of tensile specimen.

3.4. Static and cyclic tensile tests of bulk samples

Dep-II samples were used for static and cyclic tensile tests of bulk samples of nanocrystalline Co-Cu. Deposited films were detached from Cu-substrates and two tensile specimens with a dog-bone type shape were manufactured from each deposit as shown in **Figure 3.4a** with a wire cutting machine. The tensile specimens have a gauge length, a width, and thicknesses of 6 mm, 2 mm, and 0.30-0.55 mm, respectively, as shown by the schematic picture in **Figure 3.4b**. Surface preparations were performed on the tensile specimens through the typical grinding and polishing steps as described in **Section 3.2** to remove some remaining Cu-substrate (after the removal of substrate from the deposited film) and the significant surface roughness at the electrolyte side surface as shown by a SEM image and EDS line profiles in **Figure 3.4c-d**. The tensile specimens have quiet homogenous chemical composition along the cross-section. Caused by the non-standard size of the tensile specimens, a sample holder is needed to support the tensile specimens during the static and cyclic tensile tests. The design of the sample holder used in the present work is shown in **Figure 3.5a**. This sample holder and the tensile specimen were fixed to an Instron 8513 tensile testing machine as displayed in **Figure 3.5b** for static tensile tests. Static tensile tests were conducted at a single strain rate of $1.0 \times 10^{-3} \text{ s}^{-1}$. The elongation of the tensile specimens was only recorded with the cross-head displacement and no extensometer used due to insufficient dimension of the gauge length for installation of a clip gauge.

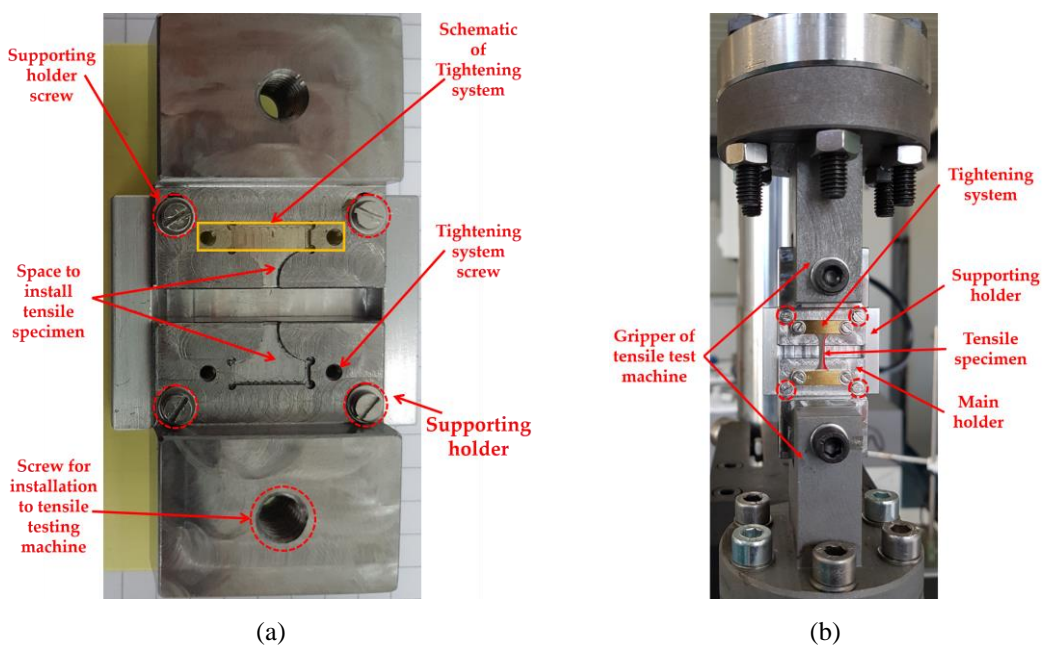


Figure 3.5 (a) Design of the tensile specimen holder (from [194]). (b) Set up of the tensile specimen and the tensile specimen holder at the static tensile testing machine in which the supporting holder is removed before the static tensile test (from [194]).

Similar test specimens and sample holder were used for the fatigue tests of bulk nanocrystalline Co-Cu. The sample holder including test specimens were fixed to a Rumul resonant fatigue testing machine as depicted in **Figure 3.6** for tension-tension fatigue tests with a different gripper system. This gripper fixes the sample and sample holder to the testing machine during the fatigue test. The load increased test (LIT) and constant amplitude test (CAT) methods were conducted under stress-control at a stress ratio of 0.1 up to 2 million load cycles for different purposes. The recorded stress, strain, and frequency were analysed to investigate the hardening or softening behaviour during the fatigue tests. Detailed information of the test parameters of individual specimens can be found in **Chapter 7**. In most of the experiments, elongation were recorded from the cross-head displacement of the fatigue testing machine. A Limes real time strain sensor (RTSS) video extensometer was also used in some experiments to record elongation accurately.

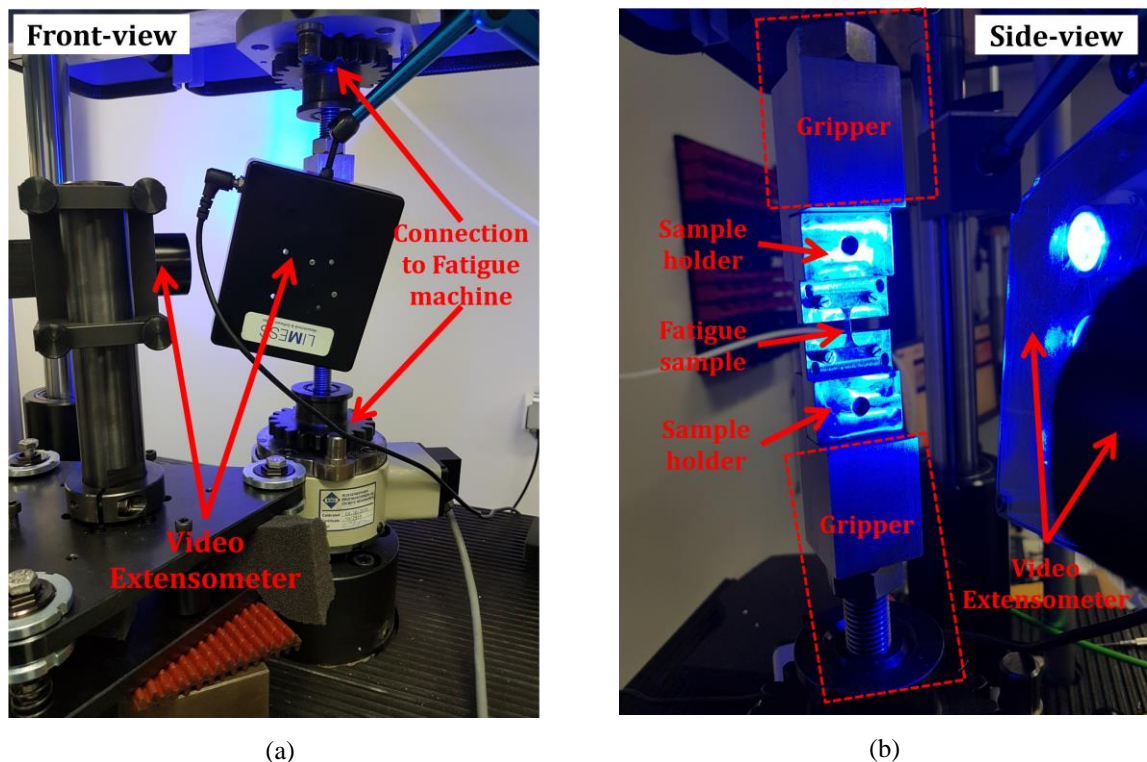


Figure 3.6 Photographs of the experimental setup of test and specimen devices were used for the fatigue tests of bulk nanocrystalline Co-Cu viewed from (a) the front and (b) the side.

Chapter 4 - Selection of the Pulse-deposition Parameters

Statement: Some results in this chapter have been published in the international journals (see Reference [188, 194]) and a conference proceeding (see Reference [189]).

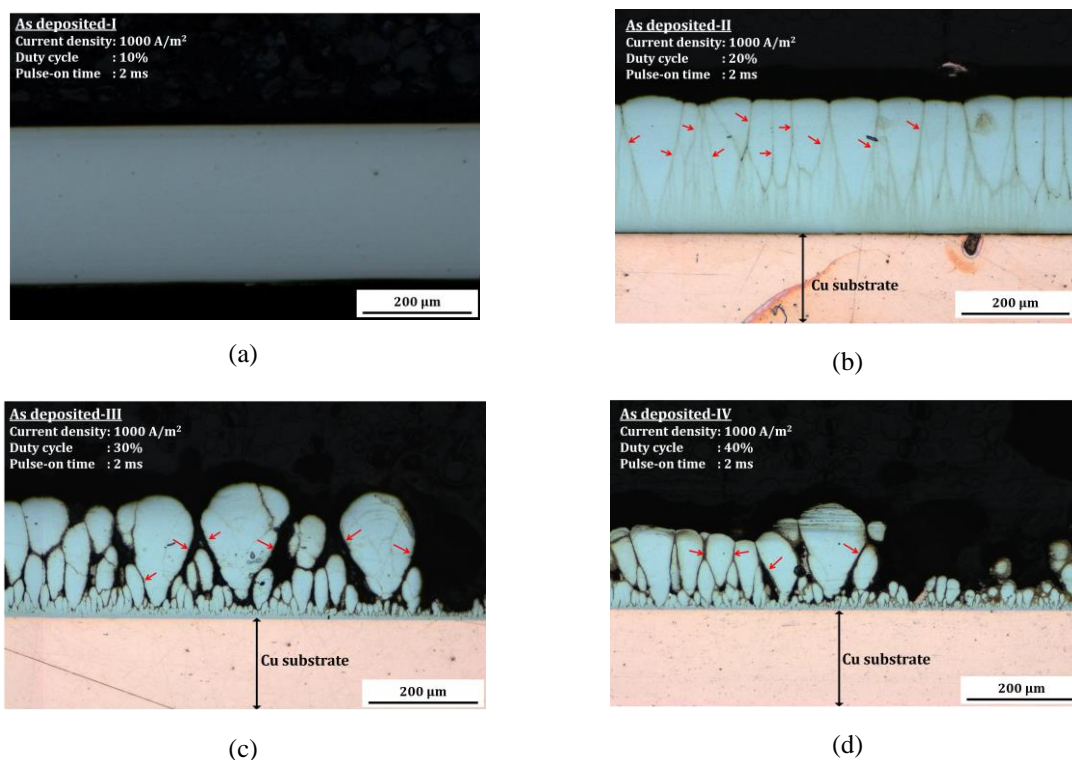


Figure 4.1 Cross-sectional images of Dep-I samples with a surface diameter of 12 mm deposited at various duty cycles of (a) 10%, (b) 20% (from [194]), (c) 30% (from [194]), and (d) 40% (from [194]). Pulse current density and on-time were fixed at 1000 A/m² and 2 ms, respectively. The films were deposited for different times of deposition which are (a) 30 h, (a) 13 h, (b) 8.5 h, and (c) 6.5 h to get ~300 μm of thickness. The crystal growth borders are marked with red arrows

Extensive investigations were conducted for selecting the optimum deposition parameters. The first point is the selection of the duty cycle. Depositions at four different duty cycles (10%, 20%, 30%, and 40%) were carried out at a pulse current density of 1000 A/m² and a pulse-on time of 2 ms. **Figure 4.1a,b** show that compact and porosity-free deposits were obtained at duty cycles of 10% and 20%. Non-compact deposits were obtained at duty cycles of 30% and 40% as shown in **Figure 4.1c,d**. Accordingly, the upper limit of duty cycle is 20% to produce compact deposits. Thus, depositions were carried out at pulse current density of 10-20% in the present work. Deposition at duty cycles of below 10% was not preferred due to a low deposition rate and a high concentration of copper, which leads to a decrease of thermal stability and

mechanical strength which is discussed in the next chapters. **Figure 4.1b-d** show the presence of crystal growth borders (marked with red arrows), whereas a combined of field-oriented (FT) and unoriented dispersion (UD) growth types is observed [195]. The crystal growth borders have a strong contribution on ductility of PED-processed nanocrystalline materials, which is discussed in **Chapter 7**.

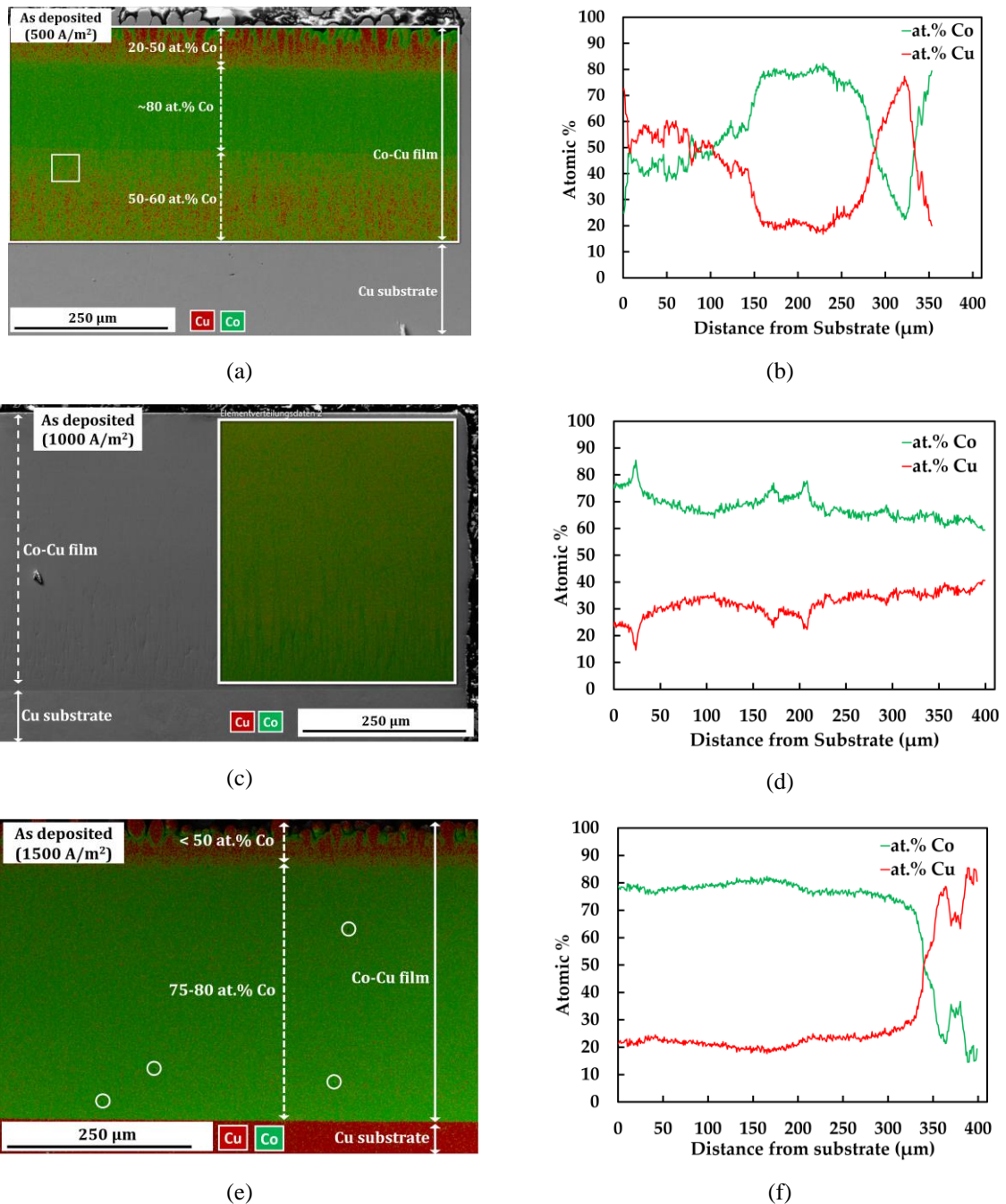


Figure 4.2 Energy dispersive spectroscopy (EDS) maps and EDS lines profiles of cross-sectional Dep-I samples (surface diameter of 12 mm) at various pulse current densities: **(a-b)** 500 A/m², **(c-d)** 1000 A/m² (from [188, 189]), and **(e-f)** 1500 A/m² at a duty cycle of 10% and a pulse-on time of 2 ms.

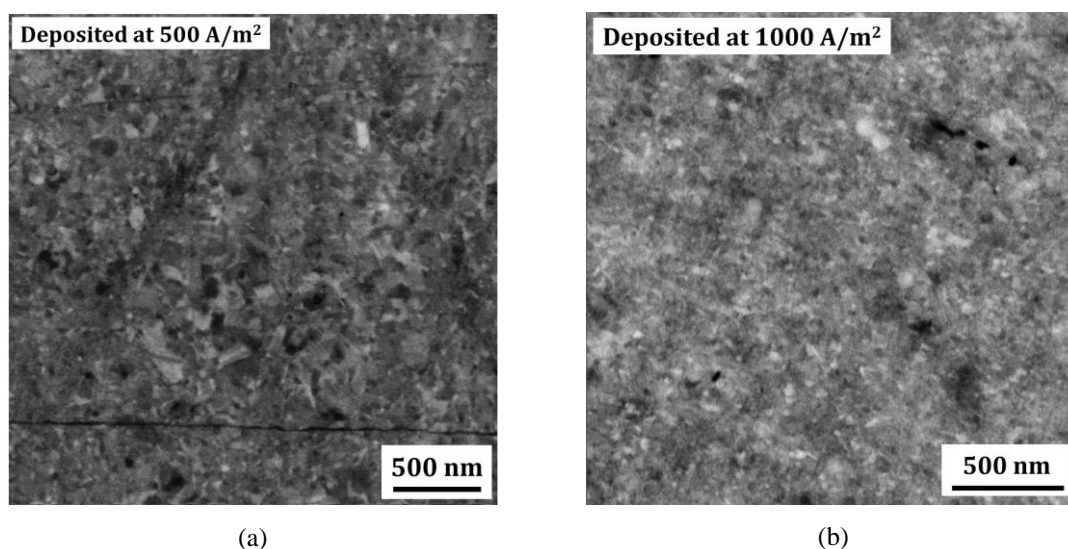


Figure 4.3 Back-scattered electron (BSE) images of Dep-I samples deposited at pulse current densities of (a) 500 A/m² (from [188]) and (b) 1000 A/m² (from [189]) at a pulse duty cycle of 10% and a pulse-on time of 2 ms. Figure (a) was taken at a position marked with a white rectangular in **Figure 4.2a**.

The next consideration is the pulse current density. Pulse electrodepositions were conducted at three different pulse current densities (500 A/m², 1000 A/m², and 1500 A/m²) at a duty cycle of 10% and a pulse-on time of 2 ms. According to the theory of electrocrystallization, pulse current density has a crucial impact on grain size, whereas the grain size decreases with increasing pulse current density. Interestingly, the current work shows that pulse current density has a contribution also to chemical composition and homogeneity as shown by the EDS-maps and EDS-lines in **Figure 4.2**. EDS measurement on samples deposited at a pulse current density of 500 A/m² (see **Figure 4.2a,d**) shows an inhomogeneous chemical distribution in which significant compositional fluctuations of Co and Cu were observed. In addition, a back-scattered image of this sample (see **Figure 4.3a**) exhibits a non-uniform microstructure, whereas ultrafine and nanocrystalline grain sizes were found. Caused by inhomogeneous microstructure and chemical composition, deposition at a pulse current density of 500 A/m² is not preferred for thick films of nanocrystalline Co-Cu.

Deposition at a pulse current density of 1000 A/m² produced a nanocrystalline Co-Cu film with considerably homogeneous chemical composition (**Figure 4.2b,e**) and microstructure (see **Figure 4.3b**). According to EDS and SEM measurements, this sample exhibits a chemical composition of 28 at% Cu and nano-grains with sizes of below 50 nm. Comprehensive investigations on microstructure, thermal stability, and micromechanical properties of this deposit are discussed in the next chapters. Nanocrystalline Co-Cu which was deposited at the highest pulse current density (1500 A/m²) exhibits homogeneous chemical composition of up to ~350 μm of thickness, but the concentration of Co drops drastically after this thickness (see

Figure 4.2c,f). A distinct appearance of micro-pores is also detected here as marked with white circles in **Figure 4.2**. It is believed that the formation of micro-pores is strongly influenced by hydrogen evolution at this high pulse current density. Accordingly, pulsed deposition at 1000 A/m² is preferred for deposition of nanocrystalline film for having a homogeneous chemical composition and microstructure with no formation of pore observed.

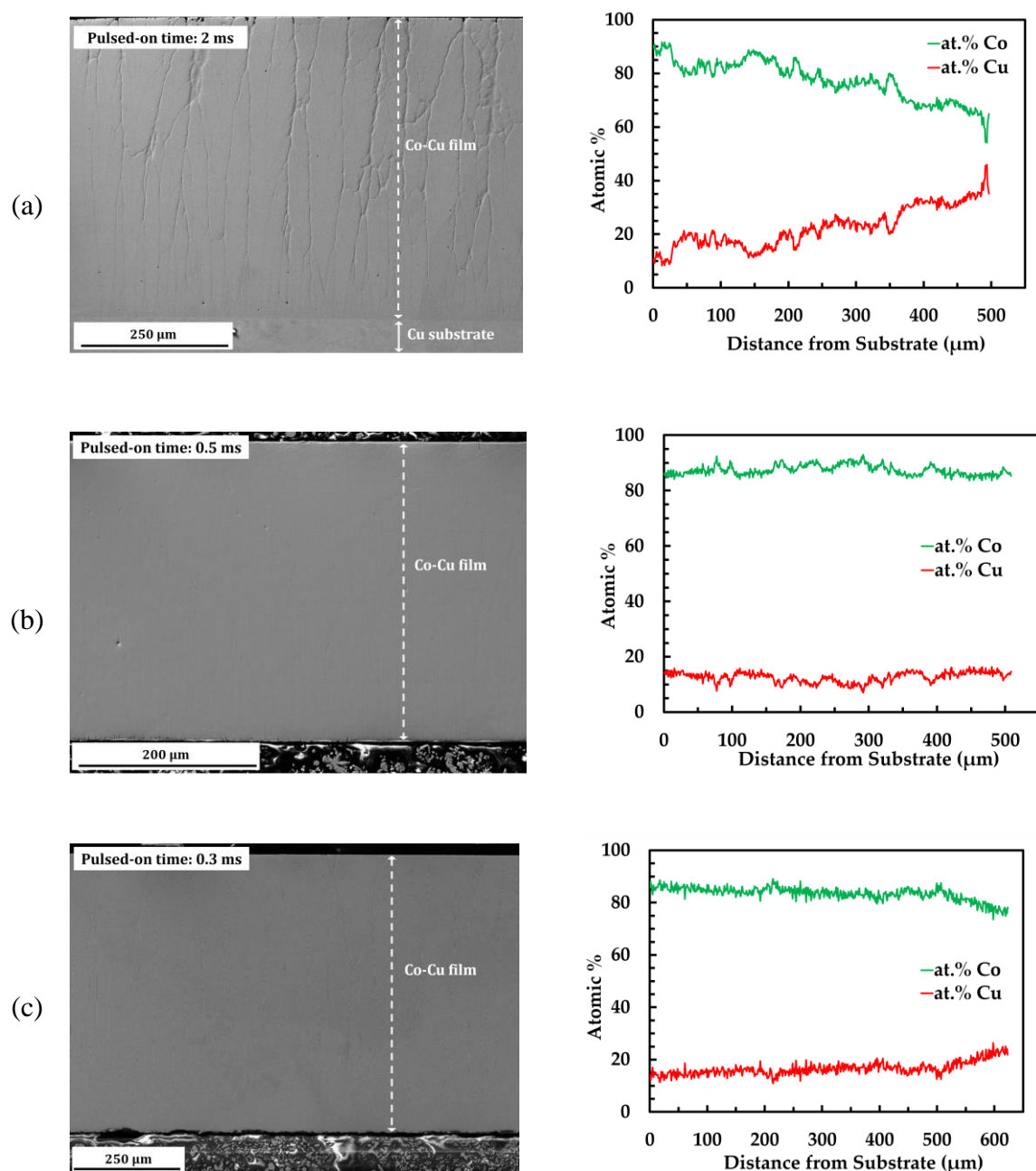


Figure 4.4 Combined SE and EDS-line profiles images of cross-sectional Dep-II samples (surface area of 21×21 mm²) at various pulse-on times: **(a)** 2 ms, **(b)** 0.5 ms, and **(c)** 0.3 ms. The PED-process were performed at a fixed pulse current density and duty cycle of 1000 A/m² and 17.5%, respectively.

Thick films (200-300 μm) of nanocrystalline Co-Cu are required for investigations on thermal stability, structural evolution, and micro-mechanical properties (i.e. Dep-I samples). For this thickness requirement, synthesis of Dep-I samples can be performed at a pulse current density, a duty cycle, and a pulse-on time of 1000 A/m^2 , 10%, and 2 ms, respectively. The investigation shows that compact and homogeneous thick deposits of up to ~ 400 μm can be obtained at these deposition parameters. However, the EDS-line profile in **Figure 4.2e** shows that a further decrease in Co concentration is expected for deposition of thickness of over 400 μm . Nanocrystalline films with at least 600-700 μm of thicknesses are needed for the investigation of bulk mechanical properties in Dep-II samples. It should be noted that the Dep-II samples have a larger dimension than the Dep-I samples, so producing homogenous deposits is a key challenge here. Further improvement is needed for producing thick and homogeneous nanocrystalline films.

Investigations on the pulse-on time for producing thick and homogeneous nanocrystalline films were tested. It can be shown that improvement on the chemical homogeneity can be obtained in Dep-II samples by varying the pulse-on times (0.3 ms, 0.5 ms, and 2 ms) at fixed pulse current density (1000 A/m^2) and duty cycle (17.5%) as shown by the EDS-line profiles in **Figure 4.4a-c**. EDS-line profiles of sample deposited at a pulse-on time of 2 ms (see **Figure 4.4a**) shows that cobalt concentration significantly decreases with increasing distance from the substrate. In addition, the cross-sectional SEM image of this sample deposited at the highest pulse-on times (2 ms) depicts a significant pore formation compared with the other samples. Caused by these limitations, deposition for Dep-II samples is not preferred at the pulse-on time of 2 ms. The pulse-on times were adjusted and **Figure 4.4b,c** show that the formation of ~ 600 μm thick deposits of nanocrystalline Co-Cu with a homogeneous chemical composition is possible at pulse-on times of 0.3 ms and 0.5 ms. Therefore, these pulse-on times (i.e. 0.3 ms and 0.5 ms) are selected for the deposition of thick films of Dep-II samples. Other parameters such as pulsed duty cycle and pulsed current density were also varied. Comprehensive investigation on the effect of pulsed deposition parameters on the characteristic and mechanical properties of bulk nanocrystalline Co-Cu are discussed in **Chapter 7**.

Chapter 5 - Thermal Stability and Microstructural Evolution

Statements: Some results in this chapter have been published in the international journal (see Reference [188]) and conference proceeding (see Reference [189]).

5.1. As deposited state

Investigations on the thermal stability and structural evolution of nanocrystalline Co-Cu were conducted with Dep-I samples. These samples were processed through at a pulse current density, a duty cycle, and a pulsed-on time of 1000 A/m², 10%, and 2 ms, respectively. According to SEM and EDS results in **Figure 4.2c, d**, compact and homogeneous deposits of supersaturated solid solution nanocrystalline Co-Cu with a thickness of up to ~400 μm and a chemical composition of 72 at.% Co and 28 at.% Cu are achieved. Back-scattered electron (BSE) images of as-deposited sample (see **Figure 4.3b**) depicts nanostructured grains with sizes of closely below 50 nm. However, determination of the grain size from BSE image is difficult because of the resolution limit, thus, investigations through other techniques (e.g. transmission electron microscope) were needed.

Figure 5.1a,b depict a bright- and a dark-field transmission electron microscope (BF- and DF-TEM) images of the PED-processed nanocrystalline Co-Cu showing some interesting microstructural features. Some twin structures are detected and marked with red arrows in **Figure 5.1a**. Twin formation in the PED-processed materials may be contributed by several factors, for instance: (i) the presence of chemical additives (e.g. saccharin and sodium dodecyl sulphate (SDS)) [145, 104], (ii) stress generation and relaxation when the current is on and off, respectively [102, 103, 178], and (iii) the high pulse current density [44, 107]. **Figure 5.1c** shows a grain size distribution of the as-deposited sample determined from a BF-TEM image confirming a mean grain size of 22.7 ± 8.2 nm. Several coarser grains with a size of larger than 50 nm are observed with a fraction number of less than 5%. A phase analysis of the as-deposited sample was evaluated from selective area diffraction (SAD-TEM) (see **Figure 5.1d**) and x-ray diffraction (XRD) (see **Figure 5.1e**) patterns observing a face-centered cubic (fcc) structure of supersaturated solid solution Co-Cu with a strong and moderate intensity of {111} and {200} planes, respectively. Low intensities of {220}, {311}, and {222} planes are also observed. Individual Co or Cu phases (e.g. Co or Cu segregation) are not observed, but investigations at higher-resolution are needed for confirmation.

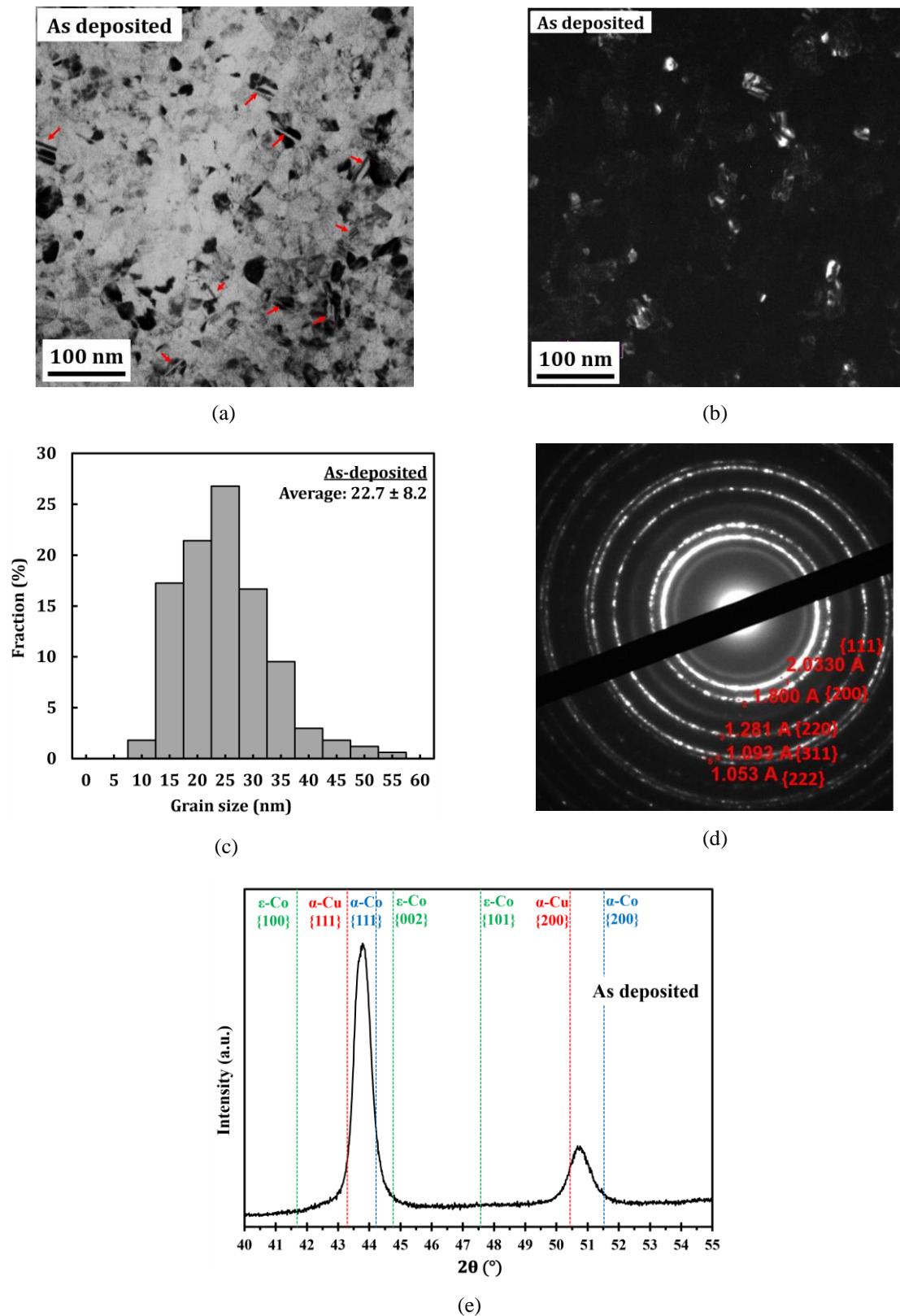


Figure 5.1 (a) Bright-field (BF) (from [188]) and (b) dark-field (DF) transmission electron microscope (TEM) images of the as-deposited sample (Dep-I). (c) Grain size distribution of the as-deposited sample measured from BF-TEM image (from [188]). (d-e) Phase and orientation observations of the as-deposited sample through (d) selected area diffraction (SAD) in TEM (from [188]) and (e) x-ray diffraction (XRD) (from [188]).

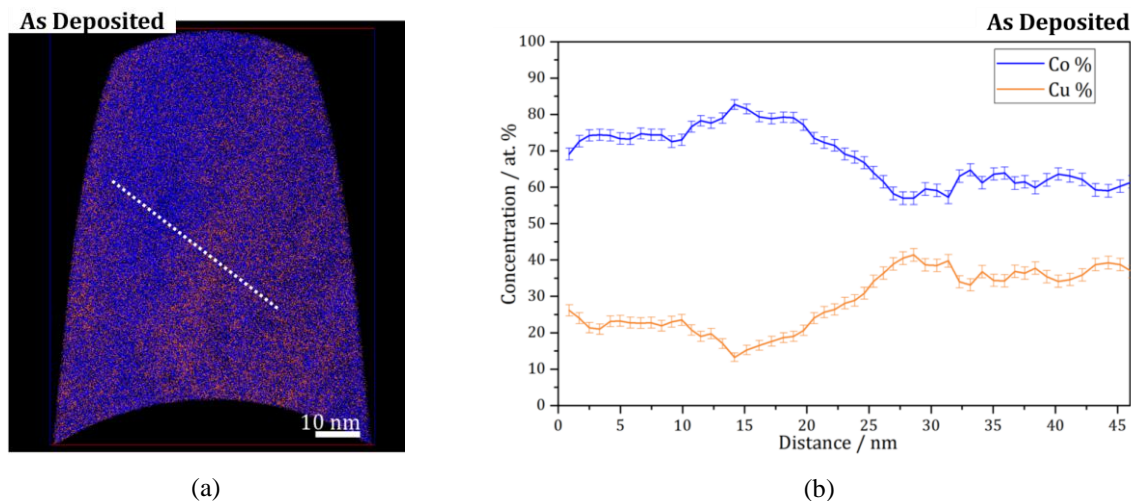


Figure 5.2 APT measurement of Co (blue) and Cu (orange) in the as-deposited sample: **(a)** Elemental map of a selected slice (5 nm thick) through a reconstruction of region of interest (ROI) (from [188]). **(b)** One-dimensional concentration profiles constructed from the white dashed line in the respective elemental map (from left to right) (from [188]).

The microhardness of this PED-processed nanocrystalline Co-Cu is 4.45 ± 0.07 GPa. This microhardness is higher compared to nanocrystalline Co [13, 40], nanocrystalline Cu [65, 196], and HPT-processed nanocrystalline Co-25%Cu [13, 29] and Co-74%Cu [27, 29]. The high microhardness in the PED-processed nanocrystalline Co-Cu may be contributed by several factors which are: (i) solid solution strengthening of Co-Cu, (ii) presence of twins, (iii) co-deposition of impurity elements (e.g. sulphur and carbon) [188], and (iv) different chemical composition, grain size, and characteristics of lattice defects.

Atom probe tomography (APT) measurements were conducted to construct elemental maps and one-dimensional concentration profiles of Co (blue) and Cu (orange) at nanometer scale as depicted in **Figure 5.2a,b**. According to APT measurements, the as deposited nanocrystalline Co-Cu exhibits solid solution region. The concentration in the solid solution region is not perfectly homogenous at nanometer scale, but short range fluctuations (i.e. spinodal structure) and segregation of Co or Cu are not found from the measurement.

5.2. Thermal stability

Investigations on the thermal stability of the PED-processed nanocrystalline Co-Cu were conducted through isothermal annealing at various temperatures (300- 600°C) for different time periods (1 h, 5 h, and 24 h). Grain size and microhardness of the annealed samples were measured and the results are provided in **Table 5.1**. A hardening effect is observed in all samples annealed at 300°C, whereas microhardness increases from 4.45 ± 0.07 GPa up to 4.89 ± 0.06 GPa (see **Table 5.1**). It is believed that spinodal decomposition has a strong contribution

on the hardening effect, but it needs more comprehensive investigations which is discussed later. BSE images of the microstructure (see **Figure 5.3a-c**) show no significant grain coarsening compared with the as-deposited sample at 300°C (see **Figure 4.3b**). According to microstructure images, grain sizes of these annealed samples remain below 50 nm.

Table 5.1 Microhardness and grains size of samples annealed at the various temperatures (300-600 °C) for different time periods (1-24 h). Grain size determinations were performed through the BSE image of individual samples as provided in **Figure 5.3**. For comparison, microhardness and grain size of the as-deposited sample are 22.7 ± 8.2 nm and 4.45 ± 0.07 GPa, respectively.

	Microhardness (GPa)			Grain size (nm)		
	1 h	5 h	24 h	1 h	5 h	24 h
300°C	4.89 ± 0.06	4.67 ± 0.18	4.56 ± 0.06	<50	<50	<50
400°C	-	-	4.35 ± 0.10	-	-	82.49 ± 28.0
450°C	4.43 ± 0.07	4.40 ± 0.06	4.31 ± 0.05	122.0 ± 19.4	124.0 ± 40.5	127.0 ± 39.0
600°C	3.94 ± 0.06	3.69 ± 0.06	3.25 ± 0.12	159.6 ± 66.2	183.6 ± 67.2	218.6 ± 73.2

Annealing treatments at the higher temperatures were performed to find the starting temperature for grain growth in the PED-processed nanocrystalline Co-Cu. A slight grain coarsening is firstly detected in samples annealed at 400°C for 24 h. A BSE image of the microstructure (see **Figure 5.3d**) reveals minor grain coarsening showing a certain number of ultrafine grains (ufg). However, major nanocrystalline structures are still observed here as an indication of in-progress grain coarsening. Annealing at 400°C leads to an increase of the average grain size to 82.49 ± 28.0 nm and is accompanied with a decrease of microhardness to 4.35 ± 0.10 GPa (see **Table 5.1**).

Significant grain coarsening is observed at 450°C. BSE images of these annealed samples depict an ultrafine grain structure with an average size of ~120 nm (see **Table 5.1** and **Figure 5.3e-g**). Interestingly, a stagnant increase of grain size is found after annealing for 5 h and 24 h (see **Table 5.1** and **Figure 5.3e-g**), whereas a grain coarsening inhibition may occur. As a result, the microhardness does not decrease significantly after annealing for 5 h and 24 h. In contrast, annealing at 600°C leads to a different grain coarsening behavior. Here, a more pronounced grain coarsening is obtained up to ~200 nm of grain size after annealing at 600°C for 24 h (see **Table 5.1** and **Figure 5.3h-j**). Grain coarsening inhibition is not observed at this annealing temperature, whereas grain size increases with increasing time of annealing. Different grain coarsening behaviour is observed at 450°C and 600°C in which spinodal or phase decomposition may have a contribution here. Further investigations are needed for comprehensive understanding on structural evolution at these annealing temperatures (i.e. 450°C and 600°C).

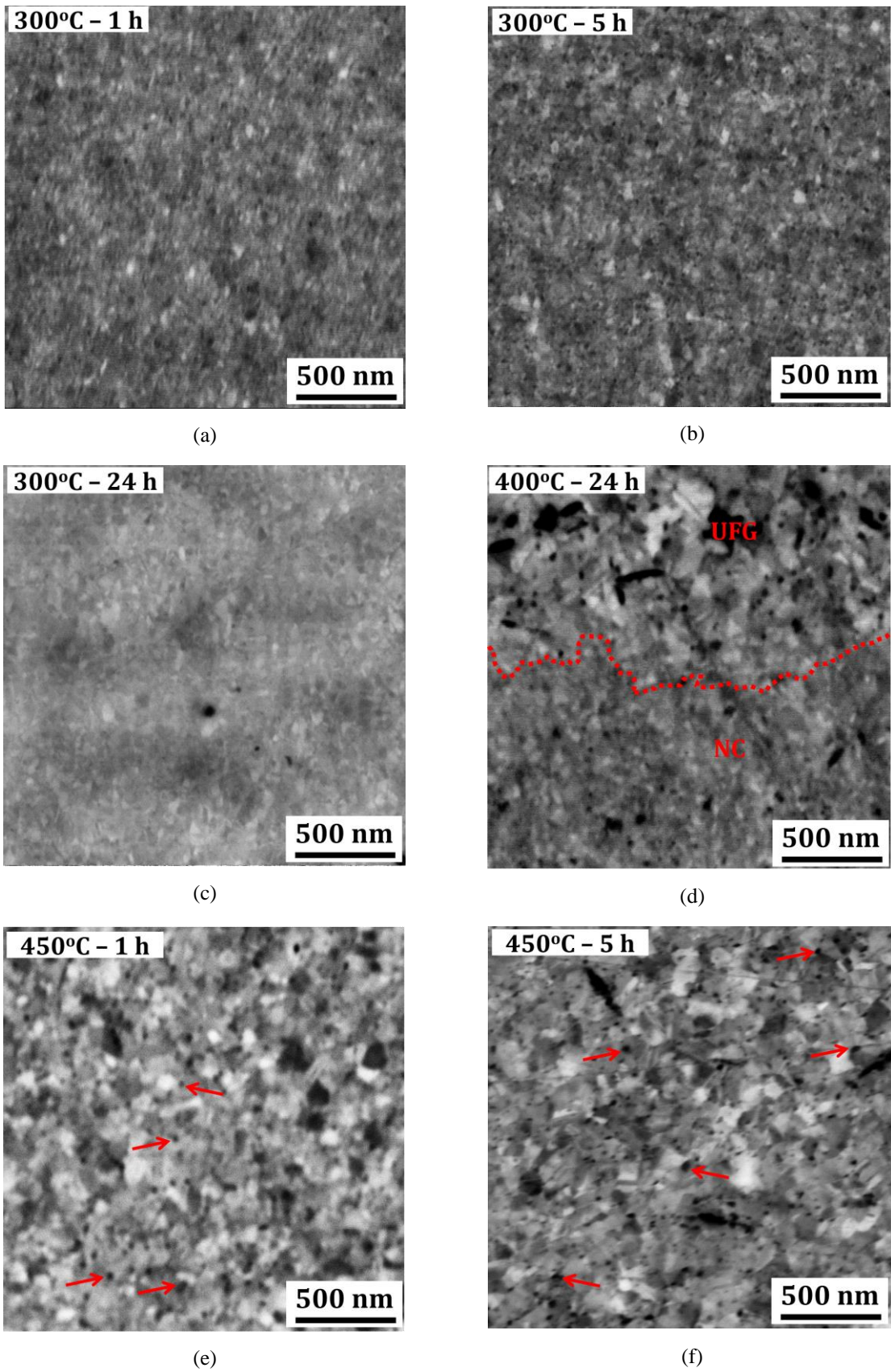


Figure 5.3 Continued

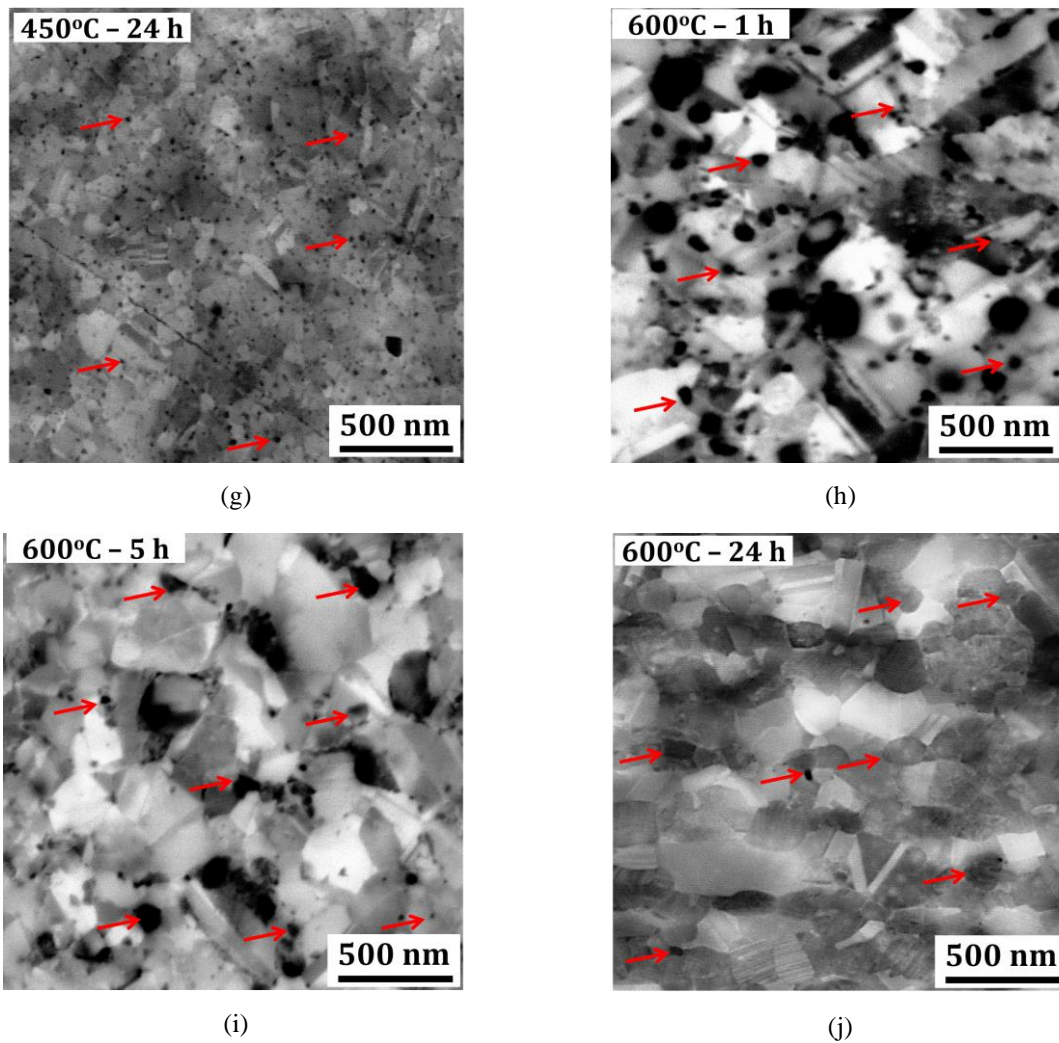


Figure 5.3 Back-scattered electron (BSE) images of microstructure of the (a) as deposited (from [189]) and (b-j) annealed (from [188]) samples in cross-sectional direction. All pictures were taken at the same magnification. Some interesting microstructural features are marked with red arrows in **Figure (e-j)**. (UFG: Ultrafine grained; NC: Nanocrystalline). Some interesting microstructural features (dark particles) are marked with red arrows.

5.3. Microstructural evolution: On the spinodal decomposition at 300°C

In this section, possible structural evolution at different annealing temperature and its effect on the thermal stability is discussed. According to the results, annealing at 300°C leads to a hardening effect with no significant grain coarsening observed. In the previous works, Cahn [197] and Kato et al. [198] proposed the theory of hardening by spinodal decomposition in the solid solution of fcc-structure alloys. It was described that dislocation movement is significantly different in the presence of compositional fluctuations and internal stresses due to spinodal decomposition, whereas an increase of strength is expected. The temperature for spinodal decomposition depends on the alloy composition. Investigations through computer simulation predicted that spinodal decomposition in Co-Cu alloys is possible at an annealing temperature of 450°C [199, 200]. The temperature for spinodal decomposition could be lower for

nanocrystalline materials due to higher number of vacancy-type defects and grain boundaries which enhances significantly the atomic diffusivity compared to microcrystalline materials [201]. For instance, Bachmaier et al. [27] observed a spinodal decomposition of the solid HPT-processed solid solution nanocrystalline Co-74%Cu at 400°C.

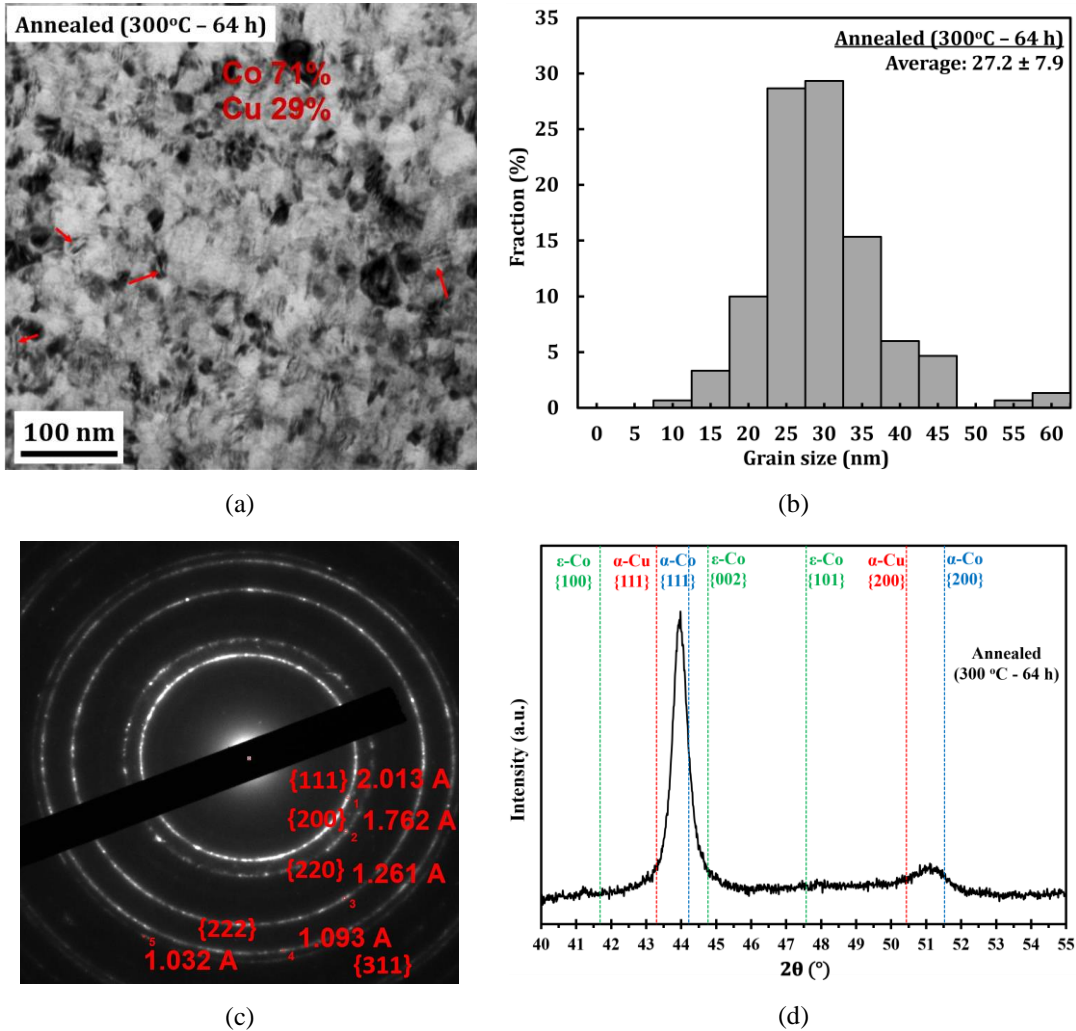


Figure 5.4 (a) BF-TEM image of a sample annealed at 300°C for 64 h (from [188]). (b) Grain size distribution corresponds to Figure (a) (from [188]). (c-d) Phase and orientation observations of an annealed sample through (c) SAD-TEM and (d) XRD measurements (from [188]).

In the present work, one sample was annealed at 300°C for a longer time period up to 64 h for investigation of the spinodal decomposition. **Figure 5.4a** depicts a bright field (BF)-TEM image of the microstructure of this sample showing an identical microstructure compared with the as-deposited state (see also **Figure 5.1a**). The microstructure of the annealed sample still comprises twin structures which are marked with red arrows in **Figure 5.4a**. Grain size distribution of this annealed sample (see **Figure 5.4b**) confirms no significant grain coarsening, whereas nanostructured grains with a size of 27.2 ± 7.9 nm were measured. The measured

microhardness of this annealed sample is 4.83 ± 0.07 GPa, observing the same hardening effect as in other samples annealed at 300°C. Phase and orientation analysis were performed for this annealed sample to observe the possibility of phase transformations (e.g. spinodal or phase decomposition from fcc-solid solution Co-Cu to fcc-Cu, fcc-Co, and hcp-Co). Comparing with the as-deposited state, significant changes of phase and orientation are not detected from SAD-TEM and XRD patterns (see **Figure 5.4c,d**). Interestingly, a minor shift of the lattice parameter of mainly {111} and {200} planes are observed from the measurements. Minor lattice shifts may be contributed by several factors, which are: (i) nano-scale spinodal or chemical decomposition, (ii) grain boundaries relaxation, (iii) internal stresses relief, and (iv) reduction of defect density. In the present work, the investigation is focussed on the spinodal or chemical decomposition. A more comprehensive investigation at the nano-scale (e.g. APT measurements) is needed for observation of spinodal decomposition.

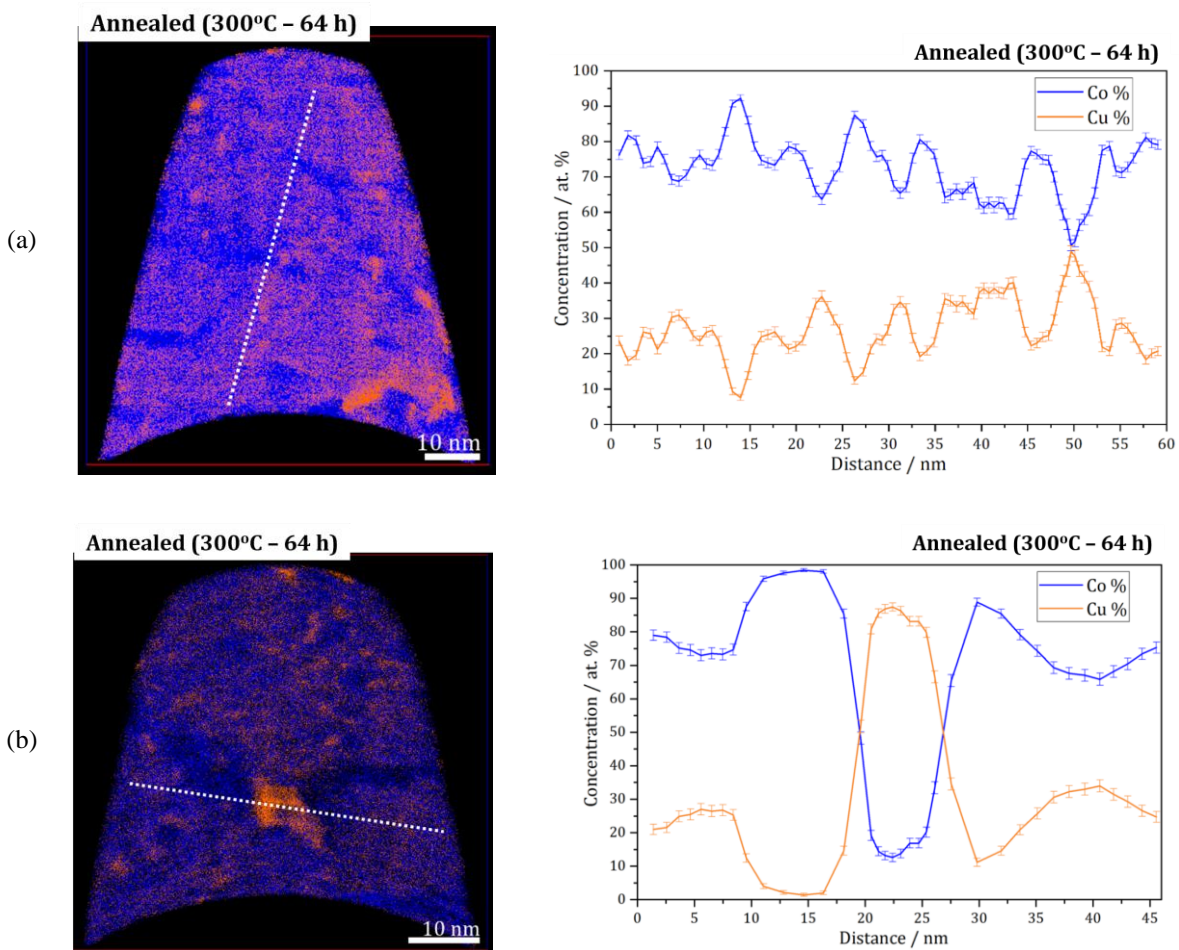


Figure 5.5 APT investigation of Co (blue) and Cu (orange) elements of a sample annealed at 300°C for 64 h: Elemental map of selected slices (5 nm thick) (**a** and **b**) of two different reconstructions from a similar sample and one-dimensional concentration profiles constructed along the a white dashed lines in the respective elemental maps (from left to right) (from [188]).

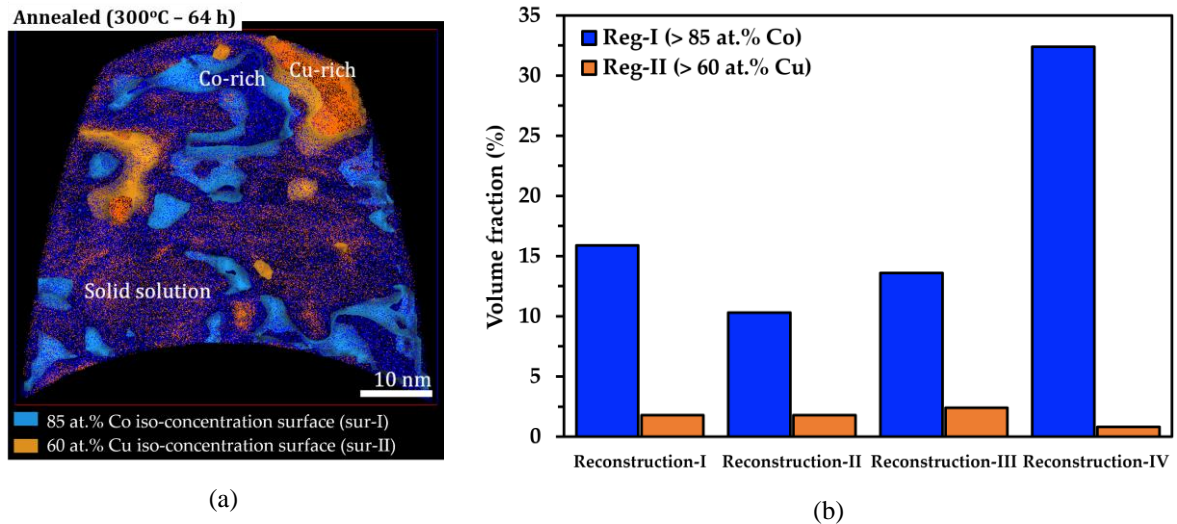


Figure 5.6 (a) A typical combined APT elemental map and iso-concentration surfaces at 85 at.% Co and 60 at.% Cu showing the regions used to calculate the approximated volume fraction of Co- and Cu-rich regions in a sample annealed at 300°C for 64 h. (b) Approximated volume fraction of Co- and Cu-rich regions (i.e. >85 at.% Co and >60 at.% Cu) measured from four different reconstructions.

Atom probe tomography (APT) was conducted for a sample annealed at 300°C for 64 h. **Figure 5.5a,b** depict APT elemental maps of selected slices from different reconstructions in an annealed sample and their one-dimensional concentration profiles observing spinodal decomposition of the solid solution Co-Cu. The first reconstruction (**Figure 5.5a**) shows short range compositional fluctuations in the solid solution regions which are not observed in the as-deposited samples (see also **Figure 5.2**). According to Cahn [202], short range compositional fluctuations are one of the crucial attribute for spinodal decomposition and it should occur uniformly within the sample. These fluctuations should raise continuously until a metastable equilibrium is achieved [202]. According to the phase diagram of the Co-Cu system [203], the formation of immiscible ϵ -Co and α -Cu phases is expected during a metastable equilibrium at 300°C. Additionally, the second reconstruction (**Figure 5.5b**) shows extensive compositional fluctuations confirming Co-rich regions (up to 95 at.% Co) and Cu-rich regions (up to 90 at.% Cu) with a size of 5-10 nm. It is believed that these Co- and Cu-rich regions may act as ‘precipitates’ which have a significant contribution to the hardening effect at 300°C.

An Estimation of the volume fractions of the Co- and Cu-rich regions was determined by iso-concentration surfaces in four reconstructions. **Figure 5.6a** shows an example of combined APT elemental map and iso-concentration surfaces at 85 at.% Co and 60 at.% Cu. The threshold value of the iso-concentration surfaces were chosen from the middle point between the highest solid solution composition (70 at.% Cu and 30 at.% Cu) and its composition in the Co-rich region (95 at.% Co) and the Cu-rich region (90 at.% Cu). **Figure 5.6b** shows the volume fraction of the regions containing high Co and Cu concentrations (>85 at.% Co and >60 at.%

Cu). The volume fractions in reconstruction-IV deviates from the other three reconstructions due to the small volume analysed by APT and the fluctuation in the element's distribution in the sample. According to the whole calculation, the number of Co- and Cu-rich regions formed upon chemical decomposition at 300°C is less than 20 vol%.

Table 5.2 Distances of atomic diffusion of Co and Cu at 300°C for 64 h calculated through the classical theory of diffusion. The diffusion coefficients were selected from some literatures and they were extrapolated to 300°C through the Arrhenius relation ($D = A \exp [-E_A/RT]$). (mc: microcrystalline; nc: nanocrystalline)

Diffusion mechanism	Diffusion coefficient at 300°C ($\text{cm}^2 \cdot \text{s}^{-1}$)	Distance of atomic diffusion (nm)	Reference
Co self-diffusion	1.03×10^{-26}	5.00×10^{-4}	Nix et al. [204]
Cu diffusion in Co	8.54×10^{-26}	1.40×10^{-3}	Arita et al. [205]
Interdiffusion Co-Cu	4.16×10^{-22}	9.80×10^{-2}	Bruni et al. [206]
<hr style="border-top: 1px dashed black;"/>			
Cu self-diffusion in mc Cu	3.36×10^{-19}	2.78	Kuper et al. [207]
	1.57×10^{-19}	1.90	Bowden et al. [208]
	1.15×10^{-19}	1.63	Surholt et al. [209]
Cu self-diffusion in nc Cu	6.69×10^{-11}	1.58×10^4	Horvart et al. [201]

Spinodal decomposition in nanocrystalline Co-Cu occurs through the atomic diffusion of Co and Cu at grain boundaries and within individual grains. Diffusion at grain boundaries may lead to a faster decomposition of Co-Cu (i.e. formation of Co- and Cu-rich regions), but diffusion for spinodal decomposition is supposed to occur dominantly within individual grains, since grain boundary diffusion is assumed negligible (i.e. no grain coarsening). According to the measured lengths of compositional fluctuations, including Co- and Cu-rich regions (see **Figure 5.5a,b**), the maximum distance of the atomic diffusion of Co and Cu at 300°C for 64 h is ~10 nm. A simple and rough calculation was conducted for determination of diffusion coefficient in Co-rich nanocrystalline Co-Cu through the classical theory of diffusion equation ($L = \sqrt{Dt}$, where D , L , and t are the diffusion coefficient, the diffusion distance, and time, respectively). The calculation confirms that the overall diffusion coefficients in nanocrystalline Co-Cu at 300°C is $4.34 \times 10^{-18} \text{ cm}^2 \cdot \text{s}^{-1}$. Regarding chemical composition (72 at.% Co and 28 at.% Cu), there are three possible diffusion mechanisms in the Co-rich nanocrystalline Co-Cu: (i) Co self-diffusion; (ii) Cu diffusion in Co; (iii) interdiffusion of Co-Cu. For comparison, the diffusion distances of Co and Cu in conventional bulk or microcrystalline Co [204, 205] and Co-Cu [206] were also calculated through the same equation and the results are shown in **Table 5.2**. According to these calculations, spinodal decomposition in conventional bulk Co or Co-Cu is almost impossible at 300°C due to low calculated atomic mobility of less than 1 nm. It is

believed that the diffusion rate in nanocrystalline and bulk/microcrystalline materials is significantly different due to several factors such as grain boundaries, vacancies, dislocations, and others. For instance, **Table 5.2** shows different characteristics of self-diffusion of Cu in microcrystalline [207, 208, 209] and nanocrystalline [201] materials. Here, the atomic mobility in nanocrystalline materials is ten thousand times faster than in microcrystalline materials. These results are not surprising due to a significantly higher number of mainly grain boundaries and vacancy-type defects within individual nanostructured grains [201]. Study on diffusion parameters and mechanisms in nanocrystalline materials, mainly Co-Cu systems, needs further investigation.

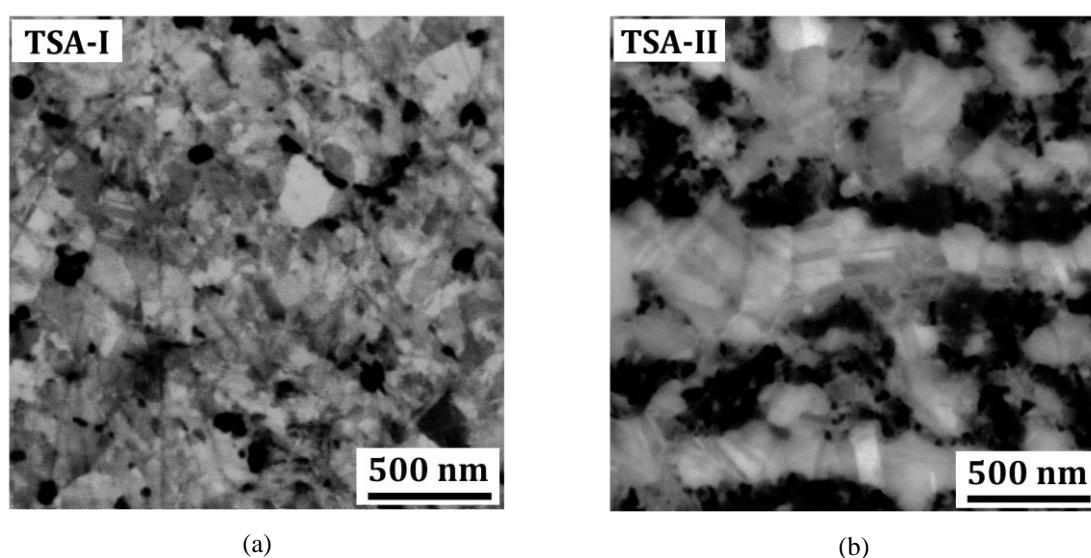


Figure 5.7 Back-scattered electron (BSE) images of the microstructure of samples subjected to two steps of annealing (TSA). **(a)** TSA-I: Annealed at 300°C for 64 h → Rapid cooling to room temperature → Annealing at 600°C for 1 h. **(b)** TSA-II: Annealing at 300°C for 64 h → Rapid cooling to room temperature → Annealing at 600°C for 5 h.

In the present work, the effect of spinodal decomposition on the thermal stability is studied. Two samples were prepared for two steps annealing (TSA) procedures. The first annealing step at 300°C for 64 h is subjected for spinodal decomposition leading to the formation of Co- and Cu-rich regions and compositional fluctuations with no grain coarsening. The second annealing step at 600°C is addressed for investigation of the thermal stability. In the first annealing step, the samples were annealed at 300°C for 64 h and followed by rapid cooling to ambient room temperature. Afterwards, the samples were annealed at 600°C for different time periods of 1 h (TSA-I) and 5 h (TSA-II). **Figure 5.7a,b** depict BSE images of microstructure of TSA-I and TSA-II samples after two annealing steps. The grain size of TSA-I and TSA-II samples are 149.2 ± 42.6 nm and 184.0 ± 51.2 nm, respectively. The microhardness of the TSA-I and TSA-

II samples are 4.14 ± 0.05 GPa and 3.82 ± 0.03 GPa respectively. Slight improvement on the thermal stability is observed here compared to samples annealed at 600°C only (see also **Table 5.1**). The formation of Co- and Cu-rich regions and compositional fluctuations may have a contribution on the improvement of thermal stability. These Co- and Cu-rich regions may act as “stabilisers” mainly at grain boundaries which block grain boundary movement (i.e. Zener pinning). In addition, compositional fluctuations are a barrier for the atomic diffusion of Co and Cu, which are necessary for grain boundary movement. It has been understood that atomic diffusion in different phases (in this case compositional fluctuation) is more difficult than atomic diffusion in a single phase structure. An improved thermal stability can be contributed also by other factors such as segregation of impurities (e.g. sulphur and carbon) at grain boundaries, however, it is not a part of investigation in this research.

5.4. Microstructural evolution: Phase decomposition at 450°C and 600°C

Figure 5.3e-g depict microstructure images of samples annealed at 450°C. The significant grain coarsening and decrease of microhardness of these annealed samples have been already described and a constant grain size was achieved after particular annealing time periods. The factors affecting the grain growth inhibition are discussed here. **Figure 5.8a,b** show XRD patterns of samples annealed at 450°C for 5 h and 24 h showing some phase decompositions and transformations. A shoulder on the peak of the {111} planes is an indication of the initial stage of spinodal decomposition in the sample annealed at 450°C for 5 h (marked with a black arrow in **Figure 5.8a**). This shoulder is supposed to be the peak of α -Cu-{111} planes. However, an obvious phase decomposition is not observed here. A simultaneous grain boundaries movement and spinodal decomposition are expected during short annealing periods (1 h and 5 h). Initial stage of spinodal decomposition within individual grain is expected to form compositional fluctuations of Co and Cu. The spinodal decomposition could be faster at grain boundaries and triple junction due to higher mobility for atomic diffusion. This may lead on the formation of some “spots” with high Cu concentration as detected from XRD pattern. BSE image of the microstructure (see **Figure 5.3f**) shows numerous “dark spots” at grain boundaries and triple junctions. These features are supposed to be Cu-precipitates formed during fast spinodal decomposition in these regions. In contrast, an obvious phase decomposition of the solid solution Co-Cu is observed from XRD pattern of a sample annealed at 450 °C for 24 h (see **Figure 5.8b**). The XRD peaks of fcc-Cu, fcc-Co, and hcp-Co are detected here. The XRD peaks of the Co-Cu solid solution remain visible as an indication of an in-progress phase decomposition. Longer annealing periods are needed for a complete phase decomposition. BSE images of the microstructure (see **Figure 5.3g**) shows a similar high quantity of “dark spots” at

grain boundaries and triple junctions, which are supposed to be the Cu- or Co-precipitates (fcc-Co and hcp-Co are also detected in this sample). These precipitates are the reason for the constant grain size due to grain growth inhibition through the pinning of grain boundaries mechanism (Zener pinning mechanism). In addition, the atomic diffusion necessary for grain boundary movement is expected to be harder in the multiple phases, for instance, moving a Cu grain into a Co grain needs a redistribution of a huge amount of atoms caused by the immiscibility gap of the system. These are the major factors for grain growth inhibition during long annealing periods at 450°C. Other factors such as segregation of impurities (e.g. sulphur and carbon) at grain boundaries may contribute also on grain growth inhibition.

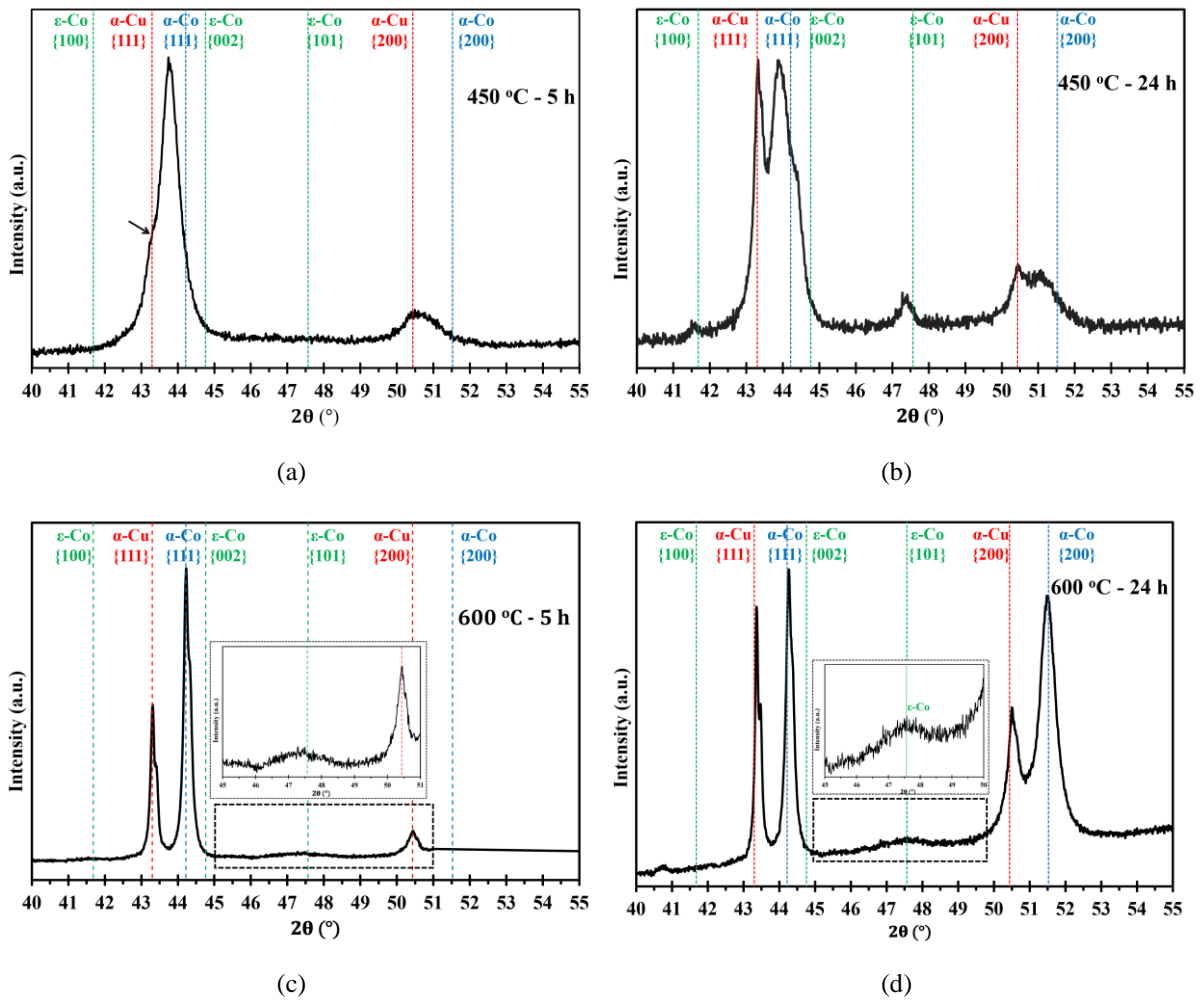
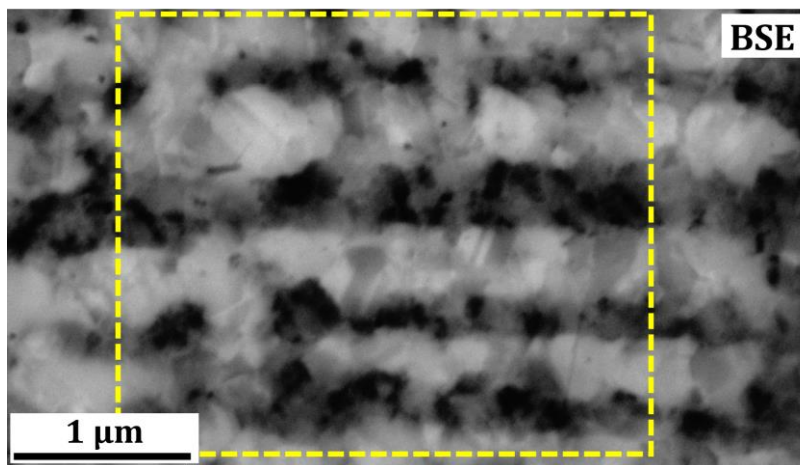


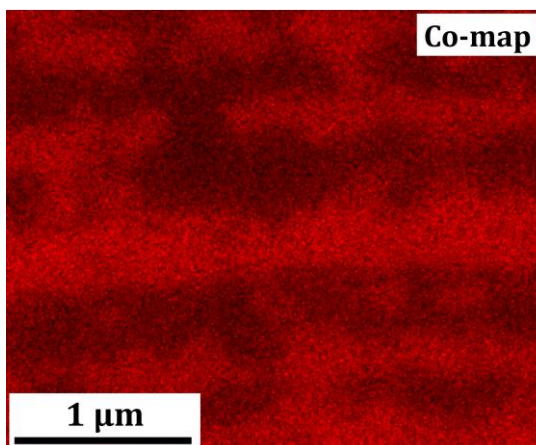
Figure 5.8 X-ray diffraction (XRD) patterns of samples annealed at (a-b) 450°C and (c-d) 600°C for different time periods of 5 h and 24 h (from [188]).

The microstructure images of samples annealed at 600°C (**Figure 5.3h-j**) show more pronounced grain coarsening, followed by a decreasing of microhardness down to below 4 GPa (**Table 5.1**). XRD measurements of samples annealed at 600 °C for 5 h and 24 h exhibit a

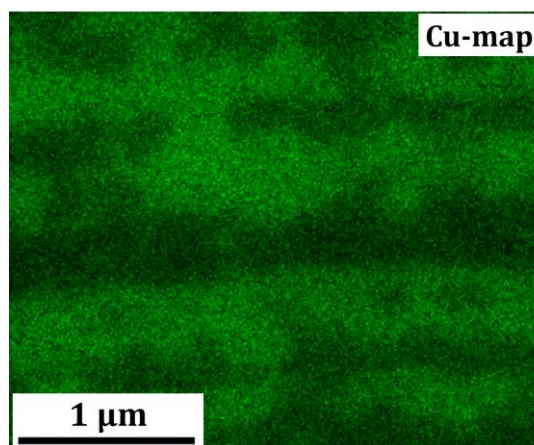
massive phase decomposition (**Figure 5.8c,d**). The{111} peaks of fcc-Cu and fcc-Co are perfectly separated after 5 h and 24 h of annealing. In addition, phase separation of fcc-Cu and fcc-Co at{200}planes are detected after 24 h of annealing too. A larger number of “dark spots”, which could be Co- or Cu-precipitates are found in the microstructure images of sample annealed for 1 h and 5 h (**Figure 5.3h-i**). In contrast, these precipitates are rarely found after 24 h of annealing (**Figure 5.3j**). These precipitates are likely to grow further and becoming grains after long time periods of annealing (24 h). The EDS map of a sample annealed at 600°C for 24 h (see **Figure 5.9**) shows a microstructure consisting of almost pure Co and Cu regions, which is an indication of almost complete phase decomposition. Furthermore, constant grain size cannot be obtained at 600°C, whereas the grain size increases with increasing annealing time. The mobility of grain boundary is rather high at 600°C, thus, the phase separation of Co-Cu cannot block the grain boundaries movement at this temperature.



(a)



(b)



(c)

Figure 5.9 (a) A back-scattered electron (BSE) image of the microstructure of a sample annealed at 600°C for 24 h. (b-c) EDS-map of (b) Co and (c) Cu elements from area marked within yellow dashed box on **Figure (a)**.

5.5. Effect of Cu concentration on the thermal stability

In this section, the effect of Cu concentration on the thermal stability of nanocrystalline Co-Cu is in the focus. Three samples with different Cu concentrations were deposited through different pulse profiles and parameters. The first sample (S1) is a similar Dep-I sample deposited at a pulse current density, a pulse-on time, and a pulse-off time of 1000 A/m^2 , 2 ms, and 18 ms, respectively. Characterization of microstructure, chemical composition, and microhardness of this sample is provided in **Section 5.1**. The sample S1 consists of 28 at.% Cu with a mean grain size of $22.7 \pm 8.2 \text{ nm}$. The microhardness of this sample is $4.45 \pm 0.07 \text{ GPa}$.

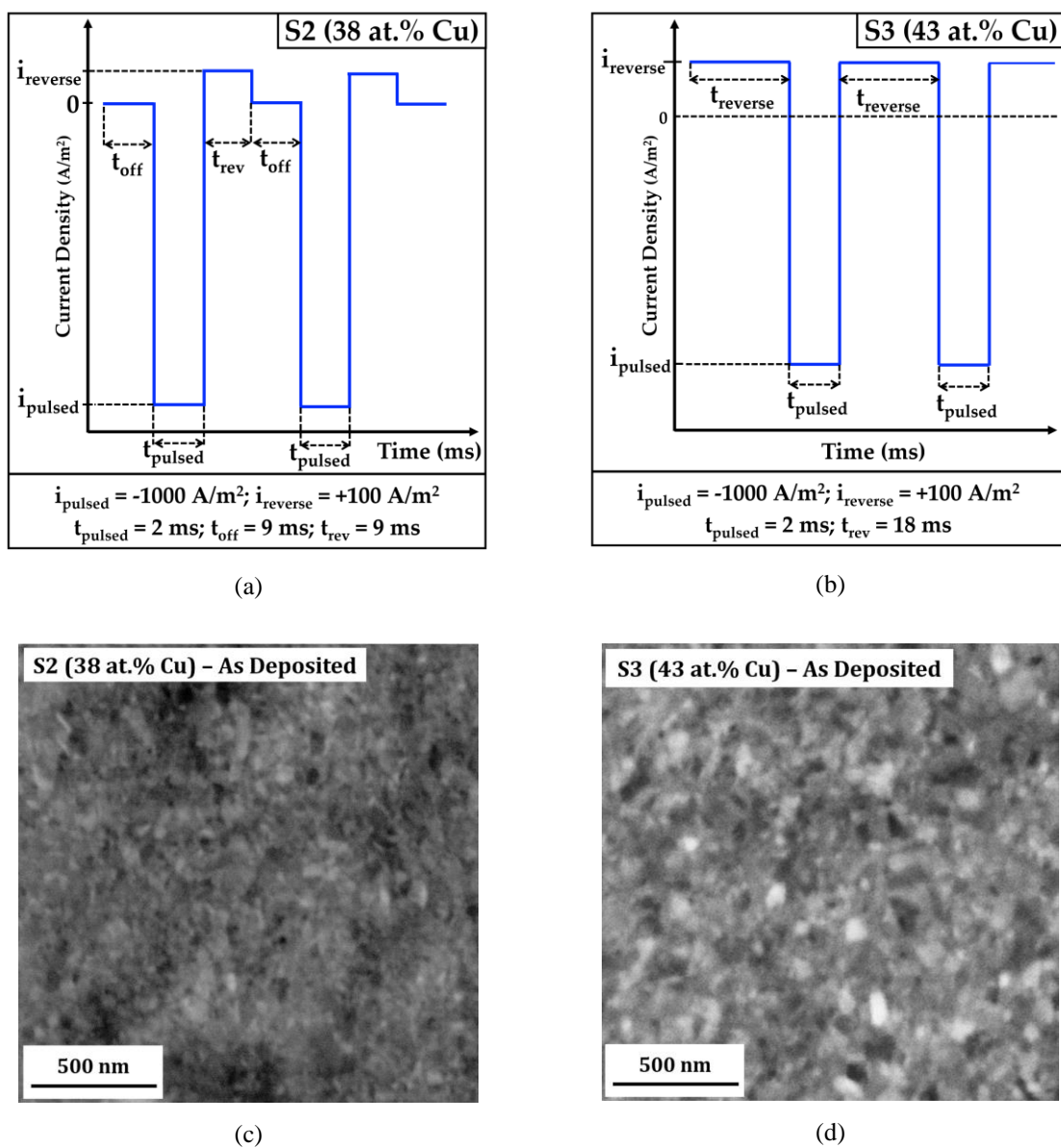
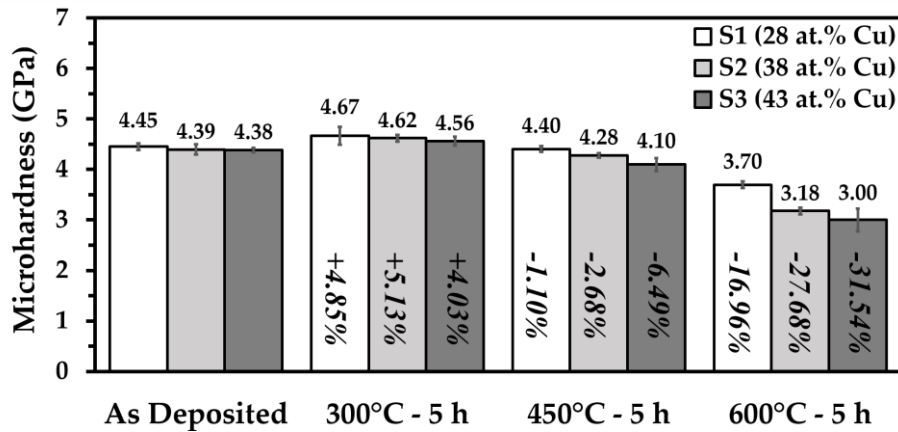


Figure 5.10 Pulse profiles and parameters of electrodeposition used to produce nanocrystalline Co-Cu with different Cu concentration: (a) 38 at.% Cu (S2) and (b) 43 at.% Cu (S3). BSE images of microstructure of (c) S2 (38 at.% Cu) and (d) S3 (43 at.% Cu) samples.

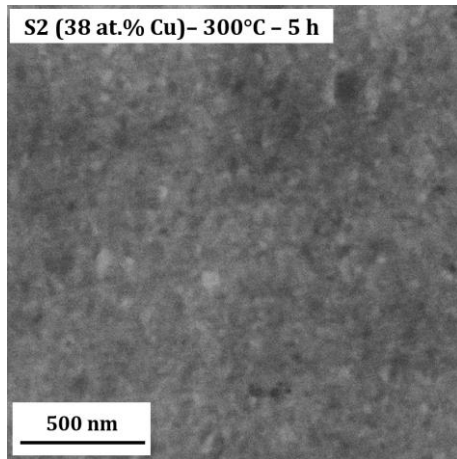
The second (S2) and third (S3) samples were produced through different pulse profiles and parameters as shown in **Figure 5.10a,b**. A reverse current of 100 A/m² (10% of pulse current) is used for different time periods. The decrease of Co content is expected from the utilization of reverse current. Caused by the more negative standard reduction potential of Co ($E^0_{(\text{Cu}^{2+}/\text{Cu})} = +0.34$ V vs. SHE and $E^0_{(\text{Co}^{2+}/\text{Co})} = -0.28$ V vs. SHE), Co dissolution is the more dominant process instead of Cu dissolution when reverse current is applied. As a result, the copper concentration increases in S2 and S3. The rate of Co dissolution increases with increasing time periods of the reverse current (t_{rev}). According to EDS measurements, the Cu concentration in S2 and S3 are 38 at.% and 43 at.%, respectively. According to Müller [77], the increase of Cu concentration might lead on the formation of a coarser grain size and decrease of microhardness in nanocrystalline Co-Cu. **Figure 5.10a,b** depict BSE images of microstructure of S2 and S3, showing a considerably coarser grain size compared to S1 (see **Figure 4.3b**). However, a determination of the grain size from BSE images is difficult due spatial resolution limit. Approximations from microstructure images shows that grain sizes of S2 and S3 samples are ranging from 30 nm to 50 nm. The microhardness of S2 and S3 are 4.39 ± 0.10 GPa and 4.38 ± 0.05 GPa, respectively. These microhardness values are slightly lower compared to S1 due to the larger grain size and higher Cu concentrations.

Annealing treatments at different temperatures (300°C, 450°C, and 600°C) for 5 h were conducted for investigation of the thermal stability. The thermal stability of S1 has been discussed already in **Section 5.2**. Grain size and microhardness of the annealed samples were measured to investigate grain coarsening due to thermal loading. The microhardness of as-deposited and annealed samples are summarized in **Figure 5.11a**. All samples (S1, S2, and S3) show a hardening effect after annealing at 300°C for 5 h. These results are not surprising as due to spinodal decomposition at 300°C is observed, the formation of 5-10 nm sized of “spots” with high Co and Cu concentration is observed (see **Section 5.3**). These “spots” may act as precipitates contributing to the hardening effect. Comparing with the as-deposited state, microhardness of S1 and S2 increase up to ~5%, while S3 exhibits the lowest increase of microhardness of ~4%. **Figure 5.11b,c** show BSE images of microstructures of the S2 and S3 samples annealed at 300°C for 5 h. The microstructure image of the 300°C-annealed S2 sample (**Figure 5.11b**) shows no significant grain coarsening with grain sizes of below 50 nm. In contrast, **Figure 5.11c** depicts a slight grain coarsening in a 300°C-annealed S3 sample. The mean grain size of S3 sample is 75.1 ± 19.8 nm. A numbers of “dark spots” are observed in the 300°C-annealed S3 sample which are marked with red arrows in **Figure 5.11c**. These “dark spots” may correspond to the Co- and Cu-precipitates formed during spinodal decomposition

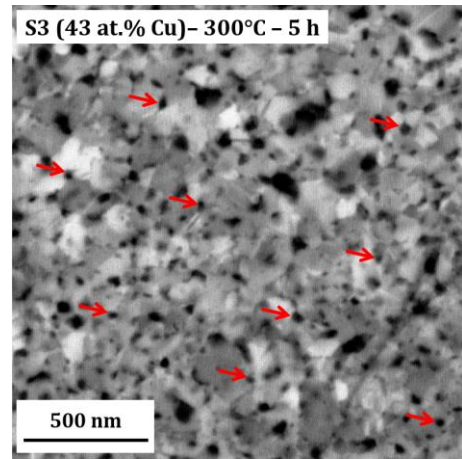
at 300°C influencing the increase of microhardness. Grain coarsening in nanocrystalline materials is usually followed by a decrease in microhardness. However, competition between grain coarsening and spinodal decomposition (formation of precipitates) is expected in a 300°C-annealed S3 sample. It is possibly the reason for the lowest increase of microhardness in a 300°C-annealed S3 sample, since grain size increase is much larger in S3.



(a)



(b)



(c)

Figure 5.11 (a) Microhardness of as deposited and annealed samples (S1, S2, and S3) containing different Cu concentration. The numbers within individual bars (in vertical direction) show the relative increase (positive) and decrease (negative) of microhardness compared with the as-deposited state (in percent). (b-c) BSE images of microstructure of (b) S2 (38 at.% Cu) and (c) S3 (43 at.% Cu) samples annealed at 300°C for 5 h

Significant grain coarsening is observed in all samples (S1, S2, and S3) annealed at 450°C for 5 h. Comparing with the as-deposited state, the microhardness of S1, S2, and S3 decrease for 1.10%, 2.68%, and 6.49% (see **Figure 5.11a**). The grain sizes of the annealed samples of S1 and S2 are quiet similar (~ 124 nm), while the annealed sample of S3 exhibit a larger grain size of 133.7 ± 39.2 nm. Annealing at 600°C for 5 h lead to a more pronounced grain coarsening. The grain sizes of S1, S2, and S3 annealed at 600°C for 5 h are 160.7 ± 67.2 nm, 173.2 ± 71.6

nm, and 193.0 ± 50.4 nm, respectively. The most significant grain coarsening and reduction of microhardness is observed in a 600°C-annealed S3 sample. Microhardness of S3 decline to 3.00 GPa or decrease for 31.54% compared to the as-deposited state. These investigations confirms that the Cu concentration has a strong impact on the thermal stability of nanocrystalline Co-Cu. In S1 (28 at.% Cu) and S2 (38 at.% Cu), grain coarsening is not observed at 300°C. The results for S1 (28 at.% Cu) show that grain coarsening is firstly detected at 400°C (see **Section 5.2**). In S3 (43 at.% Cu), grain coarsening possibly started at 300°C. A higher Cu concentration drive to lower stability against thermal loading at the higher temperatures (450°C and 600°C). In the present work, proper thermal stability of nanocrystalline Co-Cu up to 300°C can be achieved if the concentration of Cu is below 40 at.%. Further investigations are needed for revealing the starting temperature for grain coarsening and the long-term thermal stability of nanocrystalline Co-Cu at more varied Cu concentration.

5.6. Grain growth mechanisms in nanocrystalline Co-Cu

The possible grain growth mechanism at annealing temperatures of 450°C and 600°C is studied, because a significant grain coarsening was observed. The study will be more focussed on the grain growth exponent number (n) as described in **Chapter 2**. The n -value can be determined with two different approaches: (i) the initial grain size (D_0) is assumed very small compared to the final grain size (D) (equation [2.17]: $D = K \cdot t^{1/n}$); (ii) initial grain size (D_0) is included in the calculation (equation [2.16]: $D^n - D_0^n = Kt$). Whereas K and t are the rate constant and the annealing time, respectively. These two approaches were used since the D/D_0 values for all annealed samples are below 10, thus, the initial grain size cannot be neglected.

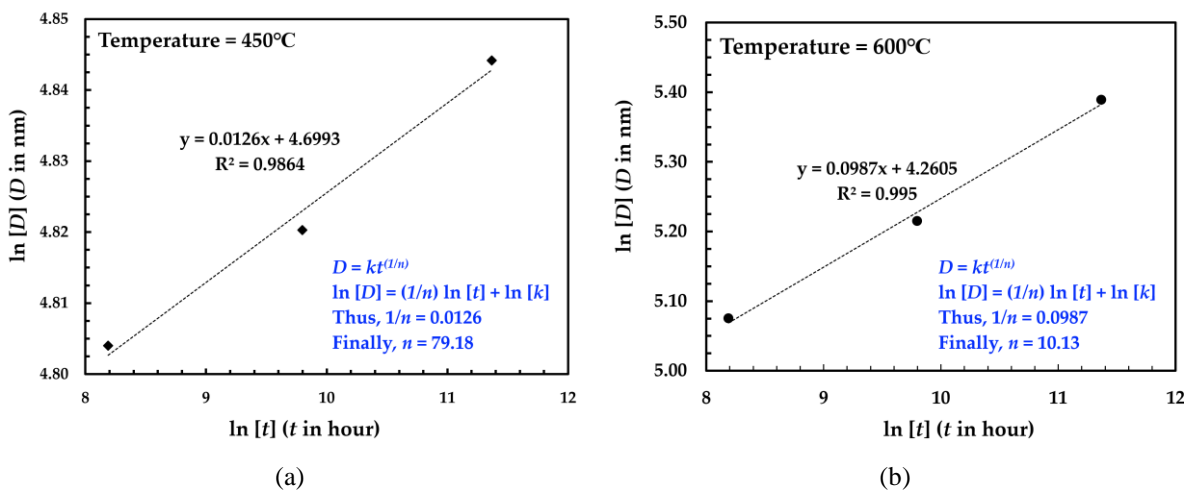


Figure 5.12 Determination of grain growth exponent (n) by using equation [2.17] ($D = K' \cdot t^{1/n}$) for nanocrystalline Co-Cu annealed at (a) 450°C and (b) 600°C. The grain sizes data were taken from **Table 5.1**.

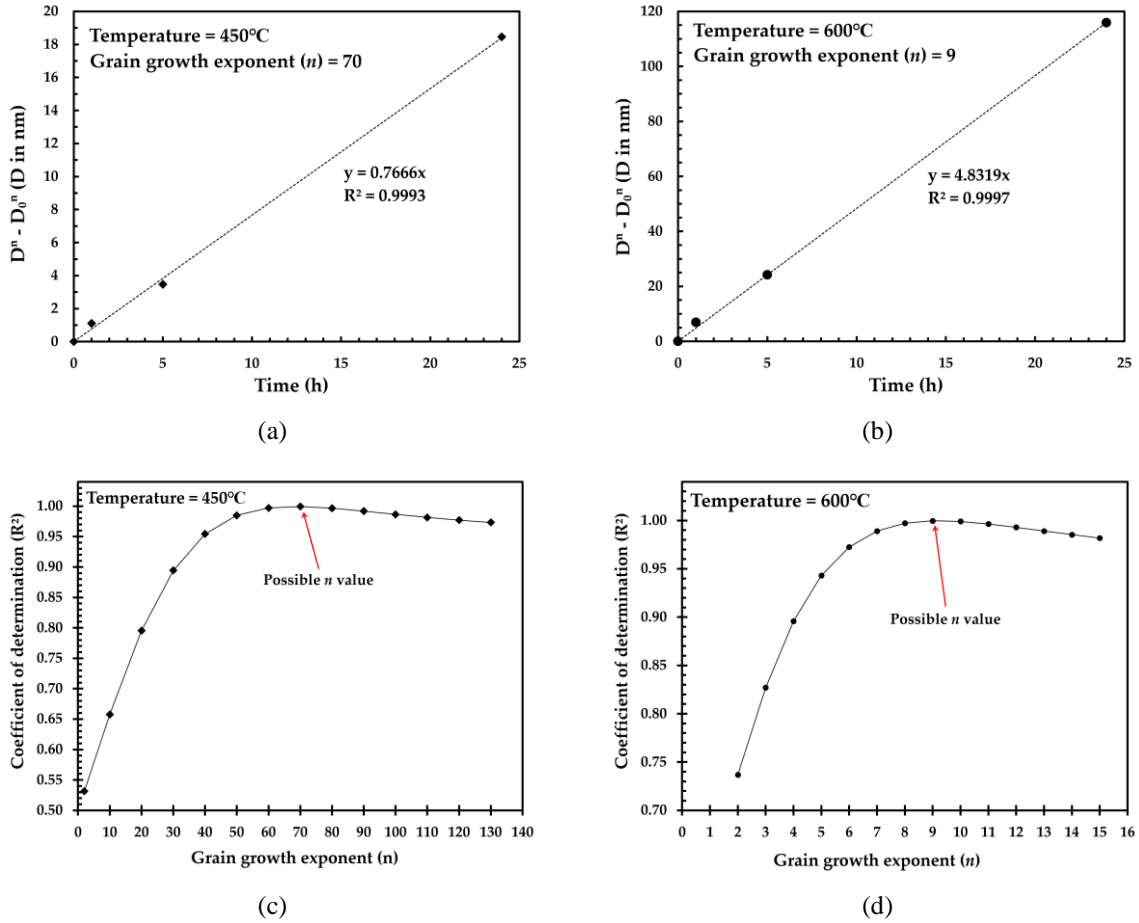


Figure 5.13 Determination of grain growth exponent (n) by using equation [2.16] ($D^n - D_0^n = Kt$). The grain sizes data were taken from **Table 5.1**. The n -value were varied to get the highest coefficient of determination for linear regression (R^2) as shown in (a) 450°C with $n = 70$ and (b) 600°C with $n = 9$. The coefficient of determination (R^2) at different grain growth exponent (n) for samples annealed at (c) 450°C and (d) 600°C.

For the first approach (equation [2.17]), the grain growth exponent (n) can be easily determined from the logarithmic plot as shown in **Figure 5.12a,b**. The n -value at 450°C and 600°C are 79.18 and 10.13, respectively. For the second approach (equation [2.16]), two parameters ($1/n$ and K) are unknown and they cannot be easily determined from the plot. Thus, the n -value must be varied as shown in **Figure 5.13a,b**. The n -value having the highest coefficient of determination for linear regression (R^2) is selected as shown in **Figure 5.13c,d**. According to the second approach, the n -value at 450°C and 600°C are 70 and 9, respectively.

The two approaches show a very high n -value at 450°C ($n = 70-79$) and 600°C ($n = 9-10$) compared to the ideal parabolic relationship ($n = 2$). It is believed that grain growth mechanism in solid solution nanocrystalline Co-Cu is not only driven by the curvature of boundaries. In addition, these n -values are extremely higher than the observed in nanocrystalline pure Cu ($n = 3-4$) [8, 124]. A high n -value in nanocrystalline Co-Cu could be an indication of grain growth inhibition at 450°C and 600°C. According to the results in **Section 5.4**, spinodal and phase

decomposition may have a significant impact to grain growth inhibition at 450°C and 600°C. A significant decrease of grain growth exponent from $n = 70-79$ at 450°C to $n = 9-10$ may indicate a higher atomic mobility at 600°C, thus a stagnant grain growth cannot be observed at this temperature. To conclude, grain growth mechanism in solution nanocrystalline Co-Cu may be attributed to some factors: (i) grain boundary curvature, (ii) solute drag effect (e.g. copper and sulphur), (iii) second phase particles drag (formation of Cu-precipitate), (iv) spinodal and phase decomposition (interdiffusion of Co-Cu), and, (v) large grain boundaries volume (e.g. vacancy drag, triple junction drag, pores drag).

5.7. Magnetic properties

Preliminary investigations on the magnetic properties of nanocrystalline (nc) and ultrafine grained (ufg) Co-Cu (28 at.% Cu) were conducted through the magnetic force microscopy (MFM). Ufg samples were obtained through annealing treatments at temperatures of 450°C, 600°C, and 800°C for 5 h. **Figure 5.14a-d** depict combined AFM-MFM images of surface morphology and magnetic domain pattern of the as-deposited and annealed samples. MFM measurement is based on Interaction between the cantilever tip and sample surface. It is worked usually in amplitude modulation mode at a certain resonance frequency or phase [210]. In case of magnetic fields exit in the sample surface, it causes a shift of resonance frequency or phase. The positive (bright contrast) and negative (dark contrast) shift of resonance frequency or phase corresponds to repulsive and attractive magnetic forces, respectively. In the present work, the magnetic behaviour of the sample is represented by the MFM phase signal. **Figure 5.14e** summarizes one-dimensional profiles of the normalized MFM phase signal of individual samples corresponding with the white dashed lines (left to right) in the respective MFM images. The normalized MFM phase is calculated through subtraction of the actual MFM phase with the median value of MFM phase. Large fluctuations and high amplitudes of the MFM phase indicate a strong magnetization of the sample surface. Regarding the MFM measurements, as-deposited and 450°C-annealed samples show a weak magnetic domain pattern. A slight enhance of MFM phase signal is visible for the sample annealed at 600°C. In contrast, a strong magnetic domain pattern is visible in the sample annealed at 800°C for 5 h. MFM phase amplitude of the 800°C-annealed sample is up to 4 times higher compared to other samples.

The magnetic properties of the Co-Cu alloy is a directly caused by the compositional modulated structure of Co and Cu. The size of the modulated structure has also a contribution on the magnetic properties due to maximum spatial resolution of MFM (typically ~50 nm) [211]. The as-deposited sample exhibits a supersaturated solid solution of Co-Cu. APT

measurements (**Section 5.1**) of as-deposited samples show no modulated structure of Co-Cu and Co- or Cu-segregation. Therefore, a weak magnetic domain pattern in as-deposited sample is not surprising. The XRD pattern of a sample annealed at 450°C for 5 h (**Section 5.4**) show an initial stage of spinodal and phase decomposition, in which the formation of regions with high Cu concentration (e.g. Cu-precipitates) is expected. However, the size of these Cu-precipitates is less than 50 nm which is difficult to detect by MFM. In addition, a significant phase decomposition is also not observed here, which has a direct impact on a weak magnetic domain pattern of this annealed sample. On the other hand, the XRD pattern of a sample annealed at 600°C for 5 h (**Section 5.4**) show a clear phase decomposition of Co and Cu, whereas the XRD peaks of {111}-Cu and {111}-Co are detected. This phase decomposition has a significant contribution on the magnetic properties in this annealed sample.

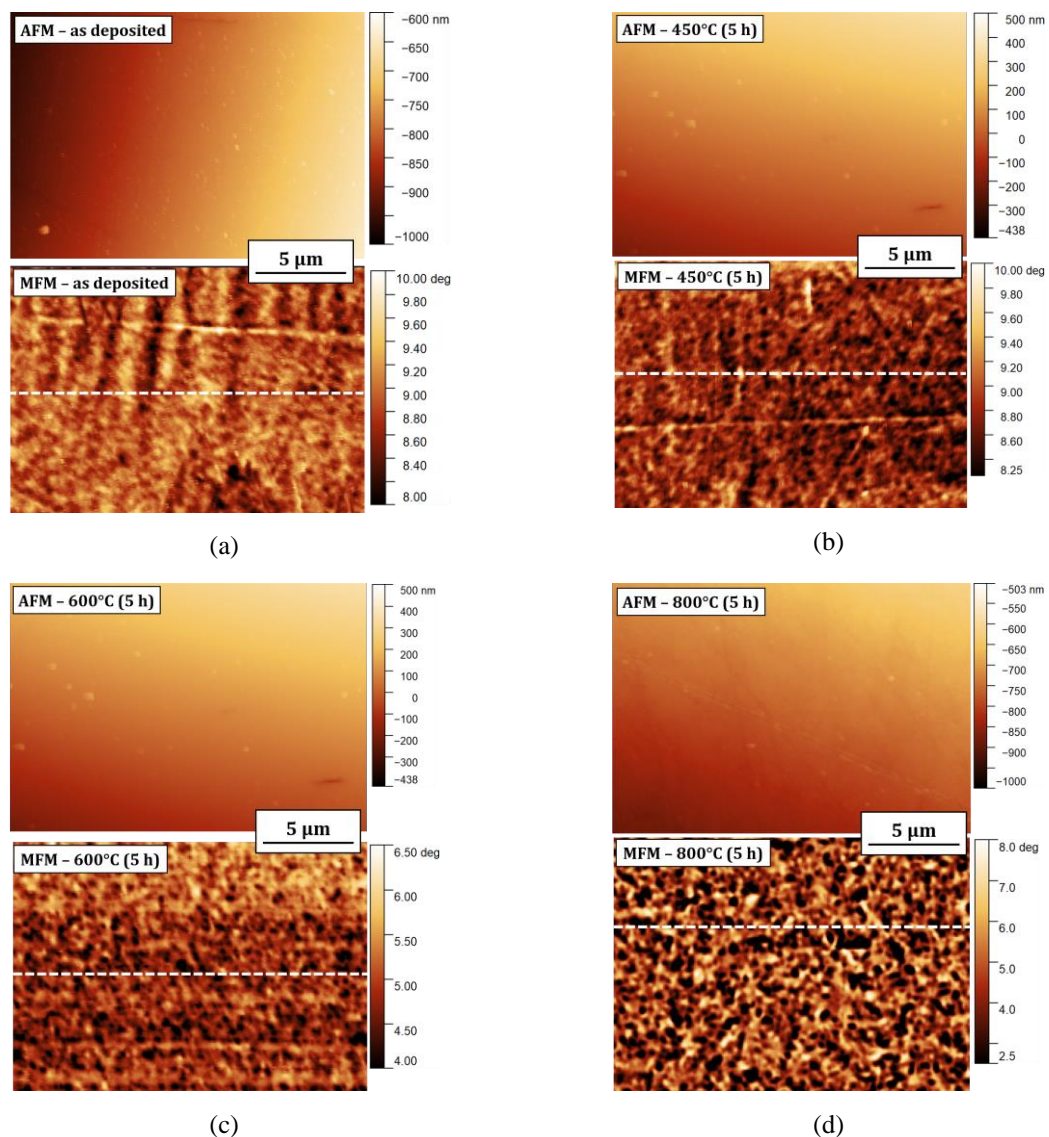


Figure 5.14 *Continued*

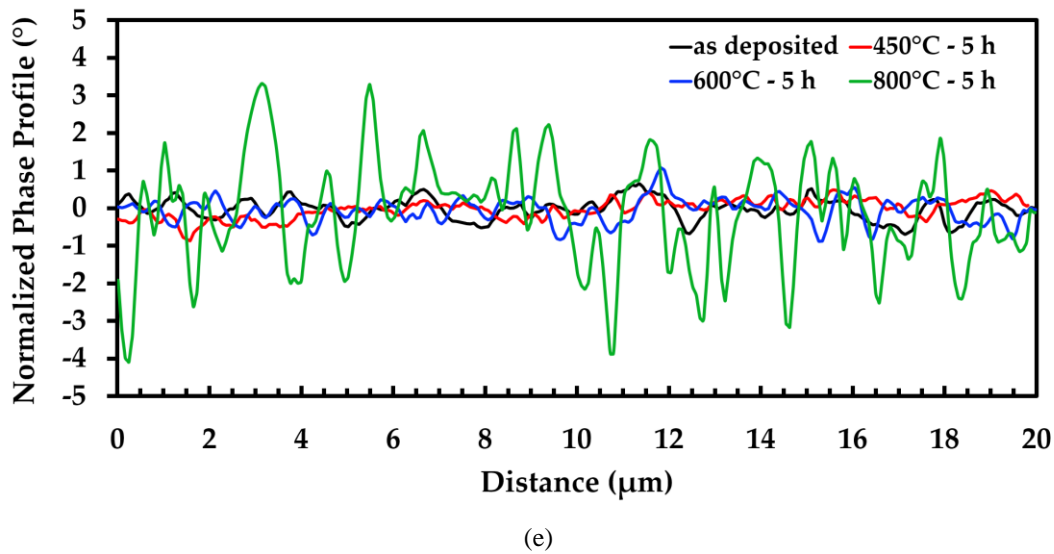


Figure 5.14 Combined AFM-MFM images of surface morphology and magnetic domain pattern of nc and ufg Co-Cu: (a) as deposited and annealed at (b) 450°C, (c) 600°C, and (d) 800°C for 5 h. (e) One-dimensional profiles of normalized MFM phase signal corresponding to the white dashed lines marked in (a-d) from left to right.

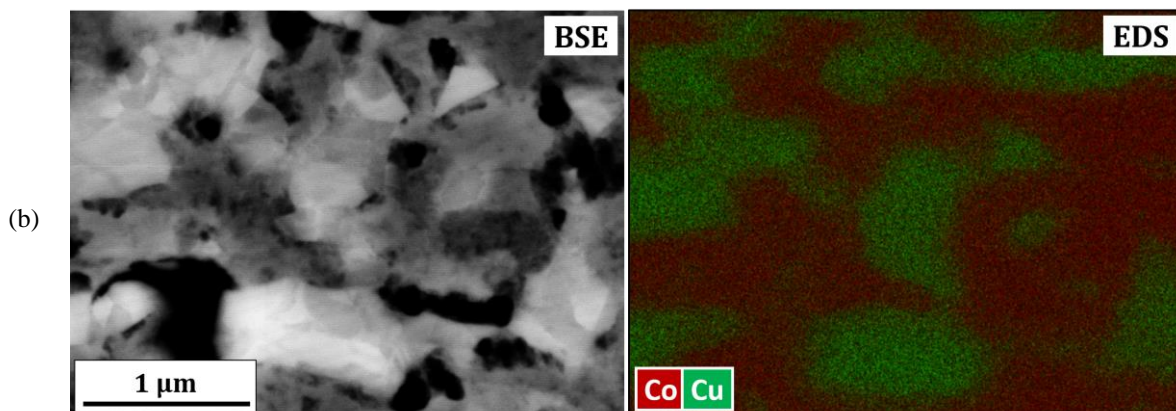
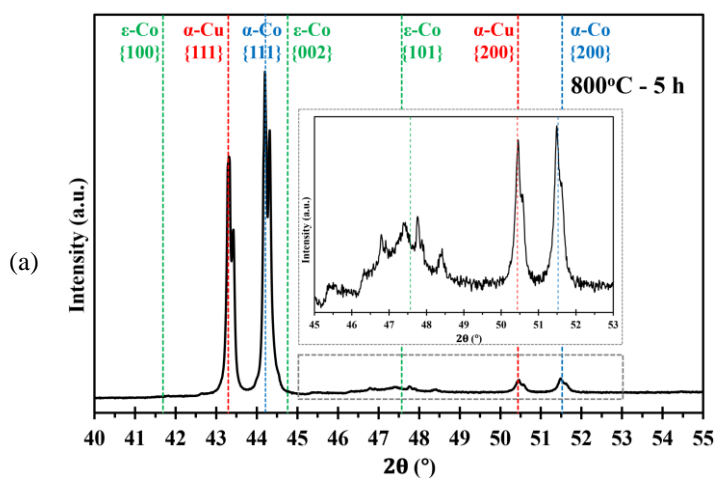


Figure 5.15 (a) X-ray diffraction (XRD) pattern and (b) energy dispersive spectroscopy (EDS) map of a sample annealed at 800°C for 5 h.

The XRD pattern of a sample annealed at 800°C for 5 h show an even more pronounced phase decomposition of Co and Cu. The XRD peaks of {111}-Cu, {200}-Cu, {111}-Co and {200}-Co planes are detected (see **Figure 5.15a**). A weak XRD peak of {101}-hcp-Co planes is also observed. In addition, the EDS map of this annealed sample (see **Figure 5.15b**) shows microstructure consisting of almost pure Co and Cu regions with sizes of 0.5-2.0 μm , showing a perfect phase decomposition. This significant phase decomposition has a high contribution to the strong magnetic domain pattern in this sample. Contributions from the existing hcp-Co phase on the magnetic properties is also expected here. This investigation is just a preliminary study for exploring the physical and functional properties of this material, in which promising results can be obtained by tailoring the microstructure through the annealing treatments. Further investigations are needed for revealing and improving the magnetic properties of this material.

5.8. Discussion of the results in Chapter 5

Investigations on the thermal stability, microstructural evolution, grain growth mechanism, and magnetic properties of PED-processed supersaturated solid solution nanocrystalline Co-Cu (28 at.% Cu) have been investigated. Some interesting findings should be discussed.

PED-processed nanocrystalline Co-Cu shows a significant improvement on the thermal stability compared with nanocrystalline Cu [8, 9, 124], nanocrystalline Co [7, 13, 23, 27], and nano-twin Cu [143]. Under isothermal loading, starting temperature for grain growth for this material is 400°C, which is higher than observed in nanocrystalline Cu (75-150°C) [8, 124], nanocrystalline Co (300-350°C) [7, 13, 23, 27], and nano-twin Cu (300-400°C) [143]. Comparing with the as-deposited state, the grain size of nanocrystalline Co-Cu increased from ~23 nm to ~83 nm (~250%) after annealing at 400°C for 24 h (see **Section 5.2**). Grain coarsening in nanocrystalline materials is usually followed by a significant decrease in microhardness, for instance, the microhardness of SPD-processed nanocrystalline Co decreased for 40% after annealing at 300°C for 1 h [13]. In contrast, a massive decrease of microhardness was not found in PED-processed nanocrystalline Co-Cu after annealing at 400°C for 24 h, whereas the microhardness decreased for only ~2% (see **Section 5.2**).

The presence of Cu solute atoms in nanocrystalline Co-Cu has a significant influence for improvement of thermal stability (solute atoms drag). According to the results (**Section 5.3**), spinodal decomposition of solid solution nanocrystalline Co-Cu can be started at 300°C, whereas some “spots” (5-10 nm sizes) with high concentrations of Cu (up to 90 at.%) and Co (up to 95 at.%) were observed (**Figure 5.5b**). These “spots” may acts as “precipitates” having a hardening effect at 300°C. For stabilization of grains, these “precipitates” have an impact for

pinning grain boundaries (Zener pinning drag), thus, grain coarsening can be avoided. These “precipitates” could be also the reason for an insignificant decrease of microhardness for only ~2% at 400°C. In addition, compositional fluctuations of Co and Cu were also observed from APT measurement (**Figure 5.5a**), which could be a barrier for grain growth (interdiffusion of Co and Cu is needed). At the higher temperatures (450°C and 600°C), these compositional fluctuations developed to the immiscible phases of fcc-Cu, fcc-Co, and hcp-Co. The atomic diffusions of Co and Cu are even more difficult across the multiple phase (interdiffusion mechanism), thus, grain growth inhibition is expected. For instance, the samples annealed at 450°C showed a constant grain size of ~120 nm after annealing for 1-24 h. However, the grain boundary mobility is quiet high at 600°C, thus a more pronounced grain coarsening was observed here. The investigations in **section 5.6** shows that the grain growth exponent (n) dropped significantly at 600°C.

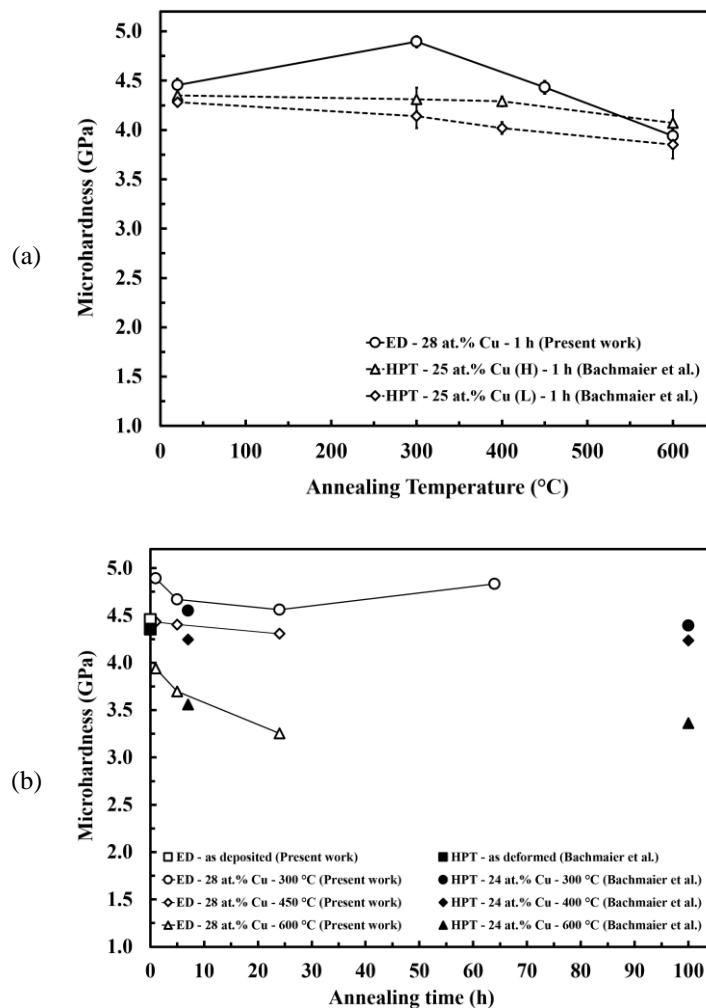


Figure 5.16 Microhardness profiles of PED-processed nanocrystalline Co-Cu (28 at.% Cu) upon isothermal annealing treatments compared with (a) HPT-processed nanocrystalline Co-Cu (25 at.% Cu) with high (H) and low (L) purity [13] and (b) HPT-processed ED nanocrystalline Co-Cu (24 at.% Cu) [29]. Pictures from [188].

Figure 5.16a,b show the microhardness profiles of PED- and HPT-processed nanocrystalline Co-Cu [13, 29] with nearly identical chemical composition at different isothermal annealing temperatures for various times. The grain sizes of PED- and HPT-processed [13, 29] nanocrystalline Co-Cu samples are ~23 nm and 90-100 nm, respectively, and they exhibit a supersaturated solid solution with fcc structure. **Figure 5.16a,b** show that the microhardness of PED-processed nanocrystalline Co-Cu is slightly higher than HPT-processed materials. Grain boundary strengthening (Hall-Petch) is possibly the reason for a higher microhardness in PED-processed nanocrystalline Co-Cu.

Figure 5.16a shows a significant increase of hardness in PED-processed nanocrystalline Co-Cu at 300°C during a short annealing time of 1 h due to spinodal decomposition, which is difficult to observe in HPT-processed materials [13]. A larger area of grain boundaries in PED-processed nanocrystalline Co-Cu, i.e. the grain size is 3-4 times smaller than in HPT-processed materials, may have a contribution for fast spinodal decomposition and formation of “precipitates” at the grain boundaries. These “precipitates” are effective for pinning grain boundaries and hindering grain coarsening at low annealing temperatures. Grain growth inhibition may be contributed also by spinodal decomposition within individual grains. However, these “precipitates” and spinodal decomposition are not effective for hindering a significant grain coarsening at 450°C, whereas the grain sizes increased to ~120 nm after 1 h of annealing time (see **Section 5.2**). Interestingly, the hardness can be maintained at the same level with the as-deposited state (see **Section 5.2**). It is believed that a competition between softening (grain coarsening) and hardening (spinodal and phase decomposition) occurs at 450°C, thus a significant decrease of hardness can be hindered. This phenomenon may be observed also in HPT-processed nanocrystalline Co-Cu after annealing at 400°C for 1 h, whereas a significant decrease of microhardness was not observed here as shown in **Figure 5.16a**. However, the hardness of PED- and HPT-processed nanocrystalline Co-Cu drops significantly after annealing at 600°C for 1 h, showing a high grain boundary mobility in these types of materials.

Figure 5.16a shows microhardness evolution of PED- and HPT-processed nanocrystalline Co-Cu [29] upon long-term isothermal annealing at different temperatures. Overall, it can be concluded that PED-processed nanocrystalline Co-Cu exhibits a better thermal stability compared with HPT-processed material at annealing temperatures up to 450°C. The improvement could be influenced by some factors. *First*, the grain size of PED-processed nanocrystalline Co-Cu is three to four times smaller than HPT-processed materials, thus, this material exhibits a larger area of grain boundaries and triple-junctions. Of course, a larger area of grain boundaries exhibits also a higher driving force for grain growth, but the grain growth

inhibition caused by grain boundary free-volume and vacancy drags [126, 127] and limited mobility of triple junctions [126, 127] have been reported elsewhere. In nanocrystalline Co, improvement on the thermal stability was reported through the grain size reduction from 20 nm to 8 nm [23]. *Second*, PED- and HPT-processed nanocrystalline Co-Cu have almost identical amount of Cu solutes atoms, which has a significant impact for grain stabilization. In the PED-processed materials, solute drag effect may be contributed also by the segregation of sulphur, which is possibly co-deposited during material processing. Organic additives were used in the deposition process (2 g/L saccharin and 0.2 g/L sodium dodecyl sulphate) could be the source for sulphur. El-Sherik et al. [115] reported co-deposition of ~1000 ppm of sulphur in nanocrystalline Ni in the presence of 2 g/L saccharin in a bath electrolyte, and it had a significant improvement of thermal stability [101]. Improvement on the thermal stability with segregation of sulphur was also reported in nanocrystalline Co [23]. In the present work, however, investigation on the effect of impurities content on the thermal stability was not a focus area for investigation. *Last*, in the PED-processed nanocrystalline Co-Cu, early spinodal decomposition and formation of “precipitates” due to a larger grain boundary area are expected for inhibition of grain growth at annealing temperatures up to 450°C. All in all, an improved thermal stability in PED-processed nanocrystalline Co-Cu compared to HPT-processed materials could be influenced by some factors, these are: (i) a smaller grain size, (ii) additional solute atoms, and (iii) early spinodal decomposition and formation of “precipitates”.

Chapter 6 – Micro-mechanical Properties

Statement: Some results in this chapter have been published in international journal (see Reference [188]) and conference proceeding (see Reference [189]).

6.1. Static micro-bending behaviour

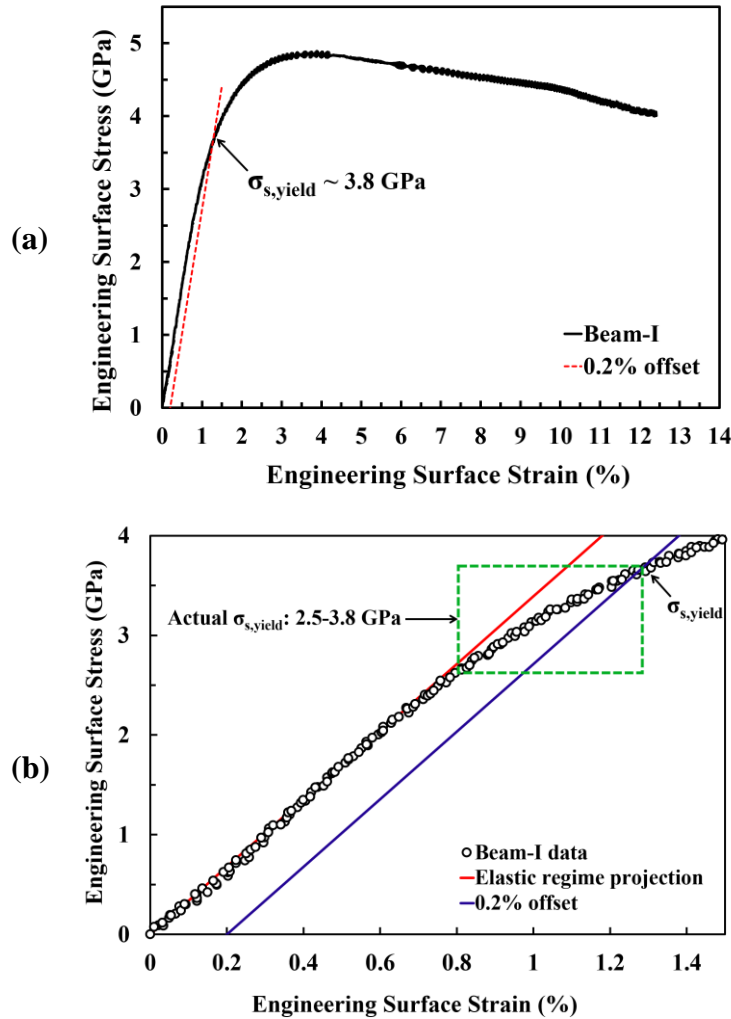


Figure 6.1 (a) Engineering surface stress vs.- strain curve of micro beam-I (black solid line) tested through the static bending test at surface strain rate of $1.24 \times 10^{-2} \text{ s}^{-1}$. Red dashed line is 0.2% offset for determination of yield stress (from [188]). (b) Detailed picture of the elastic to plastic transition shows a smooth transition regime (black solid circle). Red and blue solid lines represent elastic regime projection and 0.2% offset, respectively. The actual yield strength lays at some point marked within the green dashed box (from [188]).

Investigations on the strength of PED-processed nanocrystalline Co-Cu (28 at.% Cu) were performed through static micro bending tests. The free standing micro beam (beam-I) has a length (L), width (W), thickness (T), and bending length (L_B) of 15.77 μm , 6.75 μm , 5.26 μm ,

and 13.92 μm , respectively. A schematic picture of a micro beam-I is shown in **Figure 3.3c**. The static micro bending test of beam-I was carried out at a strain rate of $1.24 \times 10^{-2} \text{ s}^{-1}$ and its engineering surface stress vs.- strain curve is shown in **Figure 6.1a**. According to elastic bending beam theory, the surface stress-strain curve obtained through the bending test is only accurate up to the yield stress due to inhomogeneous deformation after the yield point. As a consequence, some parameters (e.g. strain hardening coefficient, ultimate strength, and surface strain to fracture) cannot be determined accurately from a surface stress-strain curve. In the present work, the discussion is focussed only up to the yield point.

The yield strength of PED-processed nanocrystalline Co-Cu (28 at.% Cu) is determined from surface stress-strain curve by using the 0.2% offset method (see **Figure 6.1a**). Determination shows that the yield strength of micro beam-I is ~ 3.8 GPa. The yield strength is extremely high compared to other nanocrystalline Co-Cu [16, 31], but the actual yield strength is expected to be lower due to inhomogeneous deformation in the bending test. During initial deformation stage, the whole micro beam is not experienced a uniform plastic deformation, whereas it occurs only at a small surface layer of the micro beam. According to **Figure 6.1b**, exact determination of the yield point is difficult due to the smooth transition of the elastic-plastic regime. **Figure 6.1b** shows that the actual yield strength places between 2.5-3.8 GPa. For comparison, the yield strength can be approximated also from microhardness measurement by using the Tabor's rule [212], whereas the yield of material is approximately one a third of the microhardness value. According to the Tabor's rule, the yield strength of nanocrystalline Co-Cu (28 at.% Cu) is ~ 1.5 GPa.

A secondary electron (SE) image of the side surface of micro beam-I (**Figure 6.2a**) shows plastic deformation with no crack formation. In addition, **Figure 6.2b** shows a clear necking effect at the top surface of micro beam-I due to tensile loading (marked with white arrows). On the other hand, the lower-part of the micro beam is experienced compression loading (marked with red arrows). According to these evidences (i.e. surface stress-strain curve and surface morphology), the micro beam of nanocrystalline Co-Cu (28 at.% Cu) exhibits ductile behaviour. Caused by the significant surface roughness formed during plastic deformation, microstructure observation by using the BSE detector is difficult. At two different positions (marked with zone-A and zone-B in **Figure 6.2a**), the surface was polished by using the focussed ion beam (FIB) to produce a smooth surface which is suitable for BSE imaging. **Figure 6.2c,d** depict BSE images of the microstructure at zone-A and zone-B showing no microstructural changes (e.g. grain coarsening) at the area experiencing the most significant plastic deformation.

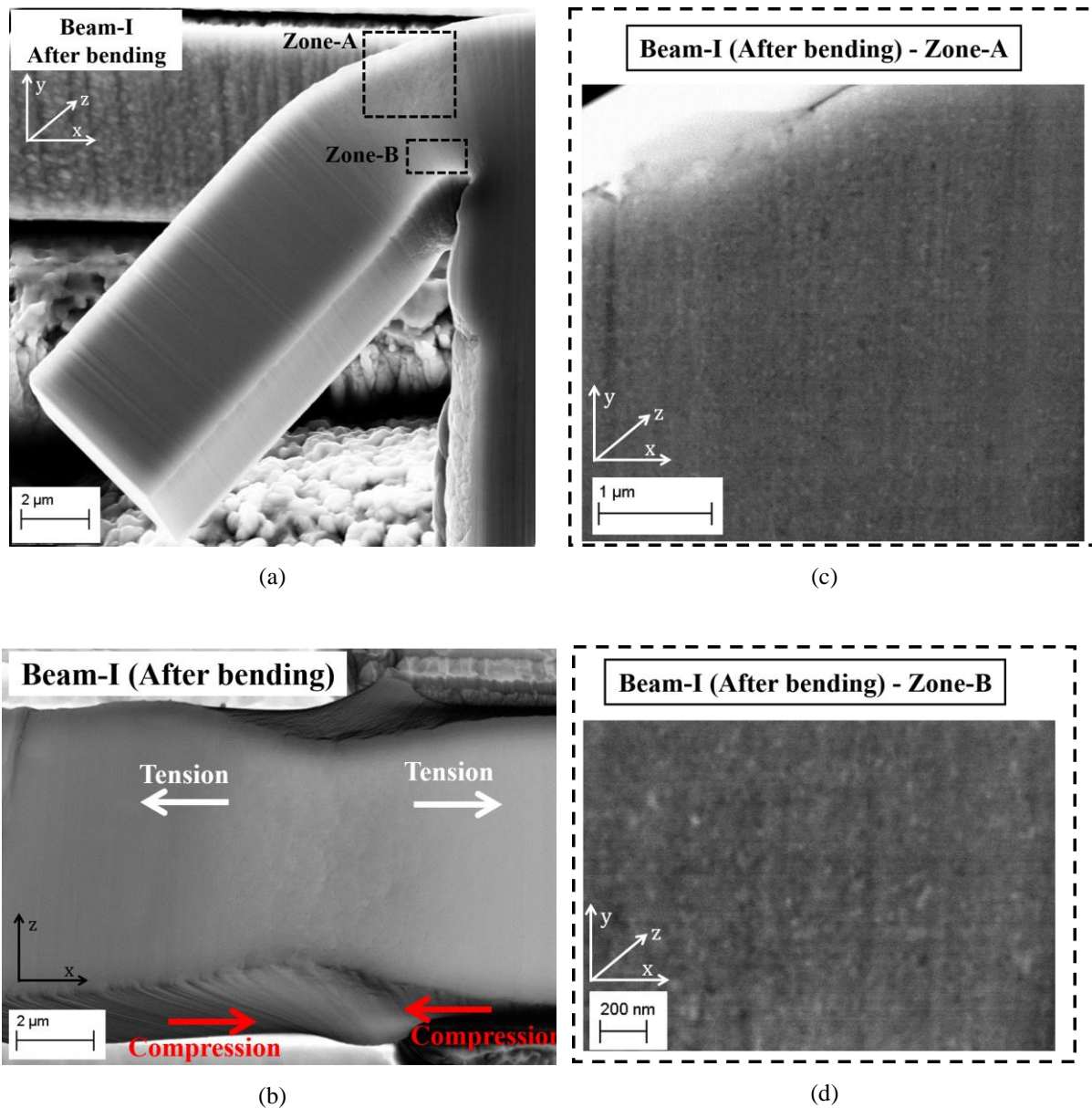


Figure 6.2 (a-b) Secondary electron (SE) images show (a) top and (b) side surfaces of micro beam-I after bending deformation (from [188]). **(c-d)** Back-scattered electron (BSE) images of microstructure were observed at two different positions marked with a black dashed box in Fig (a) namely (c) zone-A and (d) zone-B (from [188]).

The micro beam-I of nanocrystalline Co-Cu (28 at.% Cu) exhibits a much higher yield strength compared to bulk nanocrystalline pure Co [39, 40, 114]. According to works by Koch and his colleagues, a very high yield strength and ductility in nanocrystalline materials can be achieved by removing processing flaws (i.e. mainly pore's formation) as observed from subsample of in-situ consolidated nanocrystalline Cu [173, 176]. In the present work, secondary electron (SE) images of surface morphology of micro beam-I depict a very smooth surface with no pores visible in the initial condition (see **Figure 6.3a,b**). This can be a strong indication that micro beams of nanocrystalline Co-Cu are free from porosity-type processing flaws due to the small volume of samples, which have an impact on enhancement of strength. The Hall-Petch

effect (grain boundary strengthening) has a strong contribution on the strengthening mechanism of nanocrystalline materials, mainly in single component and pure nanocrystalline materials. The additional strengthening mechanism in the PED-processed nanocrystalline Co-Cu (28 at.% Cu) is caused by solid solution strengthening and (i.e. for the annealed sample) spinodal decomposition and precipitation hardening.

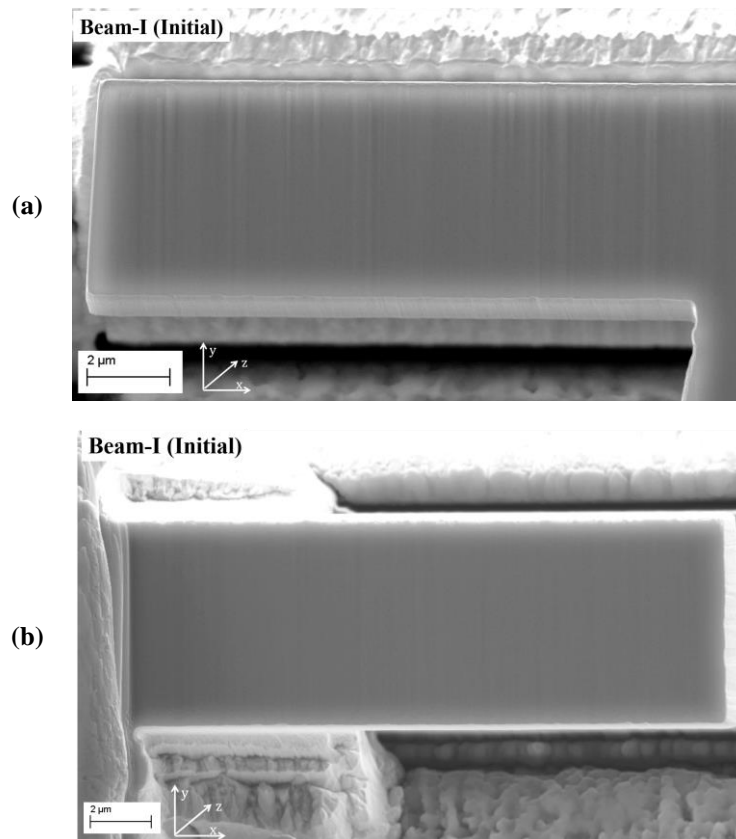


Figure 6.3 Secondary electron (SE) images of surface morphology show initial condition of (a) side and (b) top surfaces of micro beam-I.

The high yield strength in PED-processed nanocrystalline Co-Cu (28 at.% Cu) may be also attributed to a higher cobalt concentration. For instance, the HPT-processed nanocrystalline Co-Cu (74 at.% Cu) exhibits a lower tensile yield strength ($\sigma_y \approx 0.8$ GPa) [16]. Here, the mechanical test method may also have a contribution to the different values of yield strength. In the present work, type and number of lattice defects (e.g. dislocations and twins) may also have a significant impact on mechanical properties, which can be different in the PED- and HPT-processed nanocrystalline Co-Cu. In the HPT-process, dislocations formation is dominantly influenced by a large applied plastic strain during material processing [144]. On the other hand, dislocations formation in the PED-process are possibly contributed by two mechanisms: (i) stress generation and relaxation when the pulsed current on and off, respectively [102, 103,

178], and (ii) growth inhibition from chemical additives [104, 145, 146]. As a consequence, dislocation densities and types of dislocations (e.g. immobile dislocations) in the HPT- and PED-process may be different. Gubicza et al. showed that DC-electrodeposition nanocrystalline Ni-Mo exhibited a higher dislocation density and twin fault probability than the HPT-processed material [147]. The increase of dislocation density and twin fault probability are expected to be higher in PED-process instead of DC-electrodeposition as shown by Lu et al. [44, 179, 180]. Grain inhibition by the chemical additives also has a contribution on the formation on twins [145, 104]. BF-TEM image of as deposited nanocrystalline Co-Cu (28 at.% Cu) detects a number of twins as shown in **Figure 5.1a** which is not detected in the HPT-processed nanocrystalline Co-Cu [13, 16, 27]. To conclude, the strength enhancement in the PED-processed nanocrystalline Co-Cu (28 at.% Cu), particularly for micro-size bending beam, may be contributed by several factors: (i) solid solution strengthening, (ii) a number of twins, (iii) dislocation density, (iv) degree of porosity, and (v) co-deposition of impurity elements (e.g. sulphur and carbon).

6.2. Cyclic micro-bending behaviour

The microstructural and mechanical stabilities of the PED-processed nanocrystalline Co-Cu (28 at.% Cu) under cyclic micro-bending test were investigated. Four free standing micro bending beams with identical dimension were subjected to displacement controlled of cyclic bending tests at low, moderate, and high plastic strain amplitudes ($\epsilon_{s,a}$) for different number of load cycles (N). A schematic picture of one micro beam is shown in **Figure 3.3d**. The actual micro beams dimension and the test parameters are shown in **Table 6.1**.

Table 6.1 The actual micro beam dimensions, where L, W, T, L_B are the length, width, thickness, and bending length. Cyclic micro bending tests were performed at various plastic strain amplitude ($\epsilon_{s,a}$) for different number of cycles (N).

Name of Sample	L (μm)	W (μm)	T (μm)	L_B (μm)	Plastic strain amplitude	Cycle
Beam-II (low $\epsilon_{s,a}$)	15.66	7.06	5.47	13.09	1.0×10^{-4}	7500
Beam-III (low $\epsilon_{s,a}$)	15.43	6.68	4.92	14.00	1.8×10^{-4}	5000
Beam-IV (moderate $\epsilon_{s,a}$)	15.52	6.51	4.92	13.54	4.0×10^{-4} (Stage-I)	2000
					6.5×10^{-4} (Stage-II)	2000
					1.5×10^{-3} (Stage-I)	35
Beam-V (high $\epsilon_{s,a}$)	15.77	6.75	5.26	13.92	2.0×10^{-3} (Stage-II)	65
					3.5×10^{-3} (Stage-III)	40
					7.0×10^{-3} (Stage-IV)	100

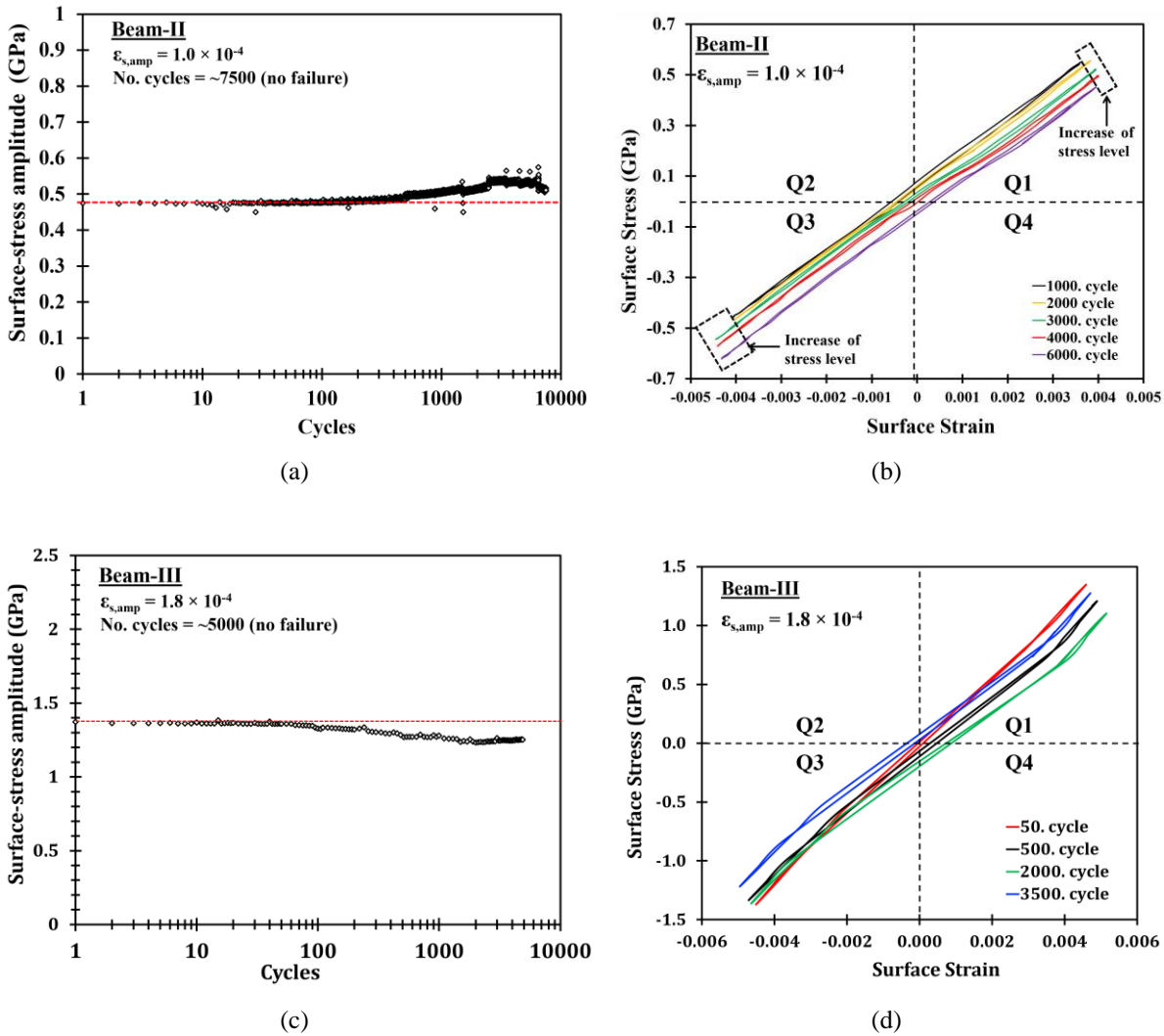


Figure 6.4 (a,c) Surface-stress amplitude as a function of load cycles at different plastic surface-strains amplitudes of (a) $\epsilon_{s,amp} = 1.0 \times 10^{-4}$ (beam-II) and (c) $\epsilon_{s,amp} = 1.8 \times 10^{-4}$ (beam-II) (from [188]). (b,d) Cyclic hysteresis loops of (b) micro beam-II ($\epsilon_{s,amp} = 1.0 \times 10^{-4}$) and (d) micro beam-III ($\epsilon_{s,amp} = 1.0 \times 10^{-4}$) at selected load cycles.

Cyclic bending test of micro beam-II was conducted at a low plastic surface-strain amplitude ($\epsilon_{s,a}$) of 1.0×10^{-4} for 7500 load cycles. No crack formation is detected after 7500 load cycles. The test cannot be performed for more prolonged cycles due to a system failure, which damaged the micro bending beam. **Figure 6.4a** shows the surface-stress amplitude of micro beam-II as a function of load cycles. At the first 500 load cycles, the stress amplitude level is ~490 MPa which is proportional to ~12% of the yield stress (i.e. yield stress is assumed to be 3.8 GPa). The stress amplitude level remains constant at ~490 MPa for 500 load cycles, but it tends to increase gradually up to ~550 MPa from the ~500th to ~6000th load cycles. The cyclic hysteresis loops of micro beam-II at selected numbers of load cycles (1000th - 6000th) were plotted for a more detailed view as shown in **Figure 6.4b**. The increase of stress amplitude is more pronounced after ~2000 load cycles as marked in **Figure 6.4b**. The increase of stress

(i.e. called as cyclic hardening effect) may be attributed to spinodal decomposition or dislocation processes during cyclic loading. It is believed that spinodal decomposition is affected by the accumulated plastic strains and local plastic deformations during cyclic loading. This phenomenon has not been observed in the previous works and other nanocrystalline systems, thus, this could be something new in nanocrystalline materials. However, further observation on the spinodal decomposition through atom probe tomography (APT) is not possible due to the highly damaged micro beam caused by a system failure.

The cyclic bending test of micro beam-III was performed at a medium to low plastic surface-strain amplitude ($\epsilon_{s,a}$) of 1.8×10^{-4} for 5000 load cycles. Crack formation is not observed after 5000 load cycles. The surface-stress amplitude level at different load cycles and the selected cyclic hysteresis loops at this strain amplitude are shown in **Figure 6.4c,d**. The stress amplitude level at this strain is proportional to ~35% of the yield stress (i.e. yield stress is assumed 3.8 GPa). In contrast to micro beam-II, the stress amplitude level decreases slightly after 100 load cycles showing a softening effect in micro beam-III (see **Figure 6.4c**). The elastic modulus is also found to be altered after 100 load cycles (see **Figure 6.4d**). BSE images of initial (**Figure 6.5a**) and final (**Figure 6.5b**) microstructures show a slight grain coarsening after 5000 load cycle as marked within red dashed lines in **Figure 6.5b**. It is believed that grain coarsening have a strong contribution on the softening effect in nanocrystalline Co-Cu. According to Kapp et al. [183] and Muhlstein et al. [184], grain boundary migration in nanocrystalline and ultrafine grained materials is possible during cyclic loading, which may be attributed to the accumulation of plastic strain mainly at high-angle grain boundaries.

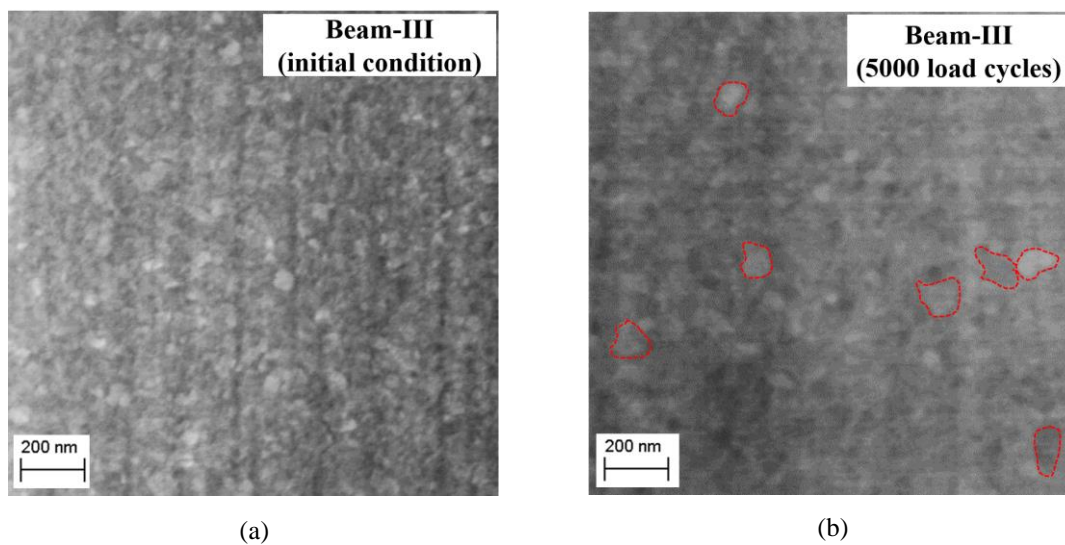
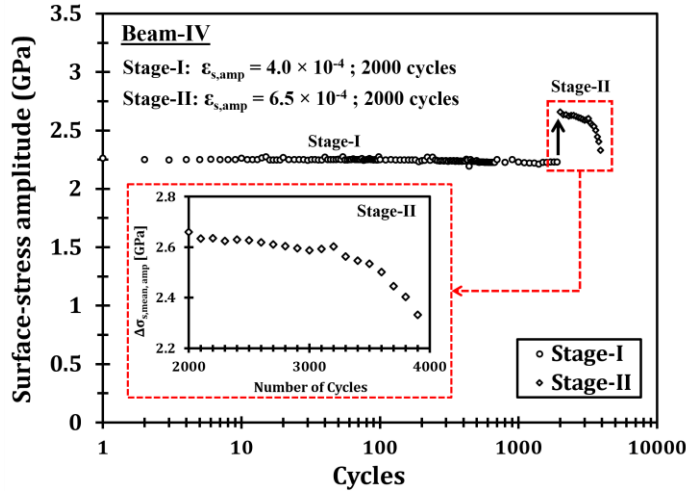
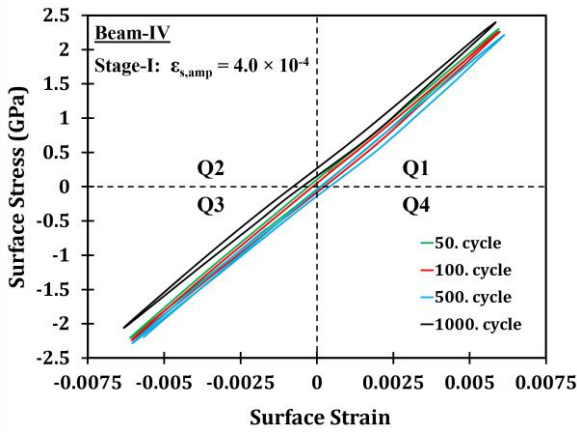


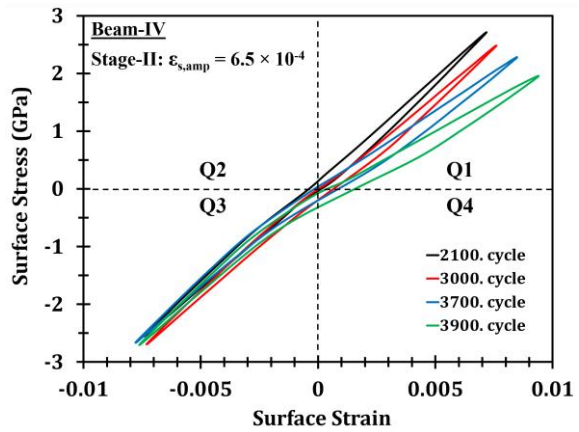
Figure 6.5 Back-scattered electron (BSE) images of microstructure observed from the same position at a side surface of micro beam-III: (a) initial condition and (b) after 5000 load cycles (from [188]). Magnifications are similar for these two pictures.



(a)



(b)



(c)

Figure 6.6 (a) Surface-stress amplitude as a function of load cycles of micro beam-IV at two different stages of plastic surface-strains amplitude of $\epsilon_{s,amp} = 4.0 \times 10^{-4}$ (stage-I) and $\epsilon_{s,amp} = 6.5 \times 10^{-4}$ (stage-II) (from [189]). (b,c) Cyclic hysteresis loops of micro beam-IV at selected cycles at different plastic surface-strain amplitudes of (b) $\epsilon_{s,amp} = 4.0 \times 10^{-4}$ (stage-I) and (c) $\epsilon_{s,amp} = 6.5 \times 10^{-4}$ (stage-II) (from [189]).

The cyclic micro bending test of micro beam-IV was conducted at two stages of medium plastic surface-strain amplitudes ($\epsilon_{s,a}$): (i) stage-I = 4.0×10^{-4} for 2000 load cycles, and (ii) stage-II = 6.5×10^{-4} for additional 2000 load cycles. **Figure 6.6a** shows a constant stress amplitude level in stage-I for the first 2000 load cycles. Cyclic hysteresis loops at selected cycle numbers of stage-I (**Figure 6.6b**) show no significant change of stress level nor elastic modulus. A crack formation and surface damage are not detected after the 2000 load cycles of stage-I. In contrast to stage-I, cycling in stage-II ($\epsilon_{s,a} = 4.0 \times 10^{-4}$) leads to formation of a crack. **Figure 6.6a** shows that the stress amplitude level starts to decline after the 3000th of load cycle (i.e. after 1000 load cycles in stage-II) which could be an indication of crack formation. The decreases of stress level and elastic modulus in the positive displacement deflection (Q1) are more pronounced in the following load cycles (see **Figure 6.6c**) indicating crack propagation.

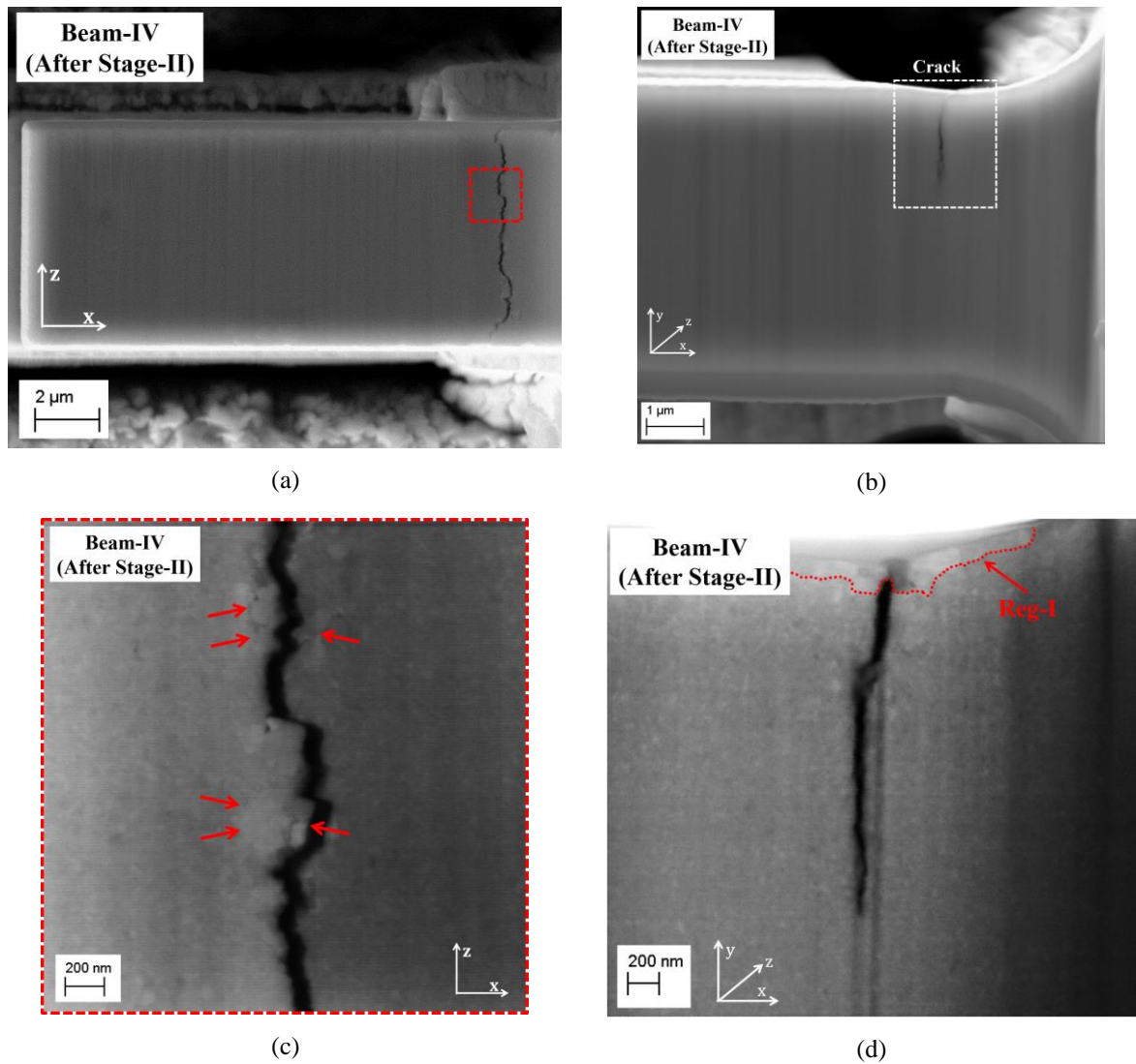


Figure 6.7 (a,b) Secondary electron (SE) images of micro beam-IV that show a crack formation after 4000 load cycles observed at (a) top and (b) side surfaces of the micro beam (from [189]). (c,d) Back-scattered electron (BSE) images of the microstructure at the area adjacent to the crack observed at (b) top surface (marked with red dashed rectangular in (a)) and (c) side surface (marked with white dashed rectangular in (b)) (from [189]).

SE images of micro beam-IV (see **Figure 6.7a,b**) show the formation of a crack with ~ 1.5 μm length in the upper-part of the micro beam. BSE image of the microstructure at a top surface of micro beam-IV shows some ultrafine grain (ufg) structures at the crack flanks (marked with red arrows in **Figure 6.7c**). It is believed that grain coarsening has a contribution to crack initiation by the following mechanisms: In the initial stage, the accumulated plastic strains lead to the coarsening of several grains (i.e. formation of ufg structures). According to the Hall-Petch effect, these ufg structures are found to have a lower strength compared to the surrounding nano-grains. As a result, strain localization is expected in these regions, in particular at the grain boundaries of ufg structures, which may lead to initiation of an intergranular crack as shown in **Figure 6.7c**. A microstructure investigation was also performed at the side surface of the micro

beam. Caused by the significant surface roughness, FIB polishing was performed at the side surface of the micro beam with a platinum coating at the top surface of the micro beam to prevent the curtaining effect. In the present work, FIB polishing caused also a grain coarsening at the transition regime of platinum coating and micro beam as marked with Reg-I in **Figure 6.7d**. Microstructure images at a selected area close to the crack (**Figure 6.7d**) shows no significant grain coarsening during crack propagation.

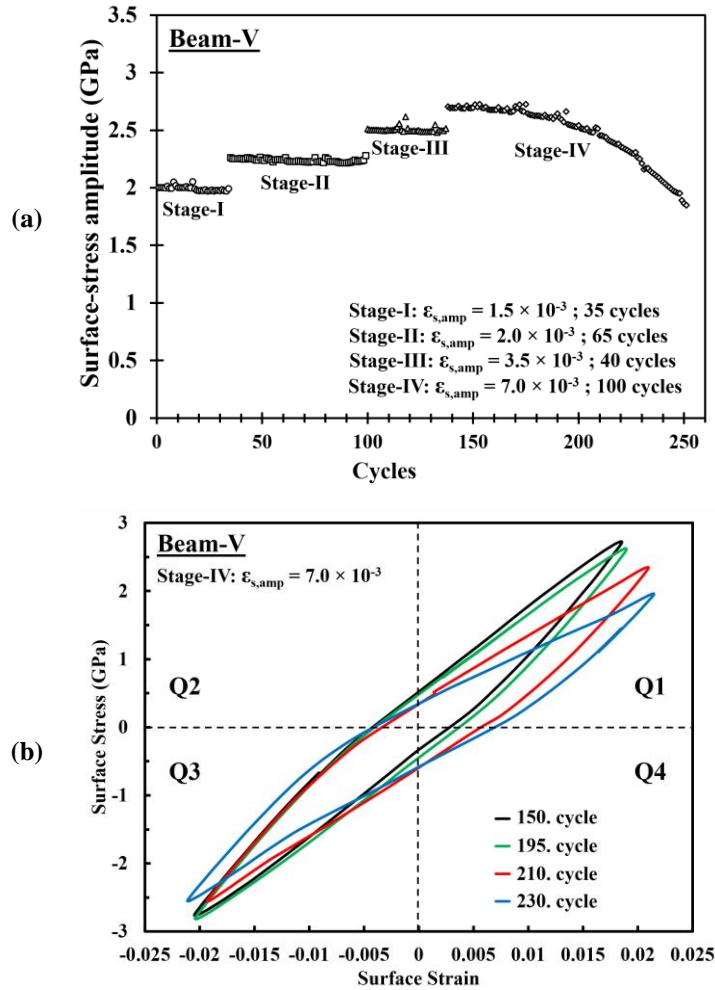


Figure 6.8 (a) Surface-stress amplitude as a function of load cycles at four different stages of plastic surface-strain amplitudes of micro beam-V (from [188]). **(b)** Cyclic hysteresis loops of micro beam-V at plastic surface-strain amplitude of stage-IV ($\epsilon_{s,amp} = 7.0 \times 10^{-3}$) at selected load cycles (from [188]).

The cyclic micro bending test of micro beam-V was conducted at four stages of high plastic surface-strain amplitudes ($\epsilon_{s,a}$): (i) stage-I = 1.5×10^{-3} for 35 load cycles, (ii) stage-II = 2.0×10^{-3} for 65 load cycles, (iii) stage-III = 3.5×10^{-3} for 40 load cycles, and (iv) stage-IV = 7.0×10^{-3} for 100 load cycles. **Figure 6.8a** shows the surface-stress amplitude level of all stages (I-IV) as a function of load cycles. The results show that the stress amplitude levels remain constant after cycling from stage-I to stage-III where no crack formation was observed. At

stage-IV, the stress amplitude level remains constant up to the 190th of load cycle, but it decreases significantly for the following load cycles. The selected cyclic hysteresis loops of stage-IV (**Figure 6.8b**) shows a small decrease of stress amplitude in the positive displacement region (Q1) after the 195th load cycle which may be ascribed to the formation of a first crack. The reduction of stress amplitude in Q1 is more pronounced after the 210th of load cycle, which may be attributed to propagation of the first crack. In addition, a small shift in negative displacement (Q3) is also detected after the 210th of load cycle, which may be ascribed to formation of a second crack. Propagation of the first and second crack is more evident after the 230th of load cycle indicated by large shifts of the stress amplitude in Q1 and Q3. SE image of micro beam-V (**Figure 6.9a**) shows that two cracks have been formed after cyclic loading at the upper and lower part of the micro beam with lengths of $\sim 0.75\ \mu\text{m}$ and $\sim 1.2\ \mu\text{m}$, respectively.

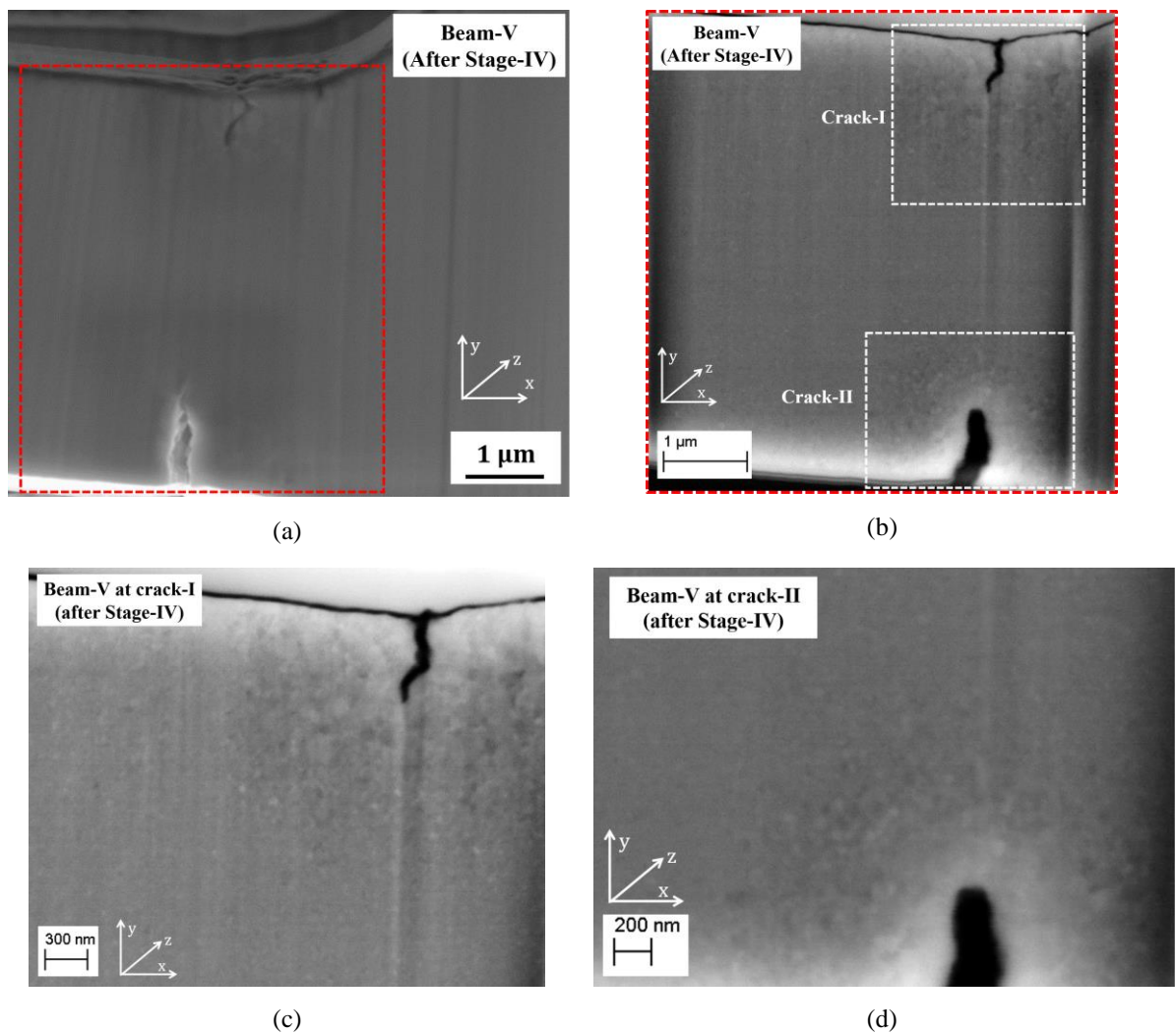


Figure 6.9 (a) Secondary electron image of micro beam-V that show cracks formation after four stages of cyclic bending from side-view (from [188]). (b,c) Back-scattered electron (BSE) images of microstructure at (b) the area marked with a red dashed rectangular shape in Fig (a) and the area adjacent to (c) crack-I and (d) crack-II marked with the white dashed rectangular shapes in Fig (b) (from [189]).

Microstructure observation were performed at a selected area (marked with red dashed rectangular in **Figure 6.9a**). The BSE image of the microstructure in this area shows significant grain coarsening next to crack-I and crack-II (see **Figure 6.9b**). **Figure 6.9c,d** show more detailed microstructure images in the area surrounding crack-I and crack-II revealing a quiet extensive region with an ultrafine grain structure. Grain coarsening in these region may be caused by the accumulation of high local plastic strain. The area surrounding the crack may exhibit higher local plastic strains compared to other positions due to stress and strain concentration at the crack tip during crack propagation (plastic zone). This accumulation of plastic strain can activate processes which increase grain boundary mobility or alter the driving force for grain boundary migration.

A spinodal decomposition of Co-Cu can also be expected through the accumulation of plastic strain. Two APT specimens were prepared from the area consisting of the ufg structure as shown in **Figure 6.9c**. However, the APT measurements were short due to an unstable sample and measurement process. The first (360,000 ions) and second (101,000 ions) reconstructions show a region with a high Co concentration of 88.81 at.% Co and 91.54% respectively. These Co concentrations are higher than the average concentration (72 at.% Co), which could be an indication of spinodal decomposition. However, this is just a first approach and the data set was very small to prove whether there is a decomposition. More analysis are needed for further measurements.

6.3. Discussion of the results in Chapter 6

The static bending test of the micro beam of supersaturated solid solution nanocrystalline Co-Cu (28 at.% Cu) showed a very high tensile strength up to 3.8 GPa and (possibly) high ductility, whereas the formation of a crack was not observed after the test. Some possible strengthening mechanisms have been proposed such as solid solution strengthening, a formation of twins, a high dislocation density, and low degree of porosity. It is believed that the small volume of micro beam, observing no porosity, has the strongest impact on a high yield strength in this material. It is believed that the yield strength of the bulk sample of nanocrystalline Co-Cu is much lower than 3.8 GPa due to a higher number of processing flaws (e.g. porosity). A work by Bachmaier et al. [16] found that the yield strength of the bulk samples of nanocrystalline Co-Cu (74 at.% Cu) are ~800 MPa. Regarding the hardness of the bulk sample of nanocrystalline Co-Cu (Tabor's rule), the yield strength of nanocrystalline Co-Cu (28 at.% Cu) is approximately 1.5 GPa. Thus, the actual yield strength of the bulk sample of nanocrystalline Co-Cu (28 at.% Cu) is predicted from 1.0 to 1.5 GPa.

The cyclic bending tests of the micro beams of nanocrystalline Co-Cu at the different plastic surface strain amplitudes showed different behaviours. The cyclic micro bending test at a low plastic surface strain amplitude (beam-II) showed a cyclic hardening effect with no crack formation observed. Spinodal decomposition and dislocation processes may have a contribution to the hardening effect. However, the phenomena was only observed by one sample, whereas more samples are needed for validation. The cyclic micro bending tests at a medium to low (beam-III) and medium (beam-IV) plastic surface strain amplitudes observed minor grain coarsening. In addition, the formation of a crack was observed in micro beam-IV, but microstructural changes during crack propagation (e.g. grain coarsening) was not observed. In contrast, the micro beam-V which was tested at a high plastic surface strain amplitude, showed the formation of two cracks and a significant grain coarsening in the area surrounding the cracks.

A large grain coarsening during crack propagation in micro beam-V may be attributed to one of these factors: (i) a high accumulation of plastic strains, and (ii) a large plastic strain amplitude. The calculations of accumulated plastic strains are performed by using the plastic surface strain amplitudes and the number of load cycles since the initiation of a first crack was possibly observed. The accumulated plastic strains for micro beam-IV and beam-V are 0.65 and 0.35, respectively. The calculations show that the accumulated plastic strains in micro beam-IV is slightly higher than micro beam-V. Thus, it is a strong indication that the accumulated plastic strains may have a low contribution to activate a large grain boundary migration. As a consequence, a large grain coarsening in micro beam-V is attributed to a high plastic strain amplitude. The applied plastic strain amplitude in micro beam-V is up to ~10 times higher compared to micro beam-IV, which may be high enough to activate grain boundary migration.

It is clear that grain boundary migration during crack propagation in micro beam-V is caused by the plastic strains, but the grain growth mechanism is still unclear. Three possible mechanisms are proposed to explain the possible grain growth mechanism. *First*, the plastic strains activate grain boundary migration through the atomic diffusion of Co and Cu. This mechanism was also observed in grain growth of nanocrystalline Co-Cu during isothermal annealing as described in **Chapter 5**. It is also believed that spinodal decomposition occurs during strain induces grain growth, but it needs further investigations. *Second*, deformation mechanism through grain rotation in this nanocrystalline Co-Cu cannot be excluded since the grain sizes are distributed from ~10 nm to ~55 nm. Moreover, this materials consist of a quite large number of grains with sizes of below 20 nm (~30%), which could be the starting grain

size for grain-boundary mediated deformation. In case of grain rotation occurs, there is a possibility for coalescence of some grains once the orientations of some adjacent grains are exactly similar. The phenomena of grain coalescence lead to the formation of elongated grain (grain coarsening) as illustrated in **Figure 2.15**. *Third*, dislocation shears induce grain boundary movement and migration. **Figure 6.10** depicts schematic illustration of dislocation motion in nanocrystalline materials. Dislocations are generated from the centre (point A) of grain-I (Frank-Read source) and they move along the slip plane to the boundary (point B). The dislocation motion is usually blocked at the boundary. Sometimes, dislocations are dissociated at this condition, whereas some parts of dislocations can move to the neighbouring grain and another parts of dislocation move along the boundary. If the number of moving dislocation at the boundary is high enough, it may results in dislocation shear. In nanocrystalline materials, grain boundaries have a high driving force for grain growth, thus, it is possible that dislocation shear activates grain boundary movement and even grain boundary migration (grain coarsening).

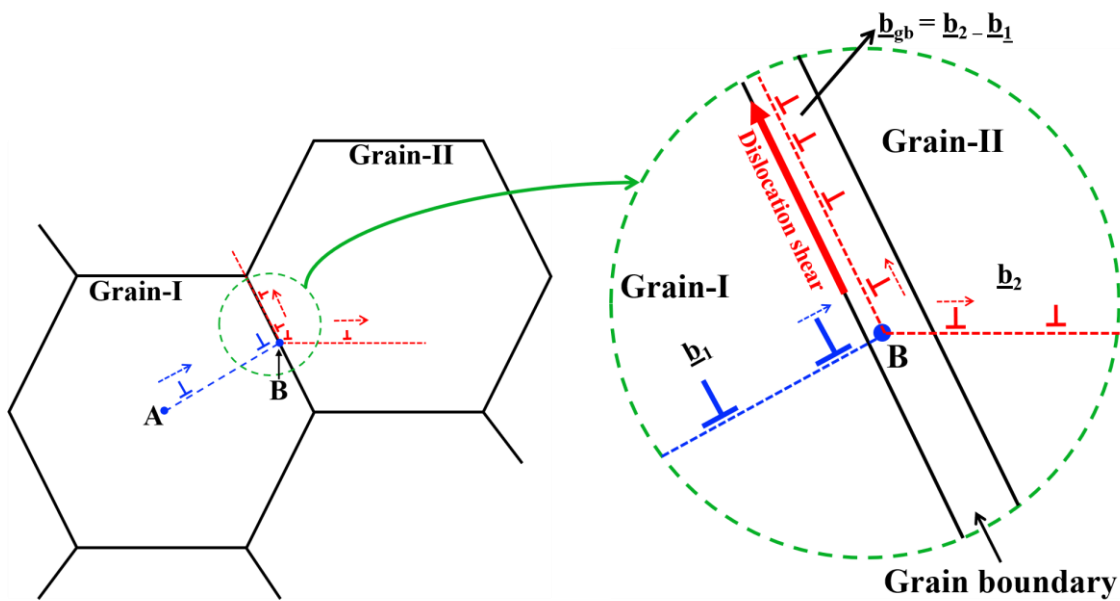


Figure 6.10 Schematic pictures illustrating dissociation of dislocations at the boundary (point B), whereas some parts of dislocations move to a neighbouring grain (grain-II) and another parts of dislocations move along the boundary. Dislocations movement along the boundary may result in dislocation shear (marked with red solid arrow).

Chapter 7 – Strength and ductility of bulk nanocrystalline Co-Cu

Statements: Some results in this chapter have been published in international journal (see Reference [194]).

7.1. Effect of pulsed deposition parameters

Tensile tests of PED-processed nanocrystalline Co-Cu were performed by using Dep-II samples having a surface area of $21 \times 21 \text{ mm}^2$ and a minimum thickness of $\sim 750 \text{ }\mu\text{m}$. According to the results in **Chapter 4**, pulsed deposition of compact and homogeneous Dep-II sample must be conducted at the following deposition parameters: (i) pulse current densities of $750\text{-}1000 \text{ A/m}^2$, (ii) duty cycle of $10\%\text{-}20\%$, and (iii) pulse-on time of $0.3\text{-}0.5 \text{ ms}$. In this section, the effects of deposition parameters on the tensile strength and ductility of bulk nanocrystalline Co-Cu were investigated. The deposition parameters and chemical composition of individual samples are summarized in **Table 7.1**. The results show that deposition parameters have a significant impact on the chemical composition, whereas the concentration of Cu increases with decreasing duty cycle, current density, and pulse-on time. Concentration of Cu is also expected to have a contribution on strength and ductility of nanocrystalline Co-Cu which is discussed further in the present work.

Table 7.1 Pulsed electrodeposition (PED) parameters which were used to produce tensile samples of nanocrystalline Co-Cu with different chemical composition. Deposition time is calculated by assuming a current efficiency of 85% and a deposit thickness of $\sim 750 \text{ }\mu\text{m}$. Chemical composition of Co and Cu elements were measured through energy dispersive spectroscopy (EDS) (from [194]).

Sample name	Pulsed deposition parameters				Composition	
	Pulsed current density (A/m^2)	Duty cycle (%)	Pulsed-on time (ms)	Deposition time (h)	Co (at.%)	Cu (at.%)
TS-1	1000	20.0	0.5	35	87.1 ± 0.1	12.9 ± 0.1
TS-2	1000	17.5	0.5	40	85.6 ± 0.1	14.4 ± 0.1
TS-3	800	17.5	0.5	50	80.3 ± 0.1	19.7 ± 0.1
TS-4	1000	17.5	0.3	40	82.8 ± 0.1	17.2 ± 0.1
TS-5	1000	15.0	0.5	46	83.0 ± 0.1	17.0 ± 0.1
TS-6	1000	12.5	0.5	56	81.7 ± 0.1	18.3 ± 0.1
TS-7	1000	10.0	0.5	70	78.3 ± 0.1	21.7 ± 0.1
TS-8	1000	10.0	0.3	70	80.1 ± 0.1	19.9 ± 0.1

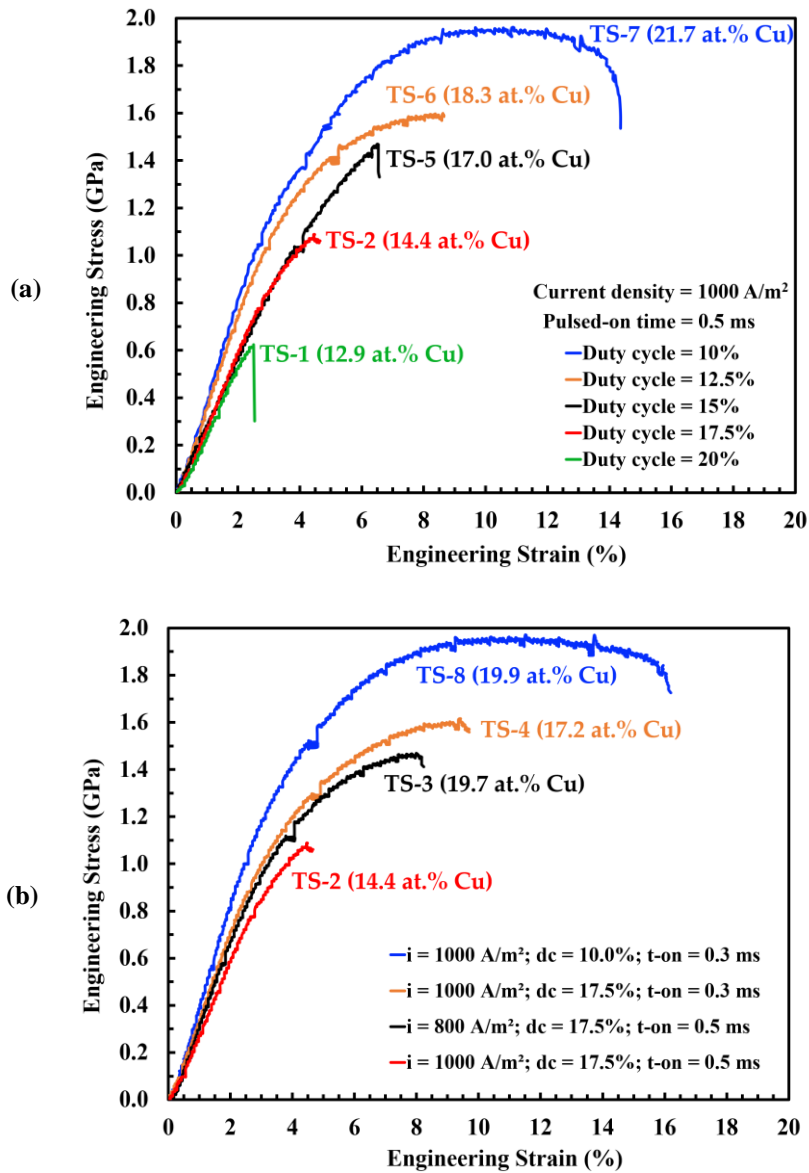


Figure 7.1 Engineering stress vs. strain curves of tensile tests of different nanocrystalline Co-Cu samples (TS1-TS8) at a strain rate of $1.0 \times 10^{-3} \text{ s}^{-1}$. (a) Effect of duty cycle and (b) effect of current density (i) and pulse-on time (t_{on}) (from [194]).

Figure 7.1a,b depict engineering stress vs. strain curves of tensile tests of bulk nanocrystalline Co-Cu samples at a strain rate of $1.0 \times 10^{-3} \text{ s}^{-1}$. Detailed information of mechanical properties of individual samples such as yield stress (σ_y), ultimate tensile stress (σ_u), and fracture strain (ϵ_f) are summarized in **Table 7.2**. The strain was measured from the tensile test machine cross-head displacement with no additional equipment used (e.g. extensometer) due to the small gauge dimension. Of course, the strain measurement is not perfectly accurate for the measurement of the modulus of elasticity, thus, the exact number of elastic modulus is not included in **Table 7.2**. However, the measured strain is accurate enough for the fracture strain measurement.

Table 7.2 Tensile sample thicknesses and mechanical properties parameters of nanocrystalline Co-Cu synthesized at different deposition parameters. Two samples were mechanically tested except for samples TS-1, TS-5, TS-6, and TS-7 (from [194]).

Sample name	Thickness (mm)	Mechanical properties		
		Yield stress (GPa)	Ultimate stress (GPa)	Fracture strain (%)
TS-1*	0.41		Fail at 0.62	2.54
TS-2	0.54	0.91 ± 0.06	1.20 ± 0.03	4.57 ± 0.05
TS-3	0.53	0.95 ± 0.05	1.51 ± 0.04	8.26 ± 1.26
TS-4	0.52	1.03 ± 0.02	1.55 ± 0.03	8.71 ± 0.47
TS-5*	0.53	1.05	1.47	6.57
TS-6*	0.35	1.10	1.59	8.65
TS-7*	0.42	1.20	1.95	14.36
TS-8	0.40	1.21 ± 0.08	1.98 ± 0.03	15.95 ± 0.09

The effect of duty cycle on the stress-strain curve characteristics of nanocrystalline Co-Cu are shown in **Figure 7.1a**, while the detailed information can be found in **Table 7.2**. Pulse current density and pulse-on time were kept constant at 1000 A/m² and 0.5 ms, respectively. The lowest strength and ductility are observed in the tensile sample-1 (TS-1), which was deposited at the highest duty cycle of 20%. The yield point is not even reached in TS-1 due to early fracture as an indication of brittle behaviour. Slight improvement of strength and ductility is obtained by reducing the duty cycle to 17.5% (TS-2). The yield stress of TS-2 is 0.91 ± 0.06 GPa, while the fracture strain is almost twice times higher (4.57 ± 0.05 %) than of TS-1, but the fracture strain remains below 5%. Significant improvements of strength and ductility is achieved by reducing the duty cycle to 15% and 12.5% as shown in samples TS-5 and TS-6. These samples exhibit identical yield stresses of 1.05 GPa (TS-5) and 1.10 GPa (TS6), while a slightly higher ultimate tensile stress is observed in a TS-6. The fracture strain of TS-6 (8.65%) is higher than of TS-5 (6.57%). Secondary electron (SE) images of the surface morphology of TS-5 and TS-6 (**Figure 7.2a,b**) show crack paths oriented at ~40° toward loading direction, which is a typical characteristic of ductile fracture. The necking effect is also detected in TS-6 (see **Figure 7.2b**) as an additional indication of ductile fracture. The highest strength and ductility are observed in TS-7 (duty cycle of 10%). The yield stress and ultimate tensile stress of TS-7 are 1.20 GPa and 1.95 GPa, respectively. The fracture strain of TS-7 is 14.36% and this number is very high compared to previous work in nanocrystalline Co-Cu [16, 31]. A significant necking effect is also found in a TA-7 as shown in **Figure 7.2c**. In addition, SE image of the fracture surface of TS-7 (**Figure 7.2d**) depicts a ductile fracture surface with dimple structures size of 50-300 nm.

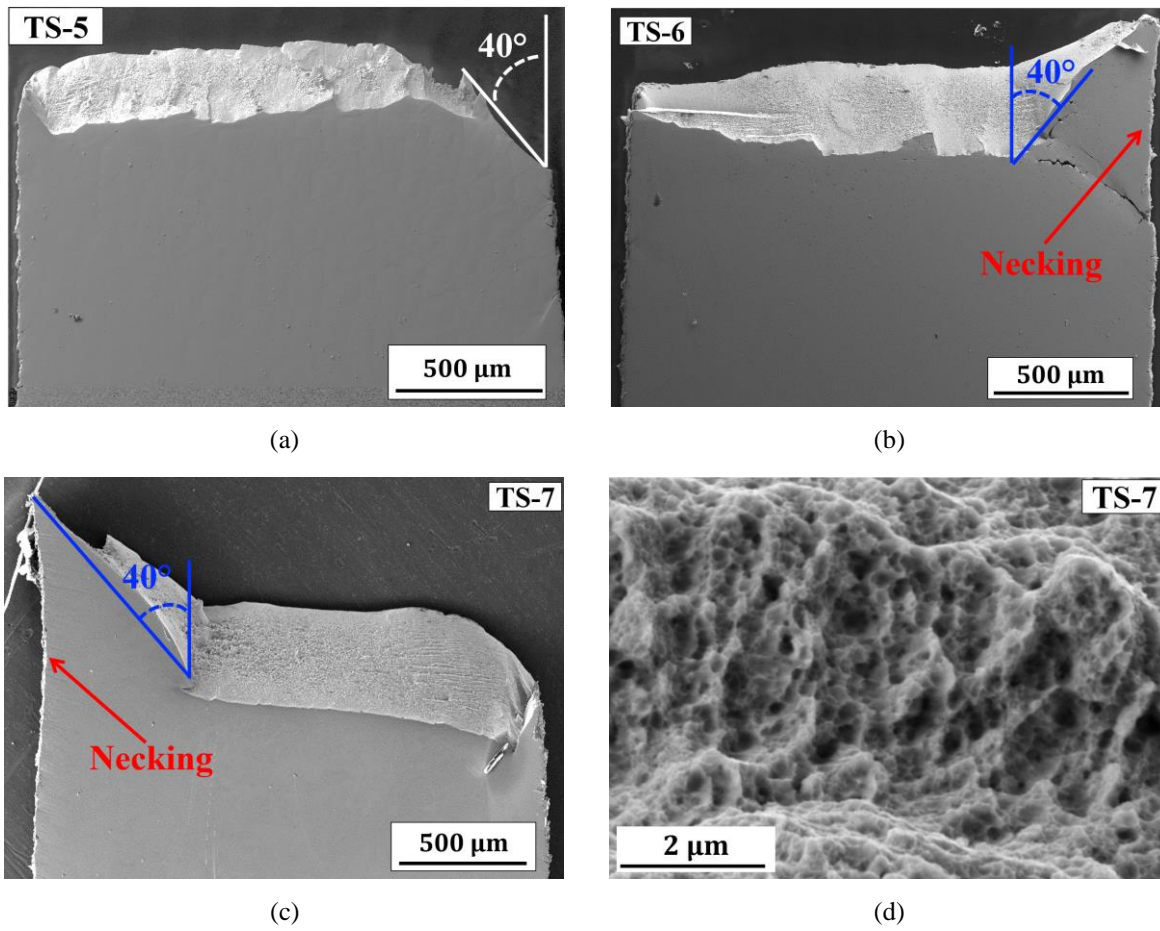


Figure 7.2 (a-c) Secondary electron images of surface morphology of (a) TS-5, (b) TS-6, and (c) TS-7 after tensile deformation. (d) Secondary electron images of fracture surface of TS-7.

The Effect of pulse current density and pulse-on time on the stress-strain curves of nanocrystalline Co-Cu are shown in **Figure 7.1b**, while detailed information can be found in **Table 7.2**. Three samples (TS-2, TS-3, and TS-4) were deposited at the same duty cycle of 17.5%, which resulting in a different fracture behaviour. Comparing with the brittle TS-2, a significant enhancement of strength and ductility is achieved through reduction of pulse current density (TS-3) and pulse-on time (TS-4). Both samples (TS-3 and TS-4) have an identical ductility with fracture strains of over 8%. The yield stress and ultimate tensile stress of TS-3 are slightly lower compared to TS-4, which may be attributed to larger grain sizes due to deposition at lower pulsed current density. The surface morphology image of TS-2 (**Figure 7.3a**) shows fracture at the shoulder instead of the gauge section. The fracture behaviour of TS-2 is supposed to be brittle as indicated by the absence of necking and shearing. In contrast, surface morphology images of TS-3 (**Figure 7.3b**) and TS-4 (**Figure 7.3c**) show necking and crack path oriented A further improvement of ductility is expected by decreasing pulse current density and pulse-on time, but those are not preferred due to deposits formation with larger grain sizes and powdery structures.

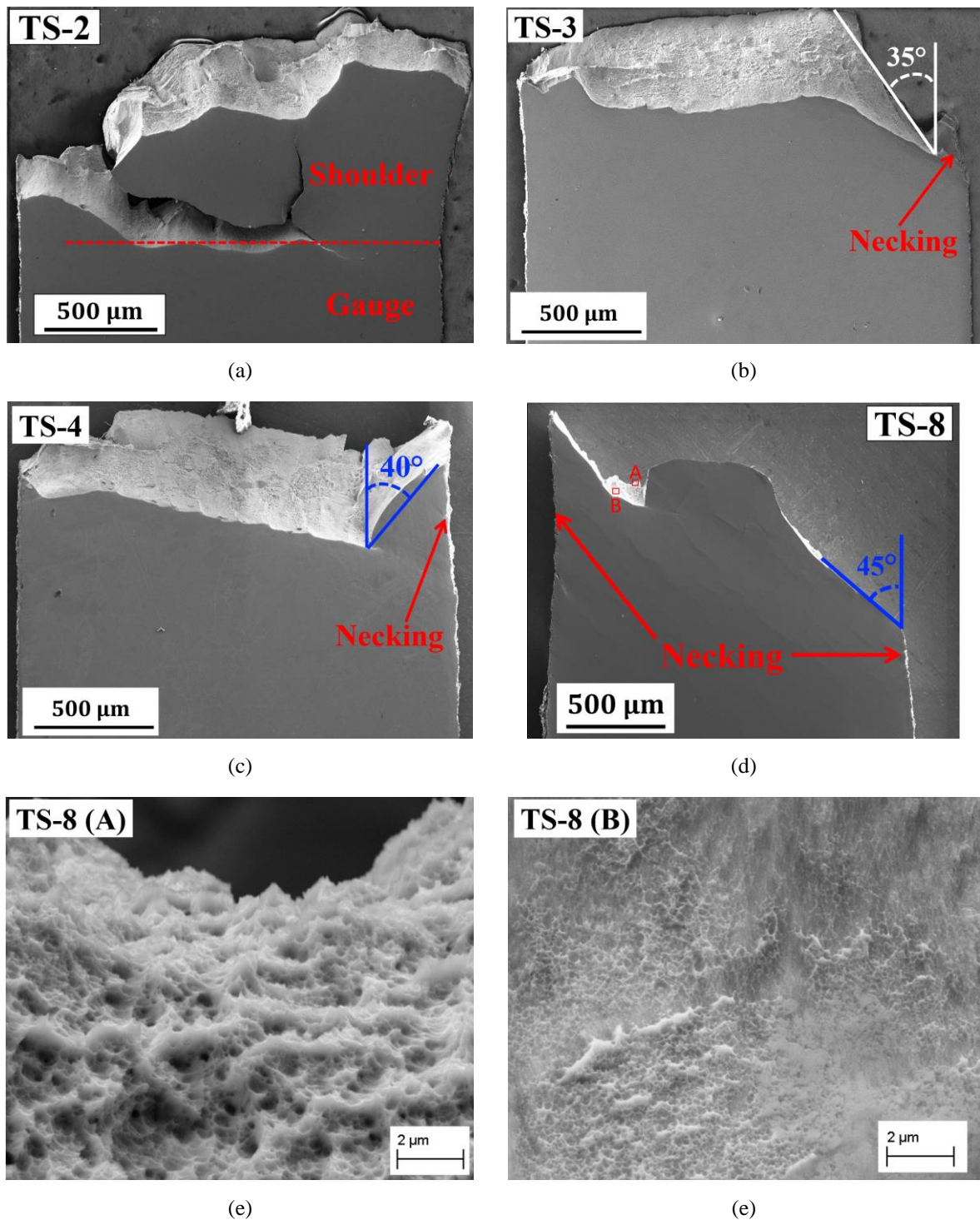


Figure 7.3 (a-d) Secondary electron images of surface morphology of (a) TS-2, (b) TS-3 (from [194]), (c) TS-4 (from [194]), and (d) TS-8 (from [194]) after tensile deformation. (e-f) Secondary electron images of fracture surface of TS-8 at areas marked with red rectangular shapes: (e) area A and (f) area B.

In the present work, the highest strength and ductility is observed in tensile sample-8 (TS-8). This sample was deposited at the lowest duty cycle (10%) and pulsed-on time (0.5 ms), with no reduction of current density (1000 A/m^2). A high current density is crucial for the formation of homogeneous nanostructured grains, which has a direct impact on the high tensile strength.

This sample exhibits a tensile yield stress and ultimate stress of 1.21 ± 0.08 GPa and 1.98 ± 0.03 GPa, respectively. The fracture strain of TS-8 is 15.95 ± 0.09 %. **Figure 7.3b** depicts the surface morphology of TS-8 showing the most significant necking compared to all other samples with a shear fracture oriented at 45° to the tensile loading direction. Fracture surface images of TS-8 (**Figure 7.3e,f**) show a ductile fracture with various sizes of micro dimples.

The strength and ductility of the PED-processed nanocrystalline Co-Cu are governed by several factors. For flat tensile specimen, the sample thickness may have a contribution on ductility. Sample thickness is crucial for accommodation of plastic strains. The thicknesses of tensile samples (TS-1 to TS-8) are unintentionally different (see **Table 7.2**) due to the surface preparation as described in **Chapter 3**. According literatures [213, 214, 215], a significant effect of sample thickness was reported in the non-uniform plastic elongation regime (i.e. indicated by a necking formation). In the present work, significant necking effects are only visible in three samples (TS-6, TS-7 and TS-8), which have a relatively small thicknesses compared to other samples. It can be concluded that sample thickness has no significant effect on ductility. There are other important factors which have a significant influences on the strength and ductility of PED-processed nanocrystalline Co-Cu. These are: (i) chemical composition (Cu concentration), (ii) microstructure (e.g. grain properties and crystal orientation), and (iii) processing flaws (e.g. porosity, crystal growth borders, and internal stresses). These factors will discussed in more details in the next sub-sections. Of course, lattice and structural defects (e.g. dislocations, vacancy, twin) have also a crucial impact on strength and ductility, but they are not investigated in the present work.

7.1.1. Effect of Cu concentration

Nanocrystalline Co exhibits a low ductility which may be attributed to the limited number of possible slip systems in hcp-structures. The addition of Cu leads to the formation of a fcc-structured solid solution Co-Cu, which is expected to enhance ductility due to a higher number of possible slip systems. In addition, an improved strength is also expected from solid solution strengthening. A high ductility of fcc-structured nanocrystalline Cu with fracture strains of over 10% have been reported in some literatures [42, 173, 176]. **Figure 7.4b** depicts a schematic graph of fracture strain as a function of Cu concentration showing a significant correlation of these parameters.

The Cu concentration in the PED-processed nanocrystalline Co-Cu can be increased through some mechanisms. Standard reduction potentials of Co and Cu are the key roles for enhancement of Cu content ($E_{\text{Co}^{2+}/\text{Co}}^0 = -0.28$ V vs. SHE; $E_{\text{Cu}^{2+}/\text{Cu}}^0 = +0.34$ V vs. SHE). Regarding

thermodynamic data, deposition of Cu is easier than Co due to the more positive standard reduction potential. Thus, a higher Cu content is expected by reducing pulse-on time and pulse current density as shown in samples TS-3 and TS-4. An increased Cu concentration can be also achieved by decreasing of duty cycle (i.e. increase of pulse-off time) as shown in **Table 7.1**. Regarding standard reduction potential, a displacement reaction of deposited Co by Cu ions from the electrolyte may occur when the current is off as shown by the following equation:



According to Cziraki [216], the formation of nanoscale multi-layered Co-Cu/Cu structure with sizes of 1-3 nm is also possible when the pulse current is off. These multi-layered structures may have an additional contribution on the improvement of ductility in nanocrystalline Co-Cu. However, APT measurement of the as deposited nanocrystalline Co-Cu (28 at.% Cu) show no detection of such multi-layered structures (see **Chapter 5**). More APT and/or TEM analysis are needed for this investigation.

In the nanocrystalline Co-Cu, improvement of ductility is achieved by increasing Cu concentration. However, an increased Cu concentration may lead to a decreasing strength due the formation of larger grains size as reported by Müller [77]. In the present work, the same effect is also found as shown in **Chapter 5** (see **Section 5.5**). In addition, the thermal stability decreases with increasing Cu concentration. Investigation on the optimum Cu concentration is needed in the future for achieving high strength and ductility with a good thermal stability of the nanocrystalline Co-Cu systems.

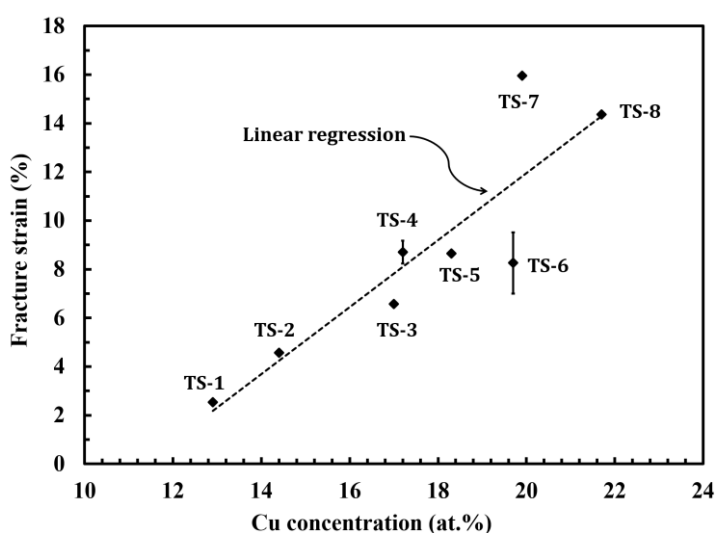


Figure 7.4 Effect of the Cu concentration on the tensile fracture strain of PED-processed nanocrystalline Co-Cu.

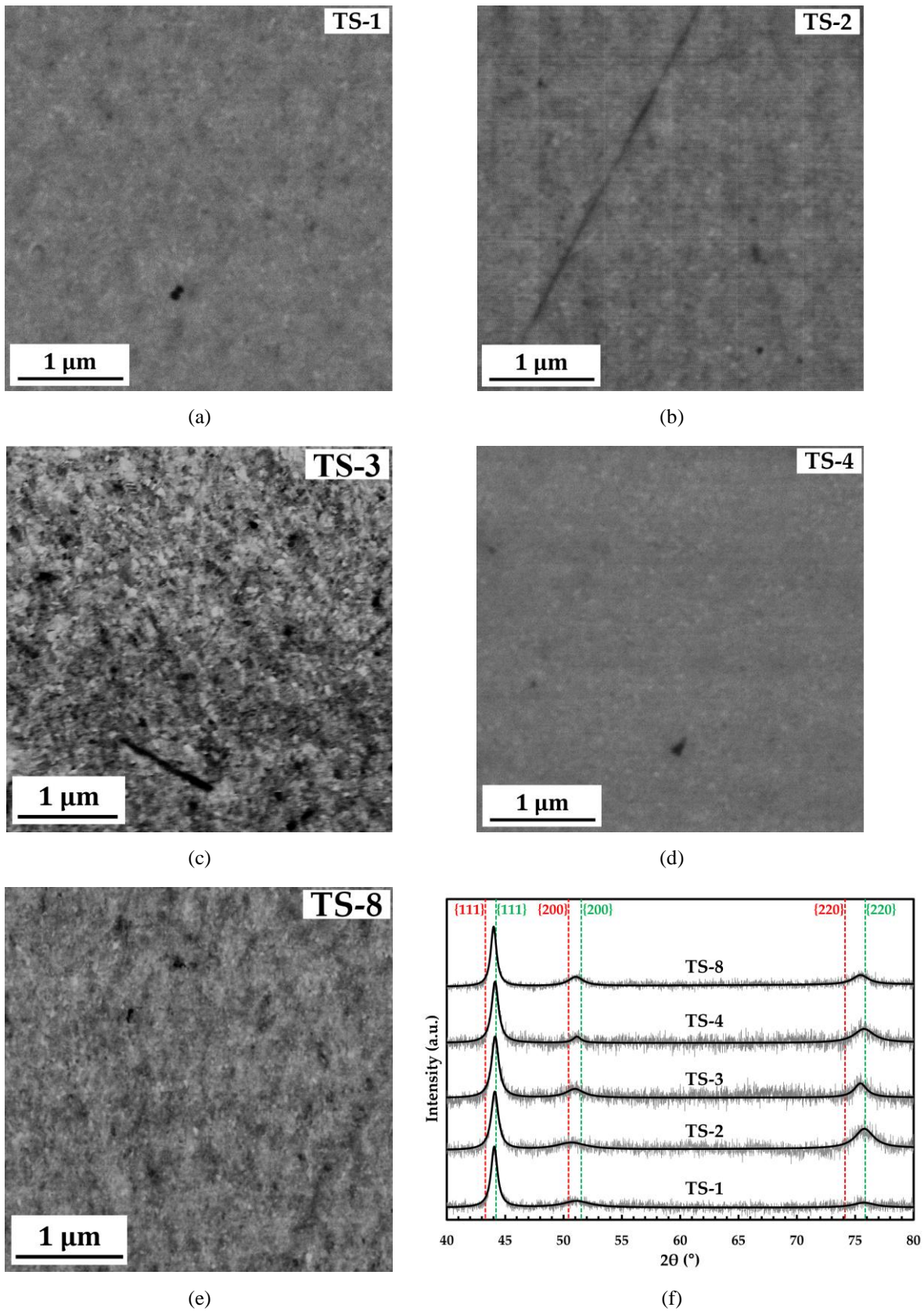


Figure 7.5 (a-e) Back-scattered electron (BSE) images of initial microstructure of (a) TS-1 (from [194]), (b) TS-2, (c) TS-3 (from [194]), (d) TS-4, and (e) TS-8 (from [194]) at the same magnification. (f) XRD patterns of selected tensile samples in which continuous black lines correspond for the fitted XRD data (from [194]). The red and green vertical dashed lines represent the position of fcc structure of Cu and Co, respectively.

7.1.2. Grain size effect

The microstructure (e.g. grains and crystal orientation) has a crucial contribution on strength and ductility of materials. In the present work, grain properties and crystal orientation of different nanocrystalline Co-Cu deposits are investigated, which are possible reasons for improvement of strength and ductility. **Figure 7.5a-e** depict BSE images of initial microstructure observed from a planar-section of selected samples exhibiting low (TS-1 and TS-2), moderate (TS-3 and TS-4) and high (TS-8) tensile fracture strains. These microstructure images show homogeneous and pure nanostructured grains with sizes of approximately below 100 nm. The microstructure image of TS-3 (**Figure 7.5c**) shows a somewhat larger grain size compared to the other samples, which may be attributed to the deposition at a lower current density of 800 A/m². Unfortunately, grain size determinations from BSE images (**Figure 7.5a-e**) are difficult due to the spatial resolution limit. Therefore, the grain size of selected samples were analyzed through XRD analysis.

Table 7.3 Grain size analysis of different nanocrystalline Co-Cu deposits approximated through Scherer and Williamson-Hall approaches as well as the mean grain size from both of these methods (from [194]).

Sample name	Scherer approach	Williamson-Hall approach		Mean grain size (nm)
	Grain size (nm)	Grain size (nm)	Micro-strain (%)	
TS-1	7.84	12.86	1.02	10.35
TS-2	7.39	7.08	0.39	7.24
TS-3	9.03	71.68	1.30	40.36
TS-4	8.30	7.76	0.16	8.03
TS-8	11.03	24.60	0.67	17.82

Figure 7.5f depicts XRD patterns of the selected nanocrystalline Co-Cu samples. Matsui et al. [217] proposed that ductility of electrodeposited nanocrystalline materials consisting of a fcc-structure depended on crystal orientation and absorbed hydrogen concentration. However, XRD analysis in the present work show almost identical XRD-peak patterns. It is supposed that crystal orientation (texture) is the same for all samples and it has no significant impact on the strength and ductility of nanocrystalline Co-Cu. Interestingly, the XRD-peaks shape (i.e. peak intensity and peak broadening) of individual samples are slightly different, which may be attributed to factors such as crystallite size, micro-strain, and others. In the present work, XRD analysis is focussed on the crystallite size and micro-strain for determination of grain size through the Scherer and Williamson-Hall approaches. Grain size determination through these approaches and the mean grain size values are presented in **Table 7.3**.

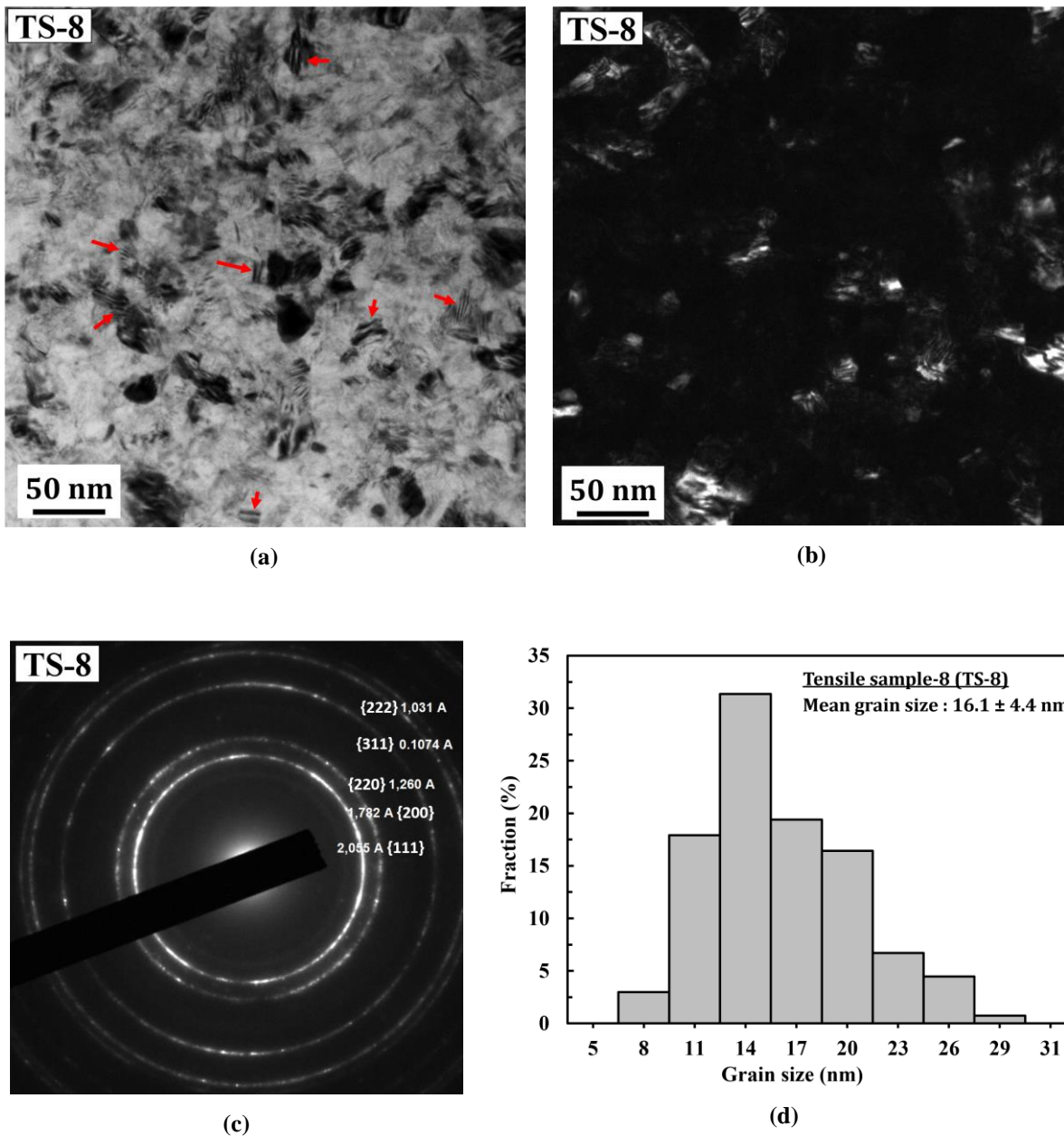


Figure 7.6 (a) Bright-field (BF) and (b) dark-field (DF) images obtained by transmission electron microscope (TEM) of tensile sample-8 (TS-8) and (c) selected area diffraction (SAD) pattern. (d) Grain size distribution of TS-8 measured from BF-TEM image.

The grain size analysis of TS-1, TS-2, and TS-4 are quite consistent through the two different methods. In contrast, grain size analysis of TS-3 and TS-8 from the Williamson-Hall approach are significantly different compared to the Scherer approach, which may be attributed to micro-strain concentration in the samples. For grain size data confirmation, one sample having the highest fracture strain (TS-8) was subjected for transmission electron microscope (TEM) measurement. **Figure 7.6a,b** show a bright-field (BF) and a dark-field (DF) TEM images of sample TS-8. A numbers of nano twins are detected in the BF-TEM image (marked

with red arrows in **Figure 7.6a**). The corresponding SAD pattern (**Figure 7.6c**) shows diffraction rings of the fcc-structure of (111), (200), (220), (311) and (222) planes. Grain size analysis of TS-8 was performed by using the BF-TEM image and the resulting grain size distribution is shown in **Figure 7.6d**. According to the TEM measurement, the mean grain size of TS-8 is 16.1 ± 4.4 nm. Grain size analysis from TEM measurement confirms a very close number to the mean grain size calculated from Scherer and Williamson-Hall approaches as shown in **Table 7.3** ($GS_{Mean} = (GS_{Scherer} + GS_{Williamson-Hall})/2$, where GS is the grain size). In the present work, these mean grain sizes are used for discussion of the dependence of strength and ductility on grain size of PED-processed nanocrystalline Co-Cu.

Deformation behaviour and dislocation mobility in nanocrystalline materials may be different compared to conventional coarse grained materials as described in **Chapter 2**. The number of dislocations in the pile-up is reduced with decreasing grain size down to the nanometer scale [3, 156]. In case of the grain sizes are smaller than the critical equilibrium distance between two dislocations, one grain cannot afford for more than one dislocation inside. Thus, dislocation pile-up is impossible at this condition (broken of the Hall-Petch effect) [155]. As a result, the strength of nanocrystalline materials will be constant or even decreases with grain size reduction. Previous investigations on nanocrystalline Cu [155, 157], Ni [218], and Pd [155, 157] showed a failure of the Hall-Petch effect at the grain sizes of below 20 nm. Thus, deformation in nanocrystalline materials will be dominated by other mechanism such as grain boundary sliding and grain rotation. In this regime, plasticity is predicted to increase with decreasing grain size, but the yield strength will be decreased. In the present work, the lowest strength and fracture strain was observed in TS-1 and TS-2, which may be attributed to very small grain sizes of below 11 nm. In this grain size regime, dislocation pile-up may be limited or even does not work, which may have a contribution on the low strength. However, the fracture strain in samples TS-1 and TS-2 should increase with decreasing grain size, which is not observed here. Low fracture strain in samples TS-1 and TS-2 may be attributed to other factors (e.g. processing flaws). Improvement of strength and ductility can be observed with increasing grain size as shown in TS-3 and TS-8, which exhibit grain sizes of more than 15 nm. In larger grain size regime, the number of dislocation at the pile-up increases which has a direct impact on the enhanced of strength and ductility. In the PED-processed nanocrystalline Co-Cu, the grain size is likely not an absolute factor for improvement of ductility, for instance, TS-4 exhibits a moderate ductility similar to TS-3, although having a large differences of grain size. Other contributing factors (e.g. processing flaws) are expected to have a crucial contribution on strength and ductility.

7.1.3. Effect of processing flaws

According to Koch et al. [171, 172], processing flaws are the most responsible factors on low ductility in nanocrystalline materials. The common processing flaws in the PED-processed nanocrystalline materials are porosity, crystal growth borders, chemical and/or structural inhomogeneity, and internal stresses. In the present work, an obvious chemical and/or structural inhomogeneities are not observed in the PED-processed nanocrystalline Co-Cu (see **Chapter 4**). Thus, this factor is not included for discussion. Initial investigations of processing flaws were performed for sample TS-1 exhibiting the lowest ductility. **Figure 7.7a** depicts a SE image the initial surface morphology of TS-1 observing micro-pores (marked with black arrows) and crystal growth borders (marked with white arrows).

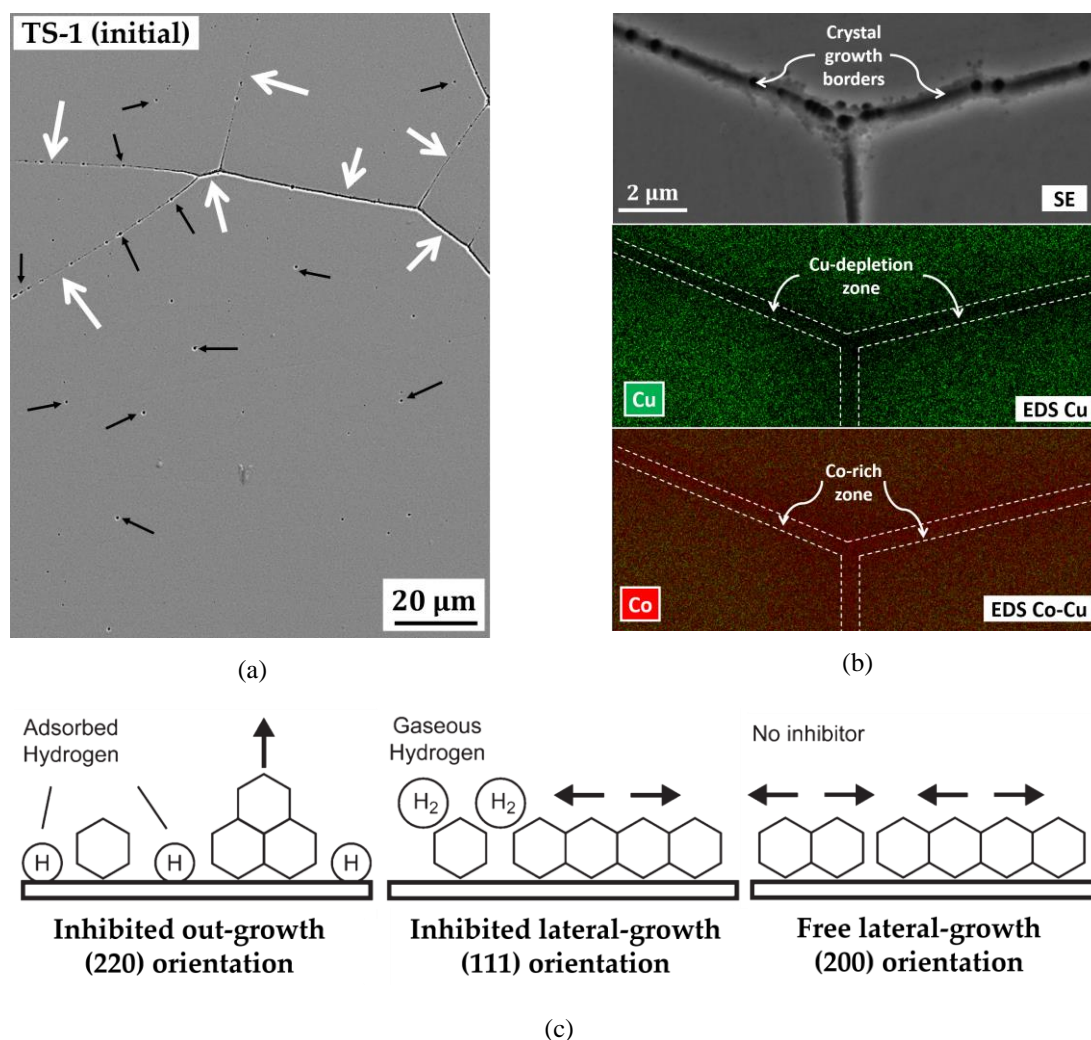


Figure 7.7 (a) Secondary electron image of initial surface morphology of sample TS-1 in planar-view showing crystal growth borders and micro-pores marked with white and black arrows, respectively (from [194]). (b) Combined SEM-EDS images of TS-1 observing chemical inhomogeneity along the crystal growth borders (from [194]). (c) Schematic illustration of growth mechanism in electrodeposition of fcc-structured materials. Black arrows correspond to the growth direction (from [217]).

Effect of porosity

Pores formation have a detrimental effect on ductility, whereas the stress concentration at pores may surpass the critical value which causes crack initiation and early failure [3]. XRD patterns of different nanocrystalline Co-Cu deposits show a strong peak intensity of (111) planes ($\{111\}$ fibre texture) reflecting inhibited lateral-growth mode in the presence of gaseous hydrogen as shown in **Figure 7.7c**. This theory was proposed by Amblard et al. [219] for electrodeposition fcc-Ni and developed by Krause et al. [220] for fcc-Co. According to Pourbaix diagram of Co, the formation of hydrogen is highly possible during deposition of Co at the solution pH of below 7, which may reduce the current efficiency. In the present work, the solution pH (pH = 4) and high deposition current density (high potential) have a significant impact for the formation of hydrogen gas, which was observable at the cathode upon electrodeposition. The hydrogen gas may be trapped in the nanocrystalline deposits leading to pore formation and hydrogen absorption. A reduction of pore and hydrogen formation in nanocrystalline Co-Cu can be performed by lowering pulse current density (TS-3) and shortening pulse-on time (TS-4) or decreasing duty cycle (TS-5, TS-6, and TS-7), whereas these samples show an improved ductility compared to TS-1 which exhibits the lowest ductility.

In the present work, sample TS-1 exhibits pores inside with sizes of 0.5-1.0 μm . Other samples (TS-2 to TS-8) may exhibit a smaller size of pores, which is not visible through SEM. Of course, the number of pore has also a significant impact to ductility, but it is not discussed here. According to Griffith theory of brittle fracture, stress concentration at a crack tip (in this case pores) decreases with reducing size of pores. The critical size of pores are crucial. The critical size of pores (a_c) can be calculated by using the following equation:

$$K_{IC} = Y\sigma_0\sqrt{\pi a_c} \quad [7.2]$$

where K_{IC} , σ_0 , and Y are the stress intensity factor, the actual applied stress, and the geometry factor. If the maximum stress at a crack tip exceeds the ultimate stress of material, thus, the material failure will occur. A simple calculation of the critical size of pores (a_c) was performed for the most brittle sample TS-1, which experienced early failure at 0.62 GPa. The stress intensity factor (K_{IC}) is assumed $1 \text{ MPa}\sqrt{\text{m}}$, which is the lowest theoretical limit for ideal brittle materials like silicon. The geometry factor (Y) can be assumed to be $Y=1$ since the ratio of the gauge width (2 mm) and the sizes of pore (0.5-1.0 μm) is very high (>1000). The calculation shows that the critical size of pore is 0.83 μm . In case of a more realistic stress concentration value ($K_{IC} = 5 \text{ MPa}\sqrt{\text{m}}$) is used in calculation, it gives a larger critical size of pore ($a_c = 20 \mu\text{m}$) which are significantly larger from the sizes of the observed pores (0.5-1.0

μm). Thus, the critical size of pores is not surpassed here. As a result, porosity may have a low impact on ductility of PED-processed nanocrystalline Co-Cu. Other processing flaws (e.g. crystal growth borders) may have a significant impact to ductility.

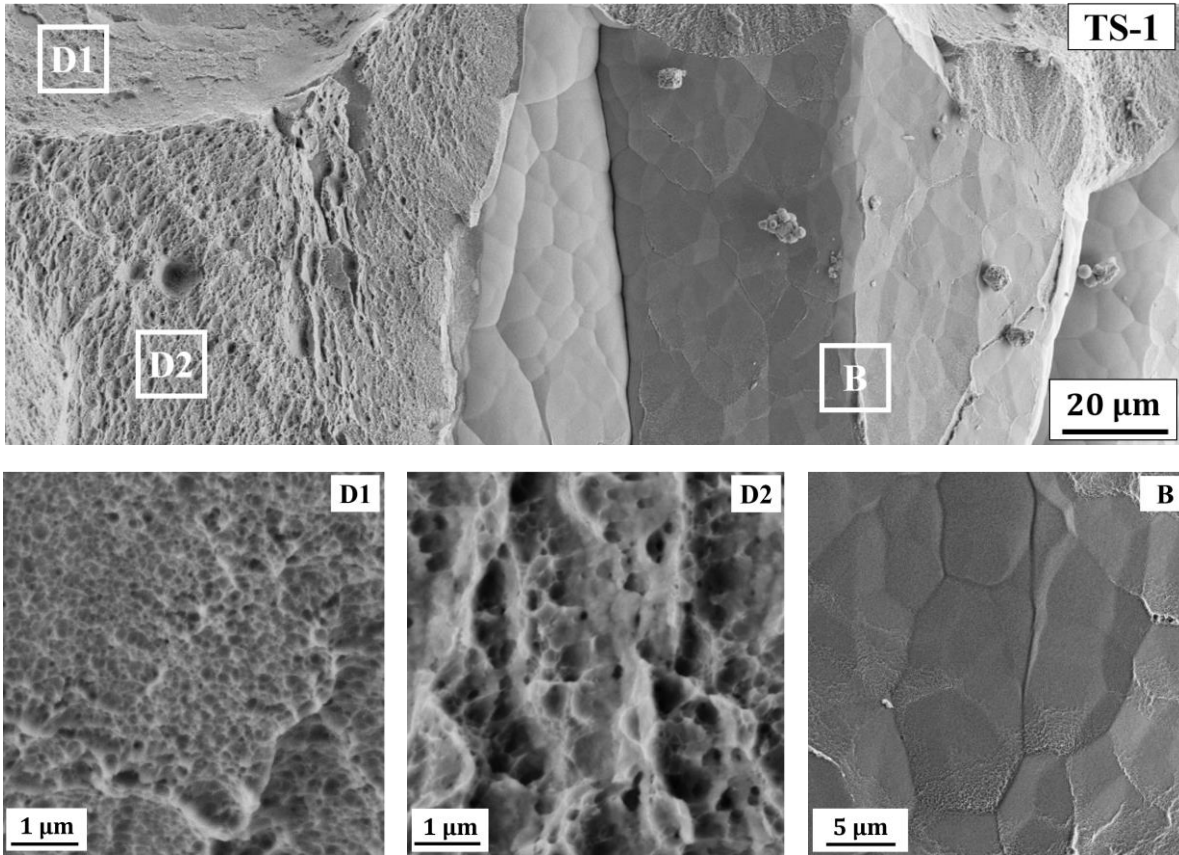
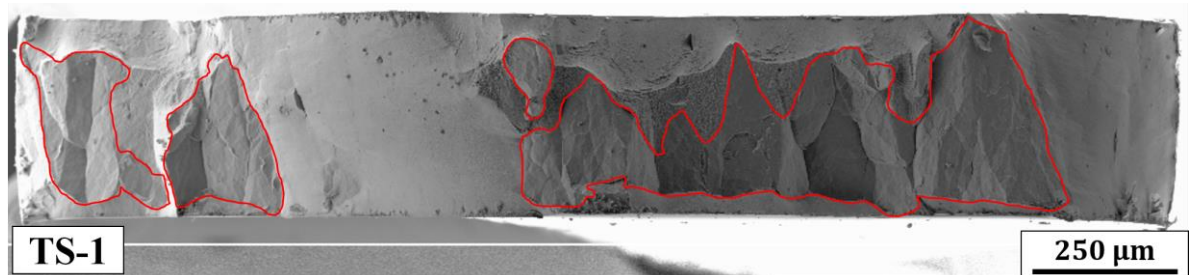


Figure 7.8 Secondary electron images of typical fracture surface of tensile sample-1 (TS-1) showing ductile (D1 and D2) and brittle (B) fracture regions with a clear visibility of crystal growth borders (from [194]).

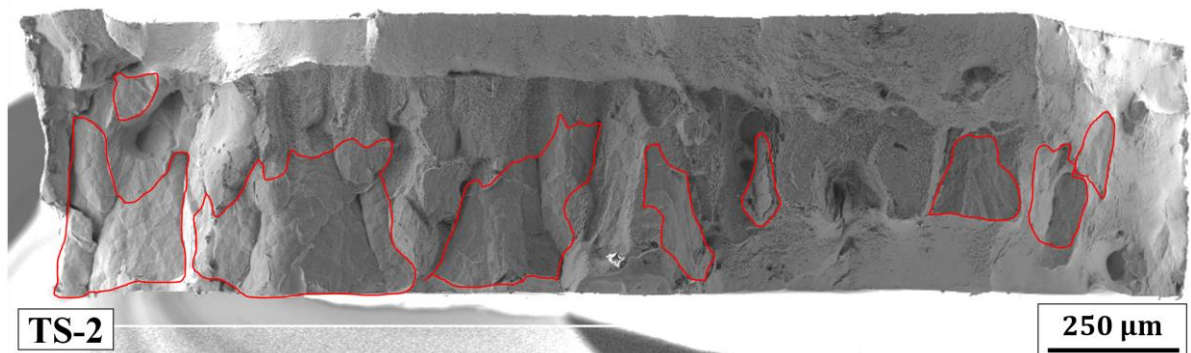
Effect of crystal growth borders

Crystal growth borders may have a crucial impact on ductility, but their effects on the mechanical properties nanocrystalline materials are rarely discussed. According to Fischer [195], crystal growth borders are formed during the nucleation and growth of “crystals” in the electrochemical deposition. One “crystal” comprises up to thousands of nanostructured grains with a similar crystal orientations or a fibre texture. Several “crystals” are expected to grow at the same time and they approach each other at some point forming crystal growth borders. The chemical composition at these borders may differ compared to the surrounding regions (e.g. depletion of particular alloying element, segregation of impurities, and others). **Figure 7.7b** depicts a combined SEM-EDS image showing elemental maps of Co and Cu at crystal growth borders. They show that these borders consist of a Cu depleted zone with a high Co

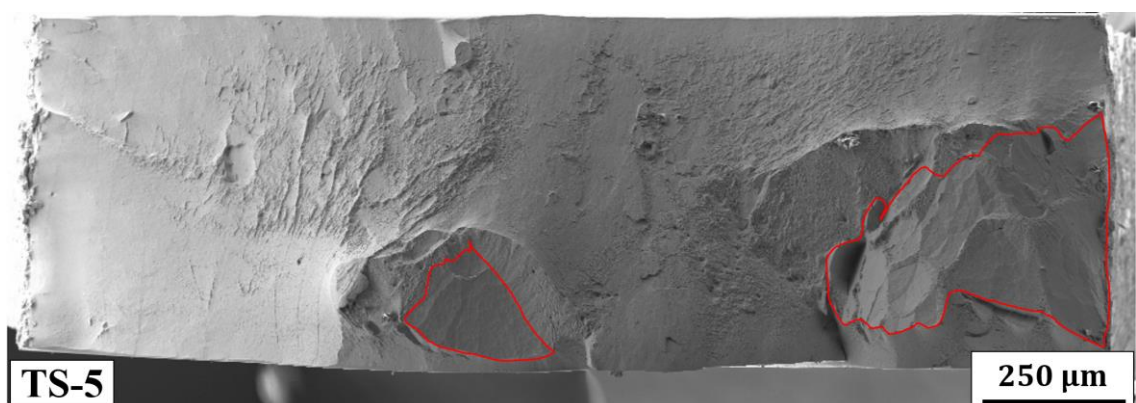
concentration. These borders are expected to be more brittle and vulnerable to crack initiation compared to the surrounding regions which consist of a higher Cu concentration. **Figure 7.8** depicts an image of the fracture surface of sample TS-1 at a selected region observing ductile (D1 and D2) and brittle (B) fracture zones. The ductile fracture surfaces (D1 and D2) comprise of two regions with different sizes of dimples. **Figure 7.8** shows that the brittle fracture at crystal growth borders are clearly observed (B) which is possibly the reason for the early failure of TS-1. Investigation of the brittle fracture at crystal growth borders of individual samples are performed for revealing the effect of this processing flaw on ductility.



(a)



(b)



(c)

Figure 7.9 Continued

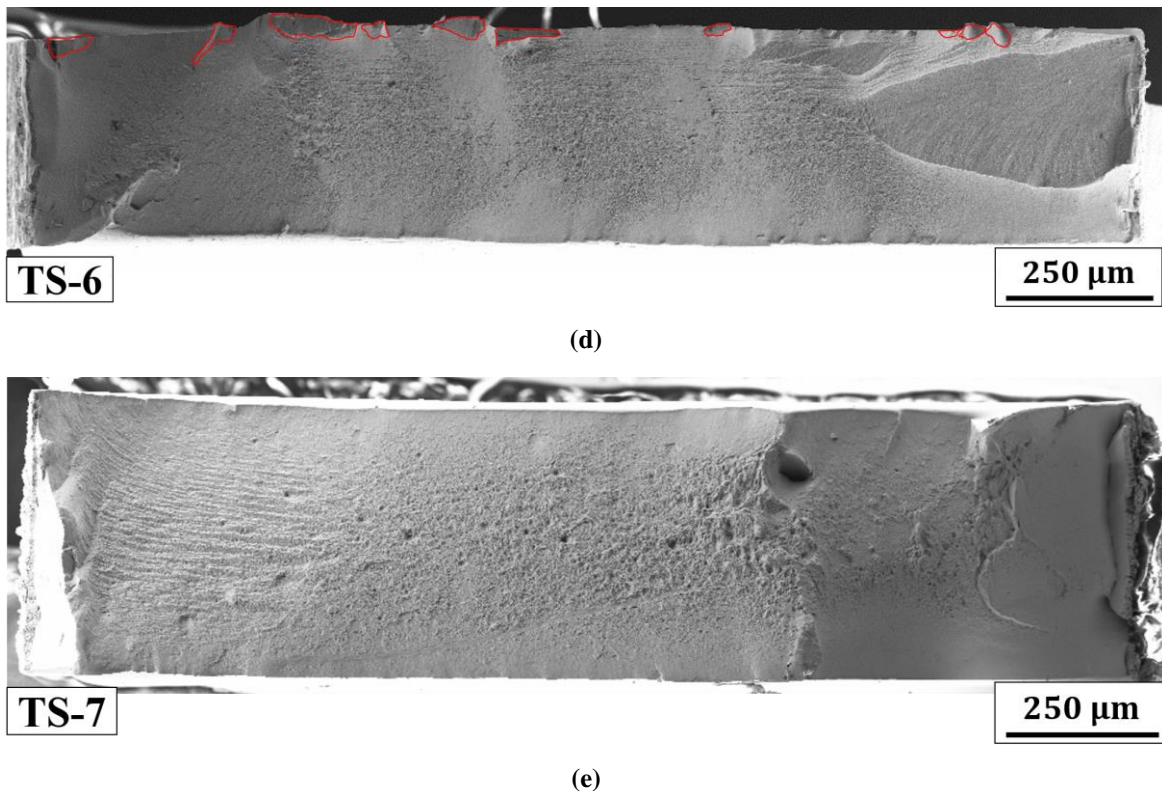


Figure 7.9 Secondary electron images of fracture surface of tensile samples deposited at a pulse current density of 1000 A/m^2 , a pulse-on time of 0.5 ms , and various duty cycles: (a) 20% (TS-1), (b) 17.5% (TS-2), (c) 15% (TS-5), (d) 12.5% (TS-6), and (e) 10% (TS-7). Brittle fracture zones at the crystal growth borders are marked with the red freeform shapes.

Figure 7.9a-e depict secondary electron images of fracture surface of different tensile samples (TS-1, TS-2, TS-5, TS-6, and TS-7) deposited at various duty cycles (10% - 20%) and fixed pulse current density (1000 A/m^2) and pulse-on time (0.5 ms). The fracture surfaces of the tensile samples show different fractional area of brittle fracture at the crystal growth borders as marked with red free-form shapes in **Figure 7.9a-d**. A brittle fracture is not observed in TS-8 (duty cycle of 10%) as shown in **Figure 7.9a-e**. A schematic graph of the fractional area of brittle fracture at the crystal growth borders as a function of duty cycle is shown in **Figure 7.10a**. It shows that the fractional area of brittle fracture decreases significantly down to 0% with reducing duty cycle from 20% to 10%. A reduction of this processing flaw can be performed also by lowering the pulse current density to 800 A/m^2 (TS-3) and shortening the pulse-on time to 0.3 ms (TS-4). These samples show a significant decrease of the fractional area of brittle fracture compared to TS-2 (duty cycle of 17.5%). A significant improvement of ductility is achieved with decreasing the fractional area of brittle fracture at crystal growth borders as shown in **Figure 7.10b**. Crystal growth border is expected to have the strongest impact on ductility of PED-processed nanocrystalline Co-Cu compared to other factors.

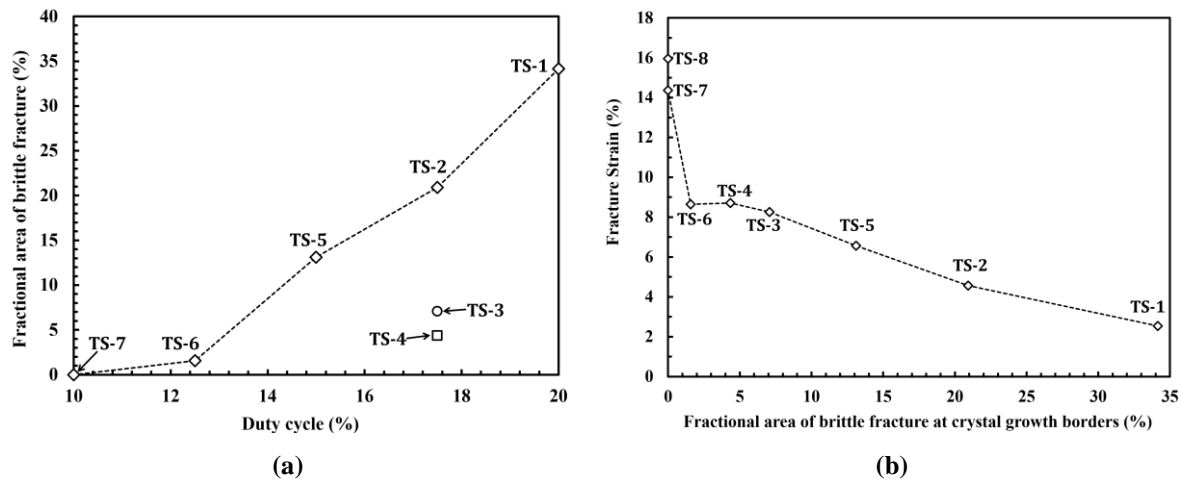


Figure 7.10 (a) Schematic graph of fractional area of brittle fracture at crystal growth borders as a function of duty cycle from 10% to 20% at a pulsed current density and a pulsed-on time of 1000 A/m² and 0.5 ms, respectively. Effect of decreasing pulsed current density to 800 A/m² (TS-3) and shortening pulsed-on time to 0.3 ms (TS-4) on the fractional area of brittle fracture at crystal growth borders is also shown in the graph. **(b)** Schematic graph of fracture strain as a function of fractional area of brittle fracture at crystal growth borders.

Effect of internal stresses

Internal stresses may also have an impact on ductility of PED-processed nanocrystalline Co-Cu. XRD analysis of selected samples (see **Figure 7.5f**) observe slightly different XRD-peaks shape (i.e. peak intensity and peak broadening), which may be attributed to micro-strain broadening. The micro-strain from XRD pattern of individual samples was calculated through the Williamson-Hall approach and the results are presented in **Table 7.3**. The micro-strain broadening is caused by interval lattice distortion, for instance, internal micro stresses. In the PED-process, internal micro stresses are generated when the pulse current is on, while stress relaxation is expected when the pulse current is off [102, 103, 178]. Stress generation is also produced from a deposition at high pulse current densities. In addition, growth inhibition from chemical additives [104, 145, 146] may have a contribution on the stress generation too. The internal micro-stresses may have a contribution on the ductility of nanocrystalline materials. This type of “processing flaw” may lead to the formation of micro- or nano-sized cracks, which could be the origin of failure. A reduction of internal micro-stresses is expected to improve ductility. This can be performed by extending the time for stress relaxation (e.g. decreasing duty cycle or increasing pulse-off time) and shortening time for stress generation (e.g. reducing pulse-off time). For instance, all tensile samples, except of TS-3, have a lower micro-strain compared to TS-1 (see **Table 7.3**), which may have a positive contribution on improvement of the ductility of these samples.

7.2. Effect of annealing temperatures

Annealing of nanocrystalline Co-Cu leads to a structural evolution as shown in **Chapter 5**. Phase decomposition of Co and Cu with slight grain coarsening is observed at temperatures of 450°C leading to the formation of an ultrafine grained alloy with two phases Co and Cu. In addition, spinodal decomposition can be obtained with no grain coarsening at annealing temperatures of 300°C. Microhardness tests of Co-Cu alloys with different microstructures (i.e. grain size and phase) show different hardening and softening effects due to spinodal and phase decomposition. Decomposition in nanocrystalline Co-Cu may change the elastic and plastic deformation properties of this material due to different dislocation behaviour and mobility in the different microstructures. An improved strength and ductility may be expected here. In this section, the effect of annealing temperatures on strength and ductility of nanocrystalline Co-Cu is investigated.

In this section, nanocrystalline Co-Cu samples were deposited at a pulse current density of 900 A/m², a duty cycle of 10%, and a pulse-on time of 0.3 ms. The pulsed deposition parameters are similar to sample TS-8 (i.e. having the highest ductility) with a slight reduction of pulse current density. A higher Cu concentration and a larger grain size may be achieved by reducing the pulse current density, whereas an enhanced ductility can be expected. Chemical composition of the as-deposited sample is 79.5 at.% Co and 20.5 at.% Cu. Some deposited samples were subjected to annealing treatments at different temperatures (200°C, 300°C, and 450°C) for the same time period of 24 h. **Figure 7.11a** depicts a back-scattered electron image of the microstructure of the as-deposited sample (TS-9) showing a slightly larger grain size compared to TS-8. Grain size analysis from XRD pattern of this sample (**Figure 7.12**) shows that the grain size is between 11-37 nm, which is higher compared to TS-8 (see also **Table 7.3**). A larger grain size is strongly attributed to the deposition at a lower current density. Identical microstructures with no significant grain coarsening are observed after annealing at 200°C and 300°C for 24 h as shown in **Figure 7.11b,c**. Grain size analysis from XRD pattern of the sample annealed at 200°C (**Figure 7.12**) shows identical result with the as deposited state (TS-9). However, TS-9 and TS-10 samples have a slightly different micro-strain broadening effect. In contrast, samples annealed at 450°C shows a significant grain coarsening (**Figure 7.11b**), whereas the grain size increases to 111.2 ± 34.6 nm. Several twins are also observed in this annealed sample. Interestingly, some distinct dark particles (marked with red arrows in **Figure 7.11b**) are also detected as an indication of phase decomposition (i.e. precipitation of Co or Cu) as shown also in **Chapter 5**.

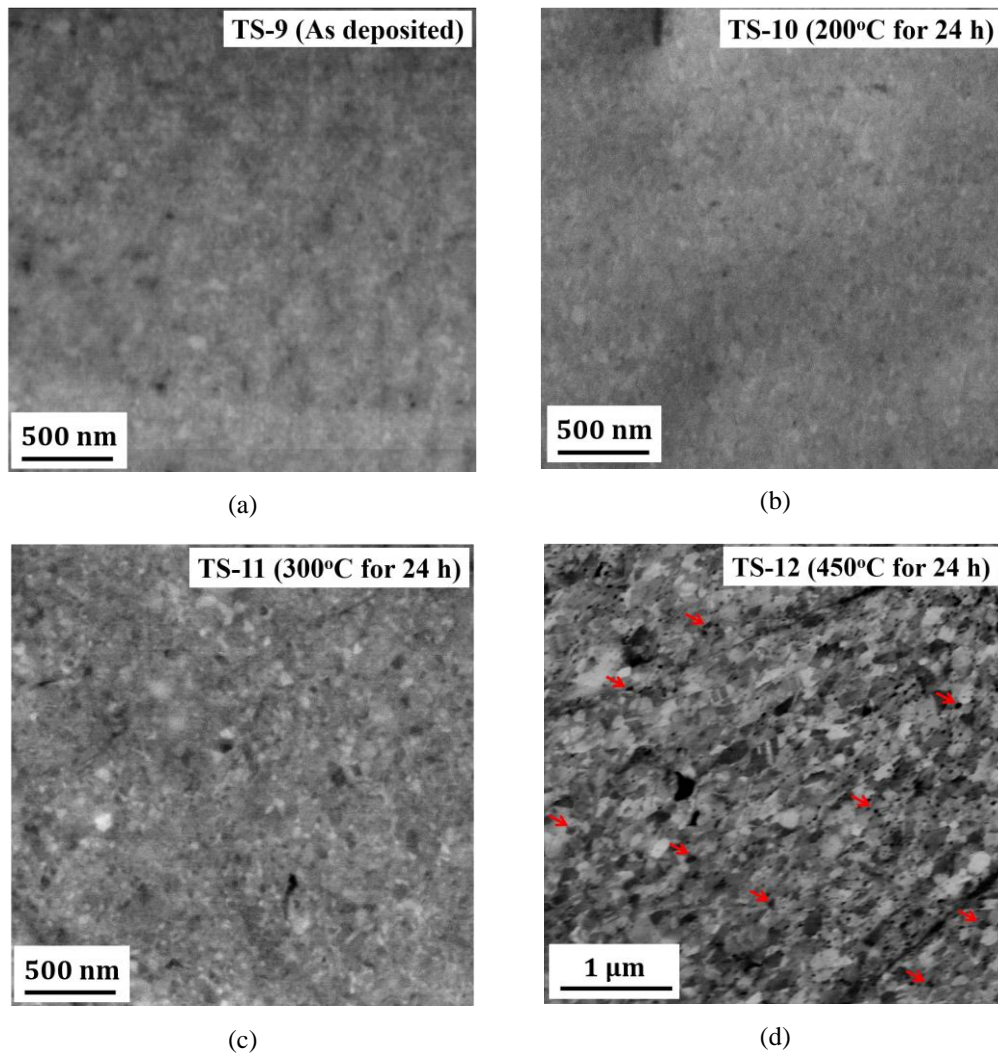


Figure 7.11 BSE images of the microstructure of (a) as deposited sample (TS-9) and (b-d) samples annealed at different temperatures for 24 h: (b) 200°C (TS-10), (c) 300°C (TS-11), and (d) 450°C (TS-12) (from [194]).

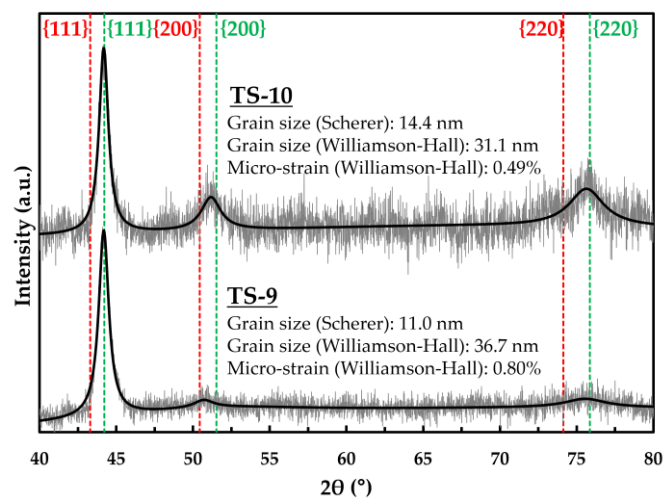


Figure 7.12 XRD patterns of TS-9 and TS-10, whereas continuous black lines correspond to the fitted XRD data (grey lines). The red and green vertical dashed lines represent the position of fcc the structure of Cu and Co, respectively (from [194]).

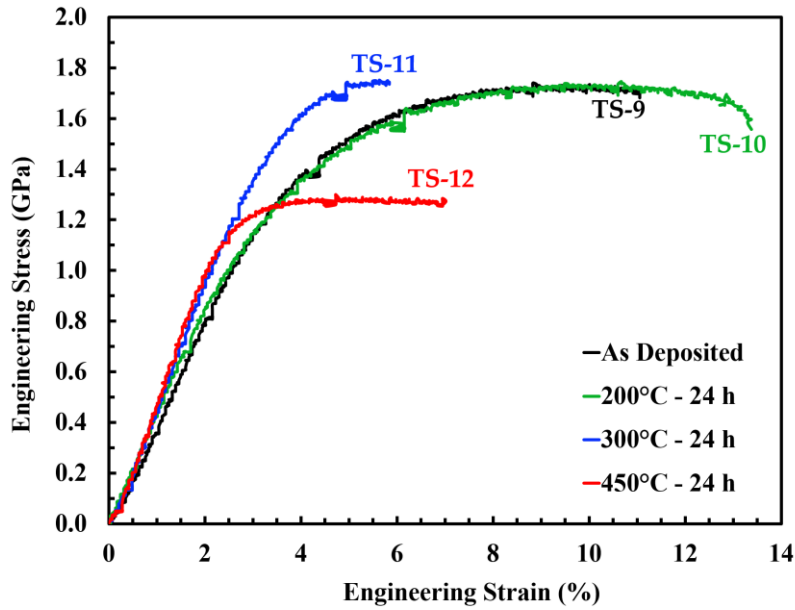


Figure 7.13 Engineering stress vs. strain curves of tensile tests at a strain rate of $1.0 \times 10^{-3} \text{ s}^{-1}$ of as deposited (TS-9) and annealed (TS-10, TS-11, and TS-12) samples (from [194]).

Table 7.4 Mechanical properties of as deposited (TS-9) and annealed (TS-10, TS-11, TS-12) samples calculated from engineering stress vs. strain curves in **Figure 7.13**. Two samples were mechanically tested for each temperature except for samples TS-10 and TS-11 (from [194]).

Sample name	Thickness (mm)	Annealing		Mechanical properties		
		Temp. (°C)	Time (h)	Yield stress (GPa)	Ultimate stress (GPa)	Fracture strain (%)
TS-9	0.31	As deposited		1.16 ± 0.01	1.71 ± 0.02	11.37 ± 0.24
TS-10	0.31	200	24	1.10	1.73	13.38
TS-11	0.31	300	24	1.40	1.75	5.84
TS-12	0.35	450	24	1.03 ± 0.08	1.28 ± 0.17	6.05 ± 0.97

Tensile tests at a strain rate of $1.0 \times 10^{-3} \text{ s}^{-1}$ were performed for the as-deposited (TS-9) and annealed (TS-10, TS-11, and TS-12) samples. The engineering stress vs. strain curves are shown in **Figure 7.13**, while the detailed information (e.g. yield stress, ultimate stress, and fracture strain) can be found in **Table 7.4**. The engineering stress-strain curves show that TS-9 exhibits a ductile behaviour, whereas uniform and non-uniform elongations are observed. The yield stress, ultimate stress, and fracture strain of the as-deposited sample (TS-9) are $1.16 \pm 0.01 \text{ GPa}$, $1.71 \pm 0.02 \text{ GPa}$, and $11.37 \pm 0.24\%$, respectively. The tensile strength of TS-9 is slightly lower compared to TS-8 (see also **Table 7.3**) which may be attributed to a larger grain size and a higher Cu concentration due to deposition at a lower current density. On the other hand, a lower fracture strain in TS-9 (i.e. compared to TS-8) may be caused by thickness effect. The ratio between the thickness (d) of samples TS-9 and TS-8 ($d_{TS-9}/d_{TS-8} = 0.775$) is close to

the ratio between the fracture strains (ϵ_f) of samples TS-9 and TS-8 ($\epsilon_{f,TS-9}/\epsilon_{f,TS-8} = 0.72$), which could be an indication of thickness effect. Secondary electron (SE) image of the surface morphology of TS-9 (**Figure 7.14a**) show a necking effect and fracture oriented at $\sim 45^\circ$ towards loading direction, which is typical for ductile fracture. In addition, ductile fracture surface with dimple structures is observed in TS-9 (**Figure 7.14b**).

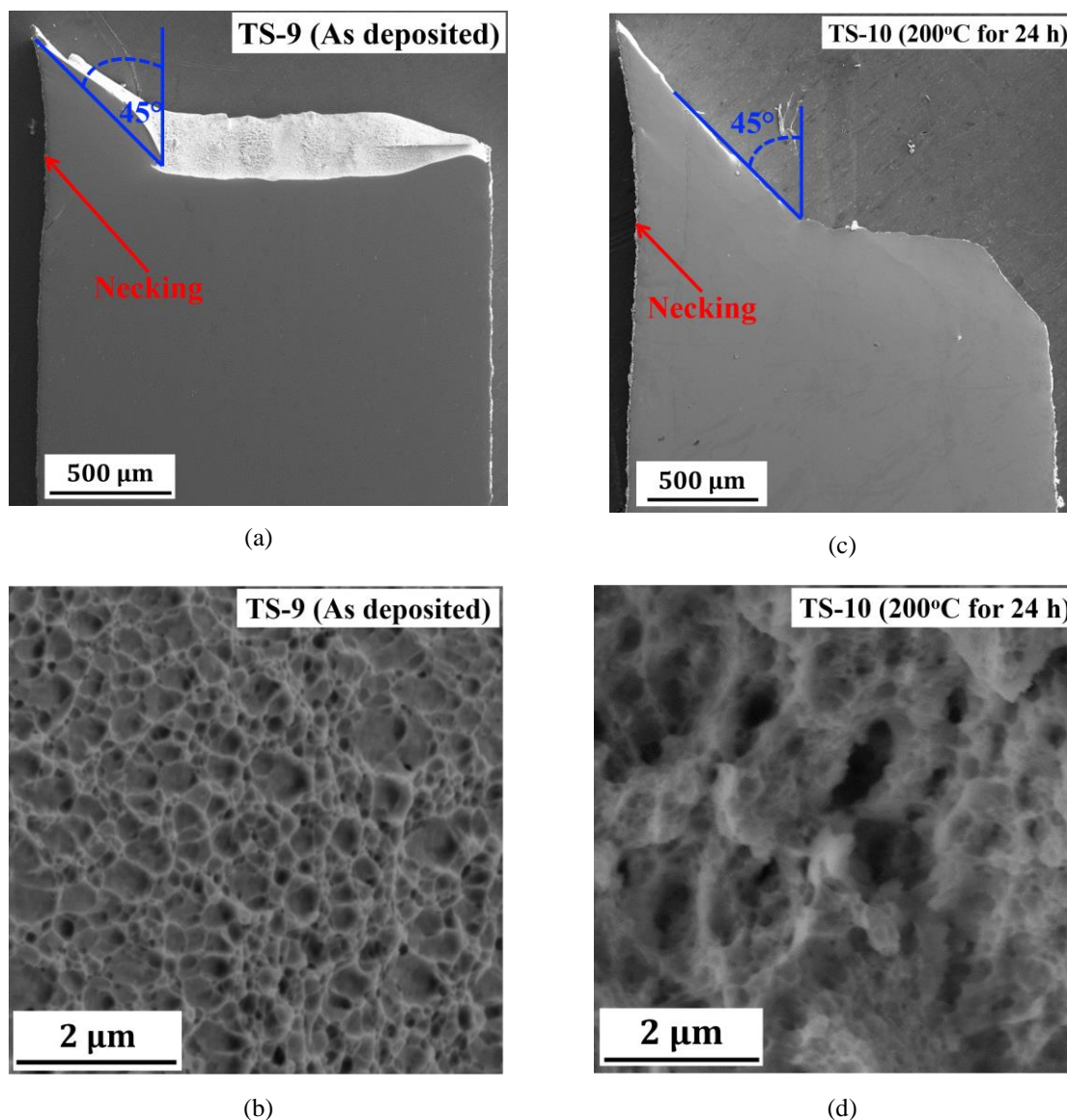


Figure 7.14 (a,c) SE images of surface morphology of (a) TS-9 and (c) TS-10 after tensile deformation (from [194]). (b,d) SE images of fracture surface of (a) TS-9 and (b) TS-10 (from [194]).

According to engineering stress-strain curves (**Figure 7.13**), the sample annealed at 200°C for 24 h (TS-10) exhibits a ductile behaviour with identical yield and ultimate stresses compared to the as-deposited state (TS-9) (see data in **Table 7.4**). Interestingly, annealing at 200°C for 24 h leads to an enhancement of ductility, whereas the fracture strain increases to 13.38%. SE

image of the surface morphology of TS-10 (**Figure 7.14a**) show more significant necking effect compared to as-deposited sample (TS-9). A ductile fracture surface with dimple structures is also observed in this annealed sample (**Figure 7.14d**). Recovery processes (e.g. grain boundary relaxation, internal stresses annihilations, and absorbed hydrogen release) may have a contribution on the improvement of ductility after annealing at 200°C for 24 h. This possibility has been proposed by Bachmaier et al. in nanocrystalline Co-Cu (74 at.% Cu) [27] and Oberdorfer et al. in nanocrystalline Cu [221]. Comparing with the as-deposited state, the micro-strain of the 200°C-annealed sample (**Figure 7.12**) decreases from 0.8% to 0.49%, which could be an indication of recovery processes. More investigation on the measurement of internal stresses and absorbed hydrogen concentration at 200°C are needed for revealing the reason of the improved ductility.

The tensile test of a sample annealed at 300°C for 24 h (TS-11) shows an increased yield strength to 1.40 GPa compared to the as-deposited state (TS-9) (**Figure 7.13** and **Table 7.4**). According to investigation in **Chapter 5**, an annealing treatment of nanocrystalline Co-Cu at 300°C leads to the spinodal decomposition of the supersaturated solid solution Co-Cu, whereas a formation of 5-10 nm sized regions with high concentration of Co (~95 at.% Co) and Cu (~90 at.% Cu) are observed. These Co- and Cu-rich regions may act as ‘precipitates’, which are distributed mainly at the grain boundaries. If these ‘precipitates’ is coherent with the matrix of crystal structure, they may have a strong contribution on the strengthening mechanism in nanocrystalline Co-Cu. However, annealing at 300°C for 24 h does not improve ductility, whereas the fracture strain decreases to 5.84%. The fracture surface image of TS-11 (**Figure 7.15a**) depicts two ductile fracture zones with different sizes of dimples (region I and II). The dimple sizes in region I and region II are 500-1000 nm and 20-300 m, respectively. The microstructure in these regions may be different, which have an impact on lower ductility compared with the as-deposited state.

Compared to as-deposited state (TS-9), the engineering stress-strain curve of a sample annealed at 450°C for 24 h (TS-12) shows a decrease of yield and ultimate strength to 1.03 ± 0.08 GPa and 1.28 ± 0.17 GPa, respectively (**Figure 7.13** and **Table 7.4**). The reduction of strength is strongly attributed to grain coarsening of nanocrystalline Co-Cu at 450°C. Regarding Hall-Petch effect, the strength of nanocrystalline materials usually decreases with grain coarsening but the ductility is likely to increase. Thus, an increased fracture strain is expected at the 450°C-annealed sample. However, the fracture strain of TS-12 unexpectedly decreases to $6.05 \pm 0.97\%$. Secondary electron image of the fracture surface of TS-12 (**Figure 7.15b**) shows no brittle fracture, whereas ductile fracture with dimple structures is dominantly

observed. Therefore, the early failure in this annealed sample may be caused by small defects or phases having a brittle behaviour within the samples. The fracture image of sample TS-12 shows some spots with different structure as marked with the red free-form shapes in **Figure 7.15b**. According to investigation in **Chapter 5**, annealing at 450°C for 24 h leads to phase decomposition of solid solution Co-Cu, whereas the formation of fcc-Co, fcc-Cu and hcp-Co are detected. The hcp-Co phase is more brittle compared to fcc-structure and this may cause the reduced fracture strain. The decreased ductility may be contributed also by segregation of impurities at grain boundaries (i.e. sulphur coming from saccharin and SDS). A previous work by Hibbard et al. [23] showed that sulphur diffusion to grain boundaries of nanocrystalline Co was possible at temperatures of higher than 300°C. Segregation of sulphur at grain boundaries may cause a grain boundary embrittlement which leads on the early failure and decrease of ductility.

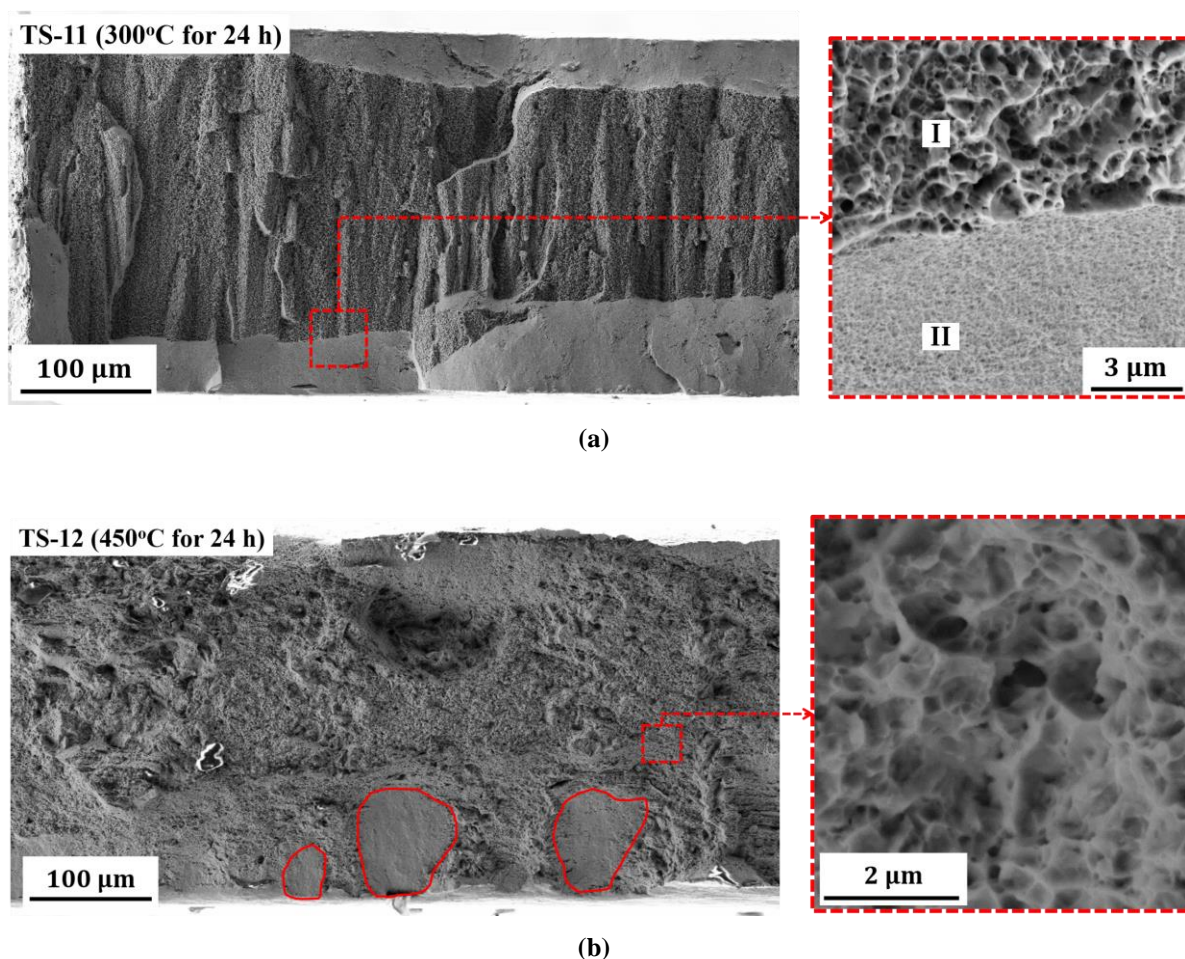


Figure 7.15 Secondary electron images of fracture surface of samples annealed at (a) 300°C (TS-9) and (b) 450°C (TS-10) for 24 h (from [194]).

7.3. Discussion of the results in Chapter 7

Investigations on the effect of deposition parameters on strength and ductility of PED-processed nanocrystalline Co-Cu have been already performed. Significant improvements of strength and ductility can be achieved by reducing duty cycle, pulse current density, and pulse on-time. Controlling these deposition parameters may change chemical composition, microstructure, and processing flaws characteristics. The strength and ductility of PED-processed nanocrystalline Co-Cu are attributed to some factors. (i) *The Cu concentration* had a significant impact to ductility of PED-processed nanocrystalline Co-Cu, whereas ductility increases with increasing Cu concentration. This Cu element has a role for solid solution strengthening of Co-Cu system, stabilizing the nanostructured grains, and increasing possible slip systems for plastic deformation (hcp Co \rightarrow fcc Co-Cu). (ii) *The grain size effect* was evident for showing the increase of strength in the PED-processed nanocrystalline Co-Cu. The samples having a grain size of below 10 nm showed the lowest strength, whereas the failure of Hall-Petch effect may occur. Thus, deformation process may be dominated by other mechanisms (e.g. grain boundary sliding). However, the effect of grain size on fracture strain or ductility is still unclear, whereas a good ductility was observed in the samples with different mean grain sizes from \sim 8 nm to \sim 40 nm. (iii) *A number of pores* sized of 0.5-1.0 μm were observed in the sample having the lowest fracture strain. However, calculations showed that the critical size of pore for brittle fracture ranges from 0.85 μm to 20 μm at stress intensity factors of 1-5 $\text{MPa}\sqrt{\text{m}}$, which is significantly larger than the size of the observed pore (0.5-1.0 μm). As a consequence, porosity may have a weak impact on low ductility of the PED-processed nanocrystalline Co-Cu. (iv) According to the results, reduction of number and size of the *crystal growth borders* had the most significant impact to ductility of the PED-processed nanocrystalline Co-Cu. The results showed that the fracture strain increased with decreasing fractional area of brittle fracture at the crystal growth borders. Reducing duty cycle had the most significant impact for reducing the crystal growth borders. In this region, the Cu depleted zones with high Co concentration were observed, whereas this area exhibited a more brittle properties than the surrounding regions with significantly higher Cu concentration. Co-deposition of impurities (e.g. sulphur, hydrogen) is also expected in these regions, which have an impact to ductility.

Investigations on the effect of annealing temperatures on strength and ductility of PED-processed nanocrystalline Co-Cu have been also performed. Annealing at 200°C led to an improved ductility, which may be attributed to recovery processes (e.g. grain boundary relaxation, internal stresses annihilations, and absorbed hydrogen release). The 200°C-annealed sample exhibited for almost identical yield and ultimate tensile stress compared to the as-

deposited state. Annealing at 300°C led to an increase of strength, but ductility tends to decrease significantly. The formation of Co and Cu ‘precipitates’, which was formed during spinodal decomposition of solid solution Co-Cu at 300°C, had a strong impact for enhancement of strength in this annealed sample. However, the reason for a decrease of fracture strain was still unclear. Annealing at 450°C led to decrease of strength and ductility. Grain coarsening in the 450°C-annealed samples had a significant impact to decrease of strength. However, a clear evidence for the decrease of ductility was not observed. Two factors may have a significant impact on ductility in this annealed sample, these are: (i) a brittle hcp-Co phase which was formed during phase decomposition at 450°C; (ii) grain boundary embrittlement due to segregation of impurities (e.g. sulphur) to grain boundary. Observation of hcp-Co phase has been revealed by the XRD measurement as shown in **Chapter 5**. Further investigations are needed in the future for revealing segregation of sulphur to grain boundaries as observed by Rathman et al. [25].

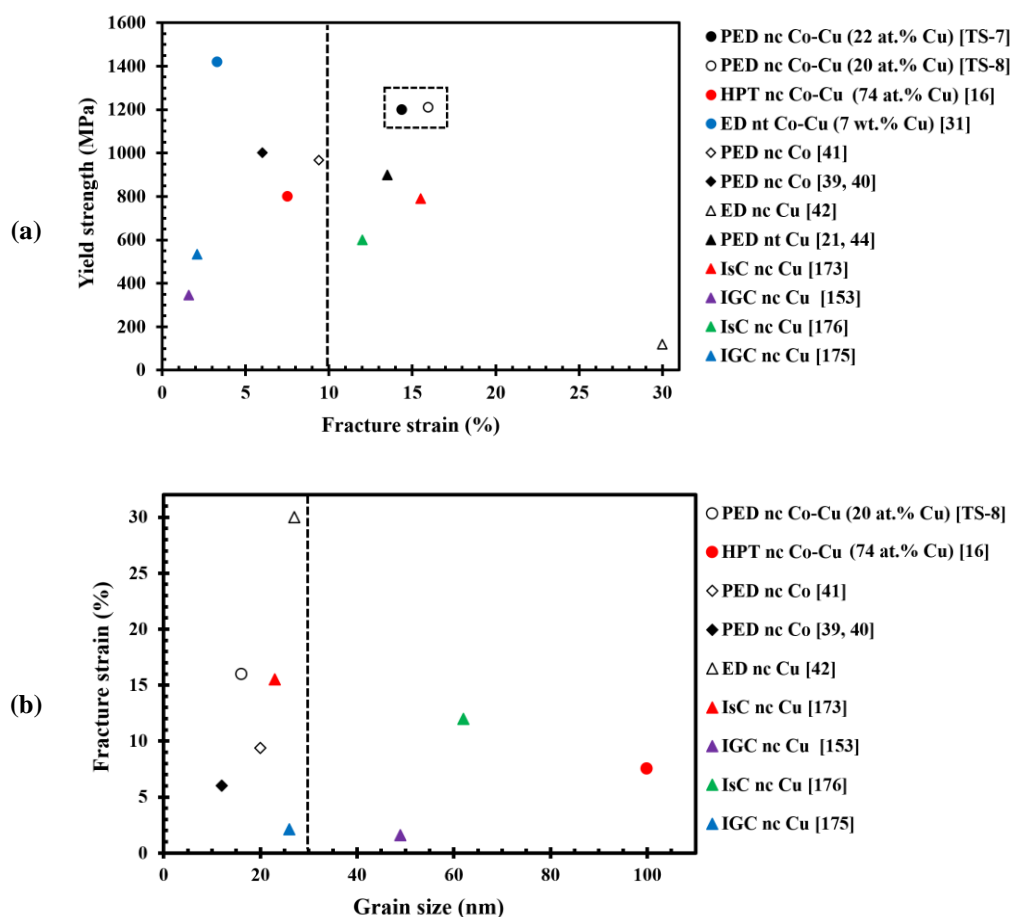


Figure 7.16 Compilation of data of the yield strength and the fracture strain of various nanocrystalline and nanotwin Cu, Co, and Co-Cu: (a) yield strength vs. fracture strain; (b) fracture strain vs. grain size. Data were collected from literatures (see the reference number in the legend notes of the respective data).

Comparison of the PED-processed nanocrystalline Co-Cu (20-22 at.% Cu) with other nanocrystalline Co, Cu, and Co-Cu is discussed. **Figure 7.16a** depicts a compilation of data of yield strength vs. fracture strain of the various nanocrystalline Co, Cu, and Co-Cu. In addition, the effect of grain size to ductility of nanocrystalline Co, Cu, and Co-Cu are also plotted in **Figure 7.16b**. The graphs show that PED-processed nanocrystalline Co-Cu alloys exhibit the highest strength compared to nanocrystalline Co and Cu. Strengthening mechanism in the PED-processed nanocrystalline Co-Cu alloys may be influenced by some factors. *First*, the grain size of PED-processed nanocrystalline Co-Cu was ~16 nm, and this number is the 2nd smallest compared to other materials (see **Figure 7.16b**). This results in grain boundary or grain size reduction strengthening (Hall-Petch effect), which improved the yield strength of this material. *Second*, PED-processed nanocrystalline Co-Cu exhibited a supersaturated solid solution phase with fcc structure, whereas solid solution strengthening can be expected. For instance, PED-processed nanocrystalline Co [39, 40] has a smaller grain size than nanocrystalline Co-Cu (see **Figure 7.16b**), but nanocrystalline Co-Cu shows a higher yield strength which may be contributed by solid solution strengthening. *Third*, a number and size of processing flaws may have an impact to the yield strength. Processing flaws (e.g. porosity) have been reported as a major challenge to achieve a high ductility in nanocrystalline materials, thus, a very high strength was rarely observed due to early failure. In contrast, the PED-processed nanocrystalline Co-Cu (samples TS-7 and TS-8) showed a very small number and size of processing flaws (e.g. porosity, crystal growth borders, etc.) Moreover, the size of pore in the PED-processed nanocrystalline Co-Cu was significantly smaller than the critical size of pore for brittle fracture, in which brittle fracture from the pore was not expected in this material.

Figure 7.16a shows that PED-processed nanocrystalline Co-Cu alloys exhibit a high ductility compared to other nanocrystalline Co and Cu. According to data, only ED-processed nanocrystalline Cu [42] has a higher fracture strain than PED-processed nanocrystalline Co-Cu, but a yield strength of this material is very low even compared with other nanocrystalline Cu. It is believed that an improved strength and ductility of PED-processed nanocrystalline Co-Cu is highly contributed by a low number and a small size of processing flaws (e.g. porosity, crystal growth borders, etc.). The effect of grain size to ductility has been reported elsewhere [172], whereas a low ductility in nanocrystalline materials may be influenced by a very small grain size of below 50 nm. However, **Figure 7.16b** show that a very small grain size may have a low impact to ductility, whereas the fracture strain of beyond 10% are observed from materials having a grain size of below 30 nm. There is no conclusion can be made concerning the grain size effect to ductility.

The PED-processed nanocrystalline Co-Cu (20-22 at.% Cu) shows a significantly higher ductility compared to ED-processed nanotwin Co-Cu (7 wt.% Cu) [31]. Of course, ED-processed nanotwin Co-Cu has a higher yield strength, but the maximum/ultimate tensile strength of this material (1857 MPa) is slightly lower than PED-processed nanocrystalline Co-Cu (1950-1980 MPa). ED-processed nanotwin Co-Cu (7 wt.% Cu) may have a lower strain hardening capacity than PED-processed nanocrystalline Co-Cu, which may have an impact to a lower ductility in this material. However, the reason of low ductility of ED-processed nanotwin Co-Cu (7 wt.% Cu) was not clearly explained by the authors [31]. Comparing with the HPT-processed nanocrystalline Co-Cu (74 at.% Cu) [16], PED-processed nanocrystalline Co-Cu (20-22 at.% Cu) showed a higher strength and ductility. However, it must be noticed that fracture strain measurement for HPT-processed nanocrystalline Co-Cu (74 at.% Cu) was performed at a strain rate of $1 \times 10^{-3} \text{ s}^{-1}$, which is a ten times higher than the strain rate used in the present work ($1 \times 10^{-4} \text{ s}^{-1}$). Bachmaier et al. [16] showed that the elongation to fracture increased to ~12% with decreasing strain rate to $2 \times 10^{-4} \text{ s}^{-1}$. The fracture strain may increase with reducing strain rate to $1 \times 10^{-4} \text{ s}^{-1}$ (used in the present work), thus, the fracture strain of HPT-processed nanocrystalline Co-Cu (74 at.% Cu) may be similar with the PED-processed nanocrystalline Co-Cu (20-22 at.% Cu). Discussion should be focussed more on the differences of the yield strength. In comparison with HPT-processed nanocrystalline Co-Cu (74 at.% Cu) [16], a significant improvement of the yield strength was found in PED-processed nanocrystalline Co-Cu (20-22 at.% Cu). This may be contributed by some factors, these are: (i) grain size reduction/grain boundary strengthening (Hall-Petch effect), whereas the grain size of this material (~16 nm) is 5-6 times smaller than HPT-processed nanocrystalline Co-Cu (74 at.% Cu); (ii) a higher concentration of Co; (iii) the different types and numbers of lattice defects (e.g. number of twins, dislocation density, etc.), whereas twin structures are observed in this material as shown in **Figure 7.6**; (v) co-deposition of impurity elements (e.g. sulphur).

Chapter 8 – Fatigue properties of bulk nanocrystalline Co-Cu

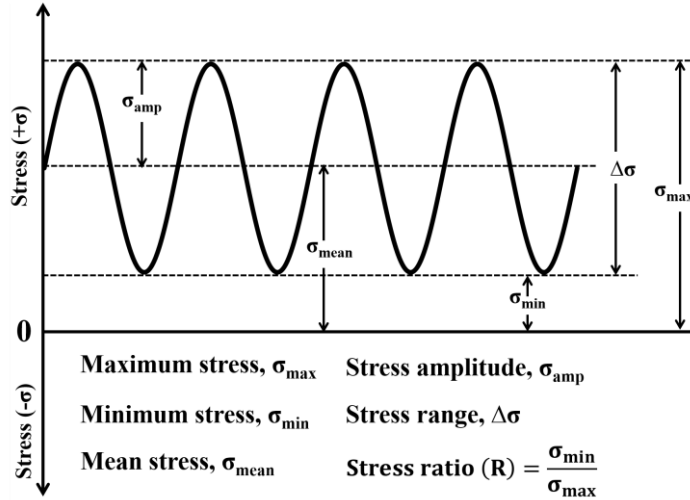


Figure 8.1 Schematic picture of stress profile used in the stress-controlled fatigue test. Fatigue tests parameters for constant amplitude test (CAT) and load increase test (LIT) are shown in **Table 8.1** and **Table 8.2**, respectively.

8.1. Fatigue test methods

The fatigue behaviour of the PED-processed nanocrystalline Co-Cu was studied by using TS-8 samples showing the highest ductility in the previous chapter (see **Chapter 7**). This sample exhibits a tensile yield stress, an ultimate tensile stress, and a fracture strain of 1.21 ± 0.08 GPa, 1.98 ± 0.03 GPa, and $15.95 \pm 0.09\%$, respectively. The samples were deposited at a pulse current density, a duty cycle, and a pulse-on time of 1000 A/m^2 , 10%, and 0.3 ms, respectively. The sample's dimension is similar with the tensile specimen as shown in **Figure 3.4b**. Stress-controlled fatigue tests were performed in two different modes: (i) constant amplitude/load test (CAT) and (ii) load increase test (LIT). **Figure 8.1** shows a schematic picture of the stress profile used in the stress-controlled fatigue tests. The stress level was varied in the present work, while the stress ratio (R) was kept constant at 0.1 for all experiments. The mean stress, stress range, and stress amplitude are calculated through the following equations:

$$\sigma_{\text{mean}} = \frac{(\sigma_{\max} + \sigma_{\min})}{2} \quad [8.1]$$

$$\Delta\sigma = \sigma_{\max} - \sigma_{\min} \quad [8.2]$$

$$\sigma_{\text{amp}} = \sigma_{\max} - \sigma_{\text{mean}} \quad [8.3]$$

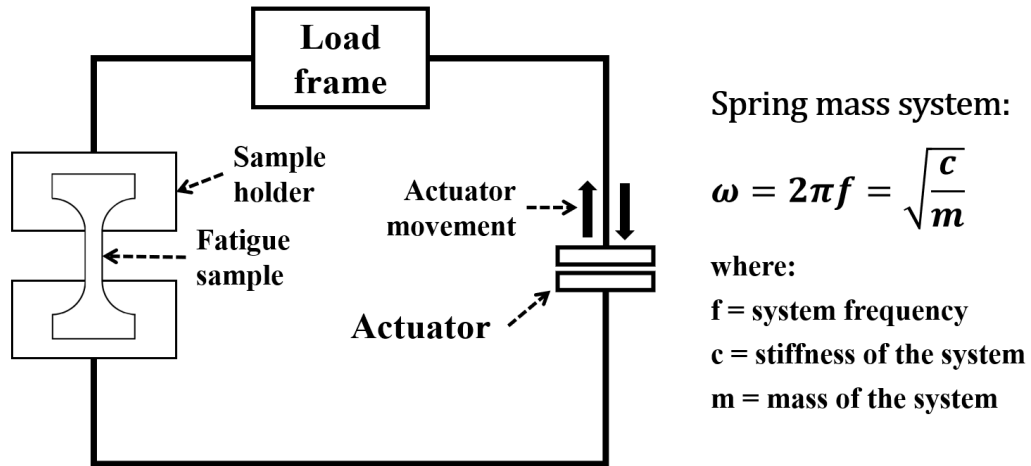


Figure 8.2 Schematic picture of the resonant fatigue testing machine showing some important components such as the load frame, the actuator, the fatigue sample, and the sample holder.

The resonant fatigue testing machine was used in the present work and the schematic picture of this machine is shown in **Figure 8.2**. This machine works based on the spring mass system, whereas the system frequency (f) is a function the stiffness of the system (c) as described in **Figure 8.2**. Thus, the system frequency may predict the stiffness behaviour during cyclic loading. The stiffness of the system is a function of factors coming from the fatigue sample, sample holder, machine, and others. For instance, a decrease of frequency may indicate a lower stiffness of the system, which may correspond to factor such as crack formation and propagation. In contrast, an increase of frequency may correspond to an increase of stiffness of the system, which may be attributed to some factors such as sample alignment, clamping of the sample holder, and others.

Table 8.1 Stress parameters that were used in constant amplitude/load fatigue test (CAT). Stress ratio was kept constant at 0.1. Description of the fatigue test parameters are shown in **Figure 8.1** (NA = Not available).

Name of sample	Thickness (mm)	Maximum Stress (MPa)	Mean Stress (MPa)	Amplitude Stress (MPa)	Stress Range (MPa)	Cycles to failure
CAT-I	0.55	397.9 ± 2.7	217.9 ± 2.7	180.0 ± 0.1	360.0 ± 0.2	64,237
CAT-II	0.55	301.6 ± 0.6	166.6 ± 0.6	135.0 ± 0.1	270.0 ± 0.1	831,193
CAT-III	0.42	148.1 ± 1.2	82.6 ± 1.2	65.5 ± 0.0	131.0 ± 0.0	276,013
CAT-IV	0.55	180.6 ± 0.5	98.8 ± 0.5	81.8 ± 0.0	163.6 ± 0.0	366,367
CAT-V	0.50	109.4 ± 1.5	60.3 ± 0.7	49.1 ± 1.3	98.3 ± 2.5	NA

Five constant amplitude/load test (CAT) and two load increase test (LIT) samples were subjected to stress-controlled fatigue tests at different stress levels as shown in **Table 8.1** and **Table 8.2**. The frequency of the system data was recorded during fatigue test for predicting the

stiffness of the system. Strain measurements of fatigue samples were recorded from the cross-head displacement. Displacement data of CAT-I and CAT-II samples was not recorded by coincidence. The displacements data of CAT-V and LIT-II samples were additionally recorded by using the video-extensometer for validation of cross-head displacement.

Table 8.2 Stress parameters that were used in load increase fatigue test (LIT). Stress ratio is kept constant at 0.1. Description of the fatigue test parameters are shown in **Figure 8.1**.

Name of sample	Thickness (mm)	Maximum Stress (MPa)	Mean Stress (MPa)	Amplitude Stress (MPa)	Stress Range (MPa)	Number of cycles
LIT-I	0.39	131.1 ± 1.1	73.4 ± 0.9	57.8 ± 0.8	115.5 ± 1.5	1,000,000
		157.8 ± 0.9	87.5 ± 0.9	70.3 ± 0.0	140.6 ± 0.1	1,000,000
		180.5 ± 1.0	98.4 ± 1.0	82.0 ± 0.0	164.1 ± 0.0	200,724
LIT-II	0.50	107.1 ± 1.8	60.2 ± 0.6	46.9 ± 1.4	93.7 ± 2.8	1,000,000
		121.5 ± 1.2	68.9 ± 0.8	52.6 ± 0.5	105.3 ± 0.9	1,000,000
		130.9 ± 1.2	73.3 ± 1.0	57.6 ± 0.6	115.2 ± 1.1	1,000,000
		141.8 ± 1.3	78.1 ± 0.8	63.7 ± 0.8	127.4 ± 1.6	1,000,000
		152.9 ± 0.4	83.7 ± 0.4	69.2 ± 0.1	138.4 ± 0.2	876,864

8.2. Constant amplitude fatigue test

Constant amplitude fatigue test of CAT-I sample was performed at the highest stress levels compared to other samples (see **Table 8.1**), which is about ~33% of the yield strength. Crack formation with a length of 1.55 mm was observed after 64,237 load cycles (see **Figure 8.3a**). **Figure 8.3b** shows a slight increase of Δ frequency up to ~58,000 load cycles (X-position), which may be caused by factor such as a sample alignment. Δ Frequency starts to decline at this load cycle, which may be attributed to crack initiation as marked with a black arrow in **Figure 8.3b**. The decline of Δ frequency is more pronounced in the following load cycles indicating crack propagation. BSE image of the microstructure at the area next to the crack tip (**Figure 8.3c**) shows no significant change of microstructure (e.g. grain coarsening) as observed in the cyclic bending test of the micro beam of supersaturated solid solution nanocrystalline Co-Cu (see **Chapter 6**). Interestingly, the crack branching is observed in BSE image (marked with the white arrows in **Figure 8.3c**), which may be attributed to interaction between crack propagation or movement and dislocation processes with the microstructure surrounding the crack.

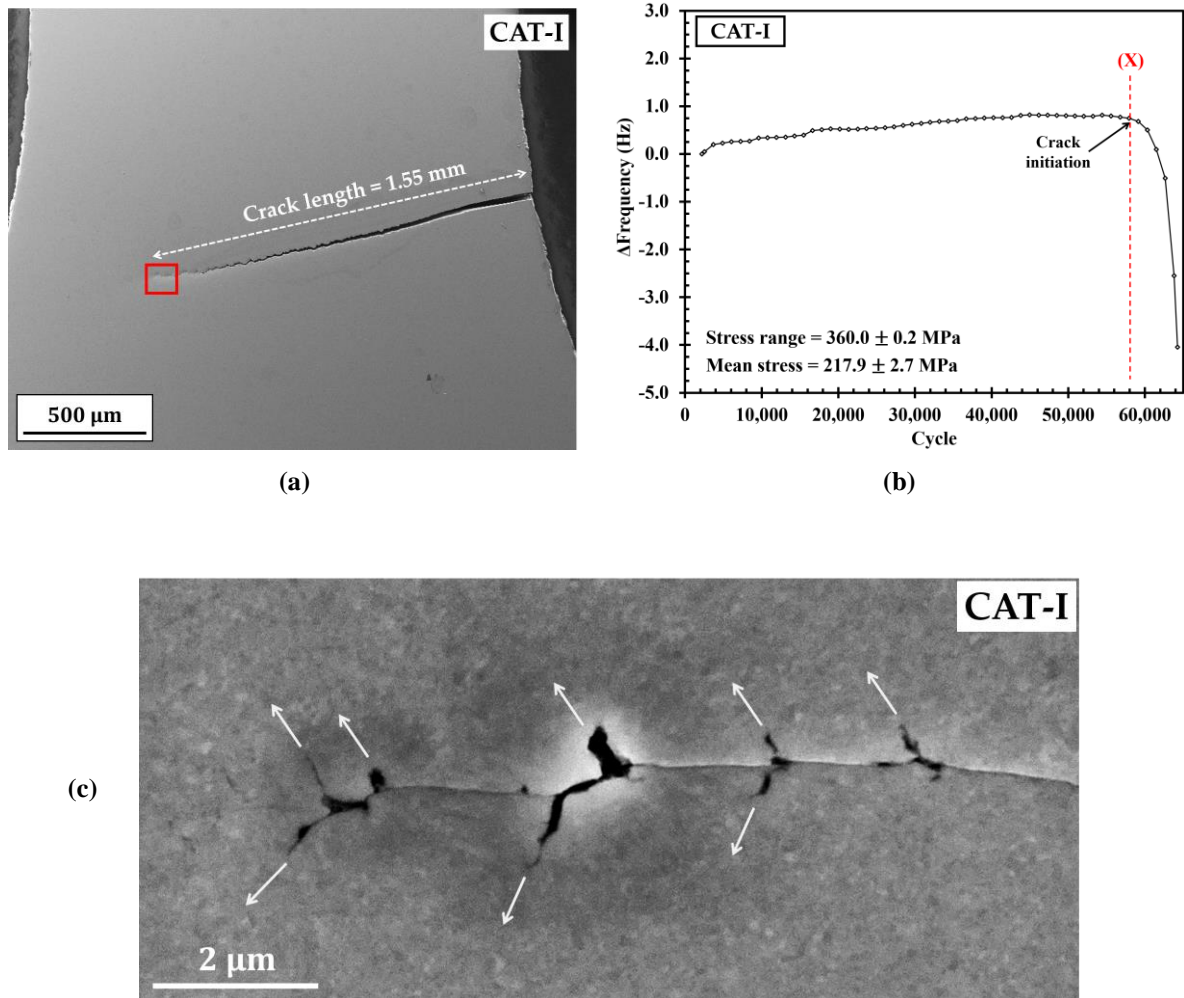


Figure 8.3 (a) Secondary electron image of surface morphology of CAT-I sample after 64,237 load cycles showing a crack formation. (b) Δ Frequency profile as a function of load cycles from fatigue test of CAT-I sample. (c) Back-scattered electron image of microstructure at the area marked with red rectangular shape in (a).

The constant amplitude fatigue test of CAT-II sample was conducted at a lower stress level compared to CAT-I sample (see **Table 8.1**). Maximum stress of CAT-II sample is proportional to ~25% of the yield strength. Surface morphology of CAT-II sample (see **Figure 8.4a**) depicts a total fracture with moderate necking after 831,193 load cycles. **Figure 8.4b** shows a slight increase of Δ frequency from initial to ~300,000 load cycles (A-position), which may be caused by the sample alignment. Δ Frequency starts to decrease at this point (A-position), which may be attributed to crack initiation. Afterwards, slight decrease of Δ frequency remains visible at the following load cycles up to the ~810,000th load cycle (B-position in **Figure 8.4b**), which may correspond to slow fatigue crack growth. Δ Frequency drops drastically after the ~810,000th load cycle (B-position) as indication of rapid fatigue crack growth. **Figure 8.4c** shows the fracture surface images of CAT-II sample, observing three regions with different surface characteristics. The first region shows a brittle fracture surface, which could be the origin of the

crack (region-i in **Figure 8.4c**). The second region depicts a different fracture surface with striation morphology, which corresponds to slow fatigue crack growth (region-ii **Figure 8.4c**). The third region observes a ductile fracture surface with dimple structures at a necking position, whereas crack propagation until failure may occur at this region (region-iii in **Figure 8.4c**).

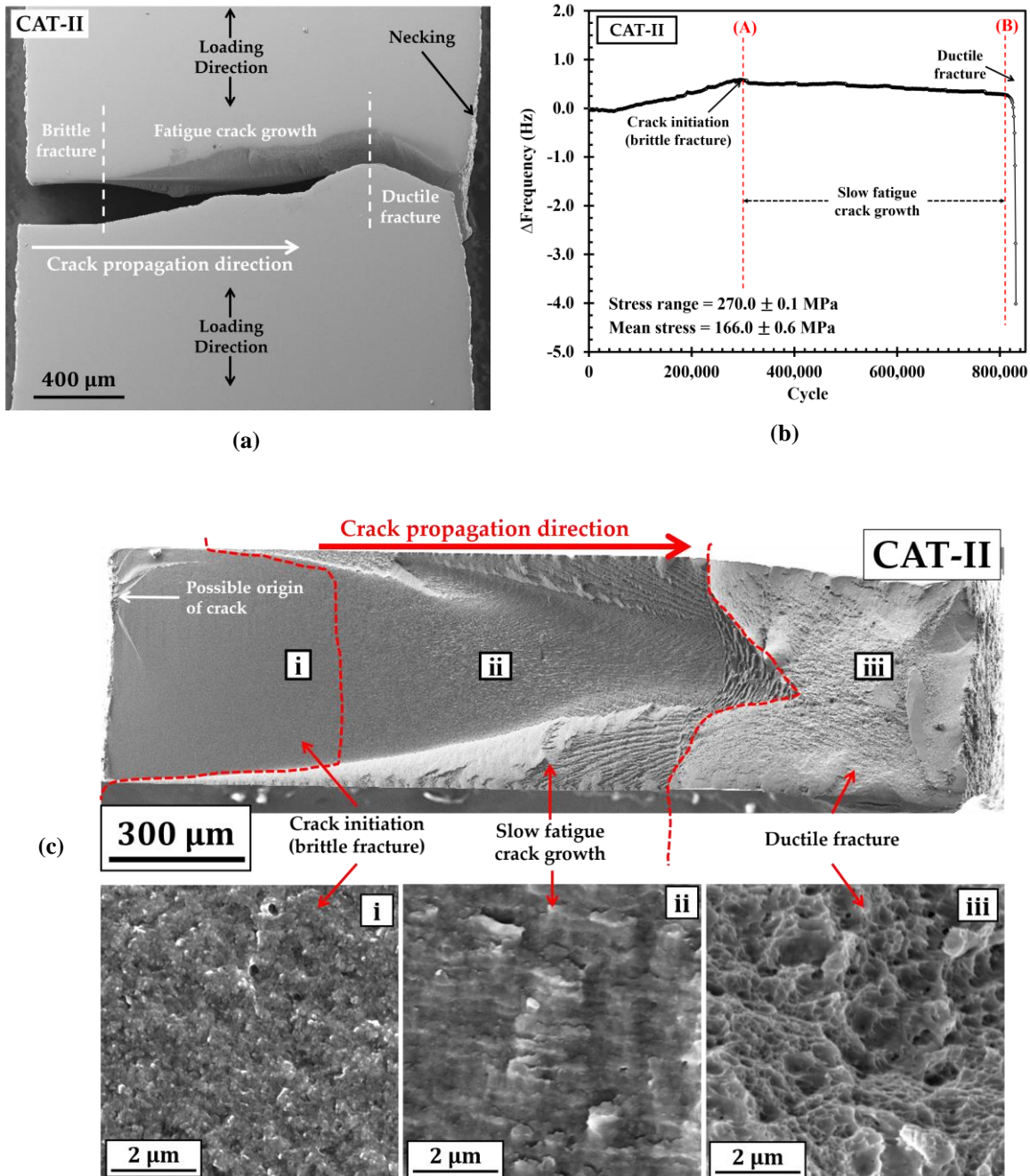


Figure 8.4 (a) Secondary electron (SE) image of surface morphology of CAT-II sample after 831,193 load cycles showing materials rupture with necking. (b) Δ Frequency profile as a function of load cycles from stress-controlled fatigue test of CAT-II sample. (c) SE electron image of fracture surface of CAT-II sample showing different characteristic of fracture surface: (i) brittle fracture surface (crack initiation region), (ii) slow fatigue fracture surface, and (iii) ductile fracture surface.

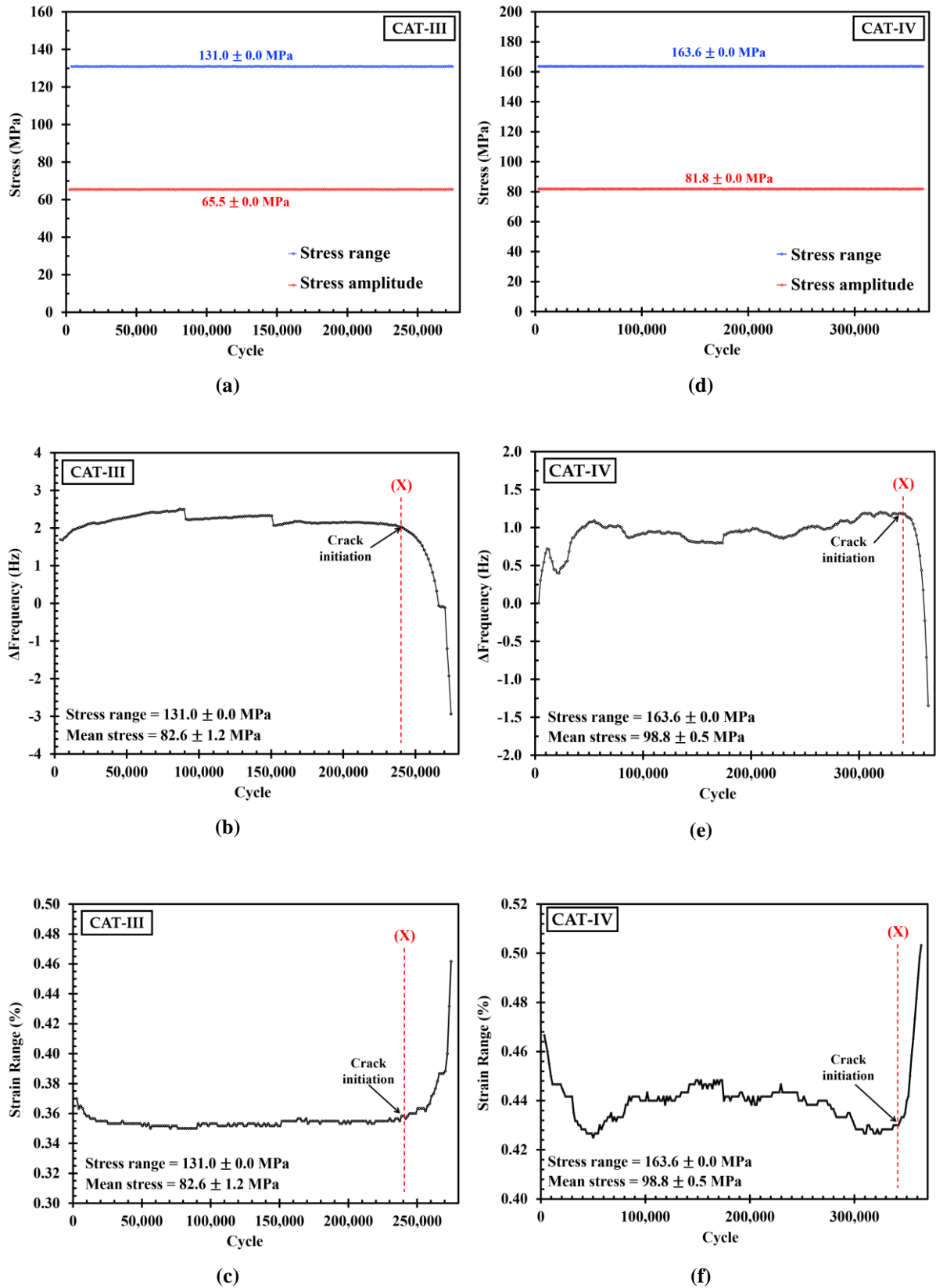


Figure 8.5 Stress level, Δ frequency, and strain range profiles as a function of load cycles from stress-controlled fatigue tests of (a-c) CAT-III and (d-f) CAT-IV samples. Strain measurement was recorded from cross-head displacement.

The constant amplitude fatigue tests of CAT-III and CAT-IV samples were performed at maximum stress and stress range of below 200 MPa as shown in **Table 8.1** and **Figure 8.5a,d**. **Figure 8.5b,e** show that Δ frequency of CAT-III and CAT-IV samples increase initially for $\sim 50,000$ load cycles, which may be caused by the sample alignment. The Δ frequency of CAT-III and CAT-IV samples decline after $\sim 240,000$ and $\sim 340,000$ load cycles (X-position in **Figure 8.5b,e**) indicating that crack initiation and propagation may be occurred. Strain range of CAT-III and CAT-IV samples (**Figure 8.5c,f**) are quiet constant up to the $\sim 240,000^{\text{th}}$ and $\sim 340,000^{\text{th}}$ load cycle (X-position), respectively. Strain range of CAT-III and CAT-IV samples start to increase at these load cycles (X-position) which may correspond to crack initiation. The increase of strains are more pronounced at the following load cycles which is attributed to crack propagation. Cracks with a length of ~ 1 mm were observed in CAT-III and CAT-IV samples after 276,013 and 366,367 load cycles, subsequently.

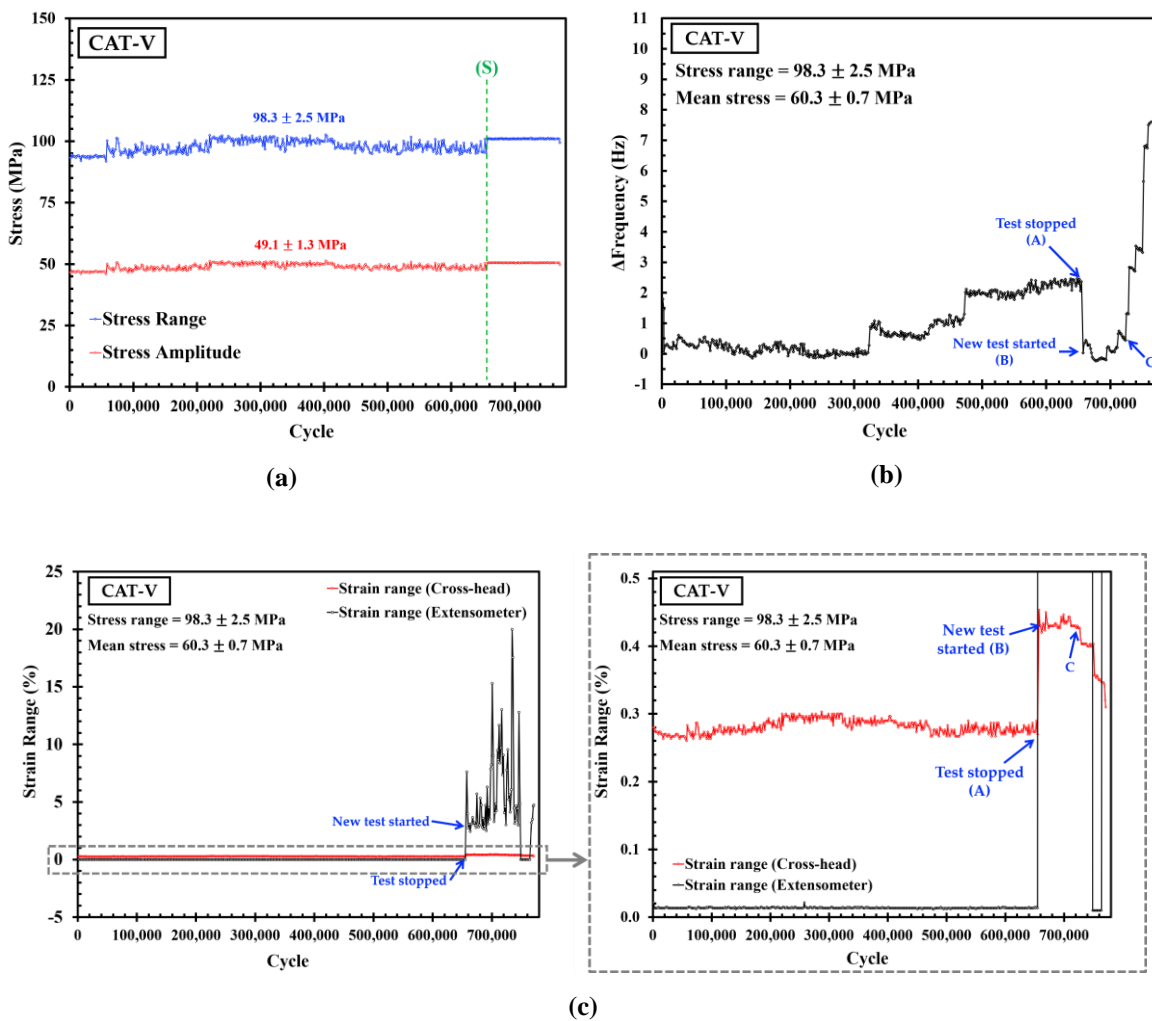


Figure 8.6 (a) Stress levels, (b) Δ frequency, and (c) strain range as a function of load cycles from stress-controlled fatigue test of CAT-V sample. Strain measurements were recorded from cross-head displacement and video extensometer.

The constant amplitude fatigue test of CAT-V sample was performed at the lowest stress levels as shown in **Table 8.1** and **Figure 8.6a**. The test was interrupted accidentally at the $\sim 660,000^{\text{th}}$ load cycle (S-position in **Figure 8.6a**) due to system failure. The test could be started again at a similar stress level up to (in total) 770,807 load cycles with no crack formation or failure detected. A significant increase of Δ frequency of 2 Hz is observed from initial to A-position, which may correspond to some factors such as sample alignment (see **Figure 8.6b**). The Δ frequency is rather constant from the $\sim 660,000^{\text{th}}$ load cycle (B-position) to the $\sim 710,000^{\text{th}}$ (C-position) load cycle, but it increases drastically up to 10 Hz in the following load cycles. Strain measurement of CAT-V sample was performed by measuring cross-head displacement and displacement with a video-extensometer. However, the strain measurement from a video-extensometer is extremely unstable as shown in the strain range profile (**Figure 8.6c**). The strain measurement from cross-head displacement is more reliable for analysis. The significant decrease of strain range and strain amplitude is observed mainly after the $\sim 710,000^{\text{th}}$ load cycle (C-position in **Figure 8.6c**), which may be caused by an error in the measurement.

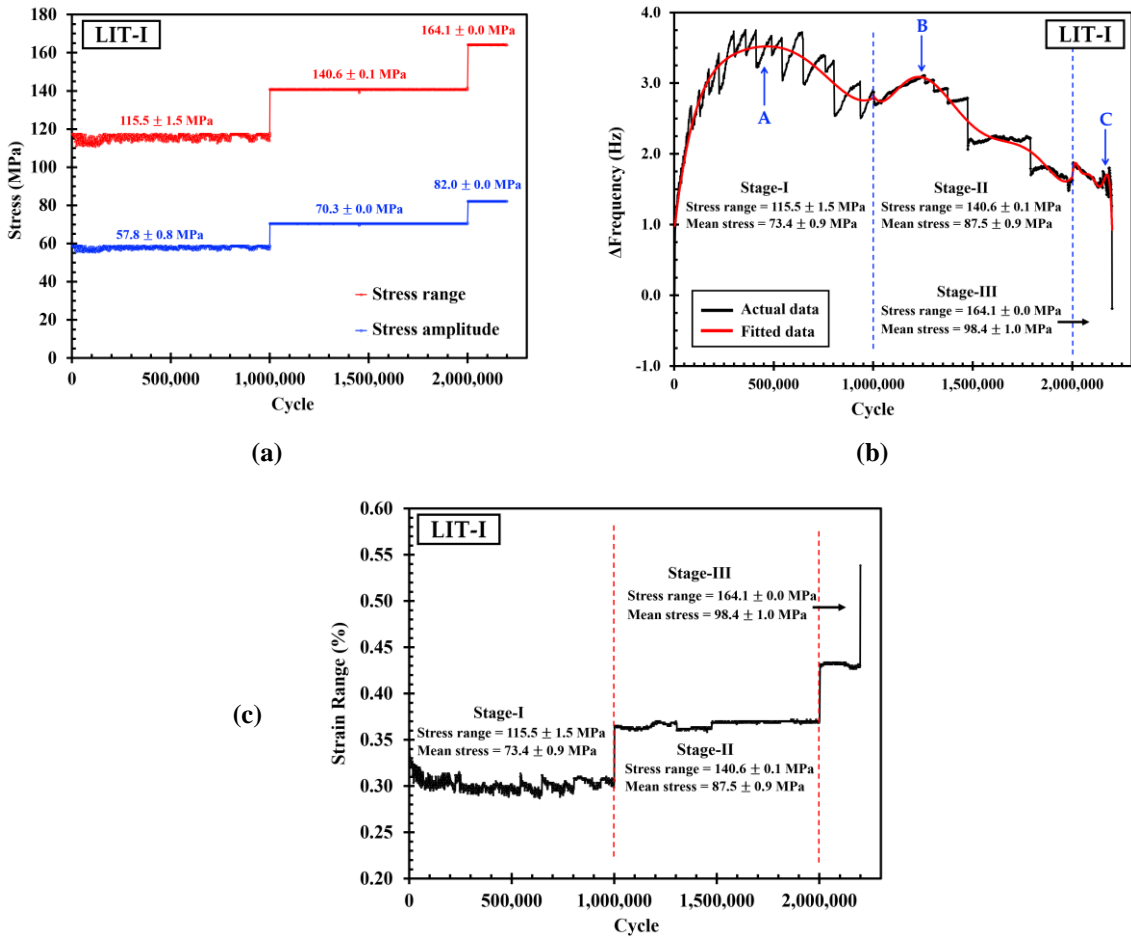


Figure 8.7 (a) Stress level, (b) Δ frequency, and (c) strain range profiles as a function of load cycles from stress-controlled fatigue test of LIT-I sample. Strain measurements were recorded from cross-head displacement.

8.3. Load increase fatigue test

The fatigue test of LIT-I sample was performed at three different stages of stress levels as shown in **Table 8.1** and **Figure 8.7a**. The first and second stage of fatigue tests were conducted individually for 1 million load cycles, while the third stage fatigue test was performed until failure (200,724 load cycles). A 0.76 mm length crack at shoulder section and a dent at gauge section were observed at the end of the fatigue test. Upon the stage-I and stage-II of fatigue test, Δ frequency increases from initial to peak position (marked with A- and B-position in **Figure 8.7b**), but it decreases gradually for the rest of cycles in the individual stages. The A- and B-positions correspond to the $\sim 450,000^{\text{th}}$ and $\sim 1,250,000^{\text{th}}$ load cycle, respectively. A significant increase of Δ frequency may be caused by the alignment of the sample or even error in the measurement. In contrast, the decrease of Δ frequency in LIT-I sample may be attributed to crack initiation and propagation. Strain analysis was performed (see **Figure 8.7c**) and show that strain range profile is rather constant upon the stage-I and stage-II. Upon the stage-III fatigue test, rapid crack propagation is also confirmed from strain analysis, whereas strain range increases significantly. Further investigation is needed for validation of the significant increase and decrease of strain and Δ frequency, respectively, which can be influenced by some factors such as the sample alignment, error in the measurement, or even the hardening effect.

The fatigue test of LIT-II sample was performed at five different stages of stress level as shown in **Table 8.1** and **Figure 8.8a**. Individual stages of the fatigue test were performed for 1 million load cycles, but the stage-V fatigue test failed after 876,864 load cycles. **Figure 8.8b** shows a gradual increase of Δ frequency upon the stage-I, -II, -III, and -IV of fatigue test, which could be an indication of sample alignment. In contrast, Δ frequency starts to decrease after $\sim 300,000$ load cycles of stage-V, which may be attributed to crack initiation and propagation. Strain measurement of LIT-II sample was recorded from cross-head displacement and video-extensometer. However, strain measurement from video-extensometer is extremely unstable as shown in the strain range profile (**Figure 8.8c**), thus, the data is not reliable for strain analysis. Strain analysis from cross-head displacement (detailed figure in **Figure 8.8c**) shows a slight decrease of strain range upon the stage-I, -II, -III, and -IV of fatigue test confirming sample alignment as observed in Δ frequency analysis. **Figure 8.8c** also depicts an increased strain range after $\sim 300,000$ load cycles of stage-V, which could be an indication of crack initiation and propagation.

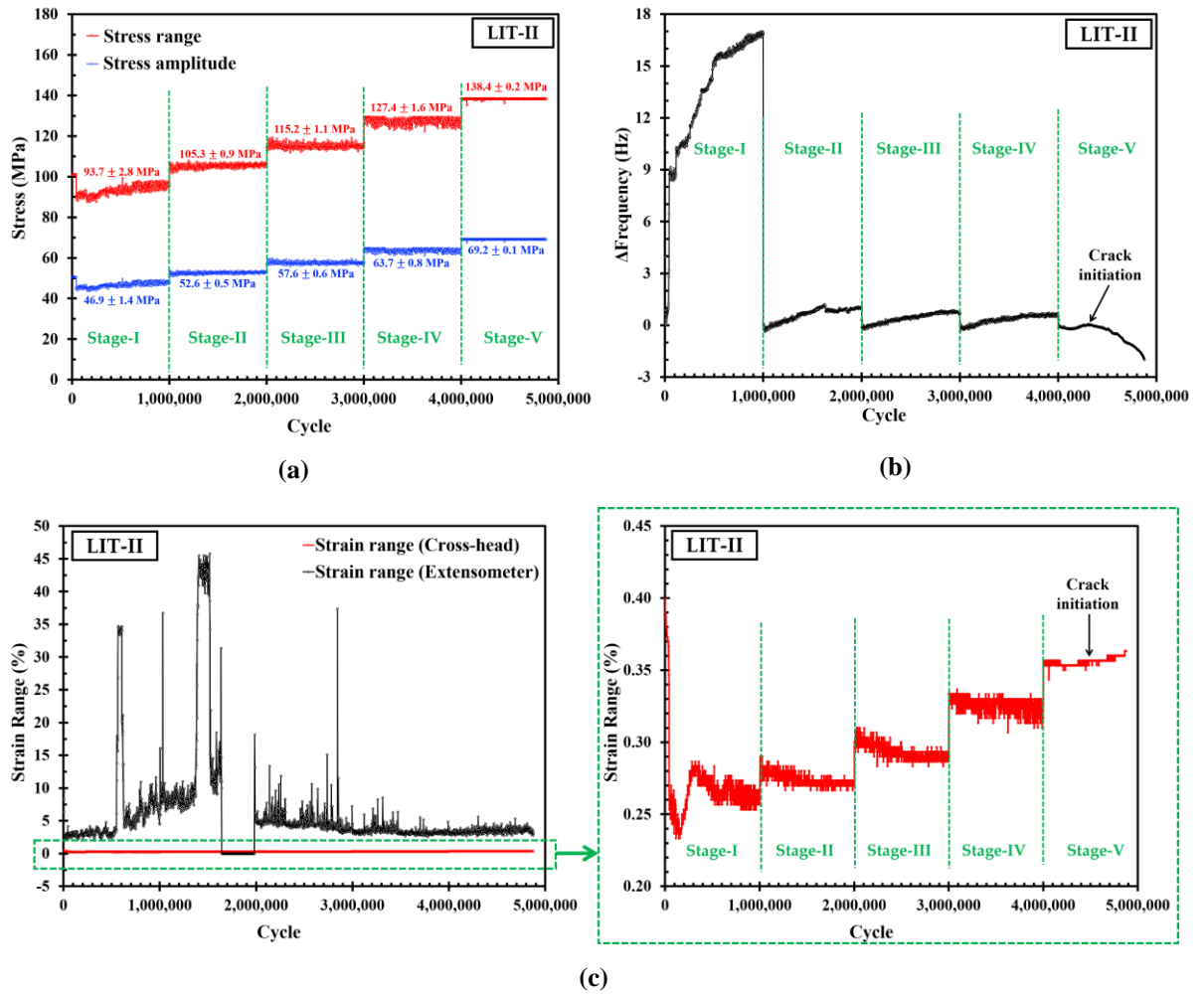


Figure 8.8 (a) Stress level, (b) Δ frequency, and (c) strain range profiles as a function of load cycles from stress-controlled fatigue test of LIT-II sample. Strain measurements were recorded from cross-head displacement and video extensometer.

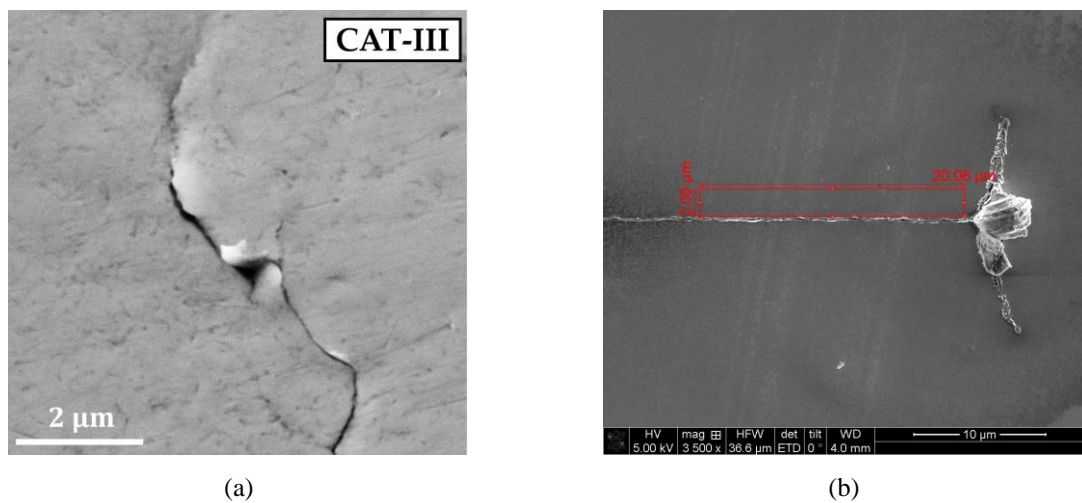


Figure 8.9 (a) Secondary electron (SE) image of surface morphology of CAT-III sample shows plastic strain at the area nearby the crack tip. (b) Secondary electron (SE) image shows the actual position for APT lift-out nearby the crack tip indicated by a red rectangular shape.

8.4. Microstructure change during fatigue test

Fatigue tests of bulk nanocrystalline Co-Cu have been performed and show some interesting results. The increase of Δ frequency is observed in all fatigue tests which may be attributed to some factors such as the sample alignment, error in the measurement, or even a hardening effect. Discussion should be focussed on the possible hardening mechanism upon mechanical cyclic loading. Accumulation of plastic strain and dislocation processes may have an impact to hardening during fatigue test. In nanocrystalline Co-Cu, a hardening effect may correspond to spinodal decomposition of solid solution Co-Cu. Further investigation is needed for investigation of the possible spinodal decomposition during mechanical cyclic loading in nanocrystalline Co-Cu and the influence on the elastic modulus

One sample is selected for microstructural investigation. **Figure 8.9a** shows a surface morphology image of CAT-III sample observing significant plastic strains at the area nearby the crack tip. This region may experience a higher stress level compared to other positions due to stress concentration at the crack tip. As a consequence, high accumulation of local plastic strain is expected at this position, which may lead to Co and Cu elemental diffusion and spinodal decomposition. Atom probe tomography (APT) measurements were performed at this selected position as marked with a red rectangular shape in **Figure 8.9b** and two APT reconstructions were made at this position.

Figure 8.10a,b show combined APT elemental maps with iso-concentration surface at 40 at.% Cu and 70 at.% Co and their one-directional concentration profiles from reconstruction-I and reconstruction-II. Regarding chemical composition, solid solution composition of this nanocrystalline Co-Cu should consists of 20-35 at.% Cu and 65-80 at.% Co. Interestingly, small compositional fluctuations up to 50 at.% Cu are observed from these APT reconstructions. In addition, APT elemental maps shows a quiet large region with iso-concentration surfaces at 40 at.% Cu. These compositional fluctuations may be influenced by some factors, for instance, inhomogeneous chemical distribution and in-progress spinodal or chemical decomposition during cyclic loading. Further analysis is needed for revealing the maximum concentration of Co or Cu in these APT reconstructions. For revealing the maximum concentration of Cu, iso-concentration surface was increased up to 50 at.% Cu, which is quiet far from the solid solution composition of 20-35 at.% Cu. **Figure 8.10c** shows the APT elemental maps from reconstruction-I show a small region with Cu concentration of higher than 50 at.%. The one-directional concentration profile in this reconstruction reveals that the maximum concentration of Cu is ~55 at.%. However, this Cu concentration is not high enough to prove whether there is a decomposition. More analysis are needed for further measurements.

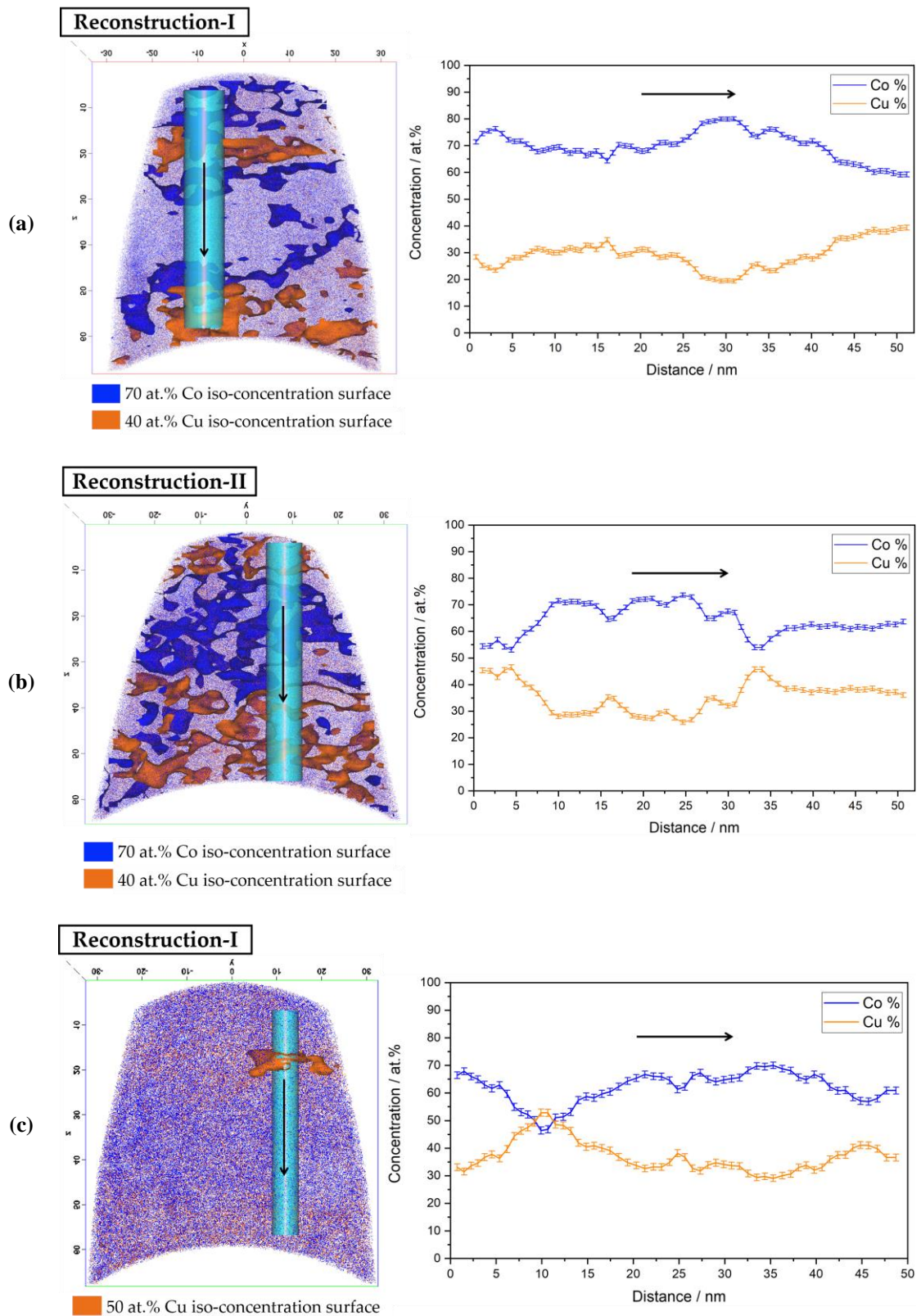


Figure 8.10 Combined APT elemental maps and iso-concentration surface profiles at 40 at.% Cu and 70 at.% Co from (a) reconstruction-I and (b) reconstruction-II. (c) Combined APT elemental maps and iso-concentration surface profiles at 50 at.% Cu from reconstruction-I. (a-c) The one-dimensional concentration profiles were constructed from blue vertical tubes on the respective elemental maps (black arrows: measurement direction). Length scale is in nm.

8.5. Discussion of the results in Chapter 8

The constant amplitude fatigue tests (CAT) and load increase fatigue tests (LIT) of PED-processed supersaturated solid solution nanocrystalline Co-Cu have been performed. This material could withstand for few million load cycles at a maximum stress of ~100 MPa (~10% of yield strength), which could be the endurance limit of this material. This number is low compared to coarse grain materials with endurance limit of ~40-50% of their yield strength. The cycles to failure of nanocrystalline Co-Cu declined with increasing the maximum stress level. For instance, the cycles to failure at the highest maximum stress level of ~400 MPa (~33% of yield strength) is only ~65,000 load cycles. Further improvement is needed to improve the fatigue resistance of PED-processed nanocrystalline Co-Cu.

In the fatigue tests of PED-processed nanocrystalline Co-Cu, the increase of frequency were observed in all fatigue tests. In the present work, the sample size was very small compared to the whole system (sample, sample holder, and testing machine), thus, interpretation of the system frequency or the stiffness of the system will be complicated since it may be caused by several factors. It is likely that alignment of the small sample is a major challenge, whereas an increase of frequency was commonly observed at the initial load cycles of fatigue test. Of course, there was a sample having a significant increase of frequency and a significant decrease of strain measurement at the end of the test (e.g. CAT-V). However, the strain measurement from cross-head displacement is not accurate enough, while the strain measurement from a video-extensometer was extremely unstable. In addition, error in measurement is highly possible due to very small sample used in the present work.

A possible hardening effect including an increase in elastic modulus from a significant increase of frequency cannot be excluded for nanocrystalline materials. In the coarse grain materials, the stiffness or elastic modulus does not change even after thermal or mechanical loading (e.g. annealing, cold rolling, etc.), which lead to the microstructural change and increase/decrease of the strength. In nanocrystalline materials, the stiffness or elastic modulus may change due to microstructural changes (e.g. hardening, softening, etc.), which may be caused by the very small grain size and the large grain boundary regions. However, APT measurements did not observed a significant decomposition of Co and Cu (e.g. Co-/Cu-rich regions or extreme compositional fluctuation). Of course, some spots with concentration of Cu up to 55 at.% were observed, whereas this composition is far from the solid solution composition (20-35 at.% Cu). However, this may be attributed to the inhomogeneous chemical distribution, which can be found in the small volume observed from APT measurement. In the present, no conclusion can be made concerning of an increase of frequency.

Chapter 9 – Conclusion and Suggestions

9.1. Conclusion

Investigations on the synthesis, characterization, thermal and mechanical stability of pulsed electrodeposited (PED) processed Co-rich nanocrystalline Co-Cu have been performed. Some important results are obtained from the investigations, which can be summarized follows.

- i. Compact, thick, and homogeneous bulk samples of Co-rich nanocrystalline Co-Cu films have been successfully deposited through the pulsed electrodeposition (PED) technique. The recommended pulsed deposition parameters are pulse current density of 1000 A/m^2 , duty cycles of below 20%, and pulse-on times of below 2 ms. Two samples with different dimension were deposited. The first type of deposit with a surface diameter of 12 mm and thickness up to $\sim 400 \text{ }\mu\text{m}$ comprises of $\sim 28 \text{ at.}\%$ Cu. The second type of deposit with a surface area of $21 \times 21 \text{ mm}^2$ and thickness up to $\sim 700 \text{ }\mu\text{m}$ has a Cu content of lower than 25 at.%.
- ii. As deposited nanocrystalline Co-Cu (28 at.% Cu) with a surface diameter of 12 mm and thickness up to $\sim 400 \text{ }\mu\text{m}$ has a mean grain size of $22.7 \pm 8.2 \text{ nm}$. Nanocrystalline Co-Cu (28 at.% Cu) exhibits a supersaturated solid solution phase with face centered cubic (fcc) structure. Chemical composition at nanometer scale is not perfectly homogeneous, but short range fluctuation is not detected from APT measurements. As deposited nanocrystalline Co-Cu (28 at.% Cu) has a high microhardness of $4.45 \pm 0.07 \text{ GPa}$, which may be contributed by factors such as very fine grain size (Hall-Petch effect), solid solution strengthening, presence of twins, co-deposition of impurity elements (e.g. sulphur and carbon), and lattice defects.
- iii. PED-processed nanocrystalline Co-Cu (28 at.% Cu) showed an improved thermal stability compared with nanocrystalline pure Co and pure Cu. Spinodal decomposition of solid solution Co-Cu was detected at annealing temperature of 300°C , whereas 5-10 nm length of regions with high concentration of Co ($>95 \text{ at.}\%$) and Cu ($>90 \text{ at.}\%$). Spinodal decomposition have a contribution on the increase of hardness (i.e. hardening) at this annealing temperature. Grain coarsening in the PED-processed nanocrystalline Co-Cu may be started at 400°C , whereas ufg and nanocrystalline structures are observed with a slight decrease of hardness. Concentration of Cu have a contribution on the thermal stability of nanocrystalline Co-Cu, whereas there must be an optimum range of Cu

concentration for good thermal stability. Significant grain coarsening and distinct phase separation of solid solution Co-Cu were observed at the higher temperatures ($\geq 400^\circ\text{C}$). Phase decomposition of Co-Cu has a significant contribution for grain coarsening inhibition and improving the magnetic properties of very fine grain Co-Cu.

- iv. Static micro-bending test showed that PED-processed nanocrystalline Co-Cu (28 at.% Cu) has a combined high yield strength (2.5–3.8 GPa) and high ductility with no crack formation observed after deformation. Cyclic micro-bending test of nanocrystalline Co-Cu (28 at.% Cu) showed different effects (i.e. hardening and softening) at different plastic strain amplitudes. Accumulation of plastic strains may have a contribution on elemental/grain boundary diffusion and dislocation processes which may lead to hardening, softening, and grain coarsening in nanocrystalline Co-Cu during mechanical cyclic loading.
- v. Investigation on the bulk samples nanocrystalline Co-Cu (i.e. surface area of $21 \times 21 \text{ mm}^2$ and thickness up to $\sim 700 \text{ }\mu\text{m}$) showed that pulsed deposition parameters have significant impacts on the chemical composition, grain size and processing flaws characteristic (e.g. porosity, crystal growth borders, and internal stresses). These factors have significant impacts on strength and ductility. The tensile sample which was deposited at a pulsed current density of 1000 A/m^2 , a duty cycle of 10%, and a pulsed-on time of 0.3 ms having the highest strength and ductility. This sample (TS-8) exhibits a tensile yield stress, an ultimate tensile stress, and a fracture strain of $1.21 \pm 0.08 \text{ GPa}$, $1.98 \pm 0.03 \text{ GPa}$, and $15.95 \pm 0.09\%$, respectively. It is likely that the crystal growth borders and Cu concentration has the most significant impact to ductility of PED-processed nanocrystalline Co-Cu. An improve ductility can be achieved also through annealing at 200°C , which may be contributed by recovery processes (e.g. internal stresses release and grain boundary relaxation).
- vi. Investigation on fatigue test of bulk nanocrystalline Co-Cu samples (i.e. surface area of $21 \times 21 \text{ mm}^2$ and thickness up to $\sim 700 \text{ }\mu\text{m}$) were performed through the constant amplitude fatigue test (CAT) and load increase fatigue test (LIT) at different stress levels with the samples having the highest strength and ductility. The endurance limit of nanocrystalline Co-Cu could be $\sim 100 \text{ MPa}$ ($\sim 10\%$ of yield strength), which is low compared to the coarse grain materials with endurance limit of $\sim 40\text{-}50\%$ of their yield strength. The cyclic to failure of nanocrystalline Co-Cu declined with increasing the maximum stress level. For instance, the cyclic to failure at the highest maximum stress level of $\sim 400 \text{ MPa}$ ($\sim 33\%$ of yield strength) is only $\sim 65,000$ load cycles.

9.2. Suggestions

In the present work, investigations on the synthesis, thermal stability, microstructure evolution, micro mechanical properties, and bulk mechanical properties of PED-processed nanocrystalline Co-Cu have been performed. This materials showed an improved thermal stability and strength and ductility compared to the previous works in nanocrystalline Co, Cu, and Co-Cu. In addition, the materials showed a good potential for advanced electronic applications, whereas a strong magnetic domain patterns can be achieved with annealing.

Further improvements are needed concerning bulk mechanical properties of this material. The ductility of this material is high enough (fracture strain of 14-16%) compared to other nanocrystalline materials with a fracture strain of below 10%. However, it lacks important information such as (i) effect of grain size and impurities (e.g. sulphur, hydrogen) to ductility, (ii) deformation mechanism, (iii) further effect of annealing treatment, which leads to microstructural evolution (e.g. grain coarsening, spinodal and phase decomposition). Further investigation is needed in this field of research.

The author also suggest that improvement on the fatigue resistance and fracture toughness of bulk sample of this material is a must. This material exhibits ductile properties, however, if a small defect exists inside (e.g. small crack formation), this material tends to be brittle. It is believed that fracture toughness of this material is low, and it needs further investigation and improvement. Small size sample used in the fatigue testing would be also a major problem, thus, producing a bigger size of sample (standard fatigue specimen) is necessary for obtaining a more accurate data of mainly strain and frequency. This can be performed by optimizing the process parameters used for deposition (e.g. varying deposition parameters, electrolyte composition, and others). In addition, this may lead also to a further reduction of processing flaws (e.g. porosity and crystal growth borders), which could be the origin of crack during cyclic loading. Effect of annealing treatment, which leads to microstructural evolution (e.g. grain coarsening, spinodal and phase decomposition), to fracture toughness of needs further investigations. The decomposition of Co and Cu (metallic composite of Co and Cu) may lead to improvement of fracture toughness, since crack behaviour in Co and Cu phases will be different.

In the present work, it is believed that mechanical loading and plastic deformation in nanocrystalline materials may have an impact for spinodal decomposition. However, it is not clearly observed in this work. Further investigation is needed, for instance, by producing a homogeneous deposits of nanocrystalline Co-Cu with chemical composition of 50 at.% Co. In this composition, small change/compositional fluctuation will be easier to detect.

References

- [1] H. Gleiter, "Nanocrystalline Materials," *Progress in Materials Science*, vol. 33, pp. 223-315, 1989.
- [2] C. Suryanarayana and C. Koch, "Nanocrystalline materials - Current research and future direction," *Hyperfine Interactions*, vol. 130, pp. 5-44, 2000.
- [3] M. Meyers, A. Mishra and D. Benson, "Mechanical properties of nanocrystalline materials," *Progress in Materials Science*, vol. 51, pp. 427-556, 2006.
- [4] U. Erb, "Electrodeposited nanocrystals: Synthesis, properties, and industrial applications," *NanoStructured Materials*, vol. 6, pp. 533-538, 1995.
- [5] H. Gleiter, "Nanostructured materials: Basic concepts and microstructure," *Acta Materialia*, vol. 48, pp. 1-29, 2000.
- [6] U. Klement, U. Erb, A. El-Sherik and K. Aust, "Thermal stability of nanocrystalline Ni," *Materials Science and Engineering A*, vol. 203, pp. 177-186, 1995.
- [7] G. Hibbard, K. Aust, G. Palumbo and U. Erb, "Thermal stability of electrodeposited nanocrystalline cobalt," *Scripta Materialia*, vol. 44, pp. 513-518, 2001.
- [8] L. Lu, N. Tao, L. Wang, B. Ding and K. Lu, "Grain growth and strain release in nanocrystalline copper," *Journal of Applied Physics*, vol. 89, pp. 6408-6414, 2001.
- [9] V. Gertsman and R. Birringer, "On the room-temperature grain growth in nanocrystalline copper," *Scripta Metallurgica et Materialia*, vol. 30, no. 5, pp. 577-581, 1994.
- [10] C. Koch, "Ductility in nanostructured and ultra fine-grained materials: Recent evidence for optimism," *Journal of Metastable and Nanocrystalline Materials*, vol. 18, pp. 9-20, 2003.
- [11] P. Sanders, C. Youngdahl and J. Weertman, "The strength of nanocrystalline metals with and without flaws," *Materials Science and Engineering A*, Vols. 234-236, pp. 77-82, 1997.
- [12] R. Valiev and I. Alexandrov, "Paradox of strength and ductility in metals processed by severe plastic deformation," *Journal of Materials Research*, vol. 17, pp. 5-8, 2002.
- [13] A. Bachmaier and C. Motz, "On the remarkable thermal stability of nanocrystalline cobalt via alloying," *Materials Science & Engineering A*, vol. 624, pp. 41-51, 2015.
- [14] G. Hibbard, K. Aust and U. Erb, "Thermal stability of electrodeposited nanocrystalline Ni-Co alloys," *Materials Science and Engineering A*, vol. 433, pp. 195-202, 2006.
- [15] Y. Chen, Y. Liu, F. Khatkhatay, C. Sun, H. Wang and X. Zhang, "Significant enhancement in the thermal stability of nanocrystalline metals via immiscible tri-phases," *Scripta Materialia*, vol. 67, pp. 177-180, 2012.
- [16] A. Bachmaier, G. Rathmayr, J. Schmauch, N. Schell, A. Stark, N. Jonge and R. Pippan, "High strength nanocrystalline Co-Cu alloys with high tensile ductility," *Journal of Materials Research*, vol. 34, no. 1, pp. 58-68, 2018.
- [17] W. Xu, P. Dai, X. Wu and D. Tang, "Study on nanocrystalline dual phase Ni-Co alloy with high strength and excellent ductility," *Materials Science and Technology*, vol. 27, no. 1, pp. 320-324, 2011.
- [18] A. Molinari, S. Libardi, M. Leoni and P. Scardi, "Role of lattice strain on thermal stability of nanocrystalline FeMo alloy," *Acta Materialia*, vol. 58, pp. 963-966, 2010.

- [19] A. Bachmaier, A. Katzensteiner, S. Wunster, K. Aristizabal, S. Suarez and R. Pippan, "Thermal stabilization of metal matrix nanocomposite by nanocarbon reinforcement," *Scripta Materialia*, vol. 186, pp. 202-207, 2020.
- [20] Y. Zhau, A. Furnish, M. Kassner and A. Hodge, "Thermal stability of highly nanotwinned copper: The role of grain boundaries and texture," *Journal of Materials Research*, vol. 27, pp. 3049-3057, 2012.
- [21] Y. Shen, L. Lu, Q. Lu, Z. Jin and K. Lu, "Tensile properties of copper with nano-scale twins," *Scripta Materialia*, vol. 52, pp. 989-994, 2005.
- [22] T. Qian, I. Karaman and M. Marx, "Mechanical properties of nanocrystalline and ultrafine-grained nickel with bimodal microstructure," *Advance Engineering Materials*, vol. 16, no. 11, pp. 1323-1339, 2014.
- [23] G. Hibbard, K. Aust and U. Erb, "The effect of starting nanostructures on the thermal stability of pulsed electrodeposited nanocrystalline Co," *Acta Materialia*, vol. 54, pp. 2501-2510, 2006.
- [24] P. Choi, M. da Silva, U. Klement, T. Al-Kassab and R. Kirchheim, "Thermal stability of electrodeposited nanocrystalline Co-1.1at.%P," *Acta Materialia*, vol. 53, pp. 4473-4481, 2005.
- [25] D. Rathman, M. Marx and C. Motz, "Crack propagation and mechanical properties of electrodeposited nickel with bimodal microstructures in the nanocrystalline and ultrafine grained regime," *Journal of Materials Research*, vol. 32, no. 24, pp. 4573-4582, 2017.
- [26] A. Bachmaier, H. Aboufadi, M. Pfaff and C. Motz, "Structural evolution and strain induced mixing in Cu-Co composites studied by transmission electron microscopy and atom probe tomography," *Materials Characterization*, vol. 100, pp. 178-191, 2015.
- [27] A. Bachmaier, M. Pfaff, M. Stolpe, H. Aboufadi and C. Motz, "Phase separation of a supersaturated nanocrystalline Cu-Co alloy and its influence on thermal stability," *Acta Materialia*, vol. 96, pp. 269-283, 2015.
- [28] A. Bachmaier, J. Schmauch, H. Aboufadi, A. Verch and C. Motz, "On the process of co-deformation and phase dissolution in a hard-soft immiscible Cu-Co alloy system during high-pressure torsion deformation," *Acta Materialia*, vol. 115, pp. 333-346, 2016.
- [29] A. Bachmaier, M. Stolpe, T. Müller and C. Motz, "Phase decomposition and nano structure evolution of metastable nanocrystalline Cu-Co solid solutions during thermal treatment," *IOP Conf. Series: Materials Science and Engineering*, vol. 89, pp. 1-9, 2015.
- [30] J. Huang, Y. Yu, Y. Wu, D. Li and H. Ye, "Microstructure and homogeneity of nanocrystalline Co-Cu supersaturated solid solutions prepared by mechanical alloying," *Journal of Materials Research*, vol. 12, pp. 936-946, 1997.
- [31] Y. Nakamoto, M. Yuasa, Y. Chen, H. Kusuda and M. Mabuchi, "Mechanical properties of a nanocrystalline Co-Cu alloy with a high-density fine nanoscale lamellar structure," *Scripta Materialia*, vol. 58, pp. 731-734, 2008.
- [32] M. Yuasa, H. Nakano, K. Kajikawa, T. Nakazawa and M. Mabuchi, "Deformation behavior of nanocrystalline Co-Cu alloys," *Materials Research Society Symposium Proceeding*, vol. 1224, pp. 1-6, 2010.
- [33] S. Ghosh, T. Bera, C. Saxena, S. Bhattacharya and G. Dey, "Effect of pulse plating and additive on phase separation in Cu-Co nanogranular alloys," *Journal of Alloys and Compounds*, vol. 475, pp. 676-682, 2009.
- [34] A. Berkowitz, J. Mitchell, J. Carey, A. Young, S. Zhang, F. Spada, F. Parker, A. Hutten and G. Thomas, "Giant magnetoresistance in heterogeneous Cu-Co alloys," *Physical Review Letters*, vol. 68, pp. 3745-3748, 1992.
- [35] Y. Ueda and M. Ito, "Magnetoresistance in Co-Cu alloy films formed by electrodeposition

method,” *Japanese Journal of Applied Physics*, vol. 33, pp. 1403-1405, 1994.

- [36] T. Aizawa and C. Zhou, “Nanogranulation process into magneto-resistant Co-Cu alloy on the route of bulk mechanical alloying,” *Materials Science and Engineering A*, vol. 285, pp. 1-7, 2000.
- [37] M. Yuasa, H. Nakano, Y. Nakamoto, M. Hakamada and M. Mabuchi, “Ferromagnetic properties of Co-Cu alloy with nanoscale lamellar structure,” *Materials Transactions*, vol. 50, pp. 419-422, 2009.
- [38] A. Bachmaier, H. Krenn, P. Knoll, H. Aboufadel and R. Pippan, “Tailoring the magnetic properties of nanocrystalline Cu-Co alloys prepared by high-pressure torsion and isothermal annealing,” *Journal of Alloys and Compounds*, vol. 725, pp. 744-749, 2017.
- [39] A. Karimpoor, U. Erb, K. Aust and G. Palumbo, “High strength nanocrystalline cobalt with high tensile ductility,” *Scripta Materialia*, vol. 49, pp. 651-656, 2003.
- [40] A. Karimpoor and U. Erb, “Mechanical properties of nanocrystalline cobalt,” *Physical Status Solidi*, vol. 203, pp. 1265-1270, 2006.
- [41] Y. Wang, R. Ott, T. van Buuren, T. Willey, M. Biener and A. Hamza, “Controlling factors in tensile deformation of nanocrystalline cobalt and nickel,” *Physical Review B*, vol. 85, pp. 1-18, 2012.
- [42] L. Lu, L. Wang, B. Ding and K. Lu, “High-tensile ductility in nanocrystalline copper,” *Journal of Materials Research*, vol. 15, pp. 270-273, 2000.
- [43] Y. Wang, M. Chen, F. Zhou and E. Ma, “High tensile ductility in a nanostructured metal,” *Nature*, vol. 419, pp. 912-915, 2002.
- [44] L. Lu, Y. Shen, X. Chen, L. Qian and K. Lu, “Ultra-high strength and high electrical conductivity in copper,” *Science*, vol. 304, pp. 422-426, 2004.
- [45] C. Koch, K. Youssef, R. Scattergood, K. Murty and J. Horton, “Ultra-high strength and high ductility of bulk nanocrystalline copper,” *Applied Physics Letter*, vol. 87, pp. 1-3, 2005.
- [46] C. Suryanarayana, “Mechanical alloying of nanocrystalline materials and nanocomposites,” *Madridge Journal of Nanotechnology & Nanoscience*, vol. 4 (1), pp. 127-134, 2019.
- [47] S. Picraux, “Encyclopædia Britannica,” 4 June 2020. [Online]. Available: <https://www.britannica.com/technology/nanotechnology>. [Accessed 21 September 2020].
- [48] M. Tschopp, H. Murdoch, L. Kecskes and K. Darling, ““Bulk” nanocrystalline metals: Review of the current state of the art and future opportunities for copper and copper alloys,” *JOM*, vol. 66, no. 6, pp. 1000-1019, 2014.
- [49] U. Erb, G. Palumbo and J. McCrea, “the processing of bulk nanocrystalline metals and alloys by electrodeposition,” in *Nanostructured Metals and Alloys*, S. Whang, Ed., Woodhead Publishing Series in Metals and Surface Engineering, 2011, pp. 118-151.
- [50] U. Erb and A. El-Sherik, “Nanocrystalline metals and process of producing the same”. United States of America Patent 5,352,266, 4 October 1994.
- [51] J. Weertman, “Hall-Petch strengthening in nanocrystalline metals,” *Materials Science and Engineering A*, vol. 166, no. 1-2, pp. 161-167, 1993.
- [52] S. Brandstetter, K. Zhang, J. Weertman and H. Van Swygenhoven, “Grain coarsening during compression of bulk nanocrystalline nickel and copper,” *Scripta Materialia*, vol. 58, no. 1, pp. 61-64, 2008.
- [53] A. Goldstein, “Lithography exposure mask derived from nanocrystal precursors and a method of manufacturing the same”. United States of America Patent 5,670,279, 1997.

- [54] T. Bhuvana and G. Kulkarni, "Highly conducting patterned Pd Nanowires by direct-write electron beam lithography," *ACS Nano*, vol. 2, no. 3, pp. 457-462, 2008.
- [55] R. Valiev, R. Islamgaliev and I. Alexandrov, "Bulk nanostructured materials from severe plastic deformation," *Progress in Materials Science*, vol. 45, pp. 103-189, 2000.
- [56] A. Azushima, R. Kopp, A. Korhonen, D. Yang, F. Micari, G. G. P. Lahoti, J. Yanagimoto, N. Tsuji, A. Rosochowski and A. Yanagida, "Severe plastic deformation (SPD) processes for metals," *CIRP Annals*, vol. 57, no. 2, pp. 716-735, 2008.
- [57] A. Bachmaier, A. Hohenwarter and R. Pippan, "New procedure to generate stable nanocrystallites by severe plastic deformation," *Scripta Materialia*, vol. 61, pp. 1016-1019, 2009.
- [58] C. Suryanarayana and E. Ivanov, "Mechanochemical synthesis of nanocrystalline metal powders," in *Advances in Powder Metallurgy*, Woodhead Publishing Series in Metals and Surface Engineering, 2013, pp. 42-68.
- [59] R. Valiev, "Nanostructuring of metals by severe plastic deformation for advanced properties," *Nature Materials*, vol. 3, pp. 511-516, 2004.
- [60] S. Ghalehbandi, M. Malaki and M. Gupta, "Accumulative roll bonding - a review," *Applied Science*, vol. 9, p. 3627, 2019.
- [61] A. Bachmaier and R. Pippan, "High-pressure torsion deformation induced phase transformations and formations: New material combinations and advanced properties," *Materials Transactions*, vol. 60, no. 7, pp. 1256-1269, 2019.
- [62] R. Valiev and T. Langdon, "Principles of equal-channel angular pressing as a processing tool for grain refinement," *Progress in Materials Science*, vol. 51, pp. 881-981, 2006.
- [63] R. Valiev, Y. Estrin, Z. Horita, T. Langdon, M. Zehetbauer and T. Zhu, "Producing bulk ultrafine-grained materials by severe plastic deformation," *JOM Nanostructured Materials*, pp. 33-39, 2006.
- [64] N. Tsuji, "Bulk nanostructured metals and alloys produced by accumulative roll-bonding," in *Nanostructured Metals and Alloys*, Woodhead Publishing Series in Metals and Surface Engineering, 2011, pp. 40-58.
- [65] K. Edalati, T. Fujioka and Z. Horita, "Microstructure and mechanical properties of pure Cu processed by high-pressure torsion," *Materials Science and Engineering A*, vol. 497, pp. 168-173, 2008.
- [66] A. Vorhauer and R. Pippan, "On the homogeneity of deformation by high pressure torsion," *Scripta Materialia*, vol. 51, pp. 921-925, 2004.
- [67] A. Katzensteiner, T. Müller, K. Kormout, K. Aristizabal, S. Suarez, R. Pippan and A. Bachmaier, "Influence of processing parameters on the mechanical properties of HPT-deformed nickel/carbon nanotube composite," *Advanced Engineering Materials*, vol. 21, p. 1800422, 2019.
- [68] O. Senkov, N. Srisukhumbowornchai, M. Övecoglu and F. Froes, "High-temperature stability of nanocrystalline structure in a TiAl alloy prepared by mechanical alloying and hot isostatic pressing," *Journal of Materials Research*, vol. 13, no. 12, pp. 3399-3410, 1998.
- [69] T. Topping, B. Ahn, S. Nutt and E. Lavernia, "Influence of hot isostatic pressing on microstructure of mechanical behaviour of nanostructured Al alloy," *Powder Metallurgy*, vol. 56, no. 4, pp. 276-287, 2013.
- [70] I. Azcona et al, "Hot isostatic pressing of nanosized WC-Co hardmetals," *Proceeding of the 15th International Plansee Seminar, Reutte*, vol. 2, pp. 35-49, 2001.
- [71] H. Kessel, J. Hennicke, J. Schmidt, T. Weißgärber, B. Kieback, M. Herrmann and J. Räthel, "'FAST" field assisted sintering technology - a new process for the production of metallic and

ceramic sintering materials,” in *Pulvermetallurgie in Wissenschaft und Praxis* 22, H. Kolaska, Ed., Hemdall Verlag Witten, 2006, pp. 1-37.

- [72] O. Guillon, J. Gonzalez-Julian, B. Dargatz, T. Kessel, G. Schierning, J. Räthel and M. Herrmann, “Field-assisted sintering technology/spark plasma sintering: Mechanisms, materials, and technology development,” *Advanced Engineering Materials*, vol. 16, pp. 830-849, 2014.
- [73] Z.-Y. Hu, Z.-H. Zhang, X.-W. Cheng, F.-C. Wang, Y.-F. Zhang and S.-L. Li, “A review of multi-physical field induced phenomena and effects in spark plasma sintering: Fundamental and applications,” *Materials and Design*, vol. 191, p. 108662, 2020.
- [74] C. Hutchins, Consolidation of copper and aluminum micro and nanoparticles via equal channel angular extrusion, Texas: Master Thesis, Mechanical engineering, Texas A&M University, 2007.
- [75] I. Karaman, M. Haouaoui and H. Maier, “Nanoparticles consolidation using equal channel angular extrusion at room temperature,” *Journal of Materials Science*, vol. 42, pp. 1561-1576, 2006.
- [76] R. German, “Chapter Ten - Sintering with external pressure,” in *Sintering: from empirical observation to scientific principles*, Butterworth Heinemann, 2014, pp. 305-354.
- [77] T. Müller, “Pulsed electrodeposition of nanocrystalline cobalt and copper-cobalt alloys,” *Master Thesis of Saarland University*, 2014.
- [78] Y. Li, J. H. W. Huang and H. Tian, “Effect of peak current density on the mechanical properties of nanocrystalline Ni-Co alloys produced by pulsed electrodeposition,” *Applied Surface Science*, vol. 254, pp. 6865-6869, 2008.
- [79] W. Xu, P. Dai, X. Wu and D. Tang, “Study on nanocrystalline dual phase Ni-Co alloy with high strength and excellent ductility,” *Materials Science and Technology*, vol. 27, no. 1, pp. 320-324, 2011.
- [80] T. Müller, J. Grimwood, A. Bachmaier and R. Pippan, “Electrodeposition of Fe-C alloys from citrate baths: structure, mechanical properties, and thermal stability,” *Metals*, vol. 8, pp. 1-13, 2018.
- [81] D. Noren and M. Hoffman, “Clarifying the Butler-Volmer equation and related approximations for calculating activation losses in solid oxide fuel cell models,” *Journal of Power Sources*, vol. 152, pp. 175-181, 2005.
- [82] A. Milchev, “Electrochemical phase transformation: some fundamental concepts,” *Journal of Solid State Electrochemistry*, vol. 15, pp. 1401-1415, 2011.
- [83] A. Milchev, “Nucleation phenomena in electrochemical systems: thermodynamic concept,” *ChemTexts*, vol. 2, no. 2, pp. 1-9, 2016.
- [84] M. Volmer and A. Weber, “Keimbildung in übersättigten gebilden,” *Zeitschrift für Physikalische Chemie*, vol. 119, p. 277, 1926.
- [85] R. Becker and W. Döring, “Kinetische behandlung der keimbildung in übersättigten dämpfen,” *Annalen der Physik*, vol. 416, no. 8, pp. 719-752, 1935.
- [86] G. Gunawardena, G. Hills, I. Montenegro and B. Scharifker, “Electrochemical nucleation. Part III. The electrodeposition of mercury on vitreous carbon,” *Journal of Electroanalytical Chemistry*, vol. 138, pp. 255-271, 1982.
- [87] M. Paunovic, M. Schlesinger and D. D. Snyder, “Fundamental Consideration,” in *Modern Electroplating*, M. Schlesinger and D. D. Snyder, Eds., New York, Wiley, 2010, pp. 1-32.
- [88] N. Ibl, J. Puipe and H. Angerer, “Electrocrystallization in pulse electrolysis,” *Surface Technology*, vol. 6, no. 4, pp. 287-300, 1978.

- [89] N. Ibl, "Some theoretical aspects of pulse electrolysis," *Surface Technology*, vol. 10, pp. 81-104, 1980.
- [90] J. Puipe and F. Leaman, *Theory and practice of pulse plating*, Orlando: AESF Publication, 1986.
- [91] K. Popov, M. Maksimovic and B. Ocokoljic, "Fundamental aspects of pulsating current metal electrodeposition I: the effect of the pulsating current on the surface roughness and the porosity of metal deposits," *Surface Technology*, vol. 11, pp. 99-109, 1980.
- [92] K. Popov, M. Spasojevic, M. Maksimovic and I. Boskovic, "Fundamental aspects of pulsating current metal electrodeposition II: the mechanism of metal film formation on an inert electrode," *Surface Technology*, vol. 11, pp. 111-116, 1980.
- [93] K. Popov, M. Maksimovic and S. Djokic, "Fundamental aspects of pulsating current metal electrodeposition III: maximum practical deposition rate," *Surface Technology*, vol. 14, pp. 323-333, 1981.
- [94] K. Popov, M. Maksimovic and R. Stevanovic, "Fundamental aspects of pulsating current metal electrodeposition VIII: the effect of pause-to-pulse ratio on microthrowing power of metal deposition," *Surface Technology*, vol. 22, pp. 155-158, 1984.
- [95] E. Taylor, M. Inman, H. Garich, H. McCrabb, S. Snyder and T. Hall, "Breaking the chemical paradigm in electrochemical engineering; case studies and lessons learned from plating to polishing," in *Electrochemical Engineering: From Discovery to Product*, R. Alkire, P. Bartlett and M. Koper, Eds., New York, Wiley, 2018, pp. 193-240.
- [96] S. Roy and D. Landolt, "Determination of the practical range of parameters during reverse-pulse current plating," *Journal of Applied Electrochemistry*, vol. 27, pp. 299-307, 1997.
- [97] J. Kelly, P. Bradley and D. Landolt, "Additive effects during pulsed deposition of Cu-Co nanostructures," *Journal of The Electrochemical Society*, vol. 147, no. 8, pp. 2975-2980, 2000.
- [98] P. Bradley and D. Landolt, "Pulse-plating of copper-cobalt alloys," *Electrochimica Acta*, vol. 45, pp. 1077-1087, 1999.
- [99] D. Landolt and A. Marlot, "Microstructure and composition of pulse-plated metals and alloys," *Surface and Coating Technology*, Vols. 169-170, pp. 8-13, 2003.
- [100] E. Pavlatou and N. Spyrellis, "Influence of pulse plating conditions on the structure and properties of pure and composite nickel nanocrystalline coating," *Russian Journal of Electrochemistry*, vol. 44, no. 6, pp. 745-754, 2008.
- [101] A. El-Sherik, U. Erb and J. Page, "Microstructure evolution in pulse plated nickel electrodeposits," *Surface and Coating Technology*, vol. 88, pp. 70-78, 1996.
- [102] D. Xu, V. Sriram, V. Ozolins, J.-M. Yang and K. Tu, "In situ measurements of stress evolution for nanotwin formation during pulse electrodeposition of copper," *Journal of Applied Physics*, vol. 105, p. 023521, 2009.
- [103] D. Xu, W. Kwan, K. Chen, X. Zhang, V. Ozolins and K. Tu, "Nanotwin formation in copper thin films by stress/strain relaxation in pulse electrodeposition," *Applied Physics Letter*, vol. 91, p. 254105, 2007.
- [104] K. Kumar and K. Biswas, "Effect of thiourea on grain refinement and defect structure of the pulsed electrodeposited nanocrystalline copper," *Surface and Coating Technology*, vol. 214, pp. 8-18, 2013.
- [105] H. Natter and R. Hempelmann, "Nanocrystalline copper by pulsed electrodeposition: the effect of organic additives, bath temperature, and pH," *Journal of Physical Chemistry*, vol. 100, pp. 19525-19532, 1996.
- [106] A. Esfandiari, B. Radha, F. Wang, Q. Yang, S. Hu, S. Garaj, R. Nair, A. Geim and K. Gopinadhan,

“Size effect in ion transport through angstrom-scale slits,” *Science*, vol. 358, no. 6362, pp. 511-513, 2017.

- [107] L. Lu, X. Si, Y. Shen and K. Lu, “Nano crystals copper material with super high strength and conductivity and method of preparing thereof”. United States of America Patent US2006/0021878 A1, 2 February 2006.
- [108] F. Su, C. Liu, Q. Zuo, P. Huang and M. Miao, “A comparative study of electrodeposition techniques on the microstructure and property of nanocrystalline cobalt deposit,” *Materials Chemistry and Physics*, vol. 139, pp. 663-673, 2013.
- [109] R. Sekar, “Microstructure and crystallographic characteristic of nanocrystalline copper prepared from acetate solutions by electrodeposition technique,” *Transaction of Nonferrous Metals Society of China*, vol. 27, pp. 1423-1430, 2017.
- [110] R. Sekar, “Structural and morphological characteristic of nanocrystalline copper electrodeposits from acid sulphate electrolytes,” *Transaction of the IMF*, vol. 93, no. 5, pp. 255-261, 2015.
- [111] M. Kamel, A. El-Moemen, S. Rashwan and A. Bolbol, “Electrodeposition of nanocrystalline copper deposits using lactic acid-based plating bath,” *Metall*, vol. 71, pp. 179-183, 2017.
- [112] W. Kozłowski, I. Piwonski, W. Szmaja and M. Zielinski, “Quantitative study of the effect of current density on the morphological and magnetic domain structures of electrodeposited nanocrystalline cobalt films,” *Journal of Electroanalytical Chemistry*, vol. 769, pp. 42-47, 2016.
- [113] W. Kozłowski, I. Piwonski, M. Zielinski, E. Miekos, K. Polanski, W. Szmaja and M. Cichomski, “Investigation of nanocrystalline cobalt films electrodeposited at different current densities,” *Applied Physics A*, vol. 120, pp. 155-160, 2015.
- [114] L. Wang, Y. Gao, T. Xu and Q. Xue, “A comparative study on the tribological behavior of nanocrystalline nickel and cobalt coatings correlated with grain size and phase structure,” *Materials Chemistry and Physics*, vol. 99, pp. 96-103, 2006.
- [115] A. El-Sherik and U. Erb, “Synthesis of bulk nanocrystalline nickel by pulsed electrodeposition,” *Journal of Materials Science*, vol. 30, pp. 5743-5749, 1995.
- [116] G. Palumbo, S. Thorpe and K. Aust, “On the contribution of triple junctions to the structure and properties of nanocrystalline materials,” *Scripta Metallurgica et Materialia*, vol. 24, no. 7, pp. 1347-1350, 1990.
- [117] H. Höfler, H. Hahn and R. Averback, “Diffusion in nanocrystalline materials,” *Defect and Diffusion Forum*, vol. 75, pp. 195-210, 1991.
- [118] H. Peng, M. Gong, Y. Chen and F. Liu, “Thermal stability of nanocrystalline materials: thermodynamics and kinetics,” *International Materials Review*, vol. 62, no. 6, pp. 303-333, 2017.
- [119] J. Burke and D. Turnbull, “Recrystallization and grain growth,” *Progress in Metal Physics*, vol. 3, pp. 220-244, 1952.
- [120] H. Atkinson, “Theories of normal grain growth in pure single phase systems,” *Acta Metallurgica*, vol. 3, no. 36, pp. 469-491, 1988.
- [121] H. Natter, M. Schmelzer, M.-S. Löffler, E. Krill, A. Fitch and R. Hempelmann, “Grain-growth kinetic of nanocrystalline iron studied in situ by synchrotron real-time X-ray diffraction,” *Journal of Physical Chemistry B*, vol. 104, no. 11, pp. 2467-2476, 2000.
- [122] T. Mallow and C. Koch, “Thermal stability of nanocrystalline materials,” *Materials Science Forum*, Vols. 225-227, pp. 595-604, 1996.
- [123] S. Ganapathi, D. Owen and A. Choksi, “The kinetics of grain growth in nanocrystalline copper,” *Scripta Metallurgica et Materialia*, vol. 25, no. 12, pp. 2699-2704, 1991.
- [124] P. Cao and D. Zhang, “Thermal stability of nanocrystalline copper films,” *Internal Journal of*

Modern Physics B, vol. 20, pp. 3830-3835, 2006.

- [125] R. Vandermeer and H. Hu, "On the grain growth exponent of pure iron," *Acta Metallurgica et Materialia*, vol. 42, no. 9, pp. 3071-3075, 1994.
- [126] Y. Estrin, G. Gottstein and L. Shvindlerman, "Intermittent 'self-locking' of grain growth in fine-grained materials," *Scripta Materialia*, vol. 41, no. 4, pp. 385-390, 1999.
- [127] Y. Estrin, G. Gottstein, E. Rabkin and L. Shvindlerman, "On the kinetic of grain growth inhibited by vacancy generation," *Scripta Materialia*, vol. 43, no. 2, pp. 141-147, 2000.
- [128] G. Gottstein, Y. Ma and L. Shvindlerman, "The effect of triple-junction drag on grain growth," *Acta Materialia*, vol. 48, no. 2, pp. 397-403, 2000.
- [129] V. Novikov, "On the influence of triple junctions on grain growth kinetic and microstructure evolution in 2D polycrystals," *Scripta Materialia*, vol. 52, no. 9, pp. 857-861, 2005.
- [130] M. Ames, J. Markmann, R. Karos, A. Michels, A. Tschöpe and R. Birringer, "Unraveling the nature of room temperature grain growth in nanocrystalline materials," *Acta Materialia*, vol. 56, no. 16, pp. 4255-4266, 2008.
- [131] E. Holm and S. Foiles, "How grain growth stops: a mechanism for grain-growth stagnation in pure materials," *Science*, vol. 328, no. 5982, pp. 1138-1141, 2010.
- [132] C. Smith, "Introduction to grains, phase, and interfaces - an interpretation of microstructure (private communication from C. Zener)," *Trans. AIME*, vol. 175, pp. 15-51, 1948.
- [133] D. Chen, T. Ghoneim and Y. Kulkarni, "Effect of pinning particles on grain boundary motion from interface random walk," *Applied Physics Letters*, vol. 111, p. 161606, 2017.
- [134] K. Koch, R. Scattergood, M. Saber and H. Kotan, "High temperature stabilization of nanocrystalline grain size: Thermodynamic versus kinetic strategies," *Journal of Materials Research*, vol. 28, pp. 1785-1791, 2013.
- [135] K. Aristizabal, A. Katzensteiner, A. Bachmaier, F. Mücklich and S. Suarez, "Microstructural evolution during heating of CNT/metal matrix composites processed by severe plastic deformation," *Scientific Reports*, vol. 10, 2020.
- [136] R. Kirchheim, "Reducing grain boundary, dislocation line and vacancy formation energies by solute segregation. I. Theoretical Background," *Acta Materialia*, vol. 55, pp. 5129-5138, 2007.
- [137] R. Kirchheim, "Reducing grain boundary, dislocation line and vacancy formation energies by solute segregation. II. Experimental evidence and consequences," *Acta Materialia*, Vols. 5139-5148, p. 55, 2007.
- [138] J. Weismüller, "Alloy effect in nanostructures," *Nanostructured Materials*, vol. 3, pp. 261-272, 1993.
- [139] H. Natter, M. Schmelzer and R. Hempelmann, "Nanocrystalline nickel and nickel-copper alloys: Synthesis, characterization, and thermal stability," *Journal of Materials Research*, vol. 13, no. 5, pp. 1186-1197, 1998.
- [140] K. Boylan, D. Ostrander, E. Erb, G. Palumbo and K. Aust, "An in-situ TEM study of the thermal stability of nanocrystalline Ni-P," *Scripta Metallurgica et Materialia*, vol. 25, pp. 2711-2716, 1991.
- [141] O. Bayat, V. Abouei, H. Sabet and A. Kiasati, "Investigation of nanocrystalline Co-P coated by pulsed electrodeposition," *Nanoscale and Nanostructured Materials and Coatings*, vol. 54, pp. 63-70, 2018.
- [142] M. da Silva, C. Wille, U. Klement, P. Choi and T. Al-Kassab, "Electrodeposited nanocrystalline Co-P alloys: Microstructural characterization and thermal stability," *Materials Science and Engineering A*, Vols. 445-446, pp. 31-39, 2007.

- [143] Y. Zhao, A. Furnish, M. Kassner and A. Hodge, "Thermal stability of highly nanotwinned copper: The role of grain boundaries and texture," *Journal of Materials Research*, vol. 27, no. 24, pp. 3049-3057, 2012.
- [144] J. Gubicza, "Lattice defects and their influence on the mechanical properties of bulk materials processed by severe plastic deformation," *Materials Transactions*, vol. 60, pp. 1230-1242, 2019.
- [145] T. Kolonits, P. Jenei, L. Peter, I. Bakonyi, Z. Czigany and J. Gubicza, "Effect of bath additives on the microstructure, lattice defect density and hardness of electrodeposited nanocrystalline Ni films," *Surface and Coating Technology*, vol. 349, pp. 611-621, 2018.
- [146] T. Kolonits, P. Jenei, B. Toht, Z. Czigany, J. Gubicza, L. Peter and I. Bakonyi, "Characterization of defect structure in electrodeposited nanocrystalline Ni Films," *Journal of Electrochemical Society*, vol. 163, pp. 107-114, 2015.
- [147] G. Kapoor, L. Peter, E. Fekete and J. Gubicza, "Defect structure in electrodeposited nanocrystalline Ni layers with different Mo concentrations," *Proceeding of the 2nd International Conference on Condensed Matter and Applied Physics (ICC)*, vol. 1953, p. 030047, 2017.
- [148] A. Cottrell and B. Bilby, "Dislocation theory of yielding and strain ageing of iron," *Proceeding of the Physical Society. Section A*, vol. 62, pp. 49-62, 1949.
- [149] J. Eshelby, F. Frank and F. Nabarro, "The equilibrium of linear arrays of dislocations," *The Philosophical Magazine*, vol. 42, pp. 351-364, 1951.
- [150] W. Callister, "Chapter 8 / Deformation and Strengthening Mechanisms," in *Fundamental of Materials Science and Engineering*, Salt Lake City, Utah, John Wiley & Sons, Inc., 2001, p. 207.
- [151] G. Voyiadjis and M. Yaghoobi, "Chapter 1 - Introduction: Size effects in materials," in *Size Effects in Plasticity - From Macro to Nano*, Cambridge, Massachusetts, Academic Press - Elsevier, 2019, pp. 1-79.
- [152] E. Hall, "The deformation and ageing of mild steel: III Discussion of Results," *Proceeding of the Physical Society. Section B*, vol. 64, p. 747, 1951.
- [153] P. Sanders, J. Eastman and J. Weertman, "Elastic and tensile behavior of nanocrystalline copper and palladium," *Acta Materialia*, vol. 45, no. 10, pp. 4019-4025, 1997.
- [154] J. Greer, "Nanotwinned metals - It's all about imperfections," *Nature Materials*, vol. 12, pp. 689-690, 2013.
- [155] T. Nieh and J. Wadsworth, "Hall-Petch relation in nanocrystalline solids," *Scripta Metallurgica et Materialia*, vol. 25, pp. 955-958, 1991.
- [156] C. Pande, R. Masumura and R. Armstrong, "Pile-up based Hall-Petch relation for nanoscale materials," *Nanostructured Materials*, vol. 2, no. 3, pp. 323-331, 1993.
- [157] A. Chokshi, A. Rosen, A. Karch and H. Gleiter, "On the validity of the Hall-Petch relationship in nanocrystalline materials," *Scripta Metallurgica*, vol. 23, no. 10, pp. 1679-1683, 1989.
- [158] X. Zhang and K. Aifantis, "Interpreting the softening of nanomaterials through gradient plasticity," *Journal of Materials Research*, vol. 26, no. 11, pp. 1399-1405, 2011.
- [159] S. Naik and S. Walley, "The Hall-Petch and inverse Hall-Petch relations and the hardness of nanocrystalline metals," *Journal of Materials Science*, vol. 55, pp. 2661-2681, 2020.
- [160] H. Van Swygenhoven and P. Derlet, "Grain-boundary sliding in nanocrystalline fcc metals," *Physical Review B*, vol. 64, p. 224105, 2001.
- [161] M. Gutkin, I. Ovid'ko and N. Skiba, "Crossover from grain boundary sliding to rotational deformation in nanocrystalline materials," *Acta Materialia*, vol. 51, pp. 4059-4071, 2003.
- [162] A. Sergueeva, N. Mara, N. Krasilnikov, R. Valiev and A. Mukherjee, "Cooperative grain

boundary sliding in nanocrystalline materials,” *Philosophical Magazine*, vol. 86, no. 36, pp. 5797-5804, 2006.

- [163] I. Ovid'ko and A. Sheinerman, “Kinetics of grain boundary sliding and rotational deformation in nanocrystalline materials,” *Review on Advanced Materials Science*, vol. 35, pp. 48-58, 2013.
- [164] A. Ball and M. Hutchison, “Superplasticity in the aluminium-zinc Eutectoid,” *Metal Science Journal*, vol. 3, no. 1, pp. 1-7, 1969.
- [165] H. Conrad and J. Narayan, “On the grain size softening in nanocrystalline materials,” *Scripta Materialia*, vol. 42, pp. 1025-1030, 2000.
- [166] H. Hahn, P. Mondal and K. Padmanabhan, “Plastic deformation of nanocrystalline materials,” *Nanostructured Materials*, vol. 9, pp. 603-606, 1997.
- [167] R. Raj and M. Ashby, “On grain boundary sliding and diffusional creep,” *Metallurgical Transactions*, vol. 2, pp. 1113-1127, 1971.
- [168] M. Meyers, A. Mishra and D. Benson, “The deformation physics of nanocrystalline metals; Experiment, analysis, and computations,” *JOM*, vol. 58, pp. 41-48, 2006.
- [169] D. Jia, Y. Wang, K. Ramesh and E. Ma, “Deformation behavior and plastic instabilities of ultrafine-grained titanium,” *Applied Physics Letters*, vol. 79, p. 611, 2001.
- [170] Y. Wang and E. Ma, “Enhanced tensile ductility and toughness in nanostructured Cu,” *Applied Physics Letters*, vol. 80, p. 2395, 2002.
- [171] C. Koch, “Optimization of strength and ductility in nanocrystalline and ultrafine grained metals,” *Scripta Materialia*, vol. 49, no. 7, pp. 657-662, 2003.
- [172] C. Koch, D. Morris, K. Lu and A. Inoue, “Ductility of nanostructured materials,” *MRS Bulletin*, vol. 24, no. 2, pp. 54-58, 1999.
- [173] K. Youssef, R. Sattergood, K. Murty, J. Horton and C. Koch, “Ultrahigh strength and high ductility of bulk nanocrystalline copper,” *Applied Physics Letter*, vol. 87, p. 091904, 2005.
- [174] C. Youngdahl and P. Sanders, “Compressive yield strength of nanocrystalline Cu and Pd,” *Scripta Materialia*, vol. 37, no. 6, pp. 809-813, 1997.
- [175] M. Legros, B. Elliot, M. Rittner, J. Weertman and K. Hemker, “Microsample tensile testing of nanocrystalline metals,” *Philosophical Magazine A*, vol. 80, no. 4, pp. 1017-1026, 2000.
- [176] S. Cheng, E. Ma, Y. Wang, L. Kecskes, K. Youssef, C. Koch, U. Trociewitz and K. Han, “Tensile properties of in situ consolidated Cu,” *Acta Materialia*, vol. 53, pp. 1521-1533, 2005.
- [177] E. Ma, “Instabilities and ductility of nanocrystalline and ultrafine-grained metals,” *Scripta Materialia*, vol. 49, pp. 663-668, 2003.
- [178] J. Marro, T. Darroudi, C. Okoro, Y. Obeng and K. Richardson, “The influence of pulse plating frequency and duty cycle on the microstructure and stress state of electrodeposited copper films,” *Thin Solid Films*, vol. 621, pp. 91-97, 2017.
- [179] K. Lu, L. Lu and S. Suresh, “Strengthening materials by engineering coherent internal boundaries at the nanoscale,” *Science*, vol. 324, no. 5929, pp. 349-352, 2009.
- [180] L. Lu, X. Chen and K. Lu, “Revealing the maximum strength in nanotwinned copper,” *Science*, vol. 323, no. 5914, pp. 607-610, 2009.
- [181] A. Pineau, A. Benzerga and T. Pardoen, “Failure of metals III: Fracture and fatigue of nanostructured metallic materials,” *Acta Materialia*, vol. 107, pp. 508-544, 2016.
- [182] A. Whitney, P. Sanders, J. Weertman and J. Eastman, “Fatigue of nanocrystalline copper,” *Scripta Metallurgica et Materialia*, vol. 33, no. 12, pp. 2025-2030, 1995.

- [183] M. Kapp, T. Kremmer, C. Motz, B. Yang and R. Pippan, "Structural instabilities during cyclic loading of ultrafine-grained copper studied with micro bending experiment," *Acta Materialia*, vol. 125, pp. 351-358, 2017.
- [184] C. M. R. Muhlstein, D. Alsem and R. Polcawuich, "Fatigue-induced grain coarsening in nanocrystalline platinum films," *Acta Materialia*, vol. 59, pp. 1141-1149, 2011.
- [185] P. Cavaliere, "Mechanical properties of nanocrystalline metals and alloys studied via multi-step nanoindentation and finite element calculations," *Materials Science and Engineering A*, vol. 512, pp. 1-9, 2009.
- [186] T. Hanlon, Y.-N. Kwon and S. Suresh, "Grain size effects on the fatigue response of nanocrystalline metals," *Scripta Materialia*, vol. 49, pp. 675-680, 2003.
- [187] T. Hanlon, E. Tabachnikova and S. Suresh, "Fatigue behavior of nanocrystalline metals and alloys," *International Journal of Fatigue*, vol. 27, pp. 1147-1158, 2005.
- [188] K. Pratama, J. Barrirero, F. Mücklich and C. Motz, "Microstructure evolution and mechanical stability of supersaturated solid solution Co-rich nanocrystalline Co-Cu produced by pulsed electrodeposition," *Materials*, vol. 13, p. 2616, 2020.
- [189] K. Pratama, F. Kunz, L. Lindner, J. Schmauch, F. Mücklich and C. Motz, "Thermal stability, phase decomposition, and micro-fatigue properties of pulsed electrodeposited nanocrystalline Co-Cu," *Procedia Structural Integrity*, vol. 23, pp. 366-371, 2019.
- [190] C. Schneider, W. Rasband and K. Eliceiri, "NIH Image to ImageJ: 25 years of image analysis," *Nature Methods*, vol. 9, pp. 671-675, 2012.
- [191] M. Wojdyr, "Fityk: A general-purpose peak fitting program," *Journal of Applied Crystallography*, vol. 43, pp. 1126-1128, 2010.
- [192] D. Necas and P. Klapetek, "Gwyddion: an open-source software for SPM data," *Central European Journal of Physics*, vol. 10, no. 1, pp. 181-188, 2012.
- [193] K. Thompson, D. Lawrence, D. Larson, J. Olson, T. Kelly and B. Gorman, "In situ site-specific specimen preparation for atom probe tomography," *Ultramicroscopy*, vol. 107, pp. 131-139, 2007.
- [194] K. Pratama and C. Motz, "Strategies to achieve high strength and ductility of pulsed electrodeposited nanocrystalline Co-Cu by tuning the deposition parameters," *Molecules*, vol. 25, p. 5914, 2020.
- [195] H. Fischer, *Elektrolytische abscheidung und elektrokristallisation von metallen*, Berlin: Springer-Verlag, 1954.
- [196] S. Bansal, A. Saxena, T. Hartwig and R. Tummala, "Mechanical properties of ECAE nanocrystalline copper and nickel," *Journal of Metastable and Nanocrystalline Materials*, vol. 23, pp. 183-186, 2005.
- [197] J. Cahn, "Hardening by spinodal decomposition," *Acta Metallurgica*, vol. 11, pp. 1275-1282, 1963.
- [198] M. Kato, T. Mori and L. Schwartz, "Hardening by spinodal modulated structure," *Acta Metallurgica*, vol. 28, pp. 285-290, 1980.
- [199] J.-M. Liu, R. Busch, F. Gärtner, P. Haasen, Z.-G. Liu and Z.-C. Wu, "Spinodal decomposition of CoCu alloys," *Physica Status Solidi*, vol. 138, pp. 157-174, 1993.
- [200] T. Koyama, T. Miyazaki and A. Mebed, "Computer simulation of phase decomposition in real alloy system based on the modified Khachaturyan diffusion equation," *Metallurgical and Material Transactions A*, vol. 26A, pp. 2617-2623, 1995.
- [201] J. Horvath, R. Biringer and H. Gleiter, "Diffusion in nanocrystalline materials," *Acta*

- Metallurgica*, vol. 62, pp. 319-322, 1973.
- [202] J. Cahn, "On spinodal decomposition," *Acta Metallurgica*, vol. 9, pp. 795-801, 1961.
- [203] T. Nishizawa and K. Ishida, "The Co-Cu (Cobalt-Copper) System," *Bulletin of Alloy Phase Diagram*, vol. 5, no. 2, pp. 161-165, 1984.
- [204] F. Nix and F. Jaumot Jr., "Self-diffusion in cobalt," *Physical Review*, vol. 82, no. 1, pp. 72-74, 1951.
- [205] M. Arita, M. Nakamura, K. Goto and Y. Ichinose, "Activity and diffusivity measurements of copper in fcc cobalt by equilibration between solid Co and liquid Ag," *Transactions of the Japan Institute of Metals*, vol. 25, no. 10, pp. 703-709, 1984.
- [206] F. Bruni and J. Christian, "The chemical diffusion coefficient in dilute copper-cobalt alloys," *Acta Metallurgica*, vol. 21, pp. 385-390, 1973.
- [207] Kuper, "Self-diffusion in copper," *Physical Review*, vol. 96, no. 5, pp. 1224-1225, 1954.
- [208] H. Bowden and R. Balluffi, "Measurements of self-diffusion coefficients in copper from the annealing of voids," *Philosophical Magazine*, vol. 19, no. 161, pp. 1001-1014, 1969.
- [209] T. Surholt and C. Herzig, "Grain boundary self-diffusion in Cu polycrystals of different purity," *Acta Materialia*, vol. 45, no. 9, pp. 3817-3823, 1997.
- [210] "nanosurf.com," Nanosurf AG, [Online]. Available: <https://www.nanosurf.com/en/support/afm-modes-overview/magnetic-force-microscopy-mfm>. [Accessed 22 March 2021].
- [211] O. Kazakova, R. Puttock, C. Barton, H. Corte-Leon, M. Jaafar, V. Neu and A. Asenjo, "Frontiers of magnetic force microscopy," *Journal of Applied Physics*, vol. 125, p. 060901, 2019.
- [212] D. Tabor, "The hardness and strength of metals," *Journal of the Institute of Metals*, vol. 79, p. 1, 1951.
- [213] Y. Takeda, C. Kiattisaksri, M. Aramaki, S. Munetoh and O. Furukimi, "Effect of specimen thickness in tensile tests on elongation and deformation energy for industrially pure iron," *ISIJ International*, vol. 57, pp. 1-9, 2017.
- [214] Y. Zhao, Y. Guo, Q. Wei, A. Dangelewicz, C. Xu, Y. Zhu, T. Langdon, Y. Zhou and E. Lavernia, "Influence of specimen dimensions on the tensile behavior of ultrafine-grained Cu," *Scripta Materialia*, vol. 59, pp. 627-630, 2008.
- [215] W. Yuan, Z. Zhang, Y. Su, L. Qiao and W. Chu, "Influence of specimen thickness with rectangular cross-section on the tensile properties of structural steels," *Materials Science and Engineering A*, vol. 532, pp. 601-605, 2012.
- [216] A. Cziraki, L. Peter, V. Weihnacht, J. Toth, E. Simon, J. Padar, L. Pogany, C. Schneider, K. Wetzig, G. Tichy and I. Bakony, "Structure and giant magnetoresistance behavior of Co-Cu/Cu multilayer electrodeposited under various deposition conditions," *Journal of Nanoscience and Nanotechnology*, vol. 6, no. 7, pp. 2000-2012, 2006.
- [217] I. Matsui, Y. Takigawa, D. Yokoe, T. Kato, T. Uesugi and K. Higashi, "Strategy for electrodeposition of highly ductile bulk nanocrystalline metals with a face-centered cubic structure," *Materials Transactions*, vol. 55, no. 12, pp. 1859-1866, 2014.
- [218] N. Wang, Z. Wang, K. Aust and U. Erb, "Room temperature creep behavior of nanocrystalline nickel produced by an electrodeposition technique," *Materials Science and Engineering A*, vol. 237, no. 2, pp. 150-158, 1997.
- [219] J. Amblard, I. Epelboin, M. Froment and G. Maurin, "Inhibition and nickel electrocrystallization," *Journal of Applied Electrochemistry*, vol. 9, pp. 233-242, 1979.
- [220] A. Krause, M. Uhlemann, A. Gebert and L. Schultz, "A study of nucleation, growth, texture and

phase formation of electrodeposited cobalt layers and the influence of magnetic fields,” *Thin Solid Films*, vol. 515, pp. 1694-1700, 2006.

- [221] B. Oberdorfer, D. Setman, E. Steyskal, A. Hohenwarter, M. Sprengel, R. Zehetbauer, R. Pippan and R. Würschum, “Grain boundary excess volume and defect annealing of copper after high-pressure torsion,” *Acta Materialia*, vol. 68, pp. 189-195, 2014.
- [222] K. Konopka, J. Mizera and J. Wyrzykowski, “The generation of dislocations from twin boundaries and its effect upon the flow stresses in FCC metals,” *Journal of Materials Processing and Technology*, vol. 99, pp. 255-259, 2000.
- [223] D. Field, B. True, T. Lillo and J. Flinn, “Observation of twin migration in copper during deformation,” *Materials Science and Engineering A*, vol. 372, pp. 173-179, 2004.

Appended Papers

Some results in this thesis have been published in international journals and conference proceedings as shown in the following list. If there are any similarities with the mentioned publications, so they must be not counted as plagiarisms.

- I. Title : Microstructure evolution and mechanical stability of supersaturated solid solution Co-rich nanocrystalline Co-Co produced by pulsed electrodeposition
Author : Killang Pratama, Jenifer Barrirero, Frank Mücklich, and Christian Motz
Journal : *Materials* **2020**, 13(11), 2616
DOI : <https://doi.org/10.3390/ma13112616>

- II. Title : Strategies to achieve high strength and ductility of pulsed electrodeposited nanocrystalline Co-Cu by tuning the deposition parameters
Author : Killang Pratama and Christian Motz
Journal : *Molecules* **2020**, 25(21), 5194
DOI : <https://doi.org/10.3390/molecules25215194>

- III. Title : Thermal stability, phase decomposition, and micro-fatigue properties of pulsed electrodeposited nanocrystalline Co-Cu
Author : K. Pratama, F. Kunz, L. Lindner, J. Schmauch, F. Mücklich, C. Motz
Journal : *Procedia Structural Integrity* **2019**, 23, 366-371. Part of special issue: 9th International Conference Materials Structure & Micromechanics of Fracture (MSMF9).
DOI : <https://doi.org/10.1016/j.prostr.2020.01.114>

Article

Microstructure Evolution and Mechanical Stability of Supersaturated Solid Solution Co-Rich Nanocrystalline Co-Cu Produced by Pulsed Electrodeposition

Killang Pratama ^{1,2,*} , Jenifer Barrirero ³, Frank Mücklich ³ and Christian Motz ¹ 

¹ Chair of Materials Science and Methods, Saarland University, 66123 Saarbrücken, Germany; motz@matsci.uni-sb.de

² Department of Metallurgical Engineering, Institute Technology of Bandung, Bandung 40132, Indonesia

³ Chair of Functional Materials, Saarland University, 66123 Saarbrücken, Germany; j.barrirero@mx.uni-saarland.de (J.B.); muecke@matsci.uni-sb.de (F.M.)

* Correspondence: k.pratama@matsci.uni-sb.de or killang.pratama@gmail.com

Received: 12 May 2020; Accepted: 5 June 2020; Published: 8 June 2020



Abstract: Thick films of supersaturated solid solution nanocrystalline Co-Cu (28 at.% Cu) were synthesized through the pulsed electrodeposition technique. Microstructural changes of nanocrystalline Co-Cu were intensively studied at various annealing temperatures. Annealing at 300 °C results in a spinodal decomposition within the individual grains, with no grain coarsening. On the other hand, distinct phase separation of Co-Cu is detected at annealing temperatures beyond 400 °C. Static micro-bending tests show that the nanocrystalline Co-Cu alloy exhibits a very high yield strength and ductile behavior, with no crack formation. Static micro-bending tests also reported that a large plastic deformation is observed, but no microstructure change is detected. On the other hand, observation on the fatigue resistance of nanocrystalline Co-Cu shows that grain coarsening is observed after conducting the cyclic micro-bending test.

Keywords: nanocrystalline Co-Cu; spinodal decomposition; micro mechanics; mechanical stability

1. Introduction

Studies on the fundamental behavior [1], mechanical properties [2], and possible industrial applications [3] of nanocrystalline materials are wide-spread in the literature. Among of the promising materials in this class are supersaturated solid solution nanocrystalline alloys, e.g., Co-Cu alloy, the microstructure and phase distribution of which can be modified by annealing treatments, to enhance thermal and mechanical stability, as well as tailoring physical properties [4,5]. Investigations into the thermal stability and microstructure evolution of nanocrystalline Co-Cu have been performed in previous works, mostly at temperatures beyond 400 °C [6–8], but more research about microstructural changes at lower temperatures is required. The information about the mechanical properties of nanocrystalline Co-Cu is also limited [9–11]. On the other hand, the information about the mechanical properties of single-phase nanocrystalline Co and Cu is widely available in the literature [12–17]. Therefore, more research on the mechanical properties of nanocrystalline Co-Cu with different microstructures is required.

Nanocrystalline pure Co [12,13] and Cu [14–17] possess excellent mechanical properties compared to the conventional coarse-grained counterpart. However, slight reductions in ductility were observed, due to flaws induced during synthesis and surface preparation, as well as low strain hardening capability and low resistance to crack initiation and propagation [18–20]. In addition, mechanical

instability during fatigue test of nanocrystalline and ultrafine grained materials was also observed and intensively studied in the literature [21–23]. Considering the mechanical instability of nanocrystalline materials, strategies were developed for improvement, such as the utilization of non-uniform grain sizes [20,24] and secondary phase or particles [25,26]. Among the promising strategies is the application of multiple phases in the nanocrystalline materials [25,26], which are also termed metallic composites, in which different dislocation activity or deformation mechanisms in the primary and secondary phases are expected to improve the plastic deformation behavior of nanocrystalline materials.

The formation of metallic composite and precipitation of solute components from immiscible alloys including the Co-Cu system is possible through the spinodal decomposition [27,28]. However, spinodal decomposition and nucleation in nanocrystalline Co-Cu at high temperature (>400 °C) is usually followed by grain coarsening, such as demonstrated in previous research [6,7]. Thus, investigation of the spinodal decomposition to modify the microstructure at low temperature is needed, to minimize the grain coarsening effect. The spinodal decomposition of Co and Cu in nanocrystalline Co-Cu is crucial to produce multiple phase materials. It has been reported that nanocrystalline Cu has a good ductility, while nanocrystalline Co has a significant high strength [12–17]. Interestingly, cyclic mechanical loading shows that nanocrystalline Cu [23] and Co [29] have a different softening-hardening behavior. The different mechanical behavior of nanocrystalline Co and Cu can be used as an interesting combination for improving the mechanical stability and performance of nanocrystalline Co-Cu system.

In this research work, nanocrystalline Co-Cu were produced through the pulsed electrodeposition (PED) technique, instead of severe plastic deformation (SPD). According to the literature [30–33], lattice defects in SPD- and PED-processed nanocrystalline materials (e.g., excess vacancies, dislocation, and twins) are different in characteristic, type, and number, thus, different mechanical properties are expected. Furthermore, to investigate the impacts of the synthesis route on the microstructural changes upon heat treatment, comprehensive studies on the microstructure evolution of electrodeposited nanocrystalline Co-Cu annealed at various temperatures were performed in this study, by scanning electron microscope (SEM), transmission electron microscope (TEM), X-ray diffraction (XRD), and atom probe tomography (APT). The principal mechanical properties are investigated by microhardness measurements. At the end of the paper, the mechanical stability of nanocrystalline Co-Cu and the effect of plastic deformation on the microstructure are studied, through static and cyclic micro-bending tests.

2. Materials and Methods

Nanocrystalline Co-Cu films up to a thickness of 400 µm were deposited through PED on Cu disk cathodes (surface diameter: 12 mm) through a Pt anode under specific parameters and conditions of deposition: current density: 1000 A/m²; pulse period: 2 ms; break period: 18 ms; temperature: 40 °C. The deposition was performed in an electrolyte containing 112.20 g/L CoSO₄·7H₂O, 6.38 g/L CuSO₄, 56.44 g/L C₄H₄KNaO₆·4H₂O, 142.04 g/L Na₂SO₄, 18.55 g/L H₃BO₃, 2.00 g/L C₇H₅NO₃S (Saccharin), and 0.20 g/L C₁₂H₂₅NaO₄S (sodium dodecyl sulfate). In the present work, the parameters of deposition and composition of electrolyte were based on previous work by Müller [34], and were optimized to obtain compact and homogeneous deposits with a Cu content of 28-at.%.

The deposited samples were subjected to isothermal annealing in vacuum at a pressure of 10^{−6} mbar at various temperatures (300–600 °C) for different periods of time (1–64 h) to investigate the thermal stability and structural transformation. Microstructure and composition analysis were taken from the cross-sections of the samples and carried out in the field-emission scanning electron microscope (SEM) (Zeiss Sigma-VP, Jena, Germany) equipped with backscattered electrons (BSE) and energy dispersive spectroscopy (EDS) detectors at acceleration voltages of 17–20 kV. Grain size determination was performed manually by measuring the length of line interception within individual grains at two different orientations with the imageJ software (Ver 1, LOCI, University of Wisconsin, Madison, USA) [35], and EDS analysis were conducted with the AZtec software (Oxford Instrument Inc., Abingdon, England). Microhardness measurements (HV 0.2; test force: 1.962 N) were performed at cross-sections of the samples with a DuraScan hardness testing device (Struers, Copenhagen,

Denmark) and equipped with ecos Workflow software (EMCO-TEST Prüfmaschinen GmbH, Kuchl, Austria). Hardness measurements were performed at positions of 30 μm and 200 μm from the substrate. X-ray diffraction (XRD) measurements were conducted to investigate the phase composition of the individual samples. Cu K-alpha radiation (λ : 1.5405980 \AA) and a scan step size of $0.013^\circ 2\theta/\text{s}$ was used. Transmission electron microscope (TEM) samples were prepared from the polished samples (diameter: 3 mm) in planar mode, and then further processed by GATAN PIPS ion milling to produce an electron transparent film at the center of the disc. TEM observation was performed in a JEOL JEM 2011 (JEOL, Tokyo, Japan) at an accelerating voltage of 200 kV to acquire enhanced microstructural information, as well as diffraction patterns of selected samples.

Specimens for atom probe tomography (APT) were prepared in a dual-beam focused ion beam/scanning electron microscopy workstation (FIB/SEM) (Helios NanoLab 600TM, FEI Company, Hillsboro, OR, USA) by the lift-out technique described in the literature [36]. Material was extracted from the center of the cross section of the film. An electron beam induced Pt-capping layer was first deposited to provide protection from gallium implantation. After lift-out and thinning of the specimens, a low energy milling at 2 kV was performed to minimize Ga induced damage [36]. Laser Pulsed APT was carried out in a LEAP 3000X HR (CAMECA, Gennevilliers, France). Measurements were performed at repetition rates of 100 and 160 kHz, a pressure lower than 1.33×10^{-8} Pa, an evaporation rate of 5 atoms per 1000 pulses and a specimen temperature of about 60 K. The laser used has a wavelength of 532 nm, a pulse length of 10 ps, and a pulse energy of 0.5 nJ. Datasets were reconstructed and analyzed with IVASTM3.6.8 software (CAMECA, Gennevilliers, France). Regions-of interest (ROI) were used to construct one-dimensional concentration profiles through the specimens. Three APT specimens of the as-deposited alloy and four of the annealed sample were analyzed.

Micro bending beams were manufactured in a focused ion beam (FIB/SEM) (Helios NanoLab 600TM, FEI Company, Hillsboro, OR, USA) on the cross-section of the nanocrystalline film at a position of 200 μm from the substrate. The dimensions of the beams are presented in Table 1. One micro bending beam (beam-A) was prepared for a static micro bending test, while cyclic micro bending tests were performed on beam-B and beam-C at different plastic strain amplitudes. In situ static and cyclic micro-bending test were performed in a TESCAN-Vega scanning electron microscope (TESCAN, Brno, Czech Republic) equipped with the Advanced Surface Mechanics (ASMEC, Ulm, Germany) nanoindentation system and InspectorX Ver. 2 UNAT software (ASMEC, Ulm, Germany) to record the force-displacement data. A nano-indenter and a double blade gripper were used to impose static and cyclic mechanical loading onto micro bending beams at the test parameters, which are given in Table 1. The force-displacement data were calculated and presented as a surface stress (σ_s) and a surface strain (ϵ_s), based on elastic bending beam theory through Equations (1) and (2). The recorded force and displacement are F and D , respectively, while L_B , W , and T correspond to length, width, and thickness of the bending beam, respectively.

Table 1. Dimensions of micro bending beams with the length (L), width (W), thickness (T), and bending length (L_B). Static micro bending test were carried out at the surface strain rate $\dot{\epsilon}$, while cyclic micro bending test were performed at multiple stage plastic strain amplitude ($\epsilon_{s,a}$) and number of cycles (N).

Name of Sample	L (μm)	W (μm)	T (μm)	L_B (μm)	Static Loading	Cyclic Loading	
					$\dot{\epsilon}$ (s^{-1})	$\epsilon_{s,a}$	N (Cycles)
Beam-A	15.04	7.15	5.33	14.60	1.24×10^{-2}	-	-
Beam-B	15.43	6.68	4.92	14.00	-	1.80×10^{-4}	5000
Beam-C (4 stages)	15.77	6.75	5.26	13.92	-	1.50×10^{-3} (Stage-I)	35
						2.00×10^{-3} (Stage-II)	65
						3.50×10^{-3} (Stage-III)	40
						7.00×10^{-3} (Stage-IV)	100

$$\sigma_s = \frac{6L_B F}{W T^2} \quad (1)$$

$$\varepsilon_s = \frac{D T}{2L_B^2} \quad (2)$$

3. Results and Discussion

3.1. Structural Evolution

Figure 1a depicts a cross section image and EDS map of compact and porosity-free deposit of nanocrystalline Co-Cu film deposited at a current density of 1000 A/m² and a pulse period 2 ms (duty cycle: 10%). The EDS line profile in Figure 1b shows a quiet homogeneous concentration of Co and Cu along a cross-section of nanocrystalline Co-Cu (28 at.% Cu) film. The EDS line profile confirms that the cobalt concentration drops up to ~15 at.% from area near the Cu-substrate to the surface of nanocrystalline film. Thus, deposition for more than 400 μm of thicknesses is not preferred, due to the inhomogeneous concentration of Co and Cu. Deposition of nanocrystalline Co-Cu at a higher Cu concentration is possible by reducing current density. However, a back-scattered electron image of Co-Cu (45 at.% Cu) alloy, deposited at a current density of 500 A/m² and a pulse period of 2 ms (duty cycle: 10%), shows an inhomogeneous microstructure, in which a mixture of ultrafine grained and nanocrystalline structure are observed (see Figure 1c). Deposition at a higher current density and duty cycle [for example at current density of 1500 A/m² and duty cycle 20% (see Figure 1d)], lead to the formation of microporous (mark with blue arrows in see Figure 1d) and an inhomogeneous chemical composition. Therefore, to achieve homogeneous microstructure and chemical composition, as well as compact and porosity-free deposits, all samples used in this paper were deposited at a current density of 1000 A/m² and pulse period of 2 ms (duty cycle: 10%).

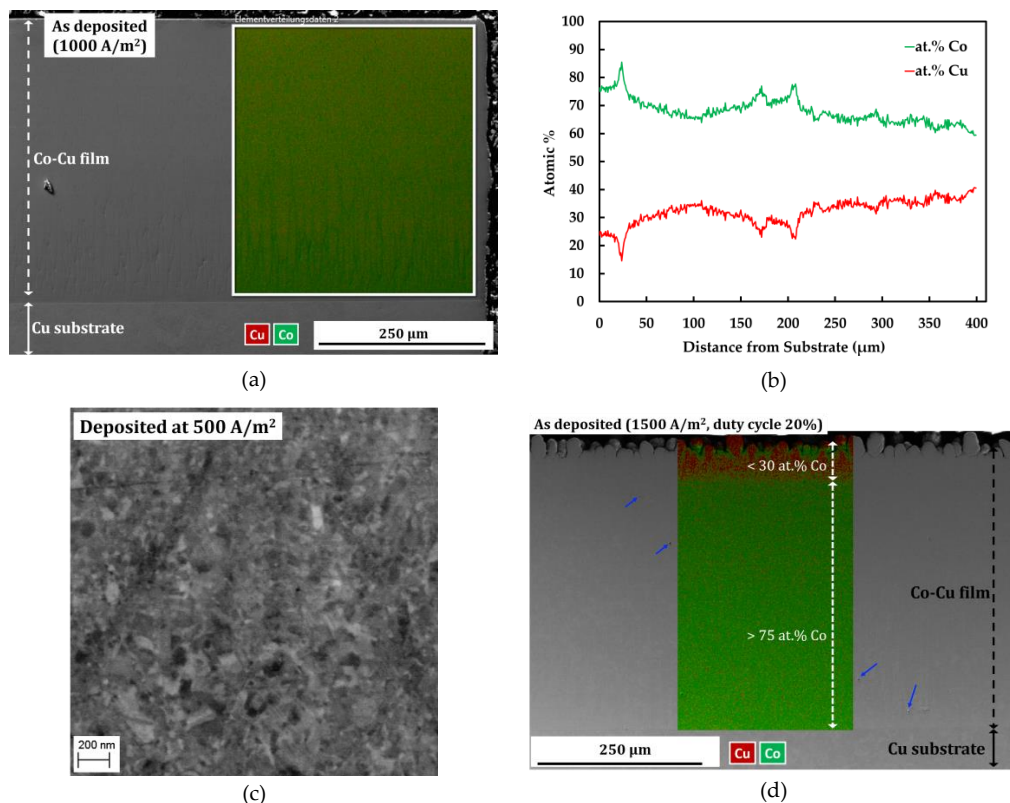


Figure 1. (a) Combined secondary electron (SE) image—energy dispersive spectroscopy (EDS) map

and (b) EDS line profile of sample deposited at a current density of 1000 A/m^2 , and a pulse period of 2 ms (duty cycle: 10%) in the cross-section mode. (c) Back-scattered electron images of the microstructure of a sample deposited at a current density of 500 A/m^2 , and a pulse period 2 ms (duty cycle: 10%). (d) Combined secondary electron image-EDS map of sample deposited at a current density of 1500 A/m^2 , and a pulse period of 2 ms (duty cycle: 20%) in cross section mode.

Figure 2a shows a combined bright-field TEM image and selected area diffraction (SAD) pattern of the PED-processed nanocrystalline Co-Cu (28 at.% Cu), in which nanometer sized grains of about $22.7 \pm 8.2 \text{ nm}$ are observed (Figure 2b). A number of twins are also observed, which are marked with red arrows in Figure 2a. The formation of *twins* is believed to be due to effect of chemical additives (saccharine and sodium dodecyl sulfate) during the electrodeposition process, as demonstrated in the previous paper [33]. The contribution from high current density and pulsed current may also have an influence on the formation twins. The XRD (Figure 2c) pattern shows that the ED nanocrystalline Co-Cu (28 at.% Cu) exhibits a supersaturated solid solution phase, in which the peaks of {111} and {200} planes of the single fcc phase are observed. The as-deposited nanocrystalline Co-Cu (28 at.% Cu) exhibit a high hardness of $4.45 \pm 0.07 \text{ GPa}$. The high value of microhardness could be contributed to by several factors, such as chemical composition, grain size, and number of lattice defects (twins, dislocations, and vacancies). The co-deposition of impurity elements (e.g., carbon, sulfur, and hydrogen) also has an influence on the hardness of the electrodeposited nanocrystalline Co-Cu.

In the present work, early stages of microstructural changes of the PED-processed nanocrystalline Co-Cu are studied at $300 \text{ }^\circ\text{C}$, which minimizes grain coarsening, as shown in previous research [6,7]. All samples annealed at $300 \text{ }^\circ\text{C}$ for different periods (1 h, 5 h, and 24 h) exhibit an increase of hardness, compared to the as-deposited state (see Table 2). Interestingly, no significant grain coarsening is observed in the sample annealed even for 24 h in which nano sized grains of less than 50 nm remain unchanged (see Figure 2d). It is believed that the hardening effect is influenced by the spinodal decomposition of the solid solution Co-Cu, as demonstrated by Kato [37]. The PED-processed nanocrystalline Co-Cu was further annealed at $300 \text{ }^\circ\text{C}$ for up to 64 h, to study its long-term thermal stability and the chemical decomposition. Figure 2e depicts a combined bright-field TEM image and SAD pattern of an at $300 \text{ }^\circ\text{C}$ for 64 h annealed sample, showing no significant grain changes nor grain coarsening. Figure 2e also shows the presence of twins (indicated by red arrows). In this annealed sample, microstructure and hardness observations show that the average grain size is about $27.2 \pm 7.9 \text{ nm}$ (see Figure 2f) and the hardness increases up to $4.83 \pm 0.07 \text{ GPa}$. In comparison with the as-deposited state, only minor changes are detected from the XRD measurement (Figure 2c). Comparing the SAD pattern of as deposited (Figure 2a) and annealed (Figure 2e) samples, lattice shifts of the {111} and {200} planes are observed, and the spinodal decomposition of the Co-Cu solid solution at the nanometer scale during annealing at $300 \text{ }^\circ\text{C}$ is expected to cause the shift. Consequently, peak shifts of the {111} and {200} planes are observed from the XRD pattern (see Figure 2c). However, it is also believed that the lattice shift is not single-handedly caused by spinodal decomposition, but could also be caused by other factors or processes during isothermal annealing at $300 \text{ }^\circ\text{C}$ for 64 h, such as the relaxation of internal stresses and grain boundaries, reducing of defect density, etc. However, an investigation on internal stress, grain boundaries relaxation, and defect density in nanocrystalline Co-Cu is not conducted in this paper, in which the observation is focused on the spinodal decomposition of nanocrystalline Co-Cu. Thus, APT measurements are conducted to investigate the possible structural and chemical decomposition at $300 \text{ }^\circ\text{C}$.

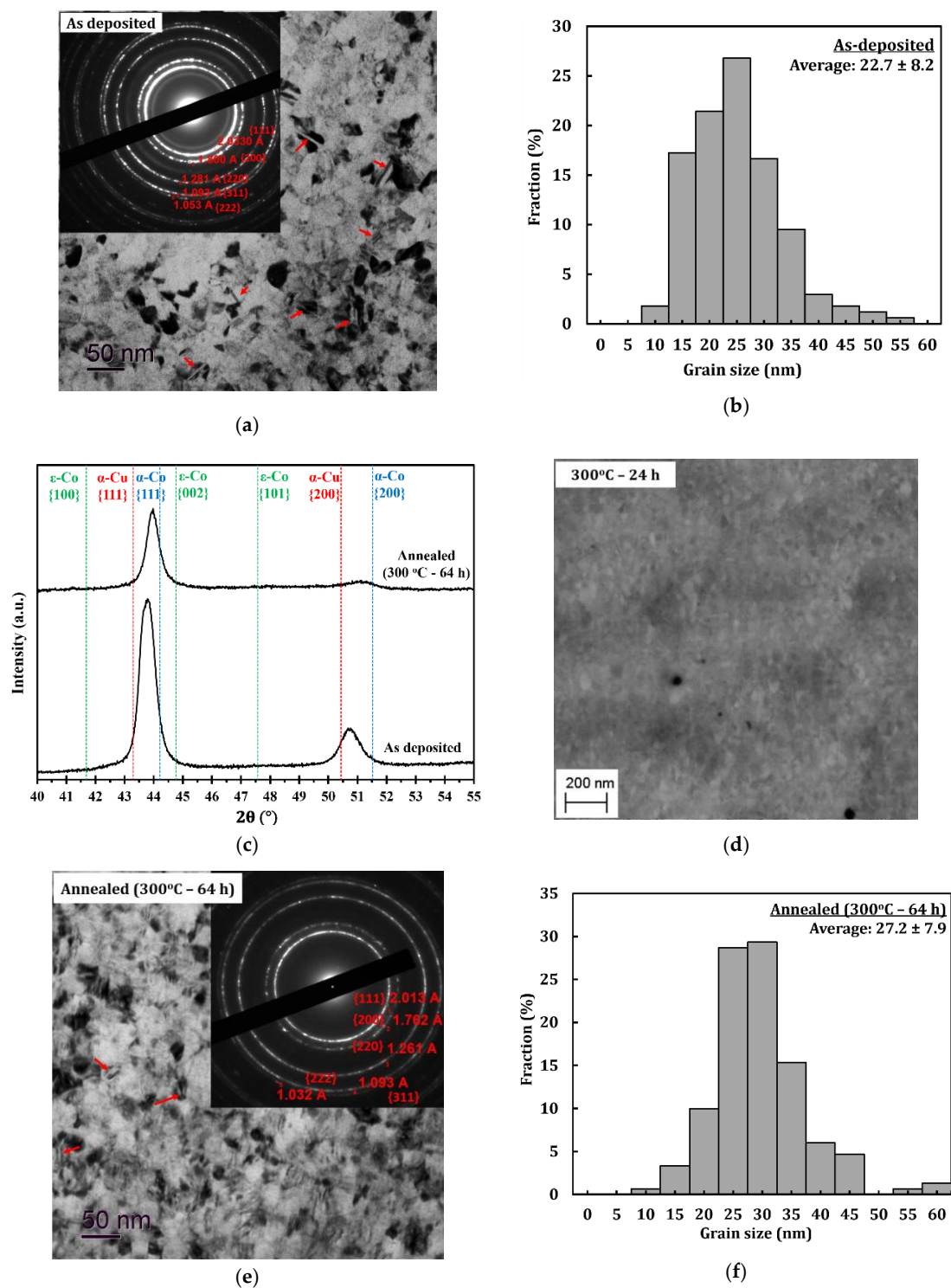


Figure 2. (a) Combined bright-field transmission electron microscope (TEM) and selected area diffraction (SAD) pattern images of sample deposited at current density of 1000 A/m² and pulse period 2 ms (duty cycle: 10%) in planar mode and (b) its grain size distribution. (c) X-ray diffraction (XRD) pattern of as deposited sample and annealed (300 °C–64 h) samples. (d) Back-scattered electron images of the microstructure of a sample annealed at 300 °C for 24 h in cross section mode. (e) Combined bright-field TEM and selected area diffraction (SAD) pattern images of annealed (300 °C–64 h) sample in planar mode and its (f) grain size distribution.

Table 2. Microhardness and average grain size of the annealed samples. Grain size measurements were determined based on the microstructure images from the scanning electron microscope (SEM) measurements.

	Microhardness (GPa)			Grain Size (nm)		
	300 °C	450 °C	600 °C	300 °C	450 °C	600 °C
1 h	4.89 ± 0.06	4.43 ± 0.07	3.94 ± 0.06	<50 *	122.0 ± 19.4	159.6 ± 66.2
5 h	4.67 ± 0.18	4.40 ± 0.06	3.69 ± 0.06	<50 *	124.0 ± 40.5	183.6 ± 67.2
24 h	4.56 ± 0.06	4.31 ± 0.05	3.25 ± 0.12	<50 *	127.0 ± 39.0	218.6 ± 73.2

* Rough estimation from SEM images.

APT measurements were conducted for the as deposited and annealed (300 °C for 64 h) samples. Figure 3a shows an APT elemental map of a slice through a reconstruction of the as-deposited sample, and a concentration profile corresponding to the white dashed line. According to these results, the as-deposited sample shows a solid solution with imperfect homogeneous concentration of Co and Cu at nanometer scale, but no short-range fluctuation (e.g., spinodal decomposition, precipitation) of Co or Cu is found. This was also observed previously on the high-pressure torsion (HPT)-processed nanocrystalline Co-Cu [7,38], and it was also shown that spinodal decomposition with minor grain coarsening was observed at 400 °C [7]. In the present work, APT measurements show that a spinodal decomposition of Co-Cu takes place also at 300 °C. Figure 3b depicts an APT elemental map of a selected slice from a reconstruction of an annealed sample. Three regions with distinctive compositions are observed: (i) Co-Cu solid solution, (ii) Co-rich regions (up to 95 at.% Co) and Cu-rich region (up to 90 at.% Cu). Moreover, an APT elemental map of another reconstruction in the annealed sample (Figure 3c) shows small compositional fluctuations in the solid solution region. Such compositional fluctuations are crucial characteristic of a spinodal decomposition [39], and these fluctuations will grow continuously until a metastable equilibrium is achieved.

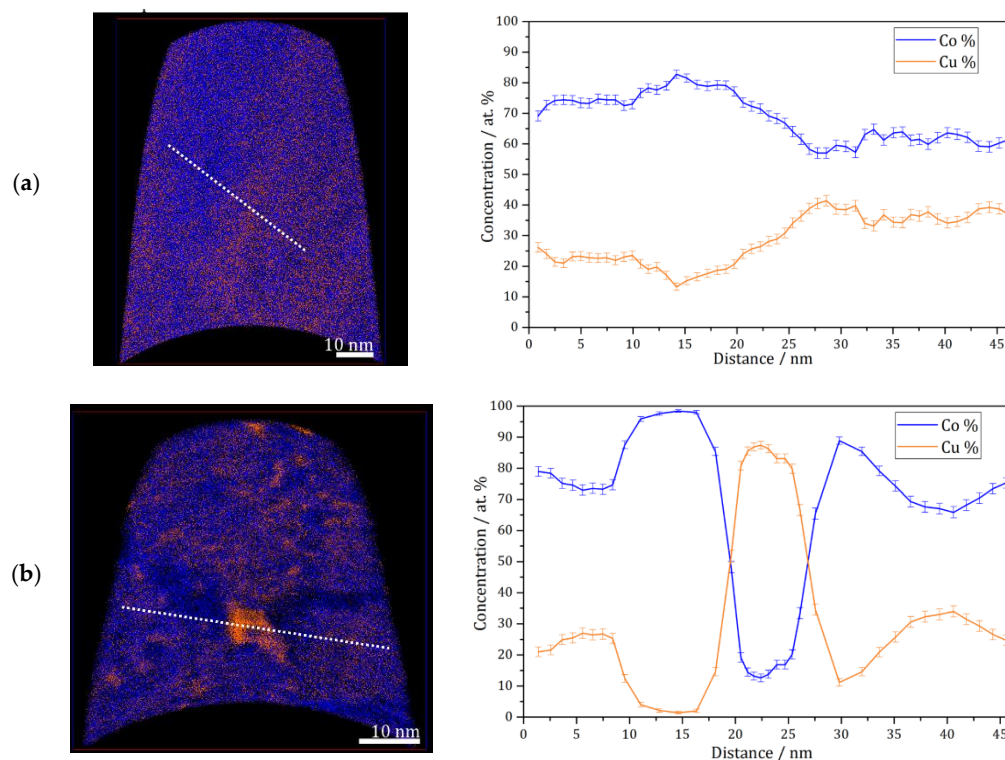


Figure 3. Cont.

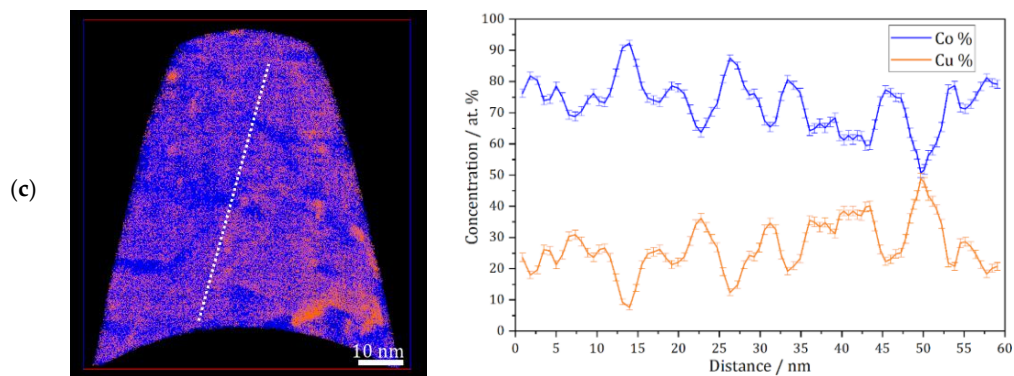


Figure 3. Atom probe tomography (APT) elemental maps of Co (blue) and Cu (orange) of 5 nm thick slices through the reconstructions and one-dimensional concentration profiles along the white dashed lines on the elemental maps (from **left** to **right**). (a) As-deposited sample; (b and c) similar annealed sample (300 °C–64 h).

The atomic diffusion at the grain boundaries is not considered here, since the compositional fluctuations occurs within the grains at 300 °C. Of course, diffusion at grain boundaries is much faster and can lead to a fast de-mixing in these regions, which is possibly the reason for the “spots” with high Co or Cu concentration in e.g., Figure 3b. However, here, it is focused on the atomic diffusion of Co and Cu, which induces a spinodal decomposition within individual grains. The diffusion rate in this nanocrystalline supersaturated solid solution may be different compared to common materials, as the defect content, lattice constant, crystal structure, etc. may be different. However, a rough estimation of the atomic mobility of the alloys’ components can be considered for an initial study. In previous research [7], atomic mobility of solute atom Co in the nanocrystalline Co-Cu (74 at.% Cu) was calculated through the classical theory of diffusion equation $L = \sqrt{Dt}$, where L , D , and t are described as distance, diffusion coefficient, and period of diffusion (time), respectively. In the present work, the atomic mobility of Co and Cu atoms in a Co-Cu solid solution system (28 at.% Cu) is also roughly estimated through the same procedure. Considering the chemical composition of the alloy system (72 at.% Co and 28 at.% Cu), the possible diffusion mechanisms that are likely to occur are Co self-diffusion, Cu diffusion in Co, and interdiffusion of Co-Cu. The diffusion coefficient data were taken from the literature [40–42]. However, since the diffusion coefficient at 300 °C is not available, the diffusion coefficient data from the literature [40–42] were extrapolated through the Arrhenius equation ($D = A \exp [-E_A/RT]$) to get the diffusion coefficient data at 300 °C (it is assumed that the diffusion mechanism doesn’t change). The calculated diffusion distance for 300 °C and 64 h from the mechanisms of Co self-diffusion, Cu diffusion in Co, and Co-Cu interdiffusion are 0.0005 nm, 0.0014 nm, and 0.098 nm, respectively. The measurements show that the atomic mobility of Co and Cu is very low, in which diffusion distances of less than 1 nm were calculated. Surprisingly, the APT measurement (Figure 3b) shows that the diffusion distance of Co and Cu atoms is in the range of 5 to 10 nm. At this point, it must be considered that all diffusion coefficients [40–42] were measured in bulk materials, so the result would be different in nanocrystalline materials, due to the larger number of lattice defects within a grain as mentioned before. The contribution from mainly vacancy-type defects in nanocrystalline materials may significantly enhance the atomic diffusivity [43].

Figure 4a,b show microstructure images of electrodeposited nanocrystalline Co-Cu (28 at.% Cu) annealed at 450 °C for 5 h and 24 h. A significant grain coarsening and hardness decrease are observed from these micrograph (see also Table 2). Interestingly, no significant differences of grain size and hardness values are observed between samples annealed for short (1 h and 5 h) and long (24 h) periods. The XRD pattern of a sample annealed at 450 °C for 5 h shows a shoulder on the peak of {111} planes (marked with black arrow in Figure 5a), but no significant phase separation is detected. It is believed that the observed shoulder is an indication of an early stage of spinodal decomposition where Cu-rich regions is formed. In contrast, XRD pattern of a sample annealed at 450 °C for 24 h

exhibits a massive phase separation of solid solution Co-Cu in which fcc-Cu, fcc-Co, and hcp-Co {101} peaks are detected (see Figure 5a). However, since the peaks of fcc-Co and fcc-Cu are hard to separate, it is believed that a certain amount of solid solution Co-Cu phase remained, and that phase separation is in progress. In addition, a number of particles (black spots in the images) are observed mainly at the grain boundary, and twins are also recognized from the micrograph (Figure 4b). Based on some evidences, microstructure and phase evolution of the electrodeposited nanocrystalline Co-Cu (28 at.% Cu) at 450 °C can be divided into different stages. During short annealing periods (1 h and 5 h), the diffusion of Co and Cu atoms leads predominantly to spinodal decomposition and grain boundary movement. The early stage of spinodal decomposition leads to the formation of Co and Cu concentration fluctuations within the grains. At the grain boundaries, where the diffusion is expected to be faster, the formation Cu-precipitates can be expected. It is believed that the dark particles that are observed in the Figure 4a,b are related to these Cu-precipitates. These Cu-precipitates are believed to block the grain boundaries movement (pinning of grain boundaries), thus, a constant grain size is obtained after a certain period of annealing. Upon annealing for longer times (24 h), the spinodal decomposition progresses, and a phase separation will also take place within the grains. The Cu precipitates at the grain boundaries will still hinder their movement, hence the grain size remains almost constant.

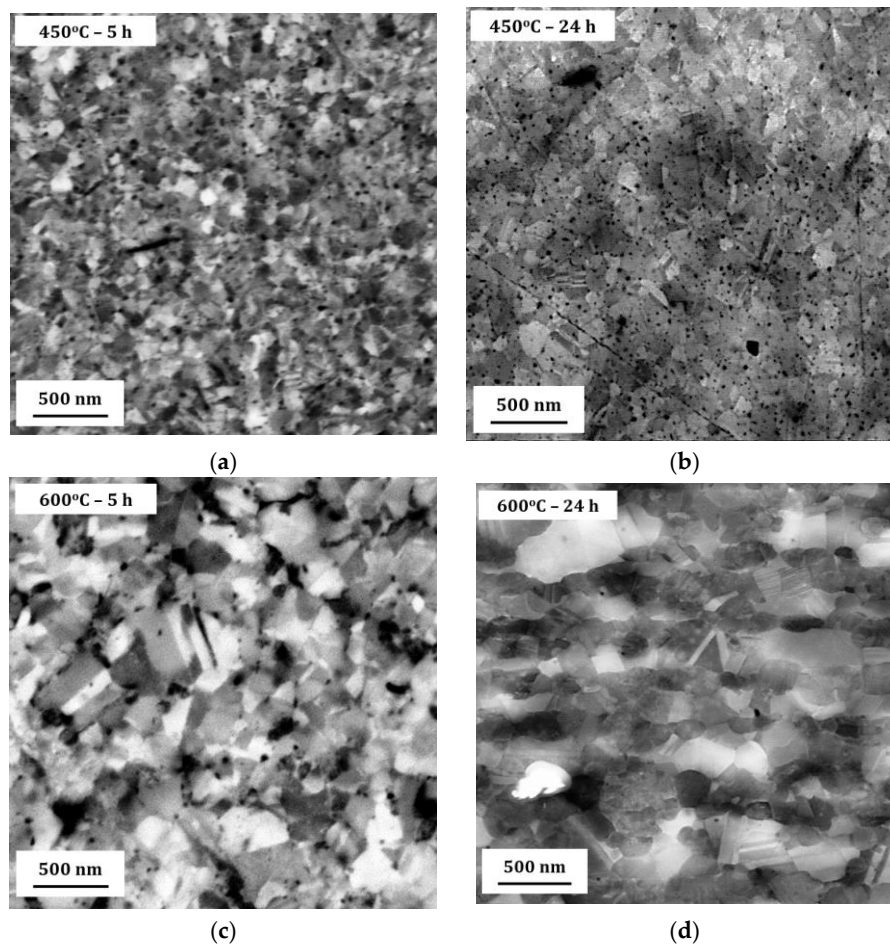


Figure 4. Back-scattered electron images of the microstructure of annealed samples at various temperatures for different periods: (a) 450 °C for 5 h, (b) 450 °C for 24 h, (c) 600 °C for 5 h, (d) 600 °C for 24 h. All microstructure images were taken in the cross section of the deposited nanocrystalline Co-Cu films. For individual images, notice the scale bar to distinguish the magnification.

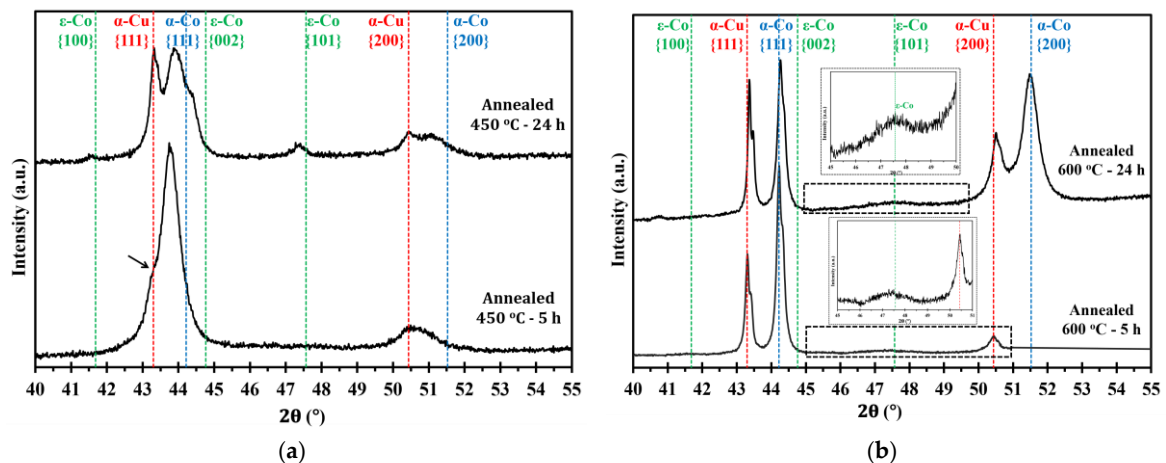


Figure 5. XRD patterns of electrodeposited nanocrystalline Co-Cu (28 at.% Cu) annealed at (a) 450 °C and (b) 600 °C for short (5 h) and long (24 h) periods of annealing. All measurements were taken in the cross section mode.

Figure 4c,d show the micrograph of electrodeposited nanocrystalline Co-Cu (28 at.% Cu) annealed at 600 °C for 5 h and 24 h. In comparison with the sample annealed at 450 °C, the grain coarsening is more pronounced, thus, as expected from the Hall-Petch relation, the microhardness values slightly decrease to lower than 4 GPa (Table 2). The XRD measurements show that the phase separation is clearly visible in the samples annealed at 600 °C for 5 h and 24 h (Figure 5b), in which the peaks of fcc-Co, fcc-Cu and a weak hcp-Co {101} are detected. According to the microstructure images (Figure 4c,d), the presence of twins and particles (which is believed as Cu-precipitates) are also detected, and their size increases with increasing the annealing period. The phase separation is almost complete, and results in a microstructure consisting of almost pure Co and Cu regions. The mobility of the grain boundaries is rather high at 600 °C and the Cu-precipitates are unable to block the grain boundary move.

According to the XRD and SEM measurements, the microstructural evolution during the annealing of the PED-processed nanocrystalline Co-Cu (28 at.% Cu) is comparable with the HPT-processed nanocrystalline Co-Cu (25 at.% Cu) [6]. Figure 6a,b show the microhardness evolution of PED- and HPT-processed [6,8] nanocrystalline Co-Cu at almost identical chemical composition annealed at different annealing temperatures and times. Upon a short annealing time of 1 h (Figure 6a), the PED-processed nanocrystalline Co-Cu shows an increased hardness at temperatures lower than 450 °C in comparison with the HPT-processed [6] materials. Moreover, Figure 6a,b show that the hardening effect due to chemical decomposition of Co-Cu at 300 °C is more obvious for the PED-processed materials [6,8]. The thermal stability of nanocrystalline materials can be influenced by several factors, which are the initial grain size, phase stability, and stabilization by solute components. The initial grain size of the PED-processed nanocrystalline Co-Cu in the present work is three to four times smaller than the HPT-processed Co-Cu [6,8]. On one hand, this results in an increased driving force for grain growth, however, on the other hand, the small grain size may speed up the segregation of Cu to grain boundaries which may result in early formation of “precipitates” at the boundaries. These small Cu-rich regions may effectively pin the boundaries and avoid grain coarsening which results, along with the spinodal decomposition within the grains, in an increase in hardness at low annealing temperatures. Of course, other mechanisms, like different defect types and densities or the relaxation of boundaries may also contribute to the difference between the PED- and HPT-processed materials. Furthermore, in the PED-processed nanocrystalline materials, additional improvement of thermal stability can also be attributed to the co-deposition of impurity elements, such as carbon and sulfur. In the literature [44], it has been reported that the segregation of sulfur to grain boundaries could significantly improve thermal stability of the PED-processed nanocrystalline Co.

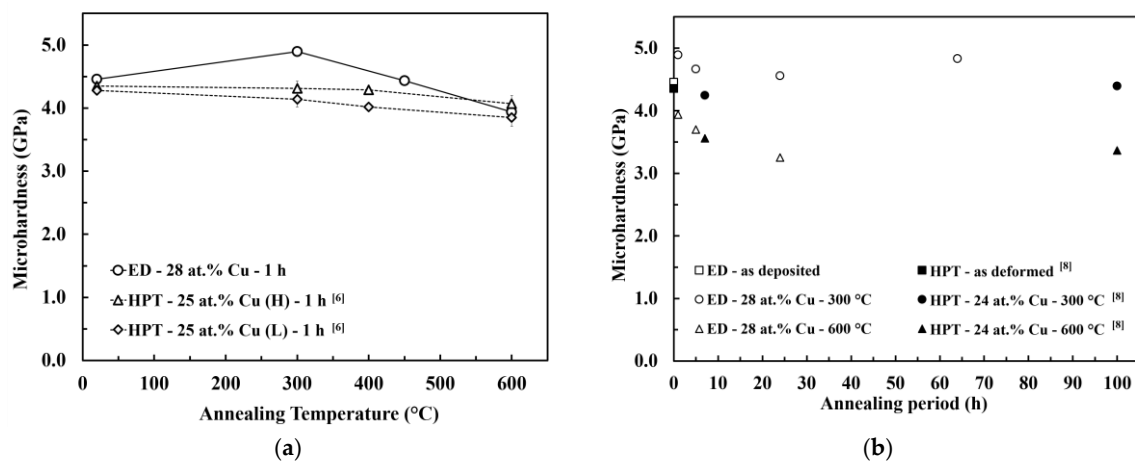


Figure 6. Microhardness evolution of electrodeposited (ED) nanocrystalline Co-Cu (28 at.% Cu) during isothermal annealing at different temperatures for different periods which is compared with HPT-processed nanocrystalline Co-Cu at chemical composition of (a) 25 at.% Cu [6] and (b) 24 at.% Cu [8]. (H) and (L) are indicating high and low purity of Co and Cu powder used in HPT process.

3.2. Mechanical Stability

The mechanical properties and microstructure development during plastic deformation of the PED-processed nanocrystalline Co-Cu (28 at.%) were investigated through static and cyclic micro bending experiments. Figure 7a depicts an engineering surface stress vs.- strain curve of micro beam-A resulted from a static micro bending test at a surface strain rate of $1.24 \times 10^{-2} \text{ s}^{-1}$. Practically, the determination of strain hardening coefficient, total surface strain, and ultimate strength is possible from the surface stress-strain curve. However, it should be carefully considered that the calculated surface stress-strain data through the elastic bending beam theory is only accurate for up to the yield point, and will fail in the plastic regime. Therefore, in the present work, the discussion on the parameters from the surface stress-strain curve will be focused only up to yield point. According to the curve, the measured yield strength is extremely high ($\sigma_y \approx 3.9 \text{ GPa}$). However, it is believed that the actual yield strength is lower, due to the inhomogeneous deformation in bending tests. At the initial stage of deformation, only a small surface layer of the micro beam is plastically deformed (the whole beam is not plastically deformed yet). Thus, the elastic-plastic transition regime is quite smooth, and an exact determination of the yield point is difficult (see Figure 7b). As a consequence, it can be assumed that the yield point is between 2.8 and 3.9 GPa (see Figure 7b). In comparison, according to Tabor's rule, the yield strength can be estimated from the microhardness measurements with $\sigma_y \approx 1.5 \text{ GPa}$.

Figure 8a,b show the secondary electron (SE) images of micro beam-A after deformation recorded from the top and side view of the bending direction (y-axis). According to Figure 8a,b micro beam-A is plastically deformed, in which no crack formation is detected. Necking effects due to plastic deformation, which are marked with white arrows, are clearly visible (see Figure 8a). The surface changes due to plastic deformation can be easily identified too (see Figure 8b). Therefore, according to the stress-strain curve and SE-detector images, it is obvious that the ED nanocrystalline Co-Cu (28 at.%) exhibits a ductile behavior. Unfortunately, the microstructure observation through the back-scattered electron (BSE) detector is difficult, due to distinct surface roughness. Thus, FIB polishing was performed to produce a smooth surface at the selected areas on micro beam-A. Figure 8c,d depict BSE images of the microstructure at two different positions (zone-A and zone-B) at the FIB polished region. According to Figure 8c,d no microstructural changes, such as grain coarsening, are observed at the areas of large plastic deformation.

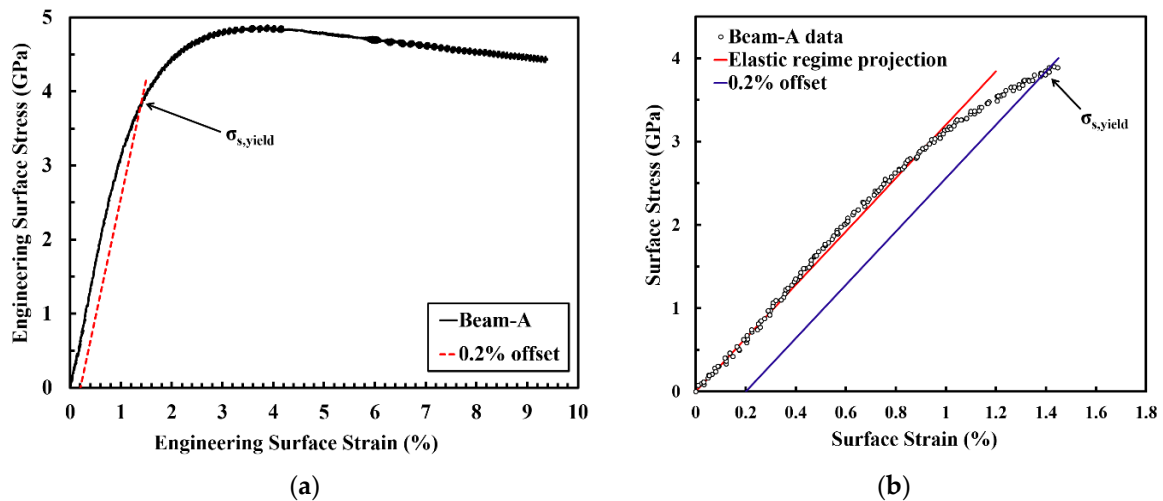


Figure 7. (a) Engineering surface stress-strain curve of micro beam-A (black solid line) and its 0.2% offset (red dashed line). (b) Detailed engineering surface stress-strain curve at the elastic-plastic transition regime equipped with an elastic regime projection (red line) and 0.2% offset (blue line).

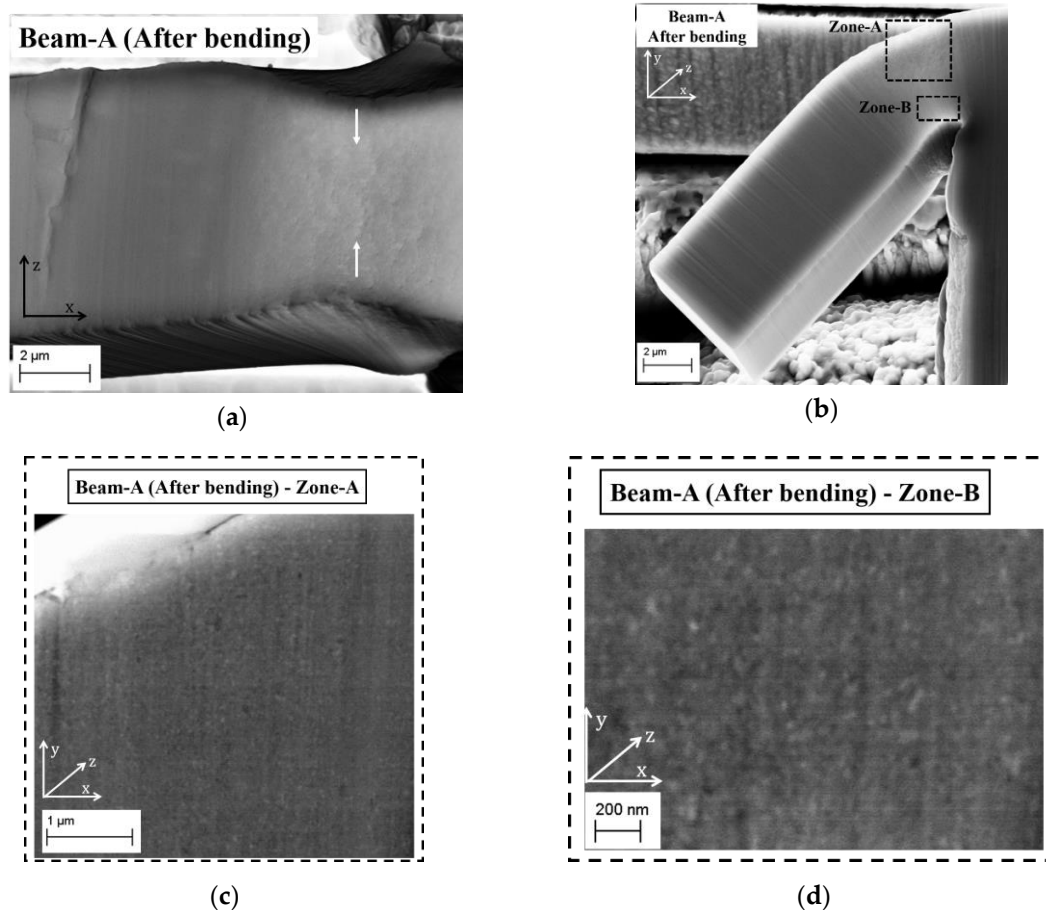


Figure 8. (a,b) Secondary electron images of micro beam-A after static bending test from (a) top and (b) side view of mechanical loading direction. (c,d) Back-scattered electron images of the microstructure of micro beam-A at two different positions, which are marked in (b).

In comparison with nanocrystalline Co [12,13], the yield strength of the PED-processed nanocrystalline Co-Cu (28 at.% Cu) is higher. In all pure nanocrystalline materials (including

nanocrystalline Co), the strengthening mechanism is dominated by grain boundary strengthening (the Hall-Petch effect). On the other hand, additional strengthening mechanisms are contributing in nanocrystalline Co-Cu (28 at.% Cu) alloys, like solid solution strengthening, including the effect of the spinodal decomposition and precipitation hardening in the case of annealed samples, thus, a higher yield strength is observed. It is assumed that the cobalt content is also an important influencing factor on the improvement of yield strength in nanocrystalline Co-Cu. For example, the PED-processed nanocrystalline Co-Cu (28 at.% Cu) exhibits a higher yield strength, compared to the HPT-processed nanocrystalline Co-Cu (74 at.% Cu) tested by tensile test ($\sigma_y \approx 0.8$ GPa) [9], whereas this significant difference can mainly be attributed to the higher Co content in the PED-processed material. Different mechanical test methods also contribute to the significant different values of yield strength. However, it is also believed that the differences may be caused also by the different type and number of lattice defects on between PED- and HPT-processed nanocrystalline Co-Cu.

The number of dislocations in the PED- and HPT-processed nanocrystalline materials is different, due to the dissimilar route of material processing. The formation of dislocations in the HPT-processed materials is predominantly affected by a large plastic strain during the processing of nanocrystalline materials [30]. In comparison, previous reports show that there are two main contributing factors to the formation of dislocations in the PED-processed nanocrystalline materials, which are stress development and relaxation generated by pulsed current [45,46] and grain growth inhibition by chemical additives [33,47]. It has been also reported in the literature [32] that the electrodeposited nanocrystalline Ni-Mo alloy exhibits a slightly different dislocations density than the HPT-processed nanocrystalline Ni-Mo at comparable chemical composition and crystallite size. The influence of chemical additives during the pulse electrodeposition process of nanocrystalline materials does not only contribute to the formation of dislocations, but also to the formation of twins. Figure 2a shows a number of twins in the ED nanocrystalline Co-Cu (28 at.% Cu), which may also contribute to the enhanced strength. The generation of dislocations from twins is expected to enhance the number of dislocations as reported from the literature [48,49]. All in all, the combination of different types of strengthening mechanisms: (i) solid solution, (ii) twins, (iii) dislocations, and (iv) the co-deposition of impurity elements contribute to an enhancement of strength in the ED nanocrystalline Co-Cu (28 at.% Cu).

The mechanical stability during cyclic loading of the ED nanocrystalline Co-Cu (28 at.% Cu) was investigated through the cyclic micro-bending experiment. A cyclic micro-bending test at a low plastic surface strain amplitude ($\epsilon_{s,a} = 2.0 \times 10^{-4}$) was conducted at micro beam-B for 5000 cycles. Figure 9a depicts the surface stress amplitude level ($\sigma_{s, amp, avg}$) as a function of number of load cycles of micro beam-B. The measurement shows that no crack formation is found after 5000 load cycles, but gradual softening is clearly visible after 100 load cycles (marked with a red arrow in Figure 9a). Microstructure investigation was conducted at the initial condition and after 5000 load cycles (Figure 9c,d). By comparing the initial and final microstructure, minor grain coarsening is observed. It is strongly believed that the observed grain coarsening causes the softening of the ED nanocrystalline Co-Cu (28 at.% Cu) materials.

Micro beam-C was subjected to four stages of cyclic micro-bending with stepwise increased plastic surface strain amplitudes. According to the results, no crack formation is observed after cycling from stage-I to stage-III, in which the observed surface stress amplitude level ($\sigma_{s, amp, avg}$) as a function of number of load cycles remain constant (Figure 9a). Micro beam-C was further subjected to cyclic bending test at stage-IV ($\epsilon_{s,a} = 7.0 \times 10^{-3}$; 100 cycles) and crack formation was observed after the test. Figure 9e depicts a secondary electron image of micro beam-C after testing at stage-IV, which shows that two cracks with different length are formed in two different positions. According to the Figure 9a, at stage-IV, the surface stress amplitude level ($\sigma_{s, amp, avg}$) remains constant for up to 40 load cycles, however, the amplitude starts to decline at the 41st of load cycle (marked with black arrow in Figure 9a), and the decrease is more significant at the following load cycles. It is believed that crack formation may start after load cycle 40 at stage-IV, and is followed by crack propagation.

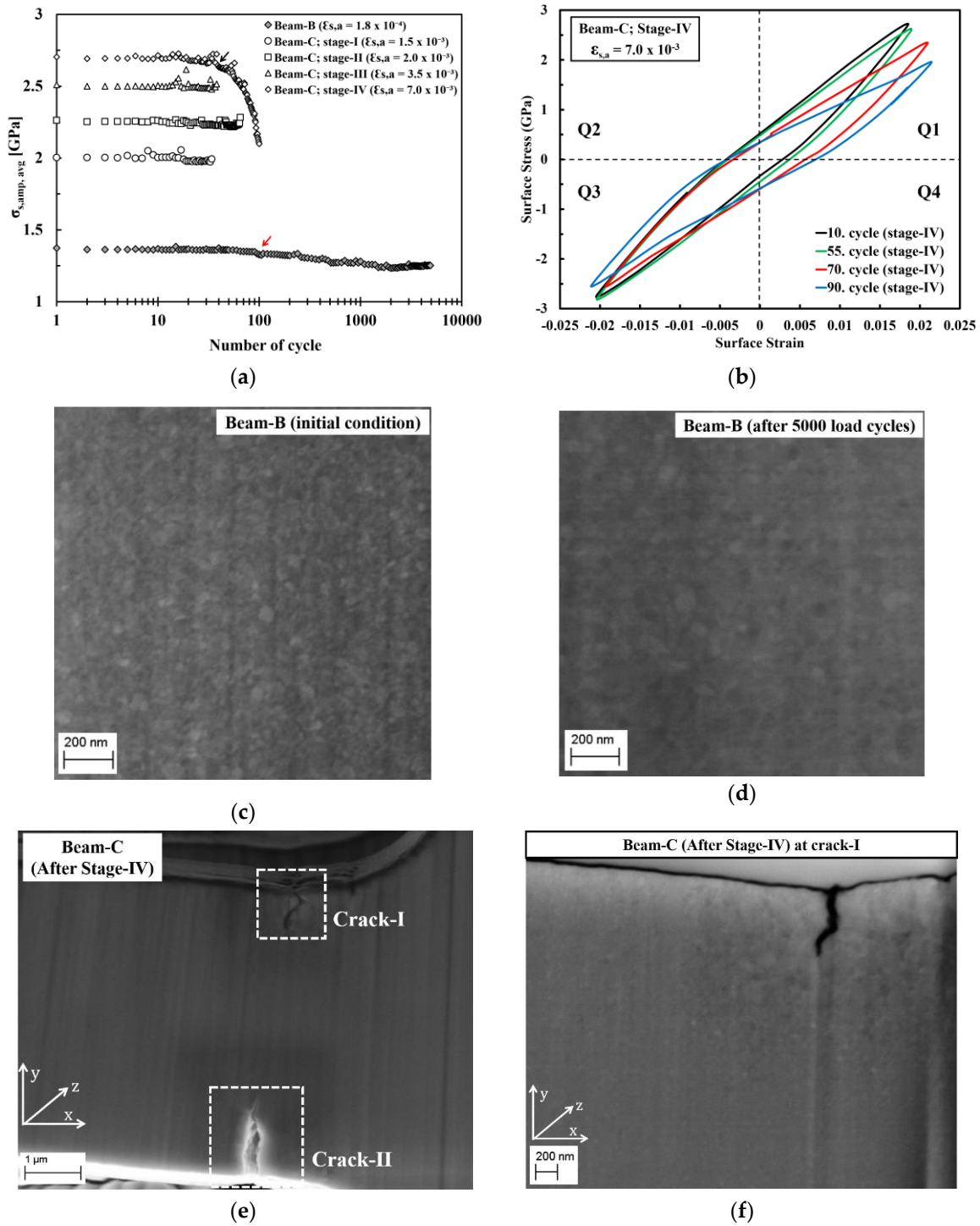


Figure 9. (a) Average surface-stress amplitude as a function of number of load cycle obtained from the cyclic micro-bending tests of micro beam-B and beam-C at different plastic surface strain amplitude. (b) Cyclic hysteresis loops of micro beam-C during cyclic bending test at stage-IV at the selected number of load cycles. (c,d) Back-scattered electron (BSE) images recorded at the same position on micro beam-B show microstructure images of (c) initial condition and (d) after 5000 load cycles without focused ion beam (FIB) polishing. (e) SE image shows a formation of cracks at two different position (crack-I and crack-II) on micro beam-C after cyclic tests of stage-IV. (f) BSE image shows a microstructure image of selected areas adjacent to the cracks on micro beam-C after FIB polishing at a position of crack-I.

Figure 9b shows the cyclic hysteresis loops of micro beam-C at selected load cycles of stage-IV. It is evident that only a small shift of the surface stress amplitude between the 10th and 55th load cycle is observed in quadrant 1 (Q1). This shift may be attributed to a crack formation, and since the shift of the surface stress amplitude is only in Q1 (Figure 9b), it is supposed that only one crack was formed after 55 load cycles. Afterwards, the surface stress amplitude is significantly altered at the 70th and 90th load cycles in Q1. At the 70th of load cycle, the shift of surface stress amplitude is more significant in Q1, and a small shift is also observable in Q3, which could be an indication that a second crack has formed. At the 90th load cycle, the shifts of the surface stress amplitude are more noticeable in Q1 and Q3, which means that crack has propagated further. After 100 load cycles, it is found that the crack length on the upper and lower side of micro beam-C are ~ 750 nm and ~ 1.2 μm , respectively. Figure 9f shows that significant grain coarsening is observed in the region adjacent to the cracks-I, in which some ultrafine grains are visible. It is supposed that the grain coarsening is induced by the local plastic deformation, which is generated during crack propagation. This local plastic deformation could induce grain boundary migration, as also demonstrated on micro beam-B in the present work, and in ultrafine-grained Cu during the cyclic micro bending test [23].

In the present work, it has been demonstrated that structural instabilities during cyclic loading are observed due to grain coarsening. Therefore, improvements are required to enhance the mechanical stability. It has been demonstrated in Section 3.1 that annealing treatment of nanocrystalline Co-Cu could widely modify the microstructure, thus, an improvement in mechanical stability is expected. In the future, research will focus on the influences of different structural characteristics obtained by annealing treatment on the mechanical stability of very fine grain Co-Cu alloy systems.

4. Summary

Investigations on microstructure and phase evolution of supersaturated solid solution nanocrystalline Co-Cu (28 at.% Cu), produced through the pulsed electrodeposition technique, have been performed through subsequent annealing treatments at different temperatures for different periods. APT showed that spinodal decomposition of Co-Cu system could start at a low annealing temperature (300 °C), in which grain coarsening is negligible. This chemical decomposition can be utilized to improve mechanical properties of nanocrystalline Co-Cu. Annealing at 450 °C induced significant grain coarsening, which results in ultrafine-grained structure (~ 125 nm). However, the microhardness could be maintained at comparable level with the as-deposited state, due to the combination of pinning of grain boundaries and phase separation. On the other hand, a gradual decrease of microhardness due to grain coarsening was found after annealing at 600 °C, although a massive phase separation occurred. The obtained various microstructures and phases through the annealing treatment can be utilized to get different mechanical behavior of very fine grain Co-Cu system, hence, the ductility and mechanical stability of very fine grain Co-Cu system could be enhanced.

The mechanical stability of deposited nanocrystalline Co-Cu (28 at.% Cu) was also investigated through static and cyclic micro bending tests. The micro beam specimens showed that the deposited nanocrystalline alloy exhibits ductile properties, in which a very high yield strength was observed. The presence of solid solution strengthening, dislocations, twins, and co-deposition of impurities elements may contribute to the high strength of electrodeposited nanocrystalline Co-Cu. Although this material exhibits very good mechanical properties, the microstructure was not stable in the fatigue tests, and further improvements can be performed here, possibly by optimizing the microstructure by annealing treatments.

Author Contributions: Conceptualization, methodology, writing-original draft preparation, K.P. and C.M.; Major experiment and data collection, K.P.; APT preparation, measurement, data processing and analysis J.B.; Draft supervision C.M., J.B., F.M. Project supervision C.M. and F.M. All authors have read and agreed to the published version of the manuscript.

Funding: The authors gratefully acknowledge the financial support by German Academic Exchange (DAAD) under GSSP (funding-ID: 57320205). The atom probe and the SEM devices were financed by DFG INST 256/298-1 FUGG and DFG INST 256/340-1FUGG, respectively, and the Federal State Government of Saarland.

Acknowledgments: We thank the INM for the access to the TEM facilities. The author thanks J. Schmauch for TEM sample preparation and experimental assistance, S. Slawik for experimental assistance at XRD, F. Kunz for experimental assistance at deposition and microhardness, and L. Lindner for experimental assistance at micro-bending tests.

Conflicts of Interest: The authors declare no conflict of interest.

References

1. Gleiter, H. Nanocrystalline materials. *Prog. Mater. Sci.* **1989**, *33*, 223–315. [[CrossRef](#)]
2. Meyers, M.A.; Mishra, A.; Benson, D. Mechanical properties of nanocrystalline materials. *Prog. Mater. Sci.* **2006**, *51*, 427–556. [[CrossRef](#)]
3. Erb, U. Electrodeposited nanocrystals: Synthesis, properties and industrial applications. *Nanostruct. Mater.* **1995**, *6*, 533–538. [[CrossRef](#)]
4. Berkowitz, A.E.; Mitchell, J.R.; Carey, M.J.; Young, A.P.; Zhang, S.; Spada, F.; Parker, F.T.; Hütten, A.; Thomas, G. Giant magnetoresistance in heterogeneous Cu-Co alloys. *Phys. Rev. Lett.* **1992**, *68*, 3745–3748. [[CrossRef](#)] [[PubMed](#)]
5. Bachmaier, A.; Krenn, H.; Knoll, P.; Aboufadel, H.; Pippan, R. Tailoring the magnetic properties of nanocrystalline Cu-Co alloys prepared by high-pressure torsion and isothermal annealing. *J. Alloys Compd.* **2017**, *725*, 744–749. [[CrossRef](#)]
6. Bachmaier, A.; Motz, C. On the remarkable thermal stability of nanocrystalline cobalt via alloying. *Mater. Sci. Eng. A* **2015**, *624*, 41–51. [[CrossRef](#)] [[PubMed](#)]
7. Bachmaier, A.; Pfaff, M.; Stolpe, M.; Aboufadel, H.; Motz, C. Phase separation of a supersaturated nanocrystalline Cu-Co alloy and its influence on thermal stability. *Acta Mater.* **2015**, *96*, 269–283. [[CrossRef](#)]
8. Bachmaier, A.; Stolpe, M.; Mueller, T.; Motz, C. Phase decomposition and nano structure evolution of metastable nanocrystalline Cu-Co solid solutions during thermal treatment. *IOP Conf. Ser. Mater. Sci. Eng.* **2015**, *89*, 012017. [[CrossRef](#)]
9. Bachmaier, A.; Rathmayr, G.B.; Schmauch, J.; Schell, N.; Stark, A.; De Jonge, N.; Pippan, R. High strength nanocrystalline Cu-Co alloys with high tensile ductility. *J. Mater. Res.* **2018**, *34*, 58–68. [[CrossRef](#)]
10. Nakamoto, Y.; Yuasa, M.; Chen, Y.; Kusuda, H.; Mabuchi, M. Mechanical properties of a nanocrystalline Co-Cu alloy with a high-density fine nanoscale lamellar structure. *Scr. Mater.* **2008**, *58*, 731–734. [[CrossRef](#)]
11. Pratama, K.; Kunz, F.; Lindner, L.; Schmauch, J.; Mücklich, F.; Motz, C. Thermal stability, phase decomposition, and micro-fatigue properties of pulsed electrodeposited nanocrystalline Co-Cu. *Procedia Struct. Integr.* **2019**, *23*, 366–371. [[CrossRef](#)]
12. Karimpoor, A.A.; Erb, U. Mechanical properties of nanocrystalline cobalt. *Phys. Status Solidi (a)* **2006**, *203*, 1265–1270. [[CrossRef](#)]
13. Karimpoor, A. High strength nanocrystalline cobalt with high tensile ductility. *Scr. Mater.* **2003**, *49*, 651–656. [[CrossRef](#)]
14. Lu, L.; Wang, L.B.; Ding, B.Z.; Lu, K. High-tensile ductility in nanocrystalline copper. *J. Mater. Res.* **2000**, *15*, 270–273. [[CrossRef](#)]
15. Wang, Y.; Chen, M.; Zhou, F.; Ma, E. High tensile ductility in a nanostructured metal. *Nature* **2002**, *419*, 912–915. [[CrossRef](#)] [[PubMed](#)]
16. Youssef, K.M.; Scattergood, R.O.; Murty, K.L.; Horton, J.A.; Koch, C. Ultrahigh strength and high ductility of bulk nanocrystalline copper. *Appl. Phys. Lett.* **2005**, *87*, 91904. [[CrossRef](#)]
17. Edalati, K.; Fujioka, T.; Horita, Z. Microstructure and mechanical properties of pure Cu processed by high-pressure torsion. *Mater. Sci. Eng. A* **2008**, *497*, 168–173. [[CrossRef](#)]
18. Koch, C.C. Ductility in Nanostructured and Ultra Fine-Grained Materials: Recent Evidence for Optimism. *J. Metastable Nanocrystalline Mater.* **2003**, *18*, 9–20. [[CrossRef](#)]
19. Koch, C. Optimization of strength and ductility in nanocrystalline and ultrafine grained metals. *Scr. Mater.* **2003**, *49*, 657–662. [[CrossRef](#)]
20. Ma, E. Instabilities and ductility of nanocrystalline and ultrafine-grained metals. *Scr. Mater.* **2003**, *49*, 663–668. [[CrossRef](#)]

21. Mughrabi, H.; Höppel, H.-W. Cyclic deformation and fatigue properties of very fine-grained metals and alloys. *Int. J. Fatigue* **2010**, *32*, 1413–1427. [[CrossRef](#)]
22. Höppel, H.-W.; Kautz, M.; Xu, C.; Murashkin, M.; Langdon, T.; Valiev, R.Z.; Mughrabi, H. An overview: Fatigue behaviour of ultrafine-grained metals and alloys. *Int. J. Fatigue* **2006**, *28*, 1001–1010. [[CrossRef](#)]
23. Kapp, M.; Kremmer, T.; Motz, C.; Yang, B.; Pippin, R. Structural instabilities during cyclic loading of ultrafine-grained copper studied with micro bending experiments. *Acta Mater.* **2017**, *125*, 351–358. [[CrossRef](#)]
24. Qian, T.; Karaman, I.; Marx, M. Mechanical Properties of Nanocrystalline and Ultrafine-Grained Nickel with Bimodal Microstructure. *Adv. Eng. Mater.* **2014**, *16*, 1323–1339. [[CrossRef](#)]
25. Ma, E. Controlling plastic instability. *Nat. Mater.* **2003**, *2*, 7–8. [[CrossRef](#)] [[PubMed](#)]
26. He, G.; Eckert, J.; Löser, W.; Schultz, L. Novel Ti-base nanostructure–dendrite composite with enhanced plasticity. *Nat. Mater.* **2002**, *2*, 33–37. [[CrossRef](#)]
27. Favvas, E.P.; Mitropoulos, A.C. What is spinodal decomposition? *J. Eng. Sci. Technol. Rev.* **2008**, *1*, 25–27. [[CrossRef](#)]
28. Liu, J.-M.; Busch, R.; Gärtner, F.; Haasen, P.; Liu, Z.-G.; Wu, Z. Spinodal decomposition of CuCo alloys. *Phys. Status Solidi (a)* **1993**, *138*, 157–174. [[CrossRef](#)]
29. Cavaliere, P. Mechanical properties of nanocrystalline metals and alloys studied via multi-step nanoindentation and finite element calculations. *Mater. Sci. Eng. A* **2009**, *512*, 1–9. [[CrossRef](#)]
30. Gubicza, J. Lattice Defects and Their Influence on the Mechanical Properties of Bulk Materials Processed by Severe Plastic Deformation. *Mater. Trans.* **2019**, *60*, 1230–1242. [[CrossRef](#)]
31. Kolonits, T.; Jenei, P.; Tóth, B.; Czigány, Z.; Gubicza, J.; Péter, L.; Bakonyi, I. Characterization of Defect Structure in Electrodeposited Nanocrystalline Ni Films. *J. Electrochem. Soc.* **2015**, *163*, D107–D114. [[CrossRef](#)]
32. Kapoor, G.; Péter, L.; Fekete, E.; Gubicza, J. Defect structure in electrodeposited nanocrystalline Ni layers with different Mo concentrations. In Proceedings of the 2ND International Conference on Condensed Matter and Applied Physics (ICC 2017), Bikaner, India, 24–25 November 2017; AIP Publishing: College Park, MD, USA, 2018; Volume 1953, p. 030047.
33. Kolonits, T.; Jenei, P.; Péter, L.; Bakonyi, I.; Czigány, Z.; Gubicza, J. Effect of bath additives on the microstructure, lattice defect density and hardness of electrodeposited nanocrystalline Ni films. *Surf. Coatings Technol.* **2018**, *349*, 611–621. [[CrossRef](#)]
34. Müller, T. Pulsed Electrodeposition of Nanocrystalline Co and Co-Cu Alloys. Master's Thesis, Saarland University, Saarbrücken, Germany, 2014.
35. Schneider, C.A.; Rasband, W.S.; Eliceiri, K.W. NIH Image to ImageJ: 25 years of image analysis. *Nat. Methods* **2012**, *9*, 671–675. [[CrossRef](#)] [[PubMed](#)]
36. Thompson, K.; Lawrence, D.; Larson, D.; Olson, J.; Kelly, T.; Gorman, B.P. In situ site-specific specimen preparation for atom probe tomography. *Ultramicroscopy* **2007**, *107*, 131–139. [[CrossRef](#)] [[PubMed](#)]
37. Kato, M.; Mori, T.; Schwartz, L. Hardening by spinodal modulated structure. *Acta Met.* **1980**, *28*, 285–290. [[CrossRef](#)]
38. Bachmaier, A.; Aboufadel, H.; Pfaff, M.; Mücklich, F.; Motz, C. Structural evolution and strain induced mixing in Cu–Co composites studied by transmission electron microscopy and atom probe tomography. *Mater. Charact.* **2015**, *100*, 178–191. [[CrossRef](#)]
39. Cahn, J.W. On spinodal decomposition. *Acta Met.* **1961**, *9*, 795–801. [[CrossRef](#)]
40. Nix, F.C.; Jaumot, F.E. Self-Diffusion in Cobalt. *Phys. Rev.* **1950**, *80*, 119. [[CrossRef](#)]
41. Arita, M.; Nakamura, M.; Goto, K.S.; Ichinose, Y. Activity and diffusivity measurements of copper in alpha cobalt by equilibrium between solid Co and liquid Ag. *J. Jpn. I. Met.* **1984**, *25*, 703–709.
42. Bruni, F.J.; Christian, J.W. The chemical diffusion coefficient in dilute copper-cobalt alloys. *Acta Metall.* **1973**, *21*, 385–390. [[CrossRef](#)]
43. Horvath, J.; Birringer, R.; Gleiter, H. Diffusion in nanocrystalline material. *Solid State Commun.* **1987**, *62*, 319–322. [[CrossRef](#)]
44. Hibbard, G.D.; Aust, K.T.; Erb, U. The effect of starting nanostructure on the thermal stability of electrodeposited nanocrystalline Co. *Acta Mater.* **2006**, *54*, 2501–2510. [[CrossRef](#)]
45. Lu, L.; Chen, X.; Lu, K. Revealing the maximum strength in nanotwinned copper. *Science* **2009**, *323*, 607–610. [[CrossRef](#)] [[PubMed](#)]
46. Lu, K.; Lu, L.; Suresh, S. Strengthening materials by engineering coherent internal boundaries at the nanoscale. *Science* **2009**, *324*, 349–352. [[CrossRef](#)] [[PubMed](#)]

47. Kumar, K.S.; Biswas, K. Effect of thiourea on grain refinement and defect structure of the pulsed electrodeposited nanocrystalline copper. *Surf. Coat. Tech.* **2013**, *214*, 8–18. [[CrossRef](#)]
48. Konopka, K.; Mizera, J.; Wyrzykowski, J.W. The generation of dislocations from twin boundaries and its effect upon the flow stresses in FCC metals. *J. Mater. Process. Technol.* **2000**, *99*, 255–259. [[CrossRef](#)]
49. Field, D.P.; True, B.W.; Lillo, T.M.; Flinn, J.E. Observation of twin migration in copper during deformation. *Mater. Sci. Eng. A* **2004**, *372*, 173–179. [[CrossRef](#)]



© 2020 by the authors. Licensee MDPI, Basel, Switzerland. This article is an open access article distributed under the terms and conditions of the Creative Commons Attribution (CC BY) license (<http://creativecommons.org/licenses/by/4.0/>).

Article

Strategies to Achieve High Strength and Ductility of Pulsed Electrodeposited Nanocrystalline Co-Cu by Tuning the Deposition Parameters

Killang Pratama^{1,2,*}  and Christian Motz¹

¹ Chair of Materials Science and Methods, Saarland University, 66123 Saarbrücken, Germany; motz@matsci.uni-sb.de

² Department of Metallurgical Engineering, Institute Technology of Bandung, Bandung 40132, Indonesia

* Correspondence: k.pratama@matsci.uni-sb.de or killang@metallurgy.itb.ac.id; Tel.: +49-681-302-5001

Academic Editors: Igor Djerdj and Jasminka Popović

Received: 29 September 2020; Accepted: 7 November 2020; Published: 8 November 2020



Abstract: Strategies to improve tensile strength and ductility of pulsed electrodeposited nanocrystalline Co-Cu were investigated. Parameters of deposition, which are pulse current density, duty cycle, and pulse-on time were adjusted to produce nanocrystalline Co-Cu deposits with different microstructures and morphologies. The most significant improvement of strength and ductility was observed at nanocrystalline Co-Cu deposited, at a low duty cycle (10%) and a low pulse-on time (0.3 ms), with a high pulse current density (1000 A/m²). Enhancement of ductility of nanocrystalline Co-Cu was also obtained through annealing at 200 °C, while annealing at 300 °C leads to strengthening of materials with reduction of ductility. In the as deposited state, tensile strength and ductility of nanocrystalline Co-Cu is strongly influenced by several factors such as concentration of Cu, grain size, and processing flaws (e.g., crystal growth border, porosity, and internal stresses), which can be controlled by adjusting the parameters of deposition. In addition, the presence of various microstructural features (e.g., spinodal and phase decomposition), as well as recovery processes induced by annealing treatments, also have a significant contribution to the tensile strength and ductility.

Keywords: nanocrystalline; pulsed electrodeposition; high tensile ductility; copper; cobalt

1. Introduction

Nanocrystalline Co is a high strength material with outstanding physical properties; however, this type of material exhibits low ductility with a typical elongation at a fracture below 10%, which is a common problem in nanocrystalline materials [1–3]. Low ductility in nanocrystalline materials could be influenced by several factors, such as formation of processing flaws (e.g., porosity), low plastic strain capability, and early strain localization and failure [4]. In nanocrystalline cobalt, alloying with other elements, e.g., Co-Cu alloys, is expected to enhance ductility caused by formation of the modified microstructures which change plasticity and deformation behavior. However, previous work on bulk high pressure torsion (HPT)-processed Cu-rich nanocrystalline Co-Cu [5] showed that an elongation at fracture of less than 10% was still reported. In addition, observation of micro-mechanical properties of the pulsed electrodeposited (PED) Co-rich nanocrystalline Co-Cu still reported unclear information [6]. Therefore, a study on mechanical properties and improvement in ductility of nanocrystalline Co-Cu needs further investigation.

Improving ductility of nanocrystalline materials, including nanocrystalline Co-Cu alloys, can be performed by controlling the microstructure and the formation of processing flaws [7–10]. The routes and parameters of materials processing will be key roles here. Currently, there are

three possible methods to produce bulk tensile specimen of nanocrystalline materials, which are electrodeposition (ED) [1,2,11,12], severe plastic deformation (SPD) [5,13,14], and mechanical alloying and compaction (MA) [15,16]. In this paper, synthesis of bulk nanocrystalline Co-Cu through the pulsed electrodeposition (PED) will be conducted due to a simple route of production and a wide range of controlling process parameters. Of course, different characteristic and a number of lattice defects (e.g., dislocation, voids, and twins) could be also produced from different processing routes, but it is not studied here. In the PED-processed nanocrystalline materials, adjusting deposition parameters (for instance: current density, pulse-on time, and duty cycle) has a significant influence on the resulting microstructure as well as on the porosity, which has a direct impact on their mechanical properties [11,12,17–19]. It is also possible to improve the mechanical properties of nanocrystalline materials, particularly nanocrystalline Co-Cu, through specific annealing treatment that leads to microstructural changes (e.g., spinodal and phase decomposition) and recovery processes (e.g., relaxation of grain boundaries and internal stresses) [6,20,21]. Improvement in strength and ductility of PED-processed nanocrystalline Co-Cu is expected by tuning deposition parameters as well as annealing treatment.

In the present work, the influences of the deposition parameters (e.g., pulse current density, duty cycle, and pulse-on time) on the microstructure and chemical composition, distribution, as well as formation of processing flaws, is investigated. The effect of annealing treatments on tensile strength and ductility is also studied by discussing the possible microstructural changes and recovery processes (i.e., release of internal stresses and absorbed hydrogen). This work addresses preferred deposition parameters as well as annealing treatment conditions to produce high strength and ductility of nanocrystalline Co-Cu.

2. Results and Discussion

2.1. Effect of Deposition Parameters on the Properties of Deposits

Extensive studies and investigations were carried out to find specific ranges of deposition parameters of nanocrystalline Co-Cu. According to previous work [6,22], deposition at a pulse current density of 500 A/m² leads to the formation of deposits with inhomogeneous distribution of microstructure and chemical composition, while porous and unstable (powdery and with high internal stresses) deposits were produced at a pulse current density of 1500 A/m². Compact and homogeneous nanocrystalline Co-Cu deposits could be obtained at pulse current densities of 750–1000 A/m²; thus, this range was selected for the deposition of bulk nanocrystalline Co-Cu. Subsequently, these investigations were continued to find a specific range of working duty cycles and pulse-on times. Figure 1 shows cross-sectional images of nanocrystalline Co-Cu films deposited at various duty cycles at the same pulse current density (1000 A/m²) and pulse-on time (2 ms). According to the theory proposed by Fischer [23], deposited Co-Cu films show a combination of field-oriented texture (FT) and unoriented dispersion (UD) growth types with a clear observation of crystal growth borders (marked with red arrows in Figure 1). Figure 1a,b show that deposition at the duty cycles of 30% and 40% produce porous and unstable deposits. On the other hand, a relatively compact deposit up to ~300 μm of thicknesses is obtained in the sample deposited at a duty cycle of 20% (see Figure 1c). However, homogeneous and stable deposits of nanocrystalline Co-Cu are only visible up to ~400 μm of thicknesses at a pulse-on time of 2 ms [6]. The inhomogeneity is strongly affected by significant concentration decrease of electrolyte components (e.g., Co and Cu ions and Saccharin), which leads to the formation of coarser grains with higher Cu concentration at the area near the surface of deposits [22]. Ideally, concentration of the electrolyte components must be kept at the same level, for example, by utilizing titration and electrolyte circulation to produce thick (>1 mm) and homogeneous deposits. However, in the present work, all deposits were produced through the single stage of deposition with no addition of electrolyte components during deposition. Further investigations reported that homogeneous and stable deposits up to ~700 μm of thicknesses could be obtained through the single stage of deposition at the pulse-on

times of 0.3 ms–0.5 ms (duty cycle of 20%). Deposition at pulse-on times lower than 0.3 ms is not possible due to formation of powdery deposits. In summary, high-quality nanocrystalline Co-Cu films could be deposited at a specific range of deposition parameters: (i) Pulse current densities of 750 A/m²–1000 A/m², (ii) pulse-on times of 0.3 ms–0.5 ms, and (iii) duty cycles of 10–20%.

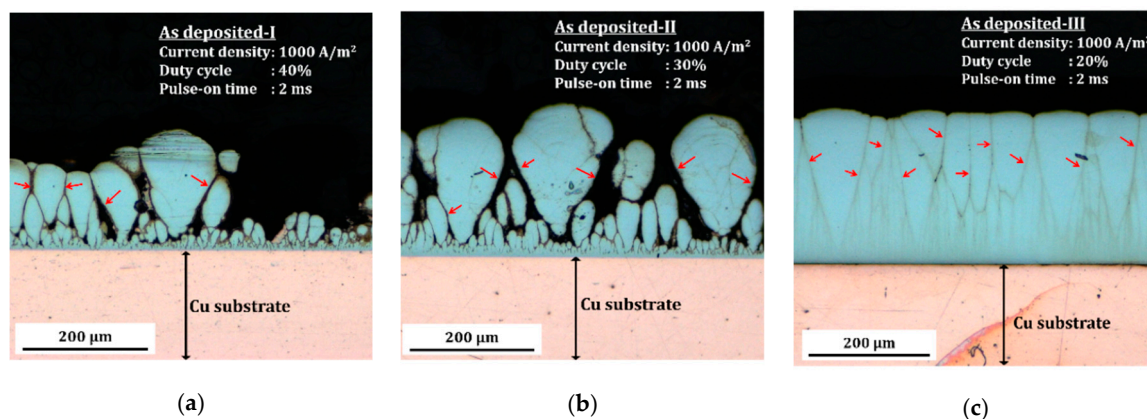


Figure 1. Cross-sectional images of nanocrystalline Co-Cu deposited at various duty cycle of (a) 40%, (b) 30%, and (c) 20% at a pulse current density of 1000 A/m² and a pulse-on time of 2 ms. The films were deposited at the same number of pulse cycles for different time of deposition which are (a) 13 h, (b) 8.5 h, and (c) 6.5 h to obtain the 300 μm of thicknesses (current efficiency 80–90%).

In the present work, the deposition parameters were varied, i.e., current density, duty cycle, and pulse-on time, as described in Table 1. Microstructural investigation through scanning electron microscopy (SEM) and X-ray diffraction (XRD) measurements were performed to investigate the impact of deposition parameters. Back-scattered electron (BSE) images of initial microstructure of sample 1 (S1) (Figure 2a) and sample 5 (S5) (Figure 2c) reveal that homogeneous and pure nanocrystalline structure with grain sizes of less than 100 nm are observed, whereas S2 and S3 exhibit the identical microstructure (BSE images are not shown here). On the other hand, a BSE image of initial microstructure of S4 (Figure 2b) shows slightly coarser grains compared to S1 and S5, which is strongly influenced by the reduction of the pulse current density. XRD patterns of S1–S5 (see Figure 2d) show no clear differences of phase or crystal orientation, whereas identical XRD patterns with a strong (111) peak are detected in S1–S5. However, the different shape of XRD-peaks (e.g., peak intensity and peak broadening) can be taken into consideration as different grain size and microstrain effects (e.g., internal stresses). Caused by limited resolution of SEM–BSE images, grain size measurements were carried out by analyzing the XRD lines of individual samples through full width at half maximum (FWHM) method of the Scherer and Williamson–Hall approaches. The Scherer approach shows that S1–S5 have identical grain at the range of 7–12 nm. On the other hand, the Williamson–Hall approach shows more significant differences of grain size mainly for S4, which conforms more to the microstructure SEM image. Of course, a more valid grain size number can be obtained through transmission electron microscopy (TEM), but it is not conducted here. According to previous work [6], the grain size number from TEM images (~23 nm) is between the grain size number from Scherer (~14 nm) and Williamson–Hall (~31 nm) approaches. According to the previous measurement characteristic, S4 may exhibit grain size in the range of 9–72 nm, which is the biggest among S1–S5. The energy dispersive X-ray spectroscopy (EDS) measurement shows that the S1 consists the lowest Cu content, while the S4 and S5 have the highest Cu-content. In comparison with S1, higher Cu-content in S4 and S5 may be caused by a deposition at a lower current density and a lower duty cycle, respectively. The possible effect of grain size and Cu-concentration on strength and ductility will be discussed further in Section 2.2.

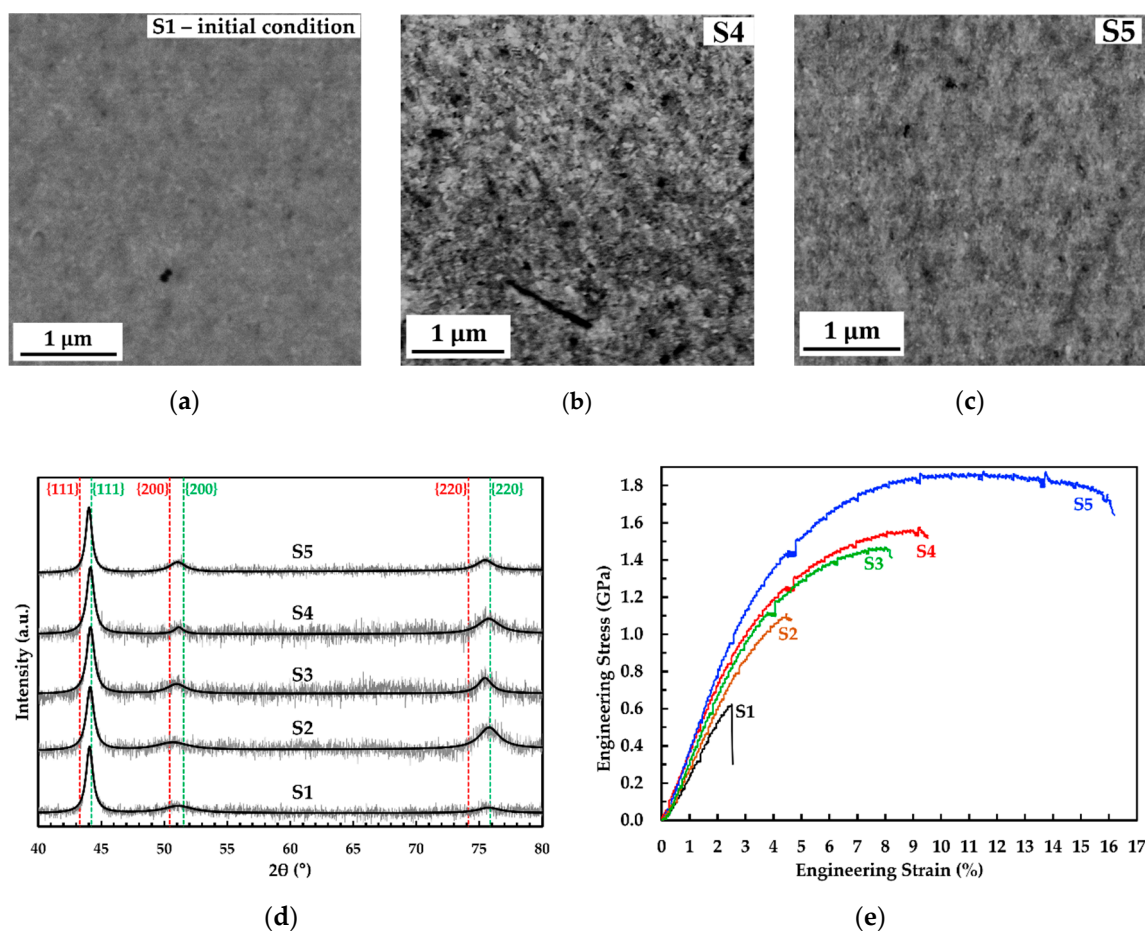


Figure 2. Back-scattered electron (BSE) image of initial microstructure of (a) S1, (b) S4, (c) S5 in planar mode; (d) X-ray diffraction (XRD) patterns of S1–S5. The red and green vertical dashed lines indicate the positions of the face-centered cubic (fcc) phase lines of Cu and Co, respectively. The continuous black thick lines correspond to the fits for the measured XRD patterns; (e) Engineering stress vs. strain curves of static tensile tests of samples S1–S5 at a strain rate of $1.0 \times 10^{-3} \text{ s}^{-1}$. Detailed descriptions for each sample are shown in Table 2.

Table 1. Chemical composition and grain size analysis of the tensile specimens, which were deposited at (various) pulse current density (i_p), duty cycle (dc), and pulse-on time (t_p). Grain size analysis is measured from the XRD lines in Figure 2a through full width at half maximum (FWHM) analysis and two different approaches: Scherer plot and Williamson–Hall plot. PED = pulsed electrodeposited.

	PED Parameters			Composition		Scherer Plot	Williamson–Hall Plot	
	i_p (A/m ²)	dc (%)	t_p (ms)	Co (at.%)	Cu (at.%)	Grain Size (nm)	Grain Size (nm)	Microstrain (%)
S1	1000	20.0	0.5	87.1 ± 0.1	12.9 ± 0.1	7.84	12.86	1.018
S2	1000	17.5	0.5	85.6 ± 0.1	14.4 ± 0.1	7.39	7.08	0.393
S3	1000	17.5	0.3	82.8 ± 0.1	17.2 ± 0.1	8.30	7.76	0.161
S4	800	17.5	0.5	80.3 ± 0.1	19.7 ± 0.1	9.03	71.68	1.297
S5	1000	10.0	0.3	80.1 ± 0.1	19.9 ± 0.1	11.03	24.60	0.673

Table 2. The yield strength (σ_y), ultimate tensile strength (σ_u), and total elongation at fracture (ϵ_f) of tensile specimens S1–S5 with different thicknesses (d) measured from the engineering stress–strain curves in Figure 2b. Two tensile specimens were mechanically tested for S2–S5.

	PED Parameters			d (mm)	Mechanical Properties		
	i_p (A/m ²)	dc (%)	t_p (ms)		σ_y (GPa)	σ_u (GPa)	ϵ_f (%)
S1	1000	20.0	0.5	0.41	Fail at 0.62		2.54
S2	1000	17.5	0.5	0.54	0.91 ± 0.06	1.20 ± 0.03	4.57 ± 0.05
S3	1000	17.5	0.3	0.52	0.95 ± 0.05	1.51 ± 0.04	8.71 ± 0.47
S4	800	17.5	0.5	0.53	1.03 ± 0.02	1.55 ± 0.03	8.26 ± 1.26
S5	1000	10.0	0.3	0.40	1.21 ± 0.08	1.98 ± 0.03	15.95 ± 0.09

2.2. Effect of Deposition Parameters on the Mechanical Properties

In this section, the effect of deposition parameters on the mechanical properties of individual samples is discussed. The stress–strain curve and the detailed data of S1–S5 are available in Figure 2e and Table 2. Figure 2e depicts an engineering stress vs. strain curve of a static tensile test of S1, which was deposited at the highest pulsed current density, duty cycle, and pulse-on time. According to the curve, S1 possess a brittle behavior in which a failure occurs even in the elastic regime (fracture stress and strain are 0.62 GPa and 2.54%, respectively). Previous work on the tensile test of bulk HPT-processed Cu-rich nanocrystalline Co-Cu [4] showed that a minimum yield strength of 0.8 GPa could be achieved and it should be higher for the Co-rich systems. A secondary electron (SE) image of the initial surface condition of S1 (Figure 3a) shows the presence of microporosity with sizes of 0.5–1.0 μm (marked with black arrows) and crystal growth borders with an average distance of $84.14 \pm 44.34 \mu\text{m}$ (marked with red dashed line), which could be possible spots for crack initiation. In addition, a combined SE-EDS image (Figure 3b) reports a local Cu-deficient region along the crystal growth borders. It is believed that these crystal growth borders are more brittle compared with the surrounding regions caused by lower Cu, as well as higher Co concentration, and it is strongly supposed that the crack initiation started here.

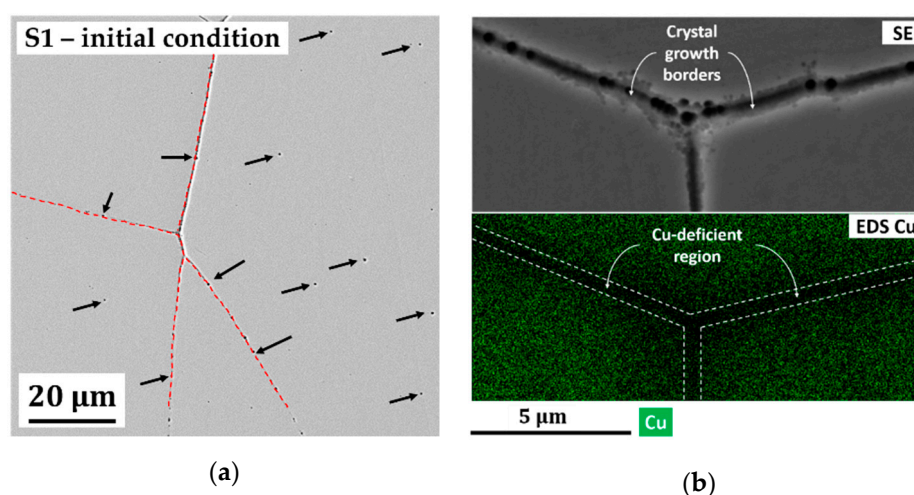


Figure 3. (a) Secondary electron (SE) image of initial condition of tensile specimen of S1 surface (planar mode), which shows the presence of micropores (marked with black arrows) and crystal growth borders (marked with red dashed line); (b) combined high magnification of a secondary electron (SE) image (upper section) and energy dispersive X-ray spectroscopy (EDS) elemental map of Cu (lower section) shows a Cu-deficient region along crystal growth borders (planar mode).

Figure 4a shows that the fracture surface of S1 is dominated by brittle fracture (region B1) and a clear fracture of the crystal growth borders is confirmed by detailed observation of B1 (Figure 4a,b).

Other factors, such as overall low Cu concentration, impurities, and processing flaws caused by deposition at high pulse current density, could also contribute to the brittle failure of the crystal growth borders. Interestingly, a moderate fraction of ductile fracture regions (see Figure 4a) and micro-dimple structures are observed within the brittle fracture region (see Figure 4c,d). It is believed that the PED-processed nanocrystalline Co-Cu exhibits ductile behavior in the absence of these processing flaws. Hence, an improvement in ductility can be achieved by reducing the number of processing flaws, for instance, through adjustment of deposition parameters (e.g., reducing duty cycle). For example, sample 2 (S2), which was deposited at a lower duty cycle shows a slightly improved ductility (see Table 2 and Figure 2b) with no distinct porosity and crystal growth borders observed. A fracture image of S2 (Figure 5a) shows that the fraction of the brittle fracture regions (B2) is slightly lower compared to S1, and the fracture surface is dominated by a ductile fracture with various dimple sizes. In addition, the EDS measurement shows that S2 exhibits a higher Cu content than S1, which might also contribute to the improvement in ductility (see Table 1). However, ductility of S2 is still low, with a total elongation at the fracture remaining below 10%, and it needs further improvement.

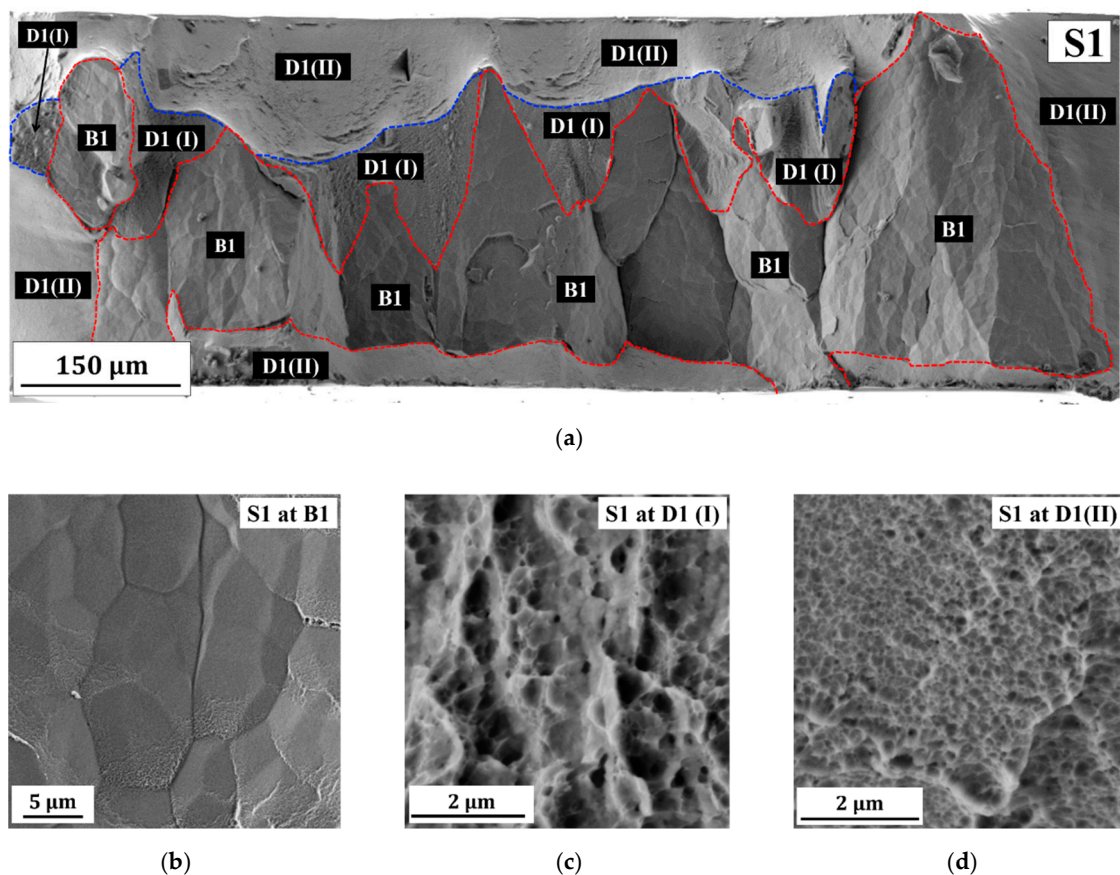
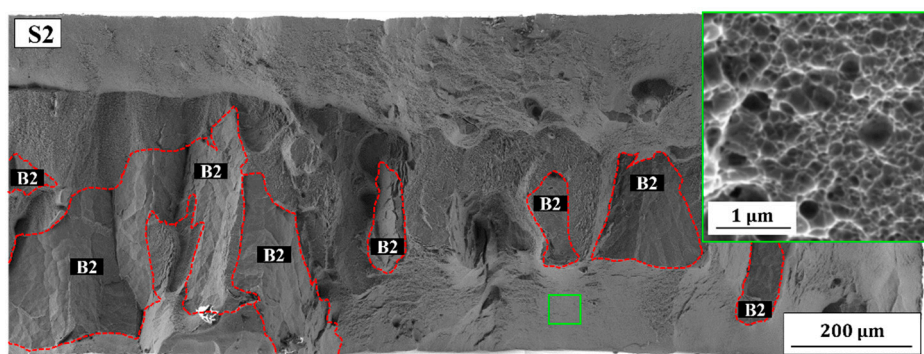
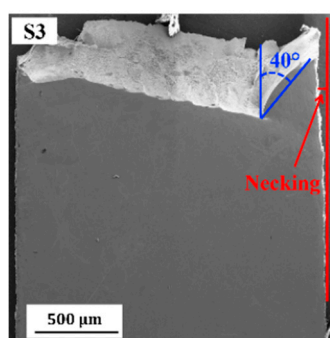


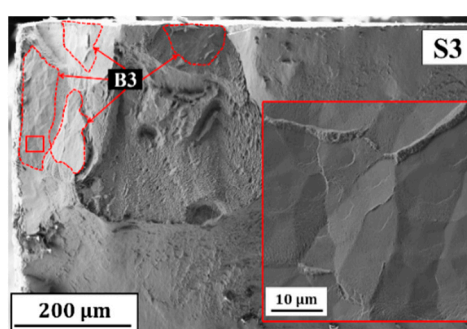
Figure 4. (a) A Secondary electron (SE) image of fracture surface of sample 1 (S1) shows brittle (B1) and ductile (D1(I) and D1(II)) fracture regions; (b–d) SE images of detailed fracture surface of S1 at three different regions marked at (a), which are (b) brittle (B1) and (c,d) ductile (D1(I), and D1(II)) fracture regions.



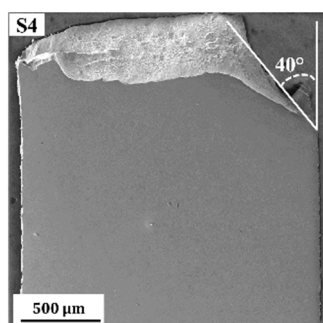
(a)



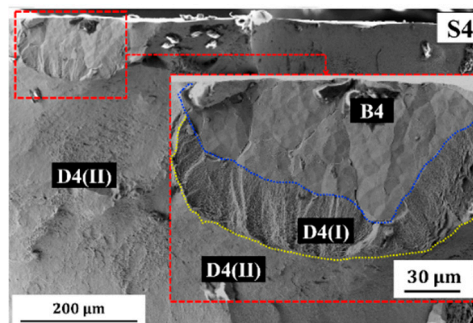
(b)



(c)



(d)



(e)

Figure 5. (a) A SE electron image of the fracture surface of sample 2 (S2) showing brittle (B2) and ductile (rest) fracture regions (inset shows a detailed image of the ductile fracture surface taken at the area marked with the green box). (b,d) SE images of surface morphology at gauge section after tensile test of (b) sample 3 (S3) and (d) sample 4 (S4); (c) a SE image of the fracture surface of S3 showing the brittle (B3) and ductile (rest) fracture regions (inset show a detailed image of the brittle region marked with the red box); (e) a SE image of the fracture surface of S4 showing brittle (B4) and ductile (D4(I) and D4(II)) fracture regions.

Sample 3 (S3) and sample 4 (S4) were deposited at lower pulse-on time and pulse current density compared with S2, respectively. EDS measurements show that S3 and S4 have a higher Cu concentration compared to S1 and S2 (see Table 1). In comparison with S1 and S2, a significant improved ductility is observed in which elongation at fracture of almost 10% is achieved (see Table 2 and Figure 2b). Surface morphology images at the gauge section of S3 (Figure 5b) and S4 (Figure 5c) exhibit a shear fracture at 40° angle relative to the tensile load direction as an indication of ductile fracture, and also some small amount of necking as an evidence of plasticity prior to ductile fracture. Fracture surface images of S3

(Figure 5d) and S4 (Figure 5e) confirm a significant reduction of brittle fracture regions (B3 and B4) compared with S1 and S2, whereas here this type of fracture is only observed in some spots.

Sample 5 (S5) was deposited at the lowest duty cycle (10%) and pulse-on time (0.3 ms). EDS measurement confirms that S5 has the highest Cu content among S1–S5 (see Table 1). An engineering stress vs. strain curve of S5 (Figure 2b) shows that a high tensile strength and ductility with a total elongation at fracture of 16.20% is observed (see the data in Table 2). A surface morphology image at the gauge section of S5 (Figure 6a) shows a moderate necking with a shear fracture at 40° angle relative to the tensile loading direction as found also in S3 and S4. No brittle fracture regions are found in S5 in which ductile fracture with dimple structures is observed (Figure 6b). Deposition at a duty cycle of less than 10% is not preferred considering the required processing time. Moreover, it also leads to deposits with higher Cu concentration and coarser grains, which results in a reduction of strength with an increased ductility.

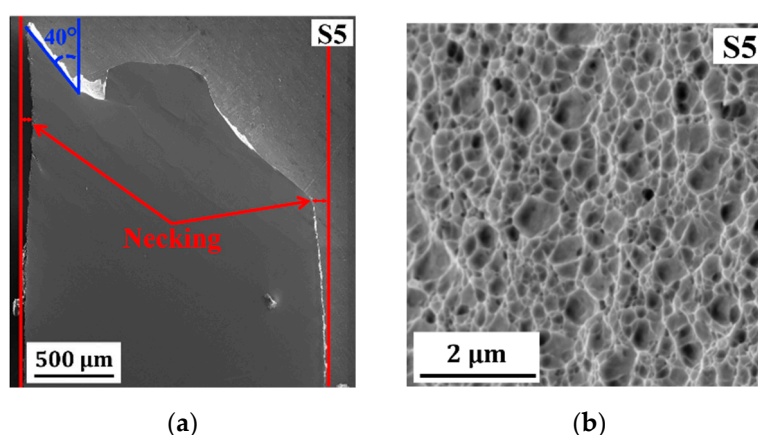


Figure 6. (a) SE images of surface morphology at the gauge section after tensile test of sample 5 (S5); (b) a SE image of the fracture surface of sample 5 (S5) showing ductile fracture with dimple structures.

The ductility of materials is controlled by factors such as sample geometry (e.g., specimen thickness and length, notches, etc.), chemical composition, microstructure (e.g., grains and crystal orientation), and processing flaws (e.g., porosity and internal stresses). Of course, lattice defects (e.g., dislocations) and their mobility have also a high contribution to ductility, but this is not discussed in this paper. The geometry of the tensile specimens, for instance, gauge thickness and length, is important to accommodate the plastic elongation, which contributes to ductility. According to some standards for flat tensile test specimens [24,25], the equation of $L_0 = 5.65 \sqrt{S_0}$ is commonly used to calculate the proportional dimension of gauge length (L_0) from the cross-sectional area of gauge section (S_0). In the present work, the width (2 mm) and length (6 mm) of the gauge section are kept constant, while the specimen thicknesses (0.31–0.54 mm) are not intentionally varied due to sample preparations (grinding and polishing). According to the equation and cross-sectional data, the applied gauge length (6 mm) complies the minimum requirement of gauge lengths of 4.5–5.9 mm; thus, the gauge length should have no influence. Considering the thickness effect, some works [26–28] reported that the major effect of specimen thickness is only observed at the non-uniform plastic elongation (post-necking zone), which is not observed in samples S1–S4. Of course, the non-uniform plastic elongation and highest elongation at fracture are observed in S5, but this sample has the smallest sample thickness among samples S1–S5, which does not comply with the thickness effect theory. Thus, it is believed that sample thickness has no significant effect here.

Considering no significant correlation between ductility with specimen thickness, it is believed that an improved ductility is influenced by other factors. Dislocation mobility and plastic deformation capability are key roles to the ductility of materials. These factors are strongly influenced by internal properties of materials, such as chemical composition, grain size, and presence of processing flaws.

Possible contributing factors, such as Cu concentration, grain size, crystal growth borders, porosity, and internal stresses are discussed with respect to the deposition parameters.

The first factor is related to Cu concentration. Pure nanocrystalline Co dominantly exhibits a hexagonal closed pack (hcp) structure, which is known to be brittle due to a limited number of active slip systems. The addition of Cu in the nanocrystalline Co is addressed to change the hcp- to fcc-structure, which exhibit a higher number of active slip systems. In addition, some research in pure nanocrystalline Cu [29,30] reported good ductility for more than 10% of elongation at fracture; thus, improvement of ductility is expected in nanocrystalline Co-Cu. According to thermodynamic data, deposition of Cu is easier than Co caused by a more positive standard reduction potential ($E_{\text{Cu}^{2+}/\text{Cu}}^0 = +0.34$ V vs. SHE and $E_{\text{Co}^{2+}/\text{Co}}^0 = -0.28$ V vs. SHE). The increase of Cu concentration in S3 and S4 is affected by this effect due to deposition at shorter pulse-on time (S3), and lower pulse current density (S4) compared to S1, respectively. Higher Cu content is also obtained at the samples deposited at longer off-time, such as observed in S2 and S5 (compared with S1), which is caused by galvanic reaction of deposited Co with Cu ions in the electrolyte when the pulsed current is off. The other possible effect relating to the presence of Cu is the formation of Co-Cu/Cu multilayered structure sizes of 1–3 nm prior to galvanic reaction when the pulsed current is off [31]. This nano-scale multilayered structure may have an impact on the ductility of the nanocrystalline Co-Cu. In the previous work [6], investigation on the Co and Cu atomic distribution was conducted through the atom probe tomography (APT) measurement in the identical sample. However, the formation of Co-Cu/Cu multilayers and Co- or Cu-segregations in the nanometer scale cannot be detected from the APT measurement. Further observation through the higher resolution of APT or TEM is needed to investigate the possible formation of these multilayers structure. In the nanocrystalline Co-Cu, ductility increases with increasing Cu content, but it should be considered that high Cu content may lead on the decrease of strength. There must be an optimum Cu content to achieve high tensile strength and good ductility.

The second factor is related to the grain size. According to the XRD grain size analysis, S4 and S5 exhibit bigger grain size compared with S1–S3 (see Table 1). Although the grain size is not accurately measured here (only estimation of grain size range), distinct observation of coarser grains in S4 is real from a BSE image (Figure 2b). In comparison with S1 and S2, more ductility can be obtained from S4 and S5. It is believed that coarser grain (i.e., still in the nanocrystalline range) have a contribution on the increase of ductility. According to Meyers [4], low plasticity in the nanocrystalline materials is contributed by a significantly lower number and mobility of dislocations within individual grain. The number and mobility of dislocations within individual grain increase with increasing grain size; thus, more plastic deformation can be obtained (i.e., more ductility). Deposition at lower current density (S4) and lower duty cycle (S5) produces the nanocrystalline Co-Cu with higher Cu-content and coarser grain. The influence of higher Cu-content on the increase of grain size in the nanocrystalline Co-Cu has been observed by Müller [22].

The third factor is related to the formation of crystal growth borders. The crystal growth was introduced by Fischer [23], relating to the nucleation and growth mechanism in the electrochemical deposition. In the nanocrystalline materials, one “crystal” growth may consist up to hundreds or thousands of nano-grains, which may have similar crystal orientations (fiber texture). Usually, many “crystals” are growing at the same time and will get into contact, at some point, to form crystal growth borders. At these borders, the chemical composition may vary (depletion of alloying element in the electrolyte, agglomeration of impurities, etc.). In the present work, inhomogeneous concentration of Co and Cu is observed at crystal growth borders in S1, as shown in Figure 3b. The formation of these borders at the surface of other tensile specimens (S2–S4) is not observed. Of course, these borders are believed remaining in the samples, and the fracture surface images of S2–S4 (see Figure 5a,c,e) show that the fracture of crystal growth borders can be reduced significantly with improved ductility. These borders are not even found in the fracture surface of S5. Adjusting deposition parameters (i.e., longer off time, lower current density, etc.) has a significant impact to reduce the formation of these borders through different mechanisms.

The fourth factor is related to hydrogen evolution and formation of porosity. Hydrogen evolution at the cathode leads on the reduction of current efficiency and the formation of porosity due to trapped hydrogen gas, and it cannot be avoided during deposition at high current density. According to works by some authors [12,32,33], the observance of strong intensity (111) orientation in samples S1–S5 (see Figure 1a), which reflects inhibited lateral growth mode, is an indication of the hydrogen gas presence during deposition. Adjustment of parameters of deposition, such as reducing duty cycle (S2–S5), shortening pulse-on time (S3 and S5), and lowering pulse current density (S4) are intended to reduce the hydrogen evolution, which has a direct impact on number of porosities, such as discussed in literatures [17,34]. Of course, it is believed that some porosities are still in the deposits (samples S2–S5), but microstructure investigation confirms that no distinct porous formation is observed in samples S2–S5. This non-observed pore formation is, maybe, related to the smaller size of porosities compared with S1, which influences ductility. Further investigations on the critical size and number of pores should be conducted in the future to obtain a more comprehensive understanding between parameters of deposition, porosity, and ductility.

The last factor is related to internal stresses. The slightly different XRD peak form (e.g., peak intensity and peak broadening) of individual crystal textures in samples S1–S5 (see Figure 1a) is an indication of different concentration of micro-strain in the different nanocrystalline Co-Cu deposits (see Table 1). Internal micro-stress is one of contributing factor to the micro-strain broadening. During the pulsed electrodeposition process, stress generation, and relaxation occur during pulse current-on and pulse current-off, respectively [35–37]. The internal stresses may have an influence on a brittle behavior in deposited materials. Reducing duty cycle (S2–S5) and shortening pulse-time (S3 and S5) are purposed to extend the time for stress relaxation and shorten the time for stress generation, respectively. Thus, lower internal stresses are expected as well as an improvement of ductility. Some works by Xu [36,37] also reported the formation of twins in nanocrystalline Cu during stress relaxation when the pulse current is off, which has an impact to the strengthening of materials.

The current investigation shows that most the significant improvement on tensile strength and ductility is observed in S5, which was deposited at a combination of significantly low duty cycle (10%) and short pulse-time (0.3 ms), where no reduction in pulse current density is needed (i.e., no decrease of strength). Thus, deposition at these parameters is favored to achieve high tensile strength and good ductility of nanocrystalline Co-Cu. Surely, further investigation and optimization, such as effect of deposition temperature and electrolyte composition are required to obtain the optimum results. These results show the importance of deposition parameters in the massive improvement on ductility of nanocrystalline Co-Cu.

2.3. Effect of Annealing Temperatures on Ductility

The effect of annealing temperatures on the ductility of Co-rich nanocrystalline Co-Cu is investigated. Figure 7a shows a back scattered electron (BSE) image of micrograph of sample 6 (S6), which was deposited at a pulse current density, duty cycle, and pulse-time of 900 A/m², 10%, and 0.3 ms, respectively. A reduced pulse current density compared with S5 is intended to enhance ductility further. In comparison with S5, nanocrystalline Co-Cu with coarser grains (Figure 7a) and higher Cu content (Table 3) is observed in S6 due to deposition at lower pulse current density. Samples deposited at the same parameter with S6 were subjected to annealing treatment at 200 °C (S7), 300 °C (S8), and 450 °C (S9) for 24 h to investigate the effect of annealing on mechanical properties. BSE images (Figure 7b–d) show that no significant grain changes (e.g., grain coarsening) are detected at the sample annealed at 200 °C (S7) and 300 °C (S8), while slight grain coarsening is observed at the sample annealed at 450 °C (S9). Previous work on nanocrystalline Co-Cu (28 at.% Cu) [6] confirms identical results with these findings.

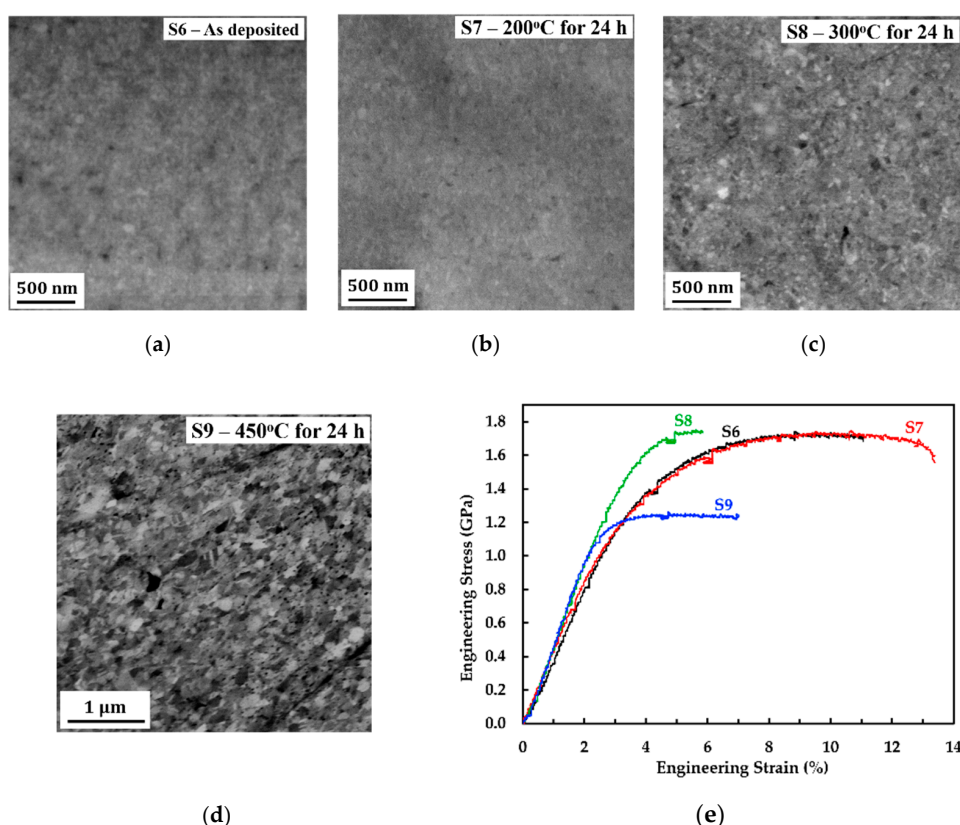


Figure 7. (a–d) BSE images of initial microstructure of (a) sample 6 (S6), (b) sample 7 (S7), (c) sample 8 (S8), and (d) sample 9 (S9) in planar mode; (e) engineering stress vs. strain curves of static tensile test at a strain rate of $1.0 \times 10^{-3} \text{ s}^{-1}$ of sample 6 (S6)–sample 9 (S9). The description for each sample is shown in the Table 3.

Table 3. Description of tensile specimens S6–S9 with the Identical thickness (D) and chemical composition which were deposited for 72 h at pulse current density (i_p), duty cycle (DC), and pulse-on time (t_p) of 900 A/m^2 , 10%, and 0.3 ms, respectively. Samples S7–S9 were annealed at different annealing temperatures for 24 h. The yield strength (σ_y), ultimate tensile strength (σ_u), and total elongation at fracture (ϵ_f) are measured from the engineering stress–strain curves in Figure 7e. Two tensile specimens were mechanically tested for S6 and S9.

	d (mm)	Annealing		Composition		Mechanical Properties		
		Temp (°C)	Time (h)	Co (at.%)	Cu (at.%)	σ_y (GPa)	σ_u (GPa)	ϵ_f (%)
S6	0.31	As deposited		79.5 ± 0.0	20.5 ± 0.0	1.16 ± 0.01	1.71 ± 0.02	11.37 ± 0.24
S7	0.31	200	24	79.5 ± 0.0	20.5 ± 0.0	1.10	1.73	13.38
S8	0.31	300	24	79.8 ± 0.1	20.2 ± 0.1	1.40	1.75	5.84
S9	0.35	450	24	79.8 ± 0.1	20.2 ± 0.1	1.03 ± 0.08	1.28 ± 0.17	6.05 ± 0.97

Figure 7e depicts engineering tensile stress vs. strain curves of S6–S9 at a strain rate of $1.0 \times 10^{-3} \text{ s}^{-1}$ and the detailed data are provided in Table 3. The stress vs. strain curve of S6 confirms that the as deposited state shows good ductility, with a total elongation at fracture of $11.37 \pm 0.24\%$. In comparison with S6, annealing at $200 \text{ }^\circ\text{C}$ for 24 h (S7) leads on the improvement of ductility while the strength is maintained at the same level (see Figure 7e and Table 3). Surface morphology images at a gauge section of S6 (Figure 8a) and S7 (Figure 8b) show moderate necking with shear fracture at an angle of 45° relative to the tensile load direction as indications of ductile fracture. Fractographies of S6 (Figure 8c) and S7 (Figure 8d) also show ductile fracture surfaces with a dimple structure. In comparison with S5, a decrease of ductility and strength are confirmed in S6, although the pulse current density has been lowered. It is believed that the decrease of ductility in S6 compared with S5 is caused by the

thickness effect, while the decrease of strength is caused by the grain size effect. On the other hand, the improved ductility in samples S7 (compared with S6) may be caused by recovery processes, such as relaxation of internal stresses, and grain boundaries, as well as the release of absorbed hydrogen. XRD patterns of samples S6 and S7 (see Figure 8e) confirm significantly dissimilar peak intensity and peak broadening of (200) and (220) peaks indicating different concentration of micro-strains (e.g., internal stresses). Of course, better XRD resolution and other contributing measurements (e.g., absorbed hydrogen measurement) are needed to obtain exact value of those mentioned factors. However, these results could be an initial indication that the improved ductility in S7 may be caused by the recovery processes. At this point, structural transformation at 200 °C must be further investigated to reveal the influencing factors on the improvement of ductility.

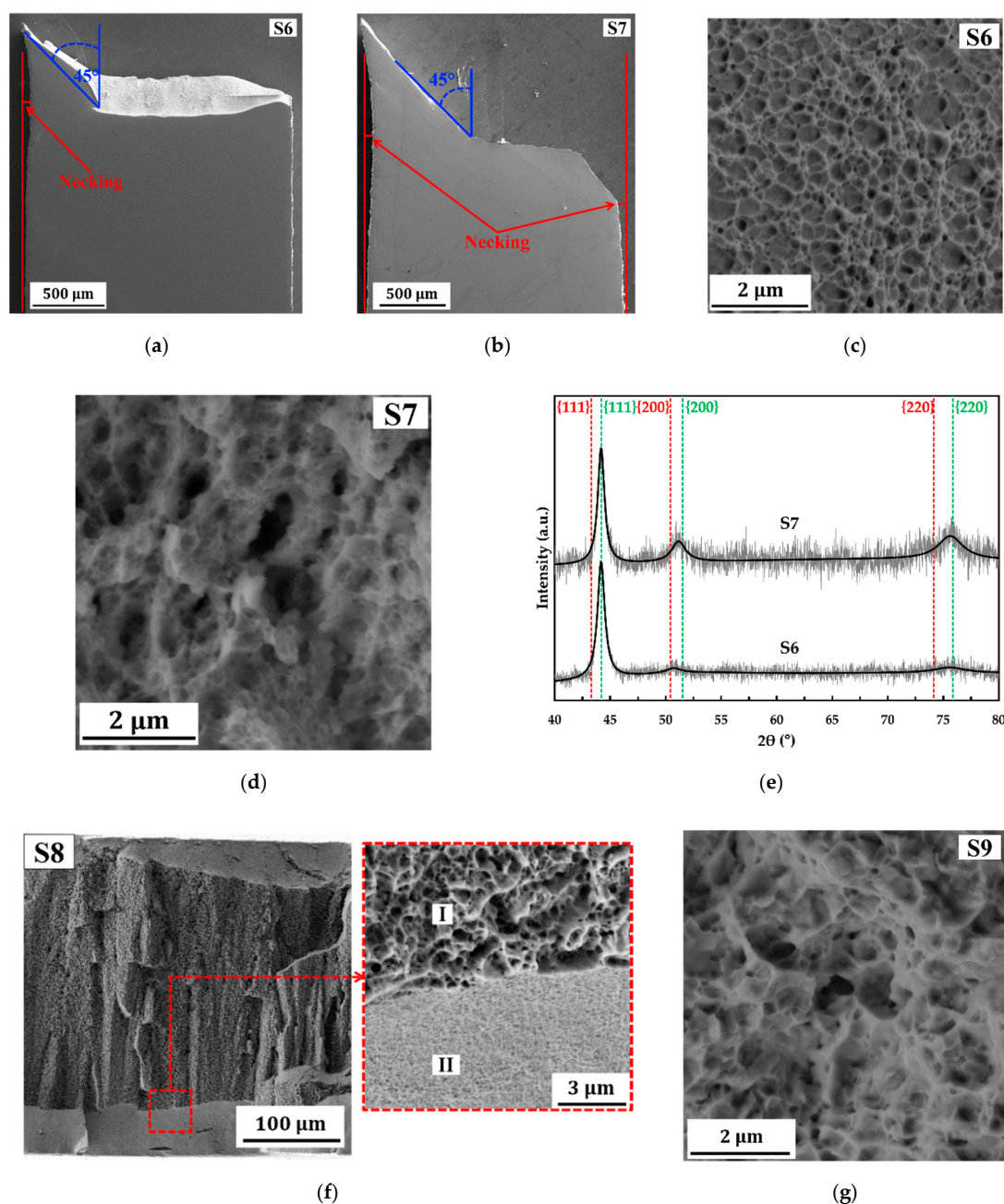


Figure 8. (a,b) SE images of surface morphology at the gauge section after tensile test of (a) sample 6 (S6) and (b) sample 7 (S7); SE images of fracture surface of (c) sample 6 (S6), (d) sample 7 (S7), (f) sample 8 (S8) and (g) sample 9 (S9); (e) XRD patterns of samples S6 and S7.

In comparison with the as deposited state (S6), annealing treatment at 300 °C for 24 h (S8) leads to a strengthening of nanocrystalline Co-Cu in which the observed yield strength increases to 1.4 GPa (see Figure 7e and Table 3). The XRD measurement shows that the as deposited state nanocrystalline Co-Cu (S6) exhibits a supersaturated solid solution phase with strong (111) orientation (see Figure 8e). According to previous work [6], the nano scale spinodal or chemical decomposition of solid solution Co-Cu was detected at 300 °C, in which three regions (solid solution Co-Cu, Co-rich, and Cu-rich) were detected. The presence of Co- and Cu-rich regions with sizes of 5–10 nm, which may act as Co- or Cu-precipitates, is expected to have a direct impact to a strengthening of nanocrystalline Co-Cu (S8). However, improved ductility is not observed here with the total elongation at fracture decreases to 5.48%. The fracture image of S8 (Figure 8f) shows two ductile fracture regions with different size of dimples. Figure 8f depicts that the dimple structures with the sizes of 0.5 μm –1 μm are observed at the center of a cross-section tensile specimen (region I), while the smaller sizes of dimples are found at the area near surface (region II).

The engineering stress vs. strain curve of S9 (Figure 7e) shows that annealing at 450 °C for 24 h leads to decrease of strength and ductility in comparison with the as deposited state (S6). Interestingly, a fracture surface of S9 shows no brittle fracture surface, whereas dimple structures (Figure 8g) as indication of ductile fracture are observed. According to previous work [6], slight grain coarsening, which is also observed in S9, as well as massive phase decomposition of Co-Cu are reported after annealing at 450 °C for 24 h. It is clear enough that the reduced strength in S9 is caused by the grain coarsening. Surprisingly, phase separation of Co-Cu, which is expected to improve the mechanical stability, is unable to improve (or even maintain) the ductility of nanocrystalline Co-Cu. According to previous work [6], phase decomposition of the fcc-structured solid solution nanocrystalline Co-Cu at 450 °C for 24 h led to the formation of fcc-Cu, fcc-Co, and hcp-Co phases. It is believed that a decreased ductility is caused by the presence of an hcp-Co phase, which is known to be more brittle compared with the fcc-structure. Other factors, such as impurity segregation at grain boundaries, may also have a contribution on reduction of ductility at 450 °C. At 450 °C, the diffusion of co-deposited impurities (e.g., sulfur) to the grain boundaries is possible as shown in the nanocrystalline Co [38] and Ni [39]. The segregation of sulfur at grain boundaries have an impact on grain boundary embrittlement, which leads to the reduction of ductility.

In this paper, high tensile ductility and strength of pulsed electrodeposited nanocrystalline Co-Cu can be achieved by adjusting the parameters of deposition. Moreover, annealing treatments show some interesting and surprising results in which an improvement of ductility can also be obtained through this method. In the future, fatigue behavior of PED-processed bulk nanocrystalline Co-Cu will be also studied.

3. Materials and Methods

Bulks nanocrystalline Co-Cu with thickness of 600–750 μm were produced through the pulsed electrodeposition technique at copper cathode plates (21 mm \times 21 mm) and double plate of titanium-mesh (120 mm \times 60 mm) was used as an anode. The PED process was conducted to produce nanocrystalline Co-Cu deposits (S1–S9 samples) at different parameters of deposition (pulse current density, duty cycle, and pulse-time) as shown in Tables 1 and 2. The times for the deposition are different for individual samples, which are 35 h for S1, 40 h for S2–S3, 50 h for S4, 69 h for S5, and 72 h for S6–S9, with a current efficiency of 80–90%. The PED process was performed with 1.10 L electrolyte containing 0.40 M $\text{CoSO}_4 \cdot 7\text{H}_2\text{O}$, 0.04 M CuSO_4 , 0.20 M $\text{C}_4\text{H}_4\text{KNaO}_6 \cdot 4\text{H}_2\text{O}$, 1.00 M Na_2SO_4 , 0.3 M H_3BO_3 , 2.00 g/L $\text{C}_7\text{H}_5\text{NO}_3\text{S}$ (Saccharin), and 0.20 g/L $\text{C}_{12}\text{H}_{25}\text{NaO}_4\text{S}$ (sodium dodecyl sulfate) at a constant temperature of 40 °C. Some deposits (S7–S9) were subjected to isothermal annealing in vacuum at a pressure of 10^{-6} mbar at various temperatures (200–450 °C) for 24 h to investigate the effect of annealing temperatures on the mechanical properties.

All deposits were removed from copper substrate and they were subjected to cutting processes to produce two tensile specimens from each deposit. Figure 9a shows a schematic picture and dimension

of a dog-bone tensile specimen used in this work. Tensile specimens were subjected to grinding and polishing procedure, and some parts (200–300 μm) of the tensile specimen thickness will be lost during this step. Polished tensile specimens were settled to the specimen holder, as shown in Figure 9b. This holder (including tensile specimen) was installed in the tensile testing machine, as demonstrated in Figure 9c. Tensile tests were carried out in a testing machine, Instron 8513 (Instron, Norwood, MA, USA), at a strain rate of $1.0 \times 10^{-3} \text{ s}^{-1}$. Caused by limitation of the samples, i.e., small dimension compared to the standard tensile specimen, the measured strain data were only recorded by the cross-head displacement of the machine with no additional devices (e.g., extensometer). Initial microstructure and fracture surface images, as well as chemical composition of tensile specimens, were investigated in the scanning electron microscope (SEM) Zeiss Sigma-VP (Jena, Thüringen, Germany) equipped with a backscattered electron (BSE) detector and energy dispersive spectroscopy (EDS) detector (Oxford Instruments, Abingdon, Oxfordshire, England) at acceleration voltages of 10–20 kV. X-ray diffraction (XRD) measurements were conducted by using Cu K-alpha radiation (λ : 1.5405980 Å) and a scan step size of $0.013^\circ 2\theta/\text{s}$. The XRD data were processed with Fityk software (Institute of High Pressure Physics, Warsaw, Poland) [40] for peak refinement and peak fitting. The SEM and XRD measurements were carried out at the surface of the tensile specimen next to the solution side.

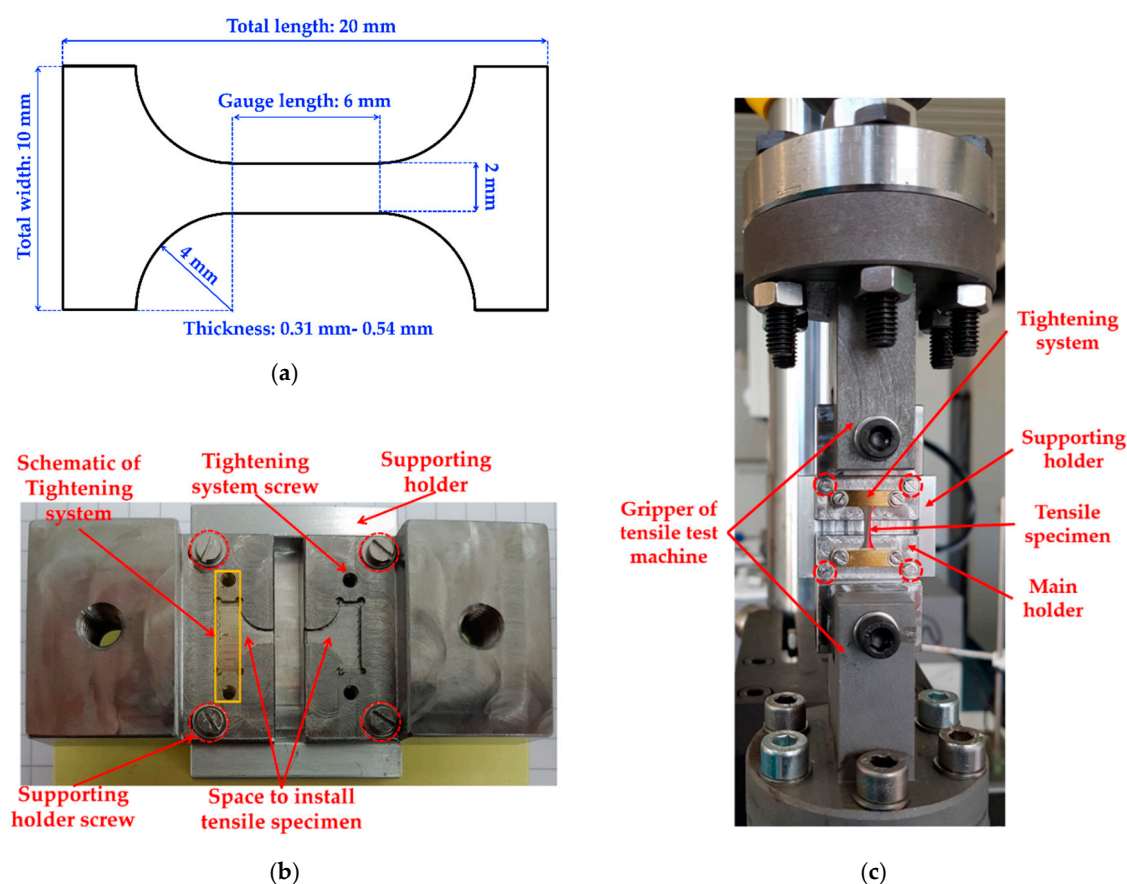


Figure 9. (a) Schematic picture of the dog-bone tensile specimen used in this work. The thickness of the specimens is intentionally varied, as shown in Tables 1 and 3; (b) design of the tensile specimen holder. A supporting holder is used to support the holder and specimen just before the test, and will be removed after installation in the tensile testing machine. The red dashed circle shows some screws to remove the supporting holder. The tightening system is used to fix the tensile specimen at its place; (c) installation of the tensile specimen holder (including tensile specimen) in the tensile testing machine. The supporting holder must be removed after the installation (before the tensile test) by removing the screws, which are marked with red dashed circle.

4. Conclusions

Strategies to obtain high tensile strength and ductility of PED-processed bulk nanocrystalline Co-Cu were investigated by adjusting pulse current density, duty cycle, and pulse-time of deposition. An improved strength and ductility can be achieved through the deposition at high pulse current density (1000 A/m²) by reducing duty cycle and pulse-time up to 10% and 0.3 ms, respectively. Specimen deposited at this parameter shows that an elongation to fracture of $15.95 \pm 0.09\%$, as well as yield and ultimate strength up to 1.21 ± 0.08 GPa and 1.98 ± 0.03 GPa, respectively, could be achieved. Improved ductility could also be acquired through isothermal annealing at 200 °C, whereas annealing at 300 °C leads to strengthening with reduction of ductility. It is believed that improvement on ductility and strength of PED-processed nanocrystalline Co-Cu is affected by several factors, such as Cu concentration, grain size, and number of flaws within materials (e.g., crystal growth borders, porosity, and internal stresses).

Author Contributions: Conceptualization, methodology, writing—original draft preparation: K.P. and C.M.; Experiment and data collection: K.P.; draft and project supervision: C.M. All authors have read and agreed to the published version of the manuscript.

Funding: The authors gratefully acknowledge the financial support by German Academic Exchange (DAAD) under GSSP (funding-ID: 57320205). The SEM device was financed by DFG INST 256/340-1FUGG and the Federal State Government of Saarland.

Acknowledgments: The authors thank M. Marx for his help designing the tensile specimen holder. The authors thank S. Slawik for his help conducting the XRD measurement.

Conflicts of Interest: The authors declare no conflict of interest.

References

1. Karimpoor, A.A.; Erb, U. Mechanical properties of nanocrystalline cobalt. *Phys. Stat. Sol.* **2006**, *203*, 1265–1270. [[CrossRef](#)]
2. Karimpoor, A.A.; Erb, U.; Aust, K.T.; Palumbo, G. High strength nanocrystalline cobalt with high tensile ductility. *Scr. Mater.* **2003**, *49*, 651–656. [[CrossRef](#)]
3. Wang, Y.M.; Ott, R.T.; van Buuren, T.; Willey, T.M.; Biener, M.M.; Hamza, A.V. Controlling factors in tensile deformation of nanocrystalline cobalt and nickel. *Phys. Rev. B* **2012**, *85*, 014101. [[CrossRef](#)]
4. Meyers, M.A.; Mishra, A.; Benson, D. Mechanical properties of nanocrystalline materials. *Prog. Mater. Sci.* **2006**, *51*, 427–556. [[CrossRef](#)]
5. Bachmaier, A.; Rathmayr, G.; Schmauch, J.; Schell, N.; Stark, A.; De Jonge, N.; Pippan, R. High strength nanocrystalline Cu–Co alloys with high tensile ductility. *J. Mater. Res.* **2019**, *34*, 58–68. [[CrossRef](#)]
6. Pratama, K.; Barrirero, J.; Mücklich, F.; Motz, C. Microstructure evolution and mechanical stability of supersaturated solid solution Co-rich nanocrystalline Co-Cu produced by pulsed electrodeposition. *Materials* **2020**, *13*, 2616. [[CrossRef](#)]
7. Koch, C.C. Optimization of strength and ductility in nanocrystalline and ultrafine grained metals. *Scr. Mater.* **2003**, *49*, 657–662. [[CrossRef](#)]
8. Ma, E. Instabilities and ductility of nanocrystalline and ultrafine-grained metals. *Scr. Mater.* **2003**, *49*, 663–668. [[CrossRef](#)]
9. Sanders, P.G.; Youngdahl, C.J.; Weertman, J.R. The strength of nanocrystalline metals with and without flaws. *Mater. Sci. Eng. A* **1997**, *234–236*, 77–82. [[CrossRef](#)]
10. Li, J.C.M. Grain boundary impurity and porosity effects on the yield strength of nanocrystalline materials. *App. Phys. Lett.* **2007**, *90*, 041912. [[CrossRef](#)]
11. Erb, U.; Palumbo, G.; McCrea, J.L. The processing of bulk nanocrystalline metals and alloys by electrodeposition. In *Nanostructured Metals and Alloys: Processing, Microstructure, Mechanical Properties and Applications*; Whang, S.H., Ed.; Woodhead Publishing Series in Metals and Surface Engineering; Part I; Woodhead Publishing: Cambridge, UK, 2011; Chapter 5; pp. 118–151.
12. Matsui, I.; Takigawa, Y.; Yokoe, D.; Kato, T.; Uesugi, T.; Higashi, K. Strategy for electrodeposition of highly ductile bulk nanocrystalline metals with a face-centered cubic structure. *Mater. Trans.* **2014**, *55*, 1859–1866. [[CrossRef](#)]

13. Valiev, R.Z.; Islamgaliev, R.K.; Alexandrov, I.V. Bulk nanostructured materials from severe plastic deformation. *Prog. Mater. Sci.* **2000**, *45*, 103–189. [[CrossRef](#)]
14. Tsuji, N. Bulk nanostructured metals and alloys produced by accumulative roll-bonding. In *Nanostructured Metals and Alloys: Processing, Microstructure, Mechanical Properties and Applications*; Whang, S.H., Ed.; Woodhead Publishing Series in Metals and Surface Engineering; Part I; Woodhead Publishing: Cambridge, UK, 2011; Chapter 2; pp. 40–58.
15. Tschoop, M.; Murdoch, H.; Kecskes, L.; Darling, K. “Bulk” nanocrystalline metals: Review of the current state of the art and future opportunities for copper and copper alloys. *JOM* **2014**, *66*, 1000–1019. [[CrossRef](#)]
16. Suryanaraya, C. Mechanical alloying of nanocrystalline materials and nanocomposites. *Madr. J. Nanotechnol. Nanosci.* **2019**, *4*, 127–134. [[CrossRef](#)]
17. Popov, K.I.; Maksimovic, M.D.; Ockoljic, B.M.; Lazarevic, B.J. Fundamental aspects of pulsating current metal electrodeposition I: The effect of the pulsating current on the surface roughness and the porosity of metal deposits. *Surf. Technol.* **1980**, *11*, 99–109. [[CrossRef](#)]
18. Matsui, I.; Omura, N. Comparison of tensile properties of bulk nanocrystalline Ni-W alloys electrodeposited by direct, pulsed, and pulsed-reverse currents. *Mater. Trans.* **2018**, *59*, 123–128. [[CrossRef](#)]
19. Ebrahimi, F.; Ahmed, Z. The effect of current density on properties of electrodeposited nanocrystalline nickel. *J. Appl. Electrochem.* **2003**, *33*, 733–739. [[CrossRef](#)]
20. Bachmaier, A.; Pfaff, M.; Stolpe, M.; Aboufadel, H.; Motz, C. Phase separation of supersaturated nanocrystalline Cu-Co alloy and its influence on thermal stability. *Acta Mater.* **2015**, *96*, 269–283. [[CrossRef](#)]
21. Bachmaier, A.; Motz, C. On the remarkable thermal stability of nanocrystalline cobalt via alloying. *Mater. Sci. Eng. A* **2014**, *624*, 41–51. [[CrossRef](#)] [[PubMed](#)]
22. Müller, T. Pulsed Electrodeposition of Nanocrystalline Co and Co-Cu Alloys. Master’s Thesis, Saarland University, Saarbrücken, Germany, 2014.
23. Fischer, H. *Elektrolytische Abscheidung und Elektrokristallisation von Metallen*; Springer: Berlin/Heidelberg, Germany, 1954.
24. IACS W2. Test specimens and mechanical testing procedures for materials. In *Requirements Concerning materials and Welding*; International Association of Classification Societies: London, UK, 2003; pp. W2-1–W2-2. Available online: <http://www.iacs.org.uk/publications/unified-requirements/ur-w/> (accessed on 12 August 2020).
25. ISO 6892-1. *Metallic Materials—Tensile Testing—Part 1: Method of Test at Room Temperature*; The International Organization for Standardization: Geneva, Switzerland, 2009; Available online: <https://www.iso.org/obp/ui#iso:std:iso:6892:-1:ed-2:v1:en> (accessed on 12 August 2020).
26. Takeda, Y.; Kiattisaksri, C.; Aramaki, M.; Munetoh, S.; Furukimi, O. Effect of specimen thickness in tensile tests on elongation and deformation energy for industrially pure iron. *ISIJ Int.* **2017**, *57*, 1–9. [[CrossRef](#)]
27. Zhao, Y.H.; Guo, Y.Z.; Wei, Q.; Dangelewicz, A.M.; Xu, C.; Zhu, Y.T.; Langdon, T.G.; Zhou, Y.Z.; Lavernia, E.J. Influence of specimen dimensions on the tensile behavior of ultrafine-grained Cu. *Scr. Mater.* **2008**, *59*, 627–630. [[CrossRef](#)]
28. Yuan, W.J.; Zhang, Z.L.; Su, Y.J.; Qiao, L.J.; Chu, W.Y. Influence of specimen thickness with rectangular cross-section on the tensile properties of structural steels. *Mater. Sci. Eng. A* **2012**, *532*, 601–605. [[CrossRef](#)]
29. Lu, L.; Wang, L.B.; Ding, B.Z.; Lu, K. High-tensile ductility in nanocrystalline copper. *J. Mater. Res.* **2000**, *15*, 270–273. [[CrossRef](#)]
30. Wang, Y.; Chen, M.; Zhou, F.; Ma, E. High tensile ductility in a nanostructured metal. *Nature* **2002**, *419*, 912–915. [[CrossRef](#)]
31. Cziraki, A.; Peter, L.; Weihnacht, V.; Toth, J.; Simon, E.; Padar, J.; Pogany, L.; Schneider, C.M.; Gemming, T.; Wetzig, K.; et al. Structure and giant magnetoresistance behavior of Co-Cu/Cu multilayer electrodeposited under various deposition conditions. *J. Nanosci. Nanotechnol.* **2006**, *6*, 2000–2012. [[CrossRef](#)]
32. Amblard, J.; Epelboin, I.; Froment, M.; Maurin, G. Inhibition and nickel electrocrystallization. *J. Appl. Electrochem.* **1979**, *9*, 233–242. [[CrossRef](#)]
33. Krause, A.; Uhlemann, M.; Gebert, A.; Schultz, L. A study of nucleation, growth, texture and phase formation of electrodeposited cobalt layers and the influence of magnetic fields. *Thin Solid Films* **2006**, *515*, 1694–1700. [[CrossRef](#)]
34. Ibl, N. Some theoretical aspects of pulse electrolysis. *Surf. Technol.* **1980**, *10*, 81–104. [[CrossRef](#)]

35. Marro, J.B.; Darroudi, T.; Okoro, C.A.; Obeng, Y.S.; Richardson, K.C. The influence of pulse plating frequency and duty cycle on the microstructure and stress state of electroplated copper films. *Thin Solid Films* **2017**, *621*, 91–97. [[CrossRef](#)]
36. Xu, D.; Sriram, V.; Ozolins, V.; Yang, J.-M.; Tu, K.N. In situ measurements of stress evolution for nanotwin formation during pulse electrodeposition of copper. *J. Appl. Phys.* **2009**, *105*, 023521. [[CrossRef](#)]
37. Xu, D.; Kwan, W.L.; Chen, K.; Zhang, X.; Ozolins, V.; Tu, K.N. Nanotwin formation in copper thin films by stress/strain relaxation in pulse electrodeposition. *Appl. Phys. Lett.* **2007**, *91*, 254105. [[CrossRef](#)]
38. Hibbard, G.D.; Aust, K.T.; Erb, U. The effect of starting nanostructure on the thermal stability of electrodeposited nanocrystalline Co. *Acta Mater.* **2006**, *54*, 2501–2510. [[CrossRef](#)]
39. Rathman, D.; Marx, M.; Motz, C. Crack propagation and mechanical properties of electrodeposited nickel with bimodal microstructures in the nanocrystalline and ultrafine grained regime. *J. Mater. Res.* **2017**, *32*, 4573–4582. [[CrossRef](#)]
40. Wojdyr, M. Fityk: A general-purpose peak fitting program. *J. Appl. Cryst.* **2010**, *43*, 1126–1128. [[CrossRef](#)]

Sample Availability: Samples of the tensile specimens S1–S9 are available from the authors.

Publisher's Note: MDPI stays neutral with regard to jurisdictional claims in published maps and institutional affiliations.



© 2020 by the authors. Licensee MDPI, Basel, Switzerland. This article is an open access article distributed under the terms and conditions of the Creative Commons Attribution (CC BY) license (<http://creativecommons.org/licenses/by/4.0/>).

9th International Conference on Materials Structure and Micromechanics of Fracture

Thermal stability, phase decomposition, and micro-fatigue properties of pulsed electrodeposited nanocrystalline Co-Cu

K. Pratama^{a,d,*}, F. Kunz^a, L. Lindner^a, J. Schmauch^b, F. Mücklich^c, C. Motz^a

^aChair of Materials Science and Methods, Saarland University, Saarbrücken 66123, Germany.

^bChair of Experimental Physics, Saarland University, Saarbrücken 66123, Germany.

^cChair of Functional Materials, Saarland University, Saarbrücken 66123, Germany.

^dDepartment of Metallurgical Engineering, Institute Technology of Bandung, Bandung 40132, Indonesia.

Abstract

Nanocrystalline (nc) immiscible Co-Cu alloys system is a promising material where the decomposition of the super-saturated solid solution can be used to obtain nano-structured materials. In this research, homogenous and solid nc Co-Cu thick films were synthesized through the pulsed electrodeposition technique in complex sodium tartrate electrolyte. Annealing procedures were conducted to evaluate its thermal stability and induce phase decomposition of cobalt and copper, which can be utilized to enhance mechanical properties and thermal stability. Initial cyclic micro-bending experiments were also conducted to observe micro-fatigue properties and structural evolution during mechanical loading.

© 2019 The Authors. Published by Elsevier B.V.

This is an open access article under the CC BY-NC-ND license (<http://creativecommons.org/licenses/by-nc-nd/4.0/>)

Peer-review under responsibility of the scientific committee of the ICMSMF organizers

Keywords: nanocrystalline; thermal stability; phase decomposition; cyclic micro-bending

1. Introduction

Nanocrystalline (nc) materials have outstanding mechanical and physical properties (Gleiter (1989); Meyers et al. (2006)). However, these types of materials are thermally and mechanically unstable and improvements are necessary for wide range applications. Many experiments have been conducted to improve the thermal stability of nc materials, for example, through the addition of alloying elements (Bachmaier and Motz (2014)), through the addition of second

* Corresponding author. Tel.: +49 (681) 302-5001; fax: +49 (681) 302-5015.

E-mail address: k.pratama@matsci.uni-sb.de

phase or oxide particle (Molonari et al. (2010)), and by studying the effect of impurities (Hibbard et al. (2006)).

Among the promising materials are immiscible Co-Cu alloys, in which the decomposition of the super-saturated solid solution can be used to obtain nano-structured materials. A series of experiment conducted by Bachmaier (Bachmaier and Motz (2014); Bachmaier and Pfaff et al. (2015); Bachmaier and Stolpe et al. (2015)) showed that nc Co-Cu alloys synthesized by the HPT method have improved thermal stability compared to pure nc Co. No significant decrease of HV numbers was observed in nc Co-Cu even after annealing them for 100 hours at the a temperature $\leq 400^\circ\text{C}$. Interestingly, despite the significant grain coarsening that was observed at 600°C , the microstructure of nc Co-Cu could be maintained in the ultrafine grain region. Phase decomposition of solid solution Co-Cu into fcc-Cu and fcc-Co phases at this annealing temperature was also detected by XRD measurement. Furthermore, phase decomposition of Co-Cu was also observed at a lower annealing temperature (400°C) and it is stable for a long annealing period. However, minor grain coarsening was also observed at this temperature, and further work is required to find the optimum condition for phase decomposition.

The synthesis of nanostructured materials by using the HPT method leads to several problems since it depends on the initial size of the copper and cobalt powder. Moreover, the vacancies and residual stresses were also observed in the nanostructured materials. Synthesis of nc materials by using other methods, for example the electrodeposition technique is possible and has been successfully performed and described in some literatures to produce nc Co (Hibbard et al. (2001)), nc Cu (Lu et al. (1999)), and nc Co-Cu ((Bachmaier and Stolpe et al. (2015); Müller (2014))). Moreover, the synthesis of nc materials through the electrodeposition technique is a simple route of production which also provides technological and economic benefits.

It was also found that nc materials are mechanically unstable since their fatigue resistance are lower compared to ultrafine grain and coarse grain (Mughrabi and Höppel (2010)). Moreover, grain coarsening induced by plastic deformation was also observed on ultrafine grain Cu during cyclic micro-bending experiments (Kapp et al. (2017)). This phenomenon indicates that interesting microstructure development or phase transformation on a nano- and very small scale is possibly observed during mechanical fatigue loading.

2. Experimental Procedures

2.1. Deposition of nc Co-Cu

Nc Co-Cu films were synthesized through the pulsed electrodeposition technique at high current density and low duty cycle (i : 100 mA/cm^2 ; t_{pulse} : 2 ms; t_{off} : 18 ms). Cu disk (ϕ_{surface} : 12 mm) and platinized-Ti rod were prepared as cathode and anode respectively. According to experiments conducted by Müller (Müller (2014)), homogenous and porosity-free deposits were obtained after deposition in complex tartrate electrolyte instead of complex citrate electrolyte, so the deposition in complex tartrate electrolyte was preferred in this experiment. Pulsed electrodeposition was conducted in the electrolyte containing 112.20 g/L $\text{CoSO}_4 \cdot 7\text{H}_2\text{O}$, 6.38 g/L CuSO_4 , 56.44 g/L $\text{C}_4\text{H}_4\text{KNaO}_6 \cdot 4\text{H}_2\text{O}$, 142.04 g/L Na_2SO_4 , 18.55 g/L H_3BO_3 , 2.00 g/L Saccharin, and 0.20 g/L sodium dedocyl sulfate. Deposition was conducted for 24 hours to produce approximately $350 \mu\text{m}$ film thicknesses and the electrolyte's temperature was maintained at 40°C .

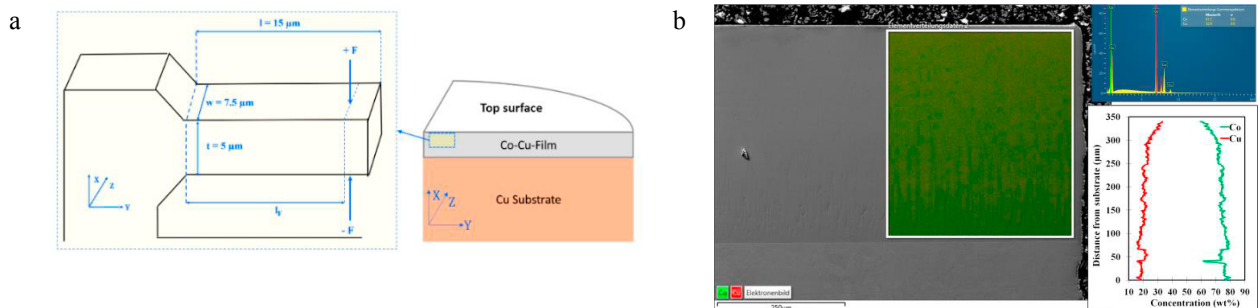


Fig. 1. (a) Schematic drawing of free standing micro bending beam and its position corresponding to the nc Co-Cu film; (a) SEM-EDS observation at the cross section of nc Co-Cu film;

2.2. Characterization and annealing procedures

Deposited nc Co-Cu films were cut in cross-section direction along with Cu substrate. Hereafter, samples were subjected to the subsequent isothermal annealing in the vacuum chamber at different temperatures (300°C, 400°C, 450°C, 600°C, and 800°C) and for different periods (1 hour, 5 hours, 24 hours, and 64 hours), then the samples were quenched to the atmospheric air. All as-deposited and annealed samples were surface prepared with a grinding and polishing machine up to a grid of 1 μm and (if required) OPS was also applied. XRD and microhardness measurement were conducted by using non-OPS polished samples, while OPS polished samples were required for SEM observation. TEM samples preparation was conducted by cutting the polished samples to disks of 3 mm and then further processing them with GATAN PIPS for ion milling.

Cu K-alpha radiation (λ : 1.5405980 Å) X-ray diffraction was used to observe the phases of each sample and the scan step size was controlled at $0.013^\circ 2\theta/s$. Microhardness measurements were carried out on the DuraScan hardness testing machine made by STRUERS and then evaluated with the associated ecos WorkflowTM software. The test force of 1.962 N (HV0.2) was applied to the sample surface for 12 seconds. Zeiss SIGMA Scanning Electron Microscope and Oxford-instruments Energy Dispersive Spectroscopy were used to observe both the microstructure and the alloys' composition at an accelerating voltage of between 17-20 kV. TEM JEOL 2011 was also used to obtain better information about at an accelerating voltage of 200 kV.

2.3. Cyclic micro-bending experiments

The free-standing micro bending beam with a dimension of 15 μm x 7.5 μm x 5 μm (length x width x thickness) was prepared by Focused Ion Beam (FIB) at the area close to the surface of the deposits. A schematic drawing of micro beams is shown in Fig. 1a. The cyclic micro-bending experiments were conducted inside the Zeiss SIGMA SEM by using Advanced Surface Mechanics (ASMEC) system and a UNAT-SEM2 nanoindenter, then the data were recorded by InspectorX Ver. 2 (UNAT software). A double blade gripper was used to transmit the cyclic loading onto the bending beam and the plastic strain amplitudes were controlled at two different values which are $\epsilon_{a,pl} = 4.0 \times 10^{-4}$ (stage-I: 1st - 2000th cycle) and $\epsilon_{a,pl} = 6.5 \times 10^{-4}$ (stage-II: 2001st - 4000th cycle). According to the method used by Kapp et al. (2017), the value of the maximum surface stress σ_s and the maximum surface strain ϵ_s were taken into account. Based on the elastic bending beam theory, the maximum surface stress σ_s and the maximum surface strain ϵ_s are calculated from force-displacement data by using equation (1) and (2). The applied displacement is u , the recorded force is F , length of bending is l_F , width of beam is w , and thickness of beam is t .

$$\sigma_s = \frac{6 F l_F}{w t^2} \quad (1)$$

$$\epsilon_s = \frac{u t}{2 l_F^2} \quad (2)$$

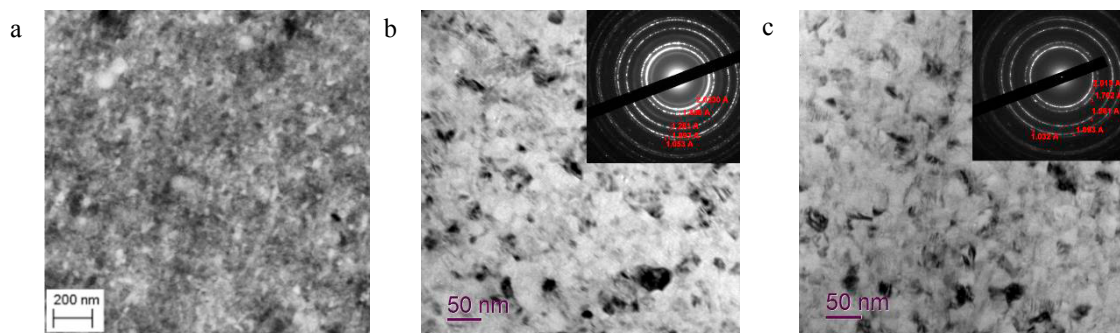


Fig. 2. (a) BSE images of microstructure of as deposited sample; BF TEM micrograph and SAD pattern of (b) as deposited sample and (c) annealed at 300°C for 64 hrs sample.

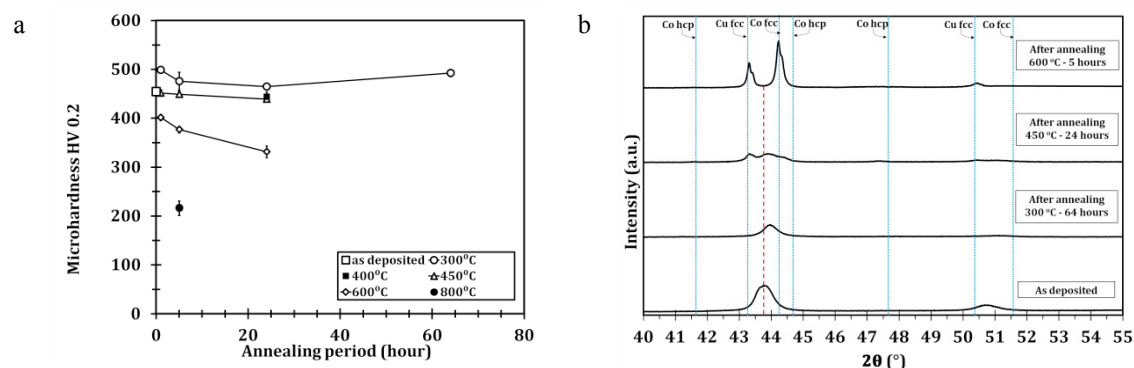


Fig. 3. (a) Microhardness HV0.2 of as-deposited nc Co-Cu and annealed samples as a function of annealing period at different annealing temperatures; (b) XRD patterns of as-deposited and annealed samples. The blue lines represent the diffraction peaks of Co and Cu, whereas the red line is located in the center of diffraction peak of as-deposited sample.

3. Results and Discussion

3.1. As deposited

Fig. 1b shows SE images of as deposited nc Co-Cu at the cross section view. The thick films of nc Co-Cu for up to 350 μm were successfully deposited with no-porosity observed. SEM-EDS measurement shows the typical composition 67wt% Co-33wt% Cu is observed. Interestingly, the Co and Cu atoms are homogeneously distributed from the Cu substrate interface next to the surface of the deposit (see Fig. 1b).

Fig. 2b shows a bright-field TEM images and a selected area diffraction (SAD) pattern of deposited nc Co-Cu film. The average grain size for about $\sim 23 \pm 8.16$ nm is confirmed and the average microhardness for about 455 ± 6.9 HV is measured (see Fig. 3a). The SAD pattern strongly indicates that deposited nc Co-Cu exhibits supersaturated solid solution phase since the diffraction rings are in the between of the fcc Co and fcc Cu Debye-Scherrer rings of {111}, {200}, {220}, and {311} planes. Supersaturated solid solution Co-Cu was also observed in previous researches with this typical alloy composition (Bachmaier and Motz (2014); Bachmaier and Stolpe et al. (2015)). Moreover, the XRD pattern of the as-deposited sample (Fig. 3b) shows a similar result with SAD pattern, where the diffraction peaks are located between the fcc Cu and fcc Co diffraction peaks.

3.2. Thermal stability and phase decomposition

As-deposited nc Co-Cu films were subjected to isothermal annealing procedures to investigate their thermal stability. Fig. 3a shows that these annealing procedures at 300°C which corresponds to $\sim 35\%$ of the melting temperature of the alloy lead to an increasing value of hardness where minor grain coarsening is observed by a bright-field TEM image (see Fig. 2c). The hardness value increases for up to 492 ± 7.27 HV for the sample annealed for the longest period (64 hours) and the measured grain size for this sample is 40 ± 13.24 nm. Interestingly, lattice distortion is also observed in the diffraction pattern of XRD (Fig. 3b) and SAD-TEM (Fig. 2c) compared to the as-deposited sample. This could be an indication of the phase decomposition which was also observed in the experiment carried out by Bachmaier (Bachmaier and Pfaff et al. (2015)) at a higher annealing temperature (400°C) with a different alloy composition. Furthermore, this will be an advantage for the tailoring phase decomposition at low temperature, where nano-sized grain below 50 nm can be maintained.

Minor grain coarsening is also observed in the sample annealed at 400°C for 24 hours, where the hardness value decreases to 444 ± 10.31 HV (see Fig. 3a) and the grain size increases to 82 ± 28.00 nm. A microstructure image of the sample annealed at 400°C for 24 hours is given in Fig. 4a. This could be an upper-limit temperature for the tailoring phase decomposition where nano-sized grain can be maintained below 100 nm, but an annealing procedure at lower temperature will be preferred. Grain coarsening is more pronounced in the samples annealed at higher temperatures (450°C and 600°C), where the hardness values significantly decrease for up to 439 ± 5.18 HV and 331 ± 11.78 HV for the sample annealed at 450°C and 600°C for 24 hours, respectively (see Fig. 3a). However, ultrafine grain structures

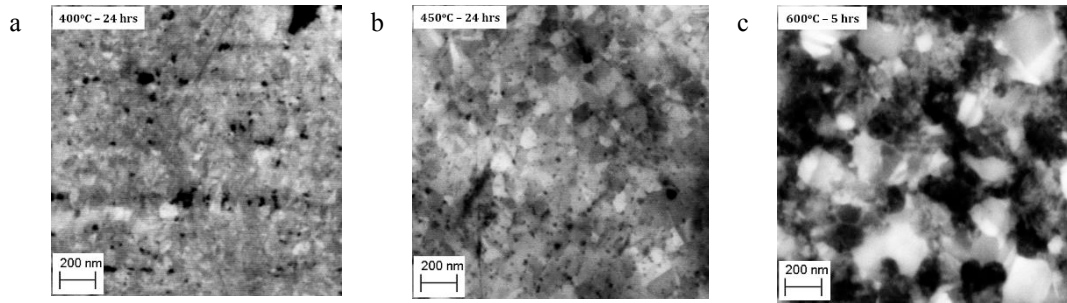


Fig. 4. Microstructure images of (a) annealed at 400°C for 24 hours; (b) annealed at 450°C for 24 hours; and (c) annealed at 600°C for 5 hours taken by BSE detector.

were remained in the sample annealed at 450°C and 600°C, in spite of an annealing period of up to 24 hours. Interestingly, distinct microstructures are clearly observed at the samples annealed at these temperatures (see Fig. 4(b-c)) and the phase decomposition to fcc Co and fcc Cu phases is confirmed by the XRD patterns (see Fig. 3b).

3.3. Initial cyclic micro-bending test

Low cyclic micro-bending tests were conducted to observe initial fatigue properties of as-deposited nc Co-Cu films. Selected surface stress as a function of surface strain data was plotted into cyclic hysteresis loop graph and shown in Fig. 5a. The average stress amplitude ($\sigma_{s,avg,amp}$) of each cycles was calculated by equation (3) and then plotted into a graph as given in Fig. 5b. This graph is very useful to observe softening/hardening phenomena and also to determine at which cycle the crack (if it appears) is initiated.

$$\sigma_{s,avg,amp} = \frac{\sigma_{s,max} - \sigma_{s,min}}{2} \quad (3)$$

The beam was subjected into two stages of the cyclic bending test. Firstly, the beam was induced to the cyclic bending loading with a plastic strain amplitude of $\epsilon_{a,pl} = 4.0 \times 10^{-4}$ for 2000 cycles and the average stress amplitude values (Fig. 5b) remain constant. Afterwards, the beam was also subjected to 2000 further bending cycles by increasing the plastic strain amplitude to $\epsilon_{a,pl} = 6.5 \times 10^{-4}$. Selected cyclic hysteresis loops (see Fig. 5a) show that Young's modulus of the beam gradually decrease at a cycle number >3000 and a crack is observed after the end of the test as given in Fig. 6 (a-b). Moreover, Fig. 5b shows that the average stress amplitude significantly decrease after cycle number of 3200 and it is believed that the crack was initiated at this point. The crack with the length of $\sim 1.5 \mu\text{m}$ is measured from the beam (see Fig. 6b) and grain coarsening is also observed from the area close to the crack (see Fig. 6c). The mechanism of the crack formation, grain coarsening, and their interaction must be studied further.

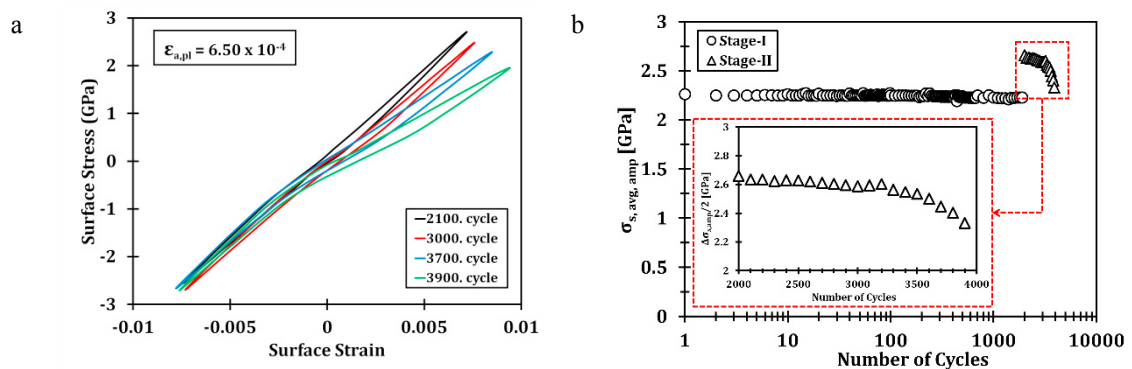


Fig. 5. (a) Selected cyclic hysteresis loop of the beam at plastic strain amplitude of stage-II (6.5×10^{-4}); (b) The average stress amplitude values ($\Delta\sigma_{s,amp}$) were calculated as a function of the number of the cycle.

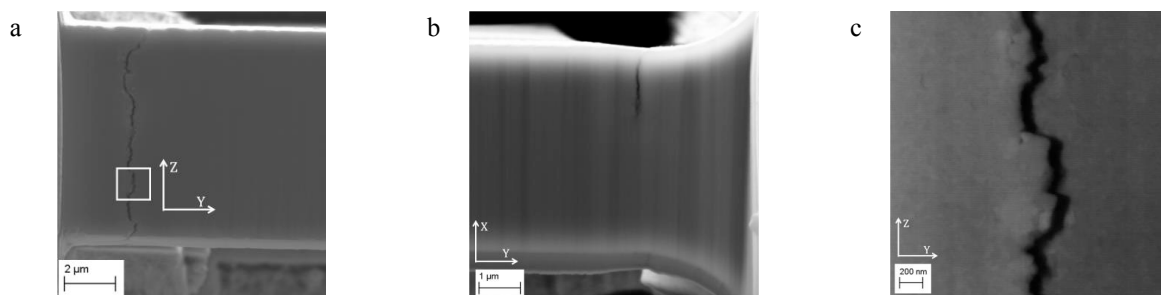


Fig. 6. SE images of the beam after 4000 cycles observed from (a) top view and (b) side view; (c) BSE images of microstructure of the beam after 4000 cycles at the position marked on (a). The axis in all images is corresponding with the axis described in Fig. 1a.

4. Conclusion

The porosity-free and homogenous nc $\text{Co}_{67\text{wt}\%}\text{-Cu}_{33\text{wt}\%}$ films have been successfully synthesized through the pulsed electrodeposition for up to 350 μm film thicknesses. Nano-sized grain of ~ 23 nm and supersaturated solid solution Co-Cu are observed in deposited nc Co-Cu films.

As-deposited nc Co-Cu has a good thermal stability at an annealing temperature of 300°C. Phase decomposition is indicated by the increase of hardness and the observed lattice distortion at this annealing temperature (300°C), where the grain size can be maintained below 50 nm. As deposited nc Co-Cu has a good thermal stability for up to 400°C. Annealing at higher temperatures (450°C and 600°C) leads to a more pronounced grain coarsening but interesting microstructure and phase decomposition are reported. Further works are required to study phase decomposition in nc Co-Cu.

Initial cyclic micro-bending tests show that the micro beam of nc Co-Cu has a good fatigue resistance for up to 2000 cycles at the plastic strain amplitude of $\epsilon_{a,\text{pl}} = 4.0 \times 10^{-4}$. However, a crack is observed on the micro beam after being subjected to 2000 further cycles at the higher plastic strain amplitude ($\epsilon_{a,\text{pl}} = 6.5 \times 10^{-4}$).

Acknowledgements

We gratefully express much thanks to the German Academic Exchange (DAAD) for supporting the funding of this research under the Graduate Scholarship Program (funding-ID: 57320205).

References

- Gleiter, H., 1989. Nanocrystalline materials. *Progress in Material Science* Vol. 33, pp 223-315.
- Meyers, M.A., Mishra, A., Benson, D.J., 2006. Mechanical properties of nanocrystalline materials. *Progress in Material Science* 51, 427-556.
- Bachmaier, A., Motz, C., 2014. On the remarkable thermal stability of nanocrystalline cobalt via alloying. *Material Science and Engineering A* 624, pp 41-51.
- Molonari, A., Libardi, S., Leoni, S. P., 2010. Role of lattice strain on thermal stability of nanocrystalline FeMo alloy. *Acta Materialia* 58, pp 963-966.
- Hibbard, G.D., Aust, K.T., Erb, U., 2006. The effect of starting nanostructure on the thermal stability of electrodeposited nanocrystalline Co. *Acta Materialia* 54, pp 2501–2510.
- Bachmaier, A., Pfaff, M., Stolpe, M., Aboufadi, H., Motz, C., 2015. Phase separation of supersaturated nanocrystalline Cu-Co alloy and its influence on thermal stability. *Acta Materialia* 96, pp 269-283.
- Bachmaier, A., Stolpe, M., Müller, T., Motz, C., 2015. Phase decomposition and nano structured evolution of metastable nanocrystalline Cu-Co solid solution during thermal treatment. *IOP Conf. Series: Materials Science and Engineering* 89 (2015) 012017.
- Hibbard, G., Aust, K.T., Palumbo G., Erb, U., 2001. Thermal stability of electrodeposited nanocrystalline cobalt. *Scripta Materialia* 44, pp 513-518.
- Lu, L., Wang, L.B., Ding, B.Z., Lu, K., 1999. High tensile ductility in nanocrystalline copper. *Journal of Material Research*, Volume 15, pp 270-273.
- Müller, T., 2014. Pulsed electrodeposition of nanocrystalline Co and Co/Cu alloys. Master thesis at Saarland University.
- Mughrabi, H., Höppel, H.W., 2010. Cyclic deformation and fatigue properties of very fine-grained metals and alloys. *International Journal of Fatigue* 32, pp 1413-1427.
- Kapp, M.W., Kremmer, T., Motz, C., Yang, B., Pippan, R., 2017. Structural instabilities during cyclic loading of ultrafine-grained copper studied with micro bending experiments. *Acta Materialia* 125, pp 351-358.